

**Exzellenzcluster**  
**Cognitive Interaction Technology**  
Kognitronik und Sensorik  
Prof. Dr.-Ing. U. Rückert

# **Ultra-wideband Based Indoor Localization of Mobile Nodes in ToA and TDoA Configurations**

zur Erlangung des akademischen Grades eines

**DOKTOR-INGENIEUR (Dr.-Ing.)**

der Technischen Fakultät  
der Universität Bielefeld

genehmigte Dissertation

von

**M.Sc. Reza Zandian**

Referent: Prof. Dr.-Ing. Ulrich Rückert



**Exzellenzcluster**  
**Cognitive Interaction Technology**  
Kognitronik und Sensorik  
Prof. Dr.-Ing. U. Rückert

# **Ultra-wideband Based Indoor Localization of Mobile Nodes in ToA and TDoA Configurations**

This dissertation is submitted for partial  
fulfilment of the degree of

Doctor of Philosophy

from technology department  
of University of Bielefeld

Submitted by:  
**M.Sc. Reza Zandian**

Supervisor: Prof. Dr.-Ing. Ulrich Rückert



# Acknowledgements

At first and the most, I would like to express my special gratitude to Professor Dr. Ulf Witkowski for supervising me during this work and also for his endless support in both technical and non-technical matters. Without his encouragement, I would not be able to reach to this stage of my life. Thank you for trusting me and providing me enough freedom to develop my own ideas and learn new fields of science and skills.

I would like to acknowledge Prof. Dr. Ulrich Rückert for accepting me in his group and providing me the possibility of pursuing my PhD degree.

I would like to admire and thank Mr. Engelbert Vahle from South Westphalia University of Applied Science for his unbelievable support both technically and emotionally in the laboratory. Thank you very much for your brilliant solutions and ideas in developing the trial setups and also your support in performing practical experiences.

I would like to acknowledge gratefully Mr. Amin Shirmohammadi, Mr. Hamed Movahedipour and Mr. Samuel Shimelis Yigezu for accurate proof-reading of my dissertation and their valuable comments and suggestions which definitely helped me to improve the quality of the manuscript in terms of scientific content as well as grammar.

Also special thanks to my friends in Soest who supported me emotionally and motivated me in my work and shared with me unforgettable moments of life.

I have to be thankful to my mother for spending most of her life to grow me up with difficulties and prayed for me in severe situations.

Last but not the least, I would like to acknowledge almighty God for keeping me healthy and inspiring me with new ideas and always brightened me with solutions to my problems.



# Abstract

This thesis discusses the utilization of ultra-wideband (UWB) technology in indoor localization scenarios and proposes system setup and evaluates different localization algorithms in order to improve the localization accuracy and stability of such systems in non-ideal conditions of the indoor environment.

Recent developments and advances of technology in the areas of ubiquitous Internet, robotics and internet of things (IoT) have resulted in emerging new application areas in daily life in which localization systems are vital. The significant demand for a robust and accurate localization system that is applicable in indoor areas lacking satellites link, can be sensed. The UWB technology offers accurate localization systems with an accuracy of below 10cm and covering the range of up to a few hundred meters thanks to their dedicated large bandwidth, modulation technique and signal power.

In this thesis, the technology behind the UWB systems is discussed in detail. In terms of localization topologies, different scenarios with the focus on time-based methods are introduced. The main focus of this thesis is on the differential time of arrival localization systems (TDoA) with unilateral constellation that is suitable for robotic localization and navigation applications.

A new approach for synchronization of TDoA topology is proposed and influence of clock inaccuracies in such systems are thoroughly evaluated. For localization engine, two groups of static and dynamic iterative algorithms are introduced. Among the possible dynamic methods, extended Kalman filter (EKF),  $H_{\infty}$  and unscented Kalman filter (UKF) are discussed and meticulously evaluated.

In order to tackle the non-line of sight (NLOS) problem of such systems, for detection stage several solutions which are based on parametric machine learning methods are proposed. Furthermore, for mitigation phase two solutions namely adjustment of measurement variance and innovation term are suggested. Practical results prove the efficiency and high reliability of the proposed algorithms with positive NLOS condition detection rate of more than 87% .

In practical trials, the localization system is evaluated in indoor and outdoor arenas in both line of sight and non-line of sight conditions. The results show that the proposed detection and mitigation methods can be successfully applied for both small and large-scale arenas with the higher performance of the localization filters in terms of accuracy in large-scale scenarios.



# Nomenclature

3GPP	Third Generation Partnership Project
A/D or ADC	Analogue to Digital Converter
ADS-TW	Asymmetric Double Sided Two-Way Ranging
AHF	Adaptive H-infinity Filter
AKF	Adaptive Kalman Filter
AoA	Angle of Arrival
ARM	Advanced RISC Machines
ASIC	Application-Specific Integrated Circuit
BEKF	Biased EKF
BLE	Bluetooth Low Energy
BPM	Burst Position Modulation
BPSK	Binary Phase Shift Keying
CAN	Controller Area Network
CDC	Communications Device Class
CDF	Cumulative Distribution Function
CDKF	Central Difference Kalman Filter
CEP	Circular Error Probability
CIR	Channel Impulse Response
CKF	Cubature Kalman Filter
CMSIS	Cortex Microcontroller Software Interface Standard
CoT	City of Things
COTS	Commercial Off-the-shelf
CRLB	Cramer-Rao Lower Bound
CSI	Chirp Spread Interface

DMA	Direct Memory Access
DoD	Department of Defense
DR-TW	Double Response Two-Way
DS	Direct Sequence
DSCR-TW	Double Sided Cascaded Reply
DS-TW	Double Sided Two-Way
ECC	Electronic Communications Committee
EDGE	Enhanced Data GSM Environment
EIRP	Effective Isotropic Radiated Power
EKF	Extended Kalman Filter
eLoran	Enhanced Long Range Aid to Navigation
EnKF	Ensemble Kalman filter
FAT	File Allocation Table
FCC	Federal Communications Commission
FNR	False Negative Rate
FPR	False Positive Rate
G-D	Gradient-Descent
G-N	Gauss-Newton
GHKF	Gauss-Hermite Kalman filter
GPS	Global Positioning System
GSM	Global System for Mobile communications
GUI	Graphical User Interface
HAL	Hardware Abstraction Layer
I <sup>2</sup> C	Inter-Integrated Circuit
IEEE	Institute of Electrical and Electronics Engineers
IMU	Inertial Motion Unit
INS	Indoor Navigation System
IoT	Internet of Things
IPS	Indoor Positioning Systems
IR-UWB	Impulse Radio UWB
ISM	Industrial Scientific Medical

JBSF	Jump Back and Search Forward
JPD	Joint Probability Distribution
KNN	k-th Nearest Neighbor
L-M	Levenberg- Marquardt
LBS	Location Based Services
Li-Po	Lithium-Polymer
LL	Low Level
LoRa	Long Range
LORAN	Long Range Aid to Navigation
LoRaWAN	Long Range Wide Area Network
LOS	Line of Sight
LPWAN	Low-Power Wide-Area Network
LS	Least Square
LTE	Long-Term Evolution
M2M	Machine to Machine
MB-OFDM	Multi-Band Orthogonal Frequency Division Multiplex
MEKF	Modified EKF
MFV	Mean of Features Voting
ML	Maximum Likelihood
MPC	Multi-Path Components
MSD	Mass Storage Device
NB	Naive Bayes
NB-IoT	Narrowband Internet of Things
NFC	Near Field Communication
NLOS	Non-Line of Sight
NOR	Not Or
OOK	On-Off Keying
PAM	Pulse Amplitude Modulation
PCA	Principal Component Analysis
PCB	Printed Circuit Board
PDF	Probability Distribution Function

PHR	Physical Layer Header
PHY	Physical Layer
PI	Proportional Integrative
PID	Proportional Integrative Differential
PII	Proportional Integrative Integrative
PMR	Peak Path to Mean Power Ratio
PoA	Phase of Arrival
PPM	Pulse Position Modulation
PR	Pseudo-Random
PSD	Power Spectrum Density
PSM	Pulse Shape Modulation
PVA	Position Velocity Acceleration
QPSK	Quadrature Phase Shift Keying
RFID	Radio Frequency Identification
RLS	Recursive Least Square
RMSE	Root Mean Squared
RSS	Received Signal Strength
RSSI	Received Signal Strength Indicator
RTLS	Real Time Location System
S/N or SNR	Signal to Noise Ratio
SBS	Serial Backward Search Algorithm
SDS-TW	Symmetric Double Sided Two-Way Ranging
SECDED	Single Error Correction Double Error Detection
SFD	Start of Frame Delimiter
SHR	Synchronization Header
SMA	Subminiature version A
SOEKF	Second Order Extended Kalman Filter
SPI	Serial Peripheral Interface
SS-TW	Single Sided Two-Way
STD	Standard Deviation
SVM	Support Vector Machines

TDoA	Time Difference of Arrival
TFC	Time Frequency Code
TH	Time Hopping
TIE	Time Interval Error
TNR	True Negative Rate
ToF	Time of Flight
TPR	True Positive Rate
UART	Universal Asynchronous Receiver-Transmitter
UKF	Unscented Kalman Filter
USB	Universal Serial Bus
UWB	Ultra-wideband
Wi-Fi	Wireless Fidelity
WLS	Weighted Least Square



# Table of content

<b>1. Introduction.....</b>	<b>1</b>
1.1. Indoor Localization Techniques .....	7
1.2. Motivation of the Thesis .....	12
1.3. Outline of the Thesis .....	14
<b>2. Ultra-wideband Technology .....</b>	<b>15</b>
2.1. UWB Characteristics .....	17
2.2. Modulation Concepts and Coding.....	20
2.2.1. Single band modulation.....	21
2.2.2. Multiple access techniques .....	23
2.2.3. Multi-band modulation .....	26
2.3. UWB Frame Format and IEEE Standard.....	28
2.3.1. Preamble .....	29
2.3.2. Start Frame Delimiter (SFD) .....	30
2.3.3. Physical Header (PHR).....	31
2.4. First Path Detection.....	32
2.4.1. Peak detection techniques.....	32
2.4.2. Two-step ToA estimators .....	32
2.4.3. Threshold-based techniques.....	33
2.5. Analysis of Commercial Platforms .....	34
2.5.1. Ubisense .....	35
2.5.2. Time Domain .....	35
2.5.3. Zebra.....	36
2.5.4. Nanotron.....	37
2.5.5. beSpoon.....	37
2.5.6. Decawave .....	38
2.5.7. Comparison of the COTS modules.....	39
<b>3. Topologies of Localization.....</b>	<b>41</b>
3.1. Clockless Approaches .....	43

3.1.1. Signal strength .....	43
3.1.2. Angle of Arrival (AoA) .....	43
3.1.3. Phase of Arrival (PoA) .....	44
3.2. Time of Arrival (ToA).....	45
3.2.1. Single Sided Two-Way ranging (SS-TW) .....	46
3.2.2. Double Sided Two-Way ranging (DS-TW) .....	48
3.2.3. Double Response Two-Way ranging (DR-TW) .....	50
3.2.4. Double Sided Cascaded Reply (DSCR).....	51
3.2.5. Comparison of the ToA approaches .....	52
3.3. Time Difference of Arrival (TDoA) .....	53
3.3.1. Multilateral TDoA.....	55
3.3.2. Unilateral TDoA .....	56
3.3.3. Comparison of the TDoA approaches .....	63
<b>4. Clock Management.....</b>	<b>65</b>
4.1. Clock Time Interval Error (TIE) .....	66
4.2. Modeling of the Clock Behavior .....	67
4.3. Clock TIE Filtering Methods .....	69
4.4. Implementation Aspects.....	72
4.4.1. Time rounding issue .....	72
4.4.2. Detection of missing packets.....	74
4.4.3. Outlier detection and filtering.....	76
4.5. Clock Source Analysis .....	77
4.5.1. Frequency accuracy analysis .....	78
4.5.2. Frequency stability analys is .....	80
4.5.3. Clock noise analys is .....	81
4.5.4. Thermal dependencies and warm-up.....	82
4.6. Performance Comparison .....	83
<b>5. Localization Algorithms.....</b>	<b>87</b>
5.1. Modeling of the TDoA Topology .....	88
5.1.1. Measurement model of the TDoA.....	88
5.1.2. Model of the system's dynamics.....	91
5.2. Static Iterative Techniques.....	94
5.2.1. Gradient-Descent (G-D) method.....	95
5.2.2. Newton method.....	97

5.2.3. Gauss-Newton (G-N).....	98
5.2.4. Levenberg-Marquardt (L-M).....	99
5.2.5. Performance comparison .....	100
5.3. Dynamic Iterative Techniques.....	105
5.3.1. Extended Kalman Filter .....	107
5.3.2. Unscented Kalman Filter.....	110
5.3.3. H-infinity Filter .....	114
5.3.4. Performance comparison .....	117
<b>6. NLOS Identification and Mitigation.....</b>	<b>127</b>
6.1. Problem Definition.....	129
6.2. Data Collection and Preparation.....	131
6.2.1. Details of the measurement setup.....	132
6.2.2. Features selection .....	132
6.2.3. Data cleaning and labeling .....	139
6.3. NLOS Identification Algorithms .....	141
6.3.1. Naive Bayes method .....	142
6.3.2. Binary classification method .....	145
6.3.3. Logistic regression method.....	147
6.3.4. Non-parametric algorithms .....	149
6.3.5. Performance evaluation and comparison .....	151
6.4. Mitigation Techniques.....	157
6.4.1. Measurement noise variance manipulation .....	158
6.4.2. Innovation term manipulation .....	160
<b>7. System Implementation Aspects.....</b>	<b>165</b>
7.1. Hardware Design .....	165
7.1.1. Prototype development .....	166
7.1.2. Peripheral components .....	167
7.1.3. Energy efficiency constraint .....	169
7.2. Software Design.....	172
7.2.1. Communication and user interaction .....	172
7.2.2. Debugging and data storage.....	174
7.2.3. Developed module software architecture .....	176
7.2.4. Frame formatting .....	179

<b>8. Experimental Results and Analysis .....</b>	<b>181</b>
8.1. Small-scale Indoor Arena .....	181
8.2. Large-scale Indoor Arena .....	189
8.3. Outdoor Experiments .....	193
8.4. Results Evaluation and Conclusion .....	196
<b>9. Conclusion.....</b>	<b>197</b>
<b>Appendices .....</b>	<b>203</b>
<b>List of Figures.....</b>	<b>211</b>
<b>List of Tables .....</b>	<b>219</b>
<b>Bibliography .....</b>	<b>221</b>

# 1. Introduction

It is not straightforward to find a unique definition of navigation and positioning in the literature. Paul Groves [1] defines the science of navigation as acquiring the position and velocity of a dynamic entity (human or objects) with reference to a stationary landmark (anchor, beacon or specific natural item). In [2] the location and position is defined to be the unambiguous placement of an entity with respect to a reference point.

Following terms are often used in the literature in the areas of localization and positioning applications [1, 3]:

- Positioning: Determining the location as well as the angular direction of an object or human with reference to certain landmarks in the vicinity
- Localization: Determining only the location of a target entity with reference to landmarks
- Tracking: Constantly observing the position of the target entity and probably recording the undergone path by a third observer
- Ranging: Calculating the distance of a point which needs to be localized to a landmark or stationary anchor
- Bearing: Calculating the angle of a point which needs to be localized in reference to a landmark or stationary anchor
- Navigation: supervision and steering of a person or an object through a certain path to move towards a desired destination

Finding the position of human or objects has been a point of concern for many decades. The initial demand of localization dates back to localization and navigation of ships in the oceans and navigation of trading caravans on common trading roads. Common solutions of those days were localization based on celestial navigation or sailing and traveling close to specific landmarks such as shores, mountains, lakes or rivers and lighthouses. Around three hundred years ago, devices such as sextant or magnetic compass helped to improve localization and navigation. However, all these solutions were prone to inaccuracies. The main sources of these inaccuracies were mostly seasonal changes of climates and celestial phenomena, erosion of landmarks and changes made by human or natural forces at the time.

## 1 Introduction

---

The first practical radio system which was introduced by Marconi around the late nineteenth century, opened up a new chapter in the science of communication and radio-based localization. The first use of radio waves for the localization was in 1904 by the invention of radar technology for detecting ships and other metallic objects. Later developments mainly aimed at tracking and detecting aircrafts in the Second World War [4]. The military requirements of that era and demands for highly reliable, stable and accurate localization and navigation system led to the appearance of terrestrial navigation systems.

Terrestrial radio localization was a very successful solution that appeared early in the 20<sup>th</sup> century replacing the traditional methods. Terrestrial radio stations were initially used for localization and navigation in maritime sector to localize ships covering a large area. A few examples of these systems are DECCA<sup>1</sup> system which was developed during World War II, LORAN<sup>2</sup> (Long Range Aid to Navigation) aimed at navigation in long-range area which was superseded by eLoran, CONSOL<sup>3</sup> also known as “Sonne” in Germany also developed during the World War II, GEE<sup>4</sup> which was developed at the same time as CONSOL and was in use until the late 1960s and the last one was OMEGA which was operational between years 1968-1997 [3, 5].

The DECCA system was one of the most famous radio-based navigation systems which was used for coastal shipping. This system was developed based on a chain of stations containing a master station and several substations positioned around the master station with distances around 100km. The localization is performed by measuring the phase difference of a continuous wave transmitted by the master station and the substations. The location is estimated based on the concept of intersection point of hyperbolic curves [6].

The CONSOL system benefited from a different localization concept in which the angle of the radio beam in reference to a transmitter is measured. This is performed using three antennas installed at a distance of 1km in a line. The center antenna is an omnidirectional transmitter sending synchronization data. A keying unit is used to switch the signal to the side antennas as well as phase shifting it forward or backward for each antenna. As an example, the left antenna would transmit a 90° shifted data containing a modulated dot Morse sign and the right one would transmit -90° phase shifted signal with the modulated data of dash Morse sign. The phase shifting is changed gradually during a certain time. At the receiver, the bearing of the measurement point to the transmitter is related to the number of dashes and dots measured in each sequence. Each sequence is the time between the synchronization signal and the point where the phases of the other

---

<sup>1</sup> Made by British Company Decca

<sup>2</sup> Developed by US Navy

<sup>3</sup> Developed by Germany during the WW II

<sup>4</sup> Developed by UK during the WW II

two signals are matching. The system was widely in service in Europe and was eventually turned off in 1991 [1].

The LORAN system had several development phases starting from LORAN-A which was eventually replaced by B and C versions. Its constellation form was similar to DECCA in which a chain of stations including a main and up to five side stations were used. However, the difference was in the transmission concept where scheduled groups of impulses are transmitted. Therefore, the localization was performed in the time domain by measuring the difference time of arrival of the signals from different stations. The system was ultimately shut down in 2010 as it was no longer required [3].

The eLoran (Enhanced LORAN) system was developed as an improvement to LORAN-C and is considered as a backup for satellite-based systems such as GPS (Global Positioning System) due to its high accuracy and reliability at a comparable level to GPS. The new features of this system compared to its predecessors are the availability of a data channel for communication purposes, identification of the stations, improvements in the accuracy of the localization and availability of a global clock time [6].

The OMEGA system was the first radio location system designed based on transistor elements in the early 1970s developed with the aim of providing a global navigation system. This system consisted of 8 transmitters distributed around the globe and transmitting signals in the form of pulses in a very low frequency range (10.2KHz – 11.33KHz). The location of the target is calculated by measuring the phase difference of the signals received from each station and performing hyperbolic curve intersection technique [6]. Due to success of the GPS system and high maintenance costs, this system was shut down in 1997.

Description of the mentioned systems including their features is listed in Table 1.1 for comparison purposes.

Table 1.1: Characteristics of different terrestrial radio-based localization systems [6]

Platform	Frequency range (KHz)	Localization method	Operation period	Radio range (km)	Accuracy
DECCA	70 -129	Phase comparison	1946-1999	555 day 140-450 night	50-100m
LORAN-C	100	Time comparison	1957-2010	1000	250-460m
eLoran	100	Time comparison	1995-Present	1000-1700	400m
OMEGA	10.2-11.333	Phase difference	1968-1997	18500	5-10km
GEE	22000-85000	Hyperbolic	1942-1970	300-650	150-1600m
CONSOL	257-363	Angular difference	1940-1991	1500	0.6°

## 1 Introduction

---

Typical problems of the terrestrial radio location systems are their dependency on the weather conditions, seasonal changes, limited covering range, complexity of installations and maintenance costs. These problems led to appearance of new localization techniques based on satellites.

Satellite-based localization systems appeared in the early 1960s by developing Transit system [1]. Later in 1973, the GPS constellation was developed parallel to the development of OMEGA [2]. Initially the system was used solely for military applications however released for civilian purposes later in the 1990s which yields in booming of the navigation-based applications. This system has currently more than 30 satellites in orbit capable of providing an accuracy of around 5 meters [7]. A similar system was developed by Russians under the name GLONASS (Global Navigation Satellite System) in 1982. The completion of this system was achieved in 2005 with 24 satellites in orbit. The accuracy of this system is claimed to be around 5 to 7 meters [8]. The third constellation is designed mainly for civilian and commercial applications that is introduced by European Union under the name Galileo which is started in 2005 and by now has 18 satellites in orbits. This system is free to access and provides higher accuracy than the GPS system (around 1 meter) [9]. The localization in all the three systems is based on the time of arrival concept which demands accurately synchronized clock of the satellites. This is normally achieved by precise atomic clocks which is also monitored by ground stations. There are a few other systems which have been released by other countries mainly for covering local regions.

Chronological appearance of the mentioned radio-based localization systems are demonstrated in Figure 1.1 graphically.

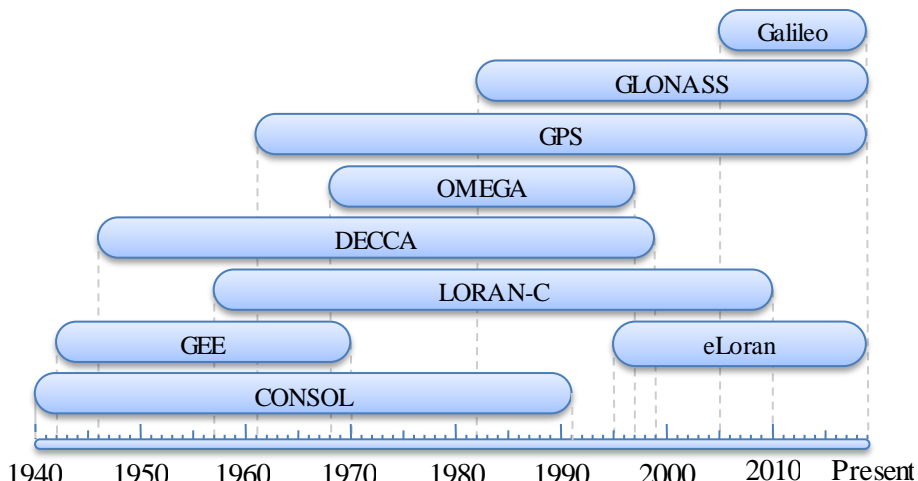


Figure 1.1: Chronological appearance of the radio-based localization technologies which are mainly used for outdoor navigation applications

Availability of the satellite-based localization systems to civil applications, led to rapid growth of localization and navigation market as well as emerging new application areas [3]. Development of cellular communication networks as well as the Internet at one hand and miniaturization of communication and positioning modules on the other hand, increased the demand for localization in the ubiquitous form in daily life. However, the satellite-based techniques have certain limitations such as range accuracy, fading of the signal inside the building and behind the barriers such as walls, dependency on the weather conditions and requirement of having direct line of sight for optimum performance. This was a problem as most of the new applications demanded a higher accuracy, especially in indoor areas. This led to the appearance of a new area in science, discussing the localization and navigation techniques in indoor areas independent from the current satellite-based techniques.

During the last two decades, several communication and positioning systems have been developed to address the demand for new applications by combining positioning and communication features into a unique system. This, resulted in the emergence of new applications and services known as LBS (Location Based Services) [2]. The LBS are generally defined to be a set of computer services that link the location of a user or an object to the context sensitive information in the vicinity of that entity. Some sources in the literature define the LBS to be a service based on three aspects namely the ability to use the data, inferring the location and communicating the information to surroundings [10].

The application range of LBS services is very wide and is constantly increasing. One example is navigation of customers in a mall and guiding them to available markets in the vicinity or navigating them to a certain shop through the building [11, p. 1347]. Another example is spotting a free parking slot in a park house and guiding the driver to that point. It could also be used to provide position sensitive advertisement to customers when they are moving around a market or advertising certain products or offers of a shop when they are inside the market. Indoor localization and navigation have also a huge number of applications in robotics either in household or industrial sector. Examples are vacuum cleaner robots, automated lawn mowers, automated lift trucks, etc. List of a few classical applications of LBS are listed below [10]:

- Emergency
- Safety and security
- Tracking and monitoring
- Traffic telematics
- Personal navigation
- Retail
- Smart advertisement
- Resource control
- Billing
- Commerce
- Management
- Logistics
- Gaming
- Social networking
- Elderly assisting services
- Child control

Considering the mentioned range of applications in mind, it can be seen that the LBS services and more generally, indoor localization science, is a common intersection point of many sciences. As an example, robotic science could be named which could not be developed so far without recent developments in the area of indoor localization. Additionally, many dependencies between the LBS applications and other branches of science can be witnessed. A few of these areas of science are listed in Figure 1.2.

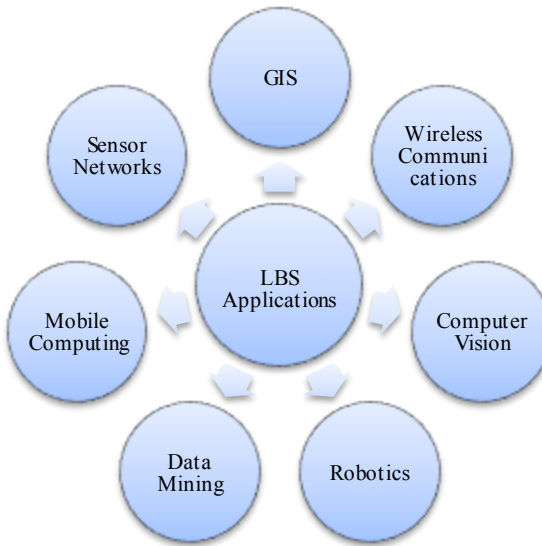


Figure 1.2: List of a few branches of science which are heavily dependent on indoor localization techniques that are integrating LBS services [10]

Application area of the indoor localization and navigation systems is constantly spreading. A few examples of new and developing areas are autonomous driving, cellphone indoor positioning, commercial drone services, industrial machines, security and safety, autonomous household robots and smart buildings. Use of IPS (Indoor Positioning Systems) in governmental organizations is also finding its place. Examples are localizing and tracking of firefighters in rescue missions, police officers in security and crime control cases and finding exit ways in case of emergency in buildings [12, p. 245].

Besides the myriad applications of LBS services, IoT (Internet of Things) could be mentioned which also addresses use of localization information in a wide range. IoT is the concept of interconnecting many possible electronic devices including sensors and actors, computers, smartphones, wearables, etc. with the aim of internally exchanging information in the form of M2M (Machine to Machine) for coping with common tasks [13, p. 8957]. It is believed that 75% of the IoT applications are linked to the integration of positioning techniques [14].

The IoT itself is covering two other fields of applications which are widely integrating positioning techniques especially indoor methods. One is smart home or smart buildings which is focusing on applications of IoT in indoor areas. Some of applications are controlling the lighting or managing the air condition systems based on the human presence in a room [15]. The second field is a broader aspect of IoT which is called CoT (City of Things) [16]. City of Things addresses the integration of IoT, data mining, cloud computing and networking solutions for the sake of improving the quality of life [17]. Possible applications of indoor localization in CoT are smart grids, mobility improvement by interconnecting vehicles which could be used for traffic control, smart parking, smart museums, smart bicycles or air quality control over wireless sensor networks [18]. The implementation of these technologies is not possible without the direct benefit of localization and navigation techniques.

The fourth industrial revolution, known under the term Industry 4.0, is another range of services based on the industrialized version of IoT systems which are also in close connection with indoor localization and positioning methods. The main idea of Industry 4.0 is integration of information and technology-based services such as IoT into manufacturing, business and engineering processes that are aimed at improving production efficiency, production rate, product quality and environmental protection [19]. Typical applications of Industry 4.0 services that are integrating positioning techniques are product monitoring and tracking in different stages of production, human safety in the areas where close cooperation of human workforce and machines are expected, smart warehouses and logistics.

In the next section, common indoor localization techniques are discussed which build up a roadmap to enlighten the motivations of discussing the importance of indoor localization systems especially those based on UWB (Ultra-wide Band) technique.

## 1.1. Indoor Localization Techniques

During the last two decades, many efforts are made to develop new localization and positioning methods with higher accuracy and reliability compared to those provided for the outdoor purposes. Reviewing the literature which address comparison and evaluation of different indoor positioning technologies, it can be seen that, different classifications are applied to describe such systems. One parameter for classification is whether a certain technology needs specific infrastructure (ex. cellular network) called "active" or it can function standalone with no support of other devices (motion sensors) called "passive" [20]. Another classification is performed based on the signal characteristics.

Brena et al. [20] describe the three steps of localization to be "evidence" where a physical signal is measured by a device, "range estimation" where the distance

## 1 Introduction

---

information is extracted from the measurement and finally the combination stage where the location of the entity (human or object) is extracted by combining the range information. Concerning the first step which is evidence, different physical characteristics such as light, sound, magnetic field, radio wave, air pressure, speed and acceleration, etc. are used with the aim of alleviating the extraction of position information with a better accuracy in indoor area. List of a few of possible methods based on the aforementioned characteristics is demonstrated graphically in Figure 1.3.

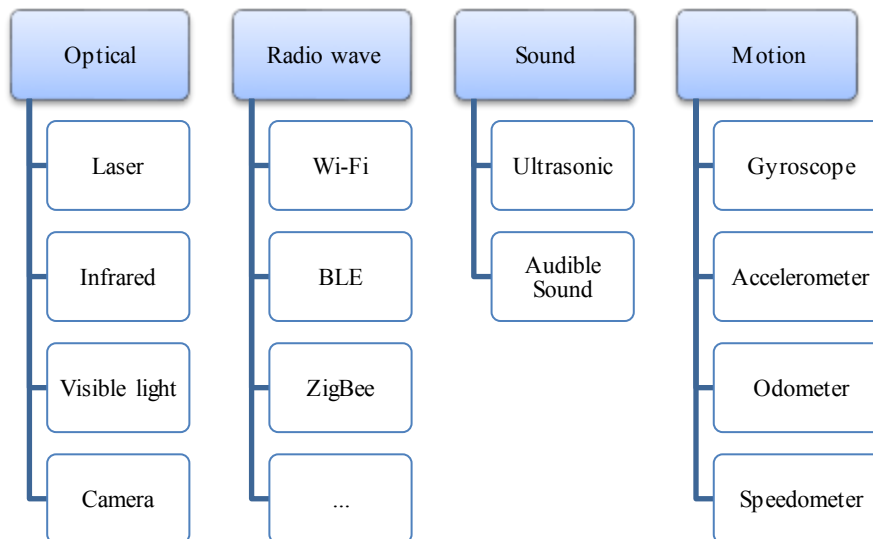


Figure 1.3: List of different physical characteristics of measurement signal which could be used for range estimation and their related sensory device or technology which integrates these characteristics

The mentioned signal characteristics and their corresponding localization technologies differ in parameters such as implementation costs, accuracy, range, scalability and robustness [12, p. 246]. The use of a certain technology is mainly dependent on the answers of the questions such as how accurate is the system? Where the system should be applied? Is the installation of infrastructure tolerated? How large is the coverage area? etc. For example, an accuracy of a few meters would be enough to guide a customer in a mall house but for autonomous landing of a drone in indoor area, higher accuracy in centimeter level is required. Considering such factors, one can decide which technology is the most suitable for that specific purpose. A few of these technologies including their pros and cons are discussed below:

- *Optical technologies*: this area covers technologies which use transmission of photons as a means of location estimation. These could be in different ranges of the light spectrum including location estimation based on visible light [21] which could be implemented using a photocell or a camera or infrared [22].

Another light-based localization technique is laser [23]. The advantages of light-based technologies are good accuracy of range estimates starting from a millimeter to a few centimeters, low sensitivity to radio noises and mostly available at lower prices. However, they suffer from the facts that the transmitter and receiver should be in direct line of sight, they have limited range of coverage and they are often extremely sensitive to sunlight.

- *Sound-based technologies*: this type of systems benefit from the measurement of sound's time of travel in air. The low speed of sound compared to light has the advantage of using cheap and simple hardware to detect the distance accurately [20]. This technology is applicable in both audible frequency range as well as ultrasonic range that is normally at 40kHz [24]. The advantages are simplicity of implementation, accuracy within the range of a few centimeters, cost, multimodal localization and immunity against radio interference. The disadvantages are distortions in loud area and signal fading by passing through barriers which limits the technique only for line of sight cases.
- *Motion-based or inertial technologies*: these are based on the measurement of parameters such as physical displacement as used in odometer, speed in speedometer, acceleration which is measured by accelerometer or rotational speed which is measured by gyroscope [25]. These technologies are only able to provide relative position information of dynamic targets. In order to extract the absolute position, knowledge of a reference at the beginning of movement is necessary. For this reason, they are mostly used as supportive technology in conjunction with another positioning system to increase the accuracy and compensation of gradual drift from the real point. An example is "dead reckoning" system which is used together with GPS to spot the position of a car in tunnel where no GPS signal is available [26].
- *Radio-based technologies*: these are the most common technologies used in indoor positioning thanks to many features they provide. The most important feature is the ability to penetrate through barriers which means they are less vulnerable to non-line of sight cases which often occur in indoor applications. Other advantages of these systems are wide coverage area, good accuracy and omnidirectional availability of the signal in ubiquitous form. Disadvantages are signal interference with other communication systems, requirement of infrastructure and complexity of implementation.

Among the mentioned technologies, the radio-based methods better tolerate the challenging requirements of indoor positioning systems which are functionality in non-line of sight, wide coverage range and signal ubiquity. The common radio systems are however not specifically designed for localization. The functionality of localization of such systems are used beside their main function which is data transfer. There are many radio technologies which are also used in localization. The most commonly used technologies are discussed as follows:

- *Wi-Fi*: this technology is a common platform for providing Internet which is almost ubiquitous [27]. Many researches are performed to use Wi-Fi signal

for localization and positioning purposes. The advantages are no need for additional infrastructure for positioning purpose, large coverage area inside or even between the buildings and less sensitivity to signal blockage [12]. Disadvantages are poor localization accuracy, channel interference and sensitivity to movable objects. The position information is mostly extracted from measuring the signal strength index and generating a map of known positions of routers. This technique is known as "Fingerprinting" [28].

- *ZigBee*: originally designed for providing wireless personal area network with the focus on low data rate and short range applications. The ZigBee protocol is based on the IEEE 802.15.4 standard and offers good network security [29]. The advantages are moderate to low cost of the hardware and low energy consumption whereas the disadvantages are band interference to other technologies and requirement of specific infra-structure which is not as widely available as other technologies [12].
- *BLE*: (Bluetooth Low Energy) is another competitor of Wi-Fi which is widely available thanks to its integration in most smartphones. The BLE uses very small bandwidth compared to Wi-Fi and is designed for interconnection of electronic gadgets and sensors which usually have lower power consumption. Additional characteristics of BLE are high scan rate and handshake procedure [11, p. 1354]. Some of the advantages are possibility of placing beacons in the vicinity of the area without requiring specific infrastructure, very low power consumption, better accuracy compared to Wi-Fi [30], availability and low cost of the hardware. Disadvantages are signal interference as the applied frequency is common with other technologies, requirement of large number of nodes to achieve acceptable accuracy, lower covering range and sensitivity to non-line of sight scenarios [12].
- *RFID*: this technology uses radio wave for both communication to a certain electronic circuit as well as transferring power required for the circuit. The nodes are either in passive mode, active mode or support both modes. Each target node has a unique ID which could be used to identify the target when it is in close vicinity of a transmitter [20]. Possible applications are commutation control at control gates, equipment and baggage tracking, logistics, shops theft protection, medical applications and parcel delivery [31]. The benefits of this system are functionality in non-line of sight and simplicity of the working concept, however it suffers from low accuracy of localization, requirement of specific infrastructure, higher power consumption in active mode and large antenna required for transmitter [12].
- *UWB*: this technology provides very good localization accuracy in indoor area. It acts based on transmission of narrow impulses in time domain which demands wide bandwidth in frequency domain. This way, a good localization accuracy in the range of tenth of a meter can be achieved. High accuracy positioning which is achieved as a result of low sensitivity to multipath effect, low interference with other radio-based technologies and penetration capability through objects are among the advantages of this type. In contrast

to these features, complexity of implementation and higher cost of infrastructure can be mentioned as disadvantages [12].

- *Cellular networks*: many generation of cellular networks have been deployed so far starting with GSM, EDGE and now LTE networks. They all support cell phone localization by performing trilateration and measuring the distance of the device to several stations. The advantages are availability of the hardware in cell phones as well as the widespread availability of the required infrastructure which leads to larger coverage area, and low interference to other radio device thanks to dedicated licensed frequency band. Among the disadvantages are lower accuracy (in the range of 100m), low signal coverage in buildings and signal congestion in crowded area [12].
- LoRa: this technology is released by LoRa (Long Range) Alliance and is available in two versions: one is standalone LoRa which is based on point to point or star connection topology and another one is based on a cell-based infrastructure known under LoRaWAN which belongs to LPWAN group of communication standards [32]. This technology works in unlicensed spectrum of 868 MHz with long covering range of more than 30 km in line of sight and upload data rate of 50 kbps. Indoor positioning techniques based on LoRa are discussed in [32] in detail. Beside the good features such as long covering range and use of unlicensed band, drawbacks such as high cost of modules, lower accuracy compared to other methods, high rate of signal interference and requirement of infrastructure are issues to be considered when designing a positioning system based on LoRa technology.
- *Sigfox*: this technology is very similar to LoRa which is also based on the LPWAN network standards and benefits from ISM band (868-869 MHz or 902-928 MHz based on regions) for data transmission. However, the data rate is limited to a bandwidth of 100Hz, maximum baudrate of 12 bytes per second and maximum 140 messages per day [33]. Another difference is in modulation technique in that Sigfox applies frequency hopping approach using three different frequency channels [25]. Sigfox utilizes cell networks which proves its dependency on fixed infrastructure in the area of deployment. Typical localization techniques are using signal strength and mapping the measurement to locations using machine learning algorithms, data statistical approaches or "fingerprinting" [33].
- *NB-IoT*: This recently emerged technology is defined by 3GPP (Third Generation Partnership Project) to address the demand of IoT using small bandwidth (180 KHz) of LTE networks [34]. This narrow bandwidth is used for low data rate communication purposes of IoT devices with the maximum update rate of 250 Kbps. The network supports large number of devices in a cell with improved coverage compared to older generations. The dedicated narrow bandwidth of NB-IoT limits the position accuracy to below 50 meters [35]. From disadvantages of this technology, monthly cost of the network, high power consumption of the modules (120-300 mA) and dependency on LTE signal coverage could be mentioned [36].

## 1 Introduction

---

List of different radio-based localization technologies which can be applied for indoor localization and positioning are provided in Table 1.2.

Table 1.2: Comparison of different radio-based localization technologies and their attributes in terms of positioning

Technology	Frequency	Bandwidth	Accuracy	Range
Wi-Fi [20]	2.4/5 GHz	40/160 MHz	5-10 m	50-100 m
ZigBee [29]	2.4 GHz	80 MHz	1-2 m	100-250 m
BLE [37]	2.4 GHz	80 MHz	1-2 m	10 cm-10 m
RFID [38]	868 MHz	5 MHz	0.02-1 m	10-40 m
UWB [39]	3-10.5 GHz	>500 MHz	10-15 cm	50-100 m
Cellular networks [40]	900/1800 MHz (GSM)	200 KHz	500-600 m	Cell area
LoRa [32]	868 MHz	125/250/500 KHz	10-30 m	15-30 km
Sigfox [33]	868 MHz	100 Hz	50-100 m	200-300 m
NB-IoT [34]	800/900 MHz	180 KHz	50-100 m	Cell area

As it can be seen from Table 1.2, different radio ranging techniques with different attributes are available. The decision of choosing a certain technology depends mainly on the application. If long range of coverage in the order of between several buildings and not a very high accuracy is demanded, then cellular type of networks like GSM, NB-IoT, LoRa, etc. could be used. Other types of technology such as Wi-Fi or ZigBee are suitable to cover areas inside a building or between rooms but also here an accuracy better than 5 meters is hardly achievable. For smaller ranges in the scale of a room, BLE and RFID technologies are recommended as these provide very good accuracy but are limited to long range applications and extremely sensitive to non-line of sight scenarios. Among the mentioned technologies, the UWB technology provides a combination of mid-range coverage, stability in non-line of sight cases and high accuracy. For this reason the UWB technology was the selected choice of most of the research groups and companies for indoor localization scenarios in the recent years.

## 1.2. Motivation of the Thesis

The initial motivation behind our project and this thesis stems from a project requested by fire fighters requiring a navigation and tracking system which could be utilized in search and rescue scenarios in complex situations. The main idea was to provide assistive navigation information to fire fighters by a group of robots who are cooperating with fire fighters guiding them on their way in indoor area with lack of sight due to intensive smoke or dust. This complex scenario

could be only accomplished by radio-based techniques which are not sensitive to barriers and lack of vision. Among the available technologies UWB provides promising qualities such as good accuracy, large covering range, less sensitivity to multipath effect and less interference with other common radio technologies due to wide range of applied frequency band. Although tracking capability is also desired in such cases for monitoring the location of fire fighters, we have limited ourselves to a project topic addressing the navigation aspects of robots in indoor area for the initial section of the whole project.

The use of UWB technology and its challenges have been extensively studied by different research groups in the past decade. Many solutions are provided for improving the accuracy, overcoming the non-line of sight problems and reducing the complexity of utilization. However, after reviewing the literature it turned out that most of the proposed solutions and applications are addressing the tracking and monitoring applications only and are mostly limited to studies of stationary nodes. Only a few projects (ex. EIGER [41], NITICS [42] or [43] performed by ETH Zurich) address the navigational aspects of localization but even these are discussing only certain aspects of it and limit themselves to known conditions. Lack of elaborate research in this area was perceptible. Therefore, this thesis covers navigational aspects of UWB indoor localization systems which could be used for navigation of a group of robots.

Another required aspect for such a navigation scenario, is the ability to support multiple nodes simultaneously in a GPS alike structure. In this case, the performance of the system is not affected by the number of nodes to be localized and the location information should be provided to the target nodes themselves. Although such a topology already exists, it was seldom used for UWB systems due to implementation complexities of this scenario. This thesis addresses this issue by simplifying the implementation process wherever applicable and by bringing about new ideas with the goal of improving the performance and overall efficiency of the localization system.

Another issue which was not addressed properly in the literature is the mobility and dynamic behavior of the robots which is important in effective and successful implementation of the localization concept. Unlike many scientific papers which only consider stationary nodes for the sake of simplicity of the models, this thesis considers these dynamics aspects at all steps of implementation and modeling.

This thesis targets algorithms and techniques relevant to indoor localization and positioning with more focus on implementation aspects therefore the hardware related topics of UWB technology such as transceiver design in semiconductor level or antenna design techniques were not in the scope of this work.

### 1.3. Outline of the Thesis

This dissertation is based on 9 chapters which cover different segments of the proposed UWB indoor localization system starting from background concept to the theory of the algorithms and practical implementation aspects.

The second chapter covers the idea behind the UWB technology explaining the modulation concept, transmission methodologies and standards, frame formats and use of UWB systems in localization scenarios. At the end of this chapter, common available commercial systems are reviewed and compared.

Chapter 3 evaluates different localization topologies including the non-time based methods such as RSSI and AoA with the focus on the time based methods. Among the time-based methods, the main focus is on TDoA technique which is widely used in this work and is the base of the implemented algorithms.

In Chapter 4, clock synchronization issues of time based localization systems are addressed. A model is suggested which can effectively mitigate the time interval error and synchronize the clock of involved nodes. Also an extensive analysis is performed to evaluate the effect of different clock sources on the accuracy of localization system.

Evaluation of different localization algorithms from classical methods up to advanced iterative techniques is the subject of the fifth chapter. Typical localization algorithms are evaluated and compared including the model based methods and error compensation techniques.

Chapter 6 is dedicated to methods and algorithms developed for detection and mitigation of the NLOS effect which lead to improvement of overall accuracy. Several parameter-based methods as well as non-parametric machine learning algorithms are proposed and evaluated in this chapter. Also proper solutions are proposed for suppressing the bias error created as a result of NLOS conditions.

Chapter 7 explains the design aspects of the experimental setup including the hardware and software implementation and their features.

Many experiments are performed in indoor and outdoor areas in different test arenas in order to evaluate the performances of localization and NLOS identification and mitigation algorithms. The results of these experiments are the subject of Chapter 8.

The last chapter is conclusion and future works which summarizes the results of the thesis and enlightens the road map of the next steps of the work in the future.

## 2. Ultra-wideband Technology

The ultra-wideband technology generally refers to systems which utilize a fractional bandwidth larger than 20% of their center frequency or covering at least 500MHz of their absolute bandwidth. This range is measured by the difference of the higher and lower frequency of the bandwidth at the point where the emission gain is -10dB [44].

The term ultra-wideband has been coined for the first time by the US Department of Defense (DoD) around 1990 for a project which was employing short pulses of microwave for transmission as well as object detection in radar devices [2]. Tracing the earliest activities in the area of UWB, the projects which have been carried out in the early 1960s could be mentioned that were aimed at developing new technologies in radar systems. At that time, extraordinary characteristics of systems with a large bandwidth which could be applied for localization purposes have been discovered. These types of systems were used for military applications because they distribute the energy of narrow pulses in a wide frequency spectrum resulting in low detection probability by other parties [45, p. 4]. This feature has been achieved by defining very wide bandwidth for the signal and at the same time keeping the energy of the signal at low level. This way the transmitted signal appears at or even under the level of the background noise which is hardly detectable by frequency scanners and other wireless devices. In addition, these systems are immune to interference created by other narrowband radios.

Although the UWB technology had been invented long time ago, less attention has been paid to the great characteristics of large bandwidth mainly due to lack of regulations, proper algorithms and suitable measurement instruments. Furthermore, this technology was restricted to military activities between 1960 to 1990 and was mainly used as a highly secure communication technique rather than benefiting from its localization potentials [2]. This has changed as Federal Communications Commission (FCC) of US in 2002 defined a set of regulations for use of UWB devices and dedicated a license-free spectrum to such devices in the range of 3.1–10.6 GHz [45, p. 5]. A few years later in 2007, Electronic Communications Committee (ECC) regulated the use of UWB in Europe which resulted in a boom in the area of UWB researches, activities and products. Beside the defined bandwidth, strict limitations are applied to the transmitted level of

energy in order to mitigate the probabilities of signal interference of the UWB with other technologies [44]. These limitations are graphically demonstrated in Figure 2.1 for different regions.

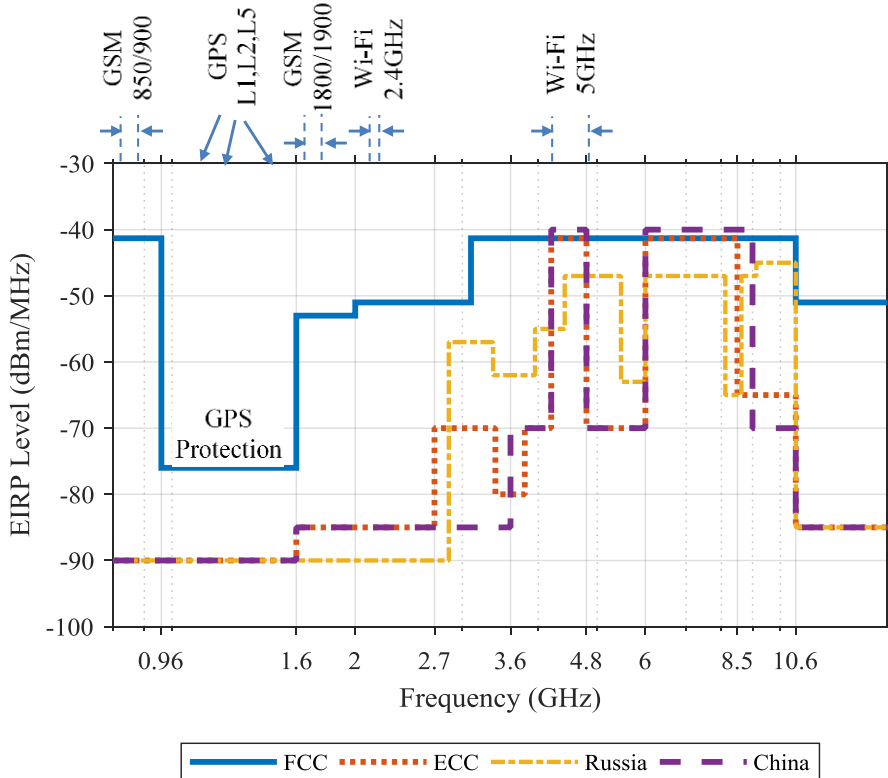


Figure 2.1: The defined bandwidth of the UWB by FCC and EEC and comparison of the effective isotropic radiated power (EIRP) with other wireless technologies

Right after regulation of the UWB, many attentions have been paid to communication aspects of such systems with the idea of defining short range wireless systems capable of transferring high baud rate of data in the range of hundreds of Mbps [45, p. 5]. Possible applications were targeted at wireless cameras, digital video broadcasting between PCs and other devices, printers, mass storage devices or even wireless devices used as replacement of USB interface. However, the manufacturers and suppliers did not welcome this technology due to the lack of clear definition of market policies and availability of other systems such as Wi-Fi and Bluetooth. In contrast to this, the great capabilities of UWB devices in localization did not hinder scientists from evaluating these aspects and researching new localization and positioning methods based on UWB devices.

## 2.1. UWB Characteristics

The large bandwidth of UWB systems in frequency domain results in a very narrow impulse in the time domain with a signal period in the order of less than a nanosecond. In order to generate such a narrow pulse, special circuitry is required which can sample the signal with a clock in the range of picoseconds [6]. These short impulses, when transferred in certain time intervals, bring the advantages that several transmitters can operate in parallel while the multipath effect is mitigated. Multipath effect is a phenomenon which is caused by receiving several replicas of the original signal created due to the signal reflection of objects in the environment or ground between the transmitter and receiver. These reflections arrive shortly one after another at the receiver. If the pulse width of the signal in time domain is large (narrow bandwidth), these reflections will be superimposed together making the detection of the original signal almost impossible. However, in a very short pulse technique (ultra-wideband), these reflections arrive much later than the width of the pulse. This way the extraction and detection of the original signal is easier. This problem is illustrated in Figure 2.2 for better understanding of the multipath effect.

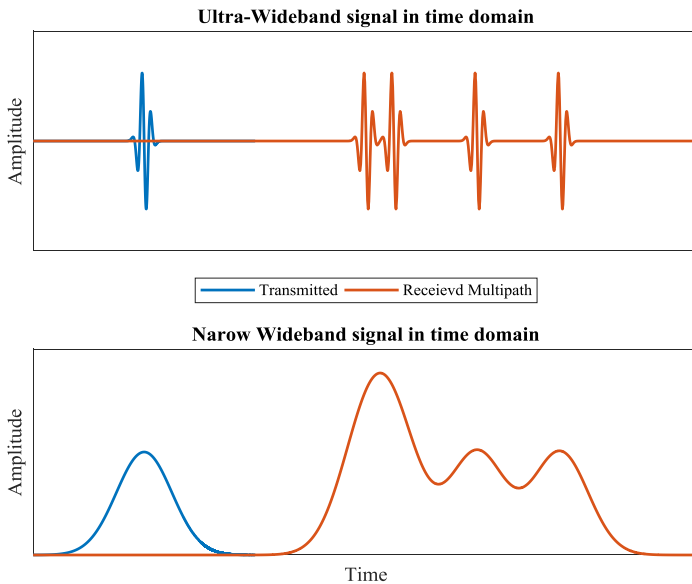


Figure 2.2: Difference of an ultra-wideband system and a narrow-wideband system in recognition of the original signal in multipath cases

Considering the short time period of these impulses, one major question is how the signal should look like in order to match the required energy limit defined by the regulations. To find the answer, different pulse shapes such as a square pulse, a signal with cosine roll-off and a Gaussian waveform is evaluated. All the three signals have the same amplitude and period. These signals are demonstrated in

Fig. 2.3 in both time and frequency domain. The signals in the frequency domain are depicted based on the power spectrum density (PSD) which can be used to evaluate the energy of the signal in given bands. As it can be seen from the graph, all the three signals generate side lobes outside their bandwidth. However, the pulse-shaped signal has much higher energy in this area whereas the Gaussian signal represents a lower amount of energy (below -100 dB). Taking these three forms into account, only the Gaussian signal could be utilized as a UWB signal without interfering with the signals outside of the defined band.

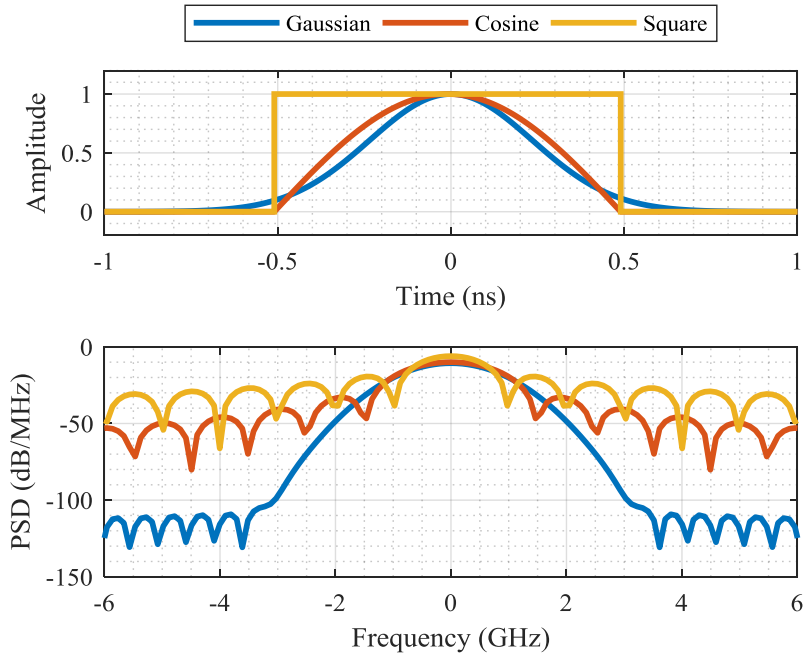


Figure 2.3: Comparison of three different pulse shapes both in time domain (top) and power spectrum density (PSD) in frequency domain (bottom) to find the best signal with less energy outside of the defined band by regulations

Suitable pulse shapes for UWB devices which are easy to create are Gaussian, modified Hermite polynomials and wavelet pulses [44]. The Gaussian pulse  $\psi$  can be expressed mathematically according to the following equation:

$$\psi(t) = A e^{\frac{-t^2}{2\sigma^2}} \quad (2.1)$$

where  $A$  is a positive number controlling the energy of the signal and  $\sigma$  is the pulse standard deviation which controls the width of the signal.

The Gaussian signal has many interesting features such as the integral of the signal is always one, the integral and derivation of the signal is also Gaussian,

and the Fourier transform of the Gauss signal  $\Psi$  can be represented also in Gaussian form. This can be described mathematically as:

$$\psi(t) = \frac{1}{\sigma\sqrt{2\pi}} e^{\frac{-t^2}{2\sigma^2}} \Leftrightarrow \Psi(f) = \int_{-\infty}^{\infty} \psi(t) e^{-j2\pi ft} dt = e^{-2(\pi\sigma f)^2} \quad (2.2)$$

One issue of the Gaussian signals visible in Figure 2.3 is its high energy in lower frequency ranges which is close to -10dB. This is obviously in contrast to the limitation which is defined to be around -41.3dB. One solution is to reduce the amplitude of the signal which results in lower energy. However, to reach the given limit, the signal amplitude should be decreased to the millivolt level which is too small to transmit and receive. Another solution is to benefit from derivative forms of the Gaussian signal in higher orders which help us to distribute the energy peak in wider range and use the whole bandwidth effectively [46]. Different orders of the Gaussian derivatives are provided in Table 2.1.

Table 2.1: Derivatives of Gaussian signal for orders from 1 to 5

Order	Signal equation
1 <sup>st</sup>	$\frac{\partial}{\partial t} \psi(t) = -t \frac{1}{\sigma^3 \sqrt{2\pi}} e^{\frac{-t^2}{2\sigma^2}}$
2 <sup>nd</sup>	$\frac{\partial^2}{\partial t^2} \psi(t) = (-\frac{1}{\sigma^3} + \frac{t^2}{\sigma^5}) \frac{1}{\sqrt{2\pi}} e^{\frac{-t^2}{2\sigma^2}}$
3 <sup>rd</sup>	$\frac{\partial^3}{\partial t^3} \psi(t) = (\frac{3t}{\sigma^5} - \frac{t^3}{\sigma^7}) \frac{1}{\sqrt{2\pi}} e^{\frac{-t^2}{2\sigma^2}}$
4 <sup>th</sup>	$\frac{\partial^4}{\partial t^4} \psi(t) = (\frac{3}{\sigma^5} - \frac{6t^2}{\sigma^7} + \frac{t^4}{\sigma^9}) \frac{1}{\sqrt{2\pi}} e^{\frac{-t^2}{2\sigma^2}}$
5 <sup>th</sup>	$\frac{\partial^5}{\partial t^5} \psi(t) = (-\frac{15t}{\sigma^7} + \frac{10t^3}{\sigma^9} - \frac{t^5}{\sigma^{11}}) \frac{1}{\sqrt{2\pi}} e^{\frac{-t^2}{2\sigma^2}}$

The original Gaussian signal with its 3rd to 5th derivatives are demonstrated both in time and frequency domain in Fig. 2.4. For the sake of comparison, the limits defined by FCC regulations are also plotted. As it can be seen from the graph, the original Gaussian is violating the frequency area of 1 to 3GHz even in its amplitude mitigated form. The 3<sup>rd</sup> derivative of the signal is also in the protected GPS band which therefore cannot be used. The 4<sup>th</sup> order is marginally close to the defined range of the given limits. The 5<sup>th</sup> order is however completely distributed in the bandwidth with enough distance to FCC limits. Hence the 5<sup>th</sup> derivative of the Gaussian signal is the most preferred signal widely used in UWB radio communication and localization devices [47].

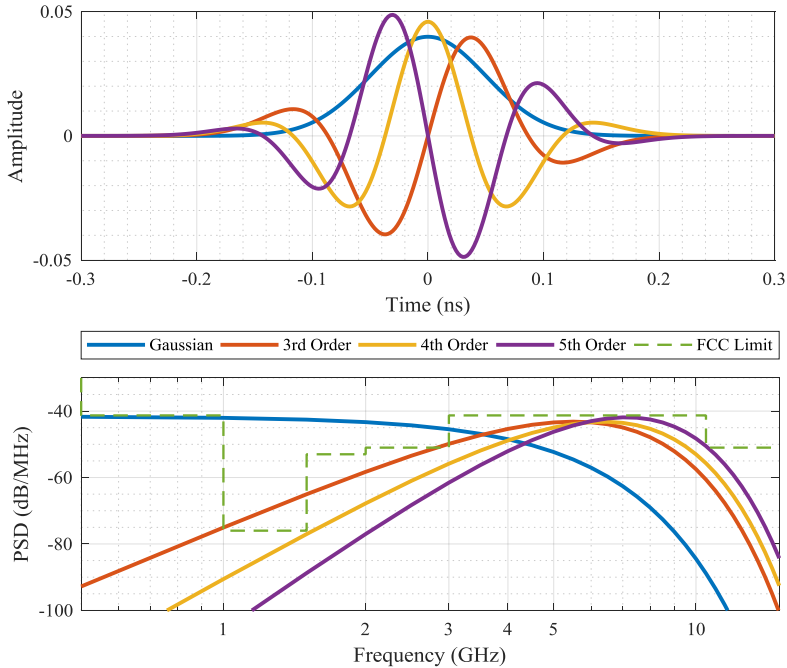


Figure 2.4: Comparison of the original Gaussian signal with its 3<sup>rd</sup> to 5<sup>th</sup> derivatives including the FCC defined limits [46, 48]

## 2.2. Modulation Concepts and Coding

All the modulation concepts of the UWB systems can be categorized into two major segments namely single band and multi-band modulation methods. The ones based on the single band use the whole range of the bandwidth dedicated to UWB devices by transmitting sequences of short impulses in the time domain. These techniques are also known as impulse radio UWB (IR-UWB). The multi-band techniques divide the available spectrum from 3.1 to 10.6 GHz into several sub-bands each with a bandwidth higher than 500 MHz which results in simplicity of analogue to digital (A/D) converters as well as reduction of sample rate [49]. An example of multi-band modulation technique is multiband orthogonal frequency division multiplex (MB-OFDM) [50] or frequency hopping modulation. The single band techniques are best suitable for localization applications as they provide a very high resolution of timestamps which results in higher accuracy of ranging measurements. On the other hand, the multiband techniques are more suitable for data communication applications where high data rates are required without increasing the energy of the spectrum and interferences. To know more about the details of each approach and their features, these two modulation structures are discussed in the following sections.

## 2.2.1. Single band modulation

The main concept of single band modulation method is based on the transmission of sequences of narrow pulses usually in the form of Gaussian signal and its derivatives (also called monocycles). The monocycles, as shown in the previous section, take the advantage of the whole bandwidth for transmission. The benefit of such a technique is that no carrier modulation is required as these types of pulses can be transmitted over radio channels [49]. However, these monocycles do not carry data by themselves. Therefore, a modulation technique is required that is capable of encoding data into pulse trains. In general, four different modulation approaches are commonly used which are described as follows:

### 2.2.1.1. Pulse Amplitude Modulation (PAM)

In this form of modulation, data are modulated in the polarity of the signal which represents the binary data. In this case, a positive signal is carrying binary 1 and a negative signal is carrying a zero. Figure 2.5.a illustrates the signal shape for both cases. This modulation concept can be described mathematically as [49]:

$$s(t) = p_i \psi(t) \quad \text{where} \quad p_i = \begin{cases} 1 & \text{Binary Data} = 1 \\ -1 & \text{Binary Data} = 0 \end{cases} \quad (2.3)$$

where  $\psi(t)$  is one of the derivatives of Gaussian signal (usually the 5<sup>th</sup> order), and  $p_i$  is the polarity factor defined by the binary data according to the above statements. This technique is usually used only for binary modulation as a higher number of bits leads to complexity of implementation and performance loss [50].

### 2.2.1.2. On-Off Keying (OOK)

This modulation concept is based on the presence or absence of an impulse in a certain time frame (Fig. 2.5.b). If the impulse is available in the scanning time period, the demodulator interprets it as binary 1 and the absence of impulse as binary 0. In this case, the modulated signal is equal to:

$$s(t) = \begin{cases} \psi(t) & \text{Binary Data} = 1 \\ 0 & \text{Binary Data} = 0 \end{cases} \quad (2.4)$$

This technique is the usual choice of low cost and simple transmitters which cannot manipulate the signal shape and time offsets [50].

### 2.2.1.3. Pulse Position Modulation (PPM)

In this technique, time shift of the signal according to a nominal time reference is used to represent the data. The binary data 0 will be transmitted as an impulse located at time 0 whereas the binary value of 1 will be transmitted with a time delay of  $\delta$  compared to the certain time interval  $T$  between each transmission.

Figure 2.5.c explains the differences between the two impulses graphically. The modulated signal can be represented in the following form:

$$s(t) = \sum_{i=-\infty}^{\infty} \psi(t - iT - \varphi_i \delta) \text{ where } \varphi_i = \begin{cases} 1 & \text{Binary Data} = 1 \\ 0 & \text{Binary Data} = 0 \end{cases} \quad (2.5)$$

In this equation,  $T$  is the time interval between each transmission and  $\delta$  as described before, represents the time delay applied according to the binary data. Higher order of modulation other than binary form is not preferred in this method otherwise higher signal to noise ratio (S/N) is required which is hard to achieve in practice [50].

#### 2.2.1.4. Pulse Shape Modulation (PSM)

In this technique, different pulse shapes are used to represent the data. Possible signal forms are Hermitian, wavelets or different derivatives of Gaussian [49]. One signal characteristic considered for selection of the pulse shapes is orthogonality of the shapes which results in simplicity of detection in the receiver as well as multiple transmission on the same channel with low interference probability. Figure 2.5.d demonstrates the PSM modulation concept.

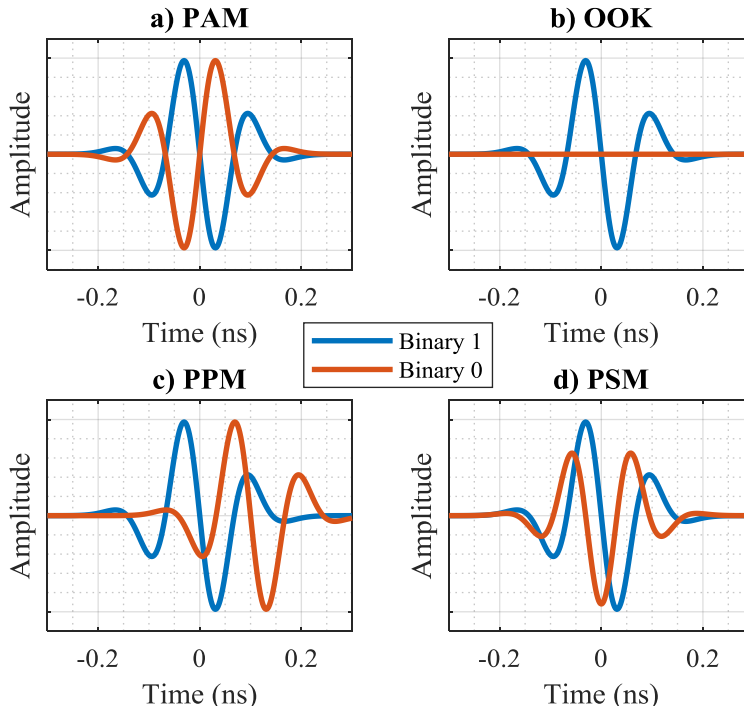


Figure 2.5: Possible single band modulation concepts applied to the Gaussian derivatives representing binary data, a) PAM, b) OOK, c) PPM and d) PSM [49]

The PSM technique can be described mathematically according to the following formula:

$$s(t) = \sum_{i=-\infty}^{\infty} \psi^{d_i}(t - iT) \text{ where } d_i = \begin{cases} 5th & \text{Binary Data} = 1 \\ 6th & \text{Binary Data} = 0 \end{cases} \quad (2.6)$$

where  $d_i$  is the derivative order of the  $\psi(t)$  signal which in this case could be either 5<sup>th</sup> or 6<sup>th</sup> depending on the data bit.

## 2.2.2. Multiple access techniques

The modulation techniques mentioned previously transmit the impulse signals in a certain time interval. Analyzing the frequency spectrum of such systems, it can be seen that these impulses create spikes in the spectrum also called comb lines (Fig. 2.6). This is due to the high density of energy in small portion of the time and no or less signal energy in the rest of the time interval. These spikes can cause interferences in other radio devices in the vicinity of the transmitter [51].

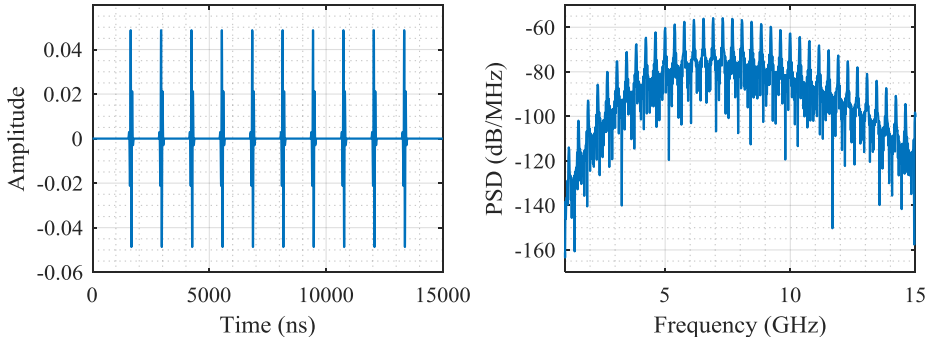


Figure 2.6: Comb line effect as a result of pulse train transmission with fix intervals [51]

In order to solve the comb line problem and use the bandwidth efficiently, so that multiple devices can access the band in parallel, multi-access techniques can be utilized. These techniques transmit the signal in pseudo-randomized form. This way, the energy of the spikes is distributed which appears to the receiver and other devices like a noise. In addition to that, the chances of interference with other UWB devices accessing the same band can be reduced. The most common multi-access techniques are time hopping (TH) and direct sequence (DS) which are described in detail in the following subsections [49].

### 2.2.2.1. Time Hopping (TH)

This technique applies the randomness of the transmission on the position of the impulses in a sense that instead of sending a signal in a certain time interval  $T$ , a shift of  $\delta$  is applied in a pseudo-random manner according to certain sequence

codes. These codes have two basic tasks. The first is to provide the receiver a way to follow these random sequences arriving from the transmitter and the second is to detect the transmission error and recover the corrupted sequences. This is beside the original idea of time hopping which is simultaneous transmission of several devices using different coding patterns. The TH method can be applied to all the modulation methods other than OOK due to the possibility of misinterpreting a time shift as binary 0. Applying the TH multi-access method to the previously mentioned modulation techniques, the equations given in 2.3, 2.5 and 2.6 could be rewritten into the following forms:

$$PAM: \quad s(t) = \sum_{i=-\infty}^{\infty} \sum_{j=0}^{N_s-1} \psi(t - iT_s - jT_f - c_j T_c) p_i \quad (2.7)$$

$$PPM: \quad s(t) = \sum_{i=-\infty}^{\infty} \sum_{j=0}^{N_s-1} \psi(t - iT_s - jT_f - c_j T_c - \varphi_i \delta) \quad (2.8)$$

$$PSM: \quad s(t) = \sum_{i=-\infty}^{\infty} \sum_{j=0}^{N_s-1} \psi^{d_i}(t - iT_s - jT_f - c_j T_c) \quad (2.9)$$

In order to explain the new parameters added in the above equations, Figure 2.7 is used. Each data bit is called information symbol which is modulated in the form of a series of sequentially transmitted impulses. According to the graph, the transmission time of modulated term is  $T_s$ . Each information symbol consists of  $N_s$  smaller time slots  $T_f$  called chip frames which are used for time hopping of the impulses depending on applied pseudo-random (PR) code. The parameter  $c_j$  is an integer number decided by the PR code which could be in the range of 1 to  $N_c$ . Finally, the  $T_c$  is the width of the pulse slot with an added guard time.

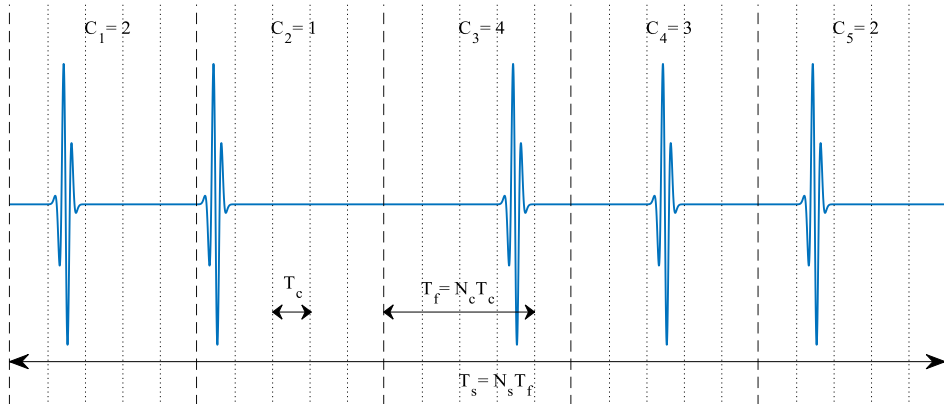


Figure 2.7: Structure of the time hopping (TH) multi-access technique [6] [49]

### 2.2.2.2. Direct Sequence (DS)

The technique used in the direct sequence method is based on the shape of UWB impulse signal which changes according to the pseudo-random (PR) codes. The resulting signal is in the continuous form with changing amplitude's polarity (for PAM and OOK) or signal shape (for PSM) as discussed before. Due to the structure of PPM which is based on the time shifts, this method cannot be applied in DS approach. Integrating DS technique into the mentioned modulation methods, the equations 2.3, 2.5 and 2.6 can be defined in the following forms:

$$\text{PAM and OOK: } s(t) = \sum_{i=-\infty}^{\infty} \sum_{j=0}^{N_s-1} \psi(t - iT_s - jT_c)c_j p_i \quad (2.10)$$

$$\text{PSM: } s(t) = \sum_{i=-\infty}^{\infty} \sum_{j=0}^{N_s-1} \psi^{d_i}(t - iT_s - jc_j T_c) \quad (2.11)$$

The parameters given in the above equations are the same as those defined in equations 2.7-2.9. For the sake of better understanding, Figure 2.8 illustrates the DS multi-access concept. The first signal is showing the data to be transmitted and the second one is the spreading code. The third signal shows the spread spectrum signal ready for transmission. The reverse process in receiver to extract the data is shown in the last three waves. As it can be seen from the spread spectrum signal, the binary phase shift of the data cancels out the inversion polarity of the code which results in no change in the carrier phase [6, p. 60].

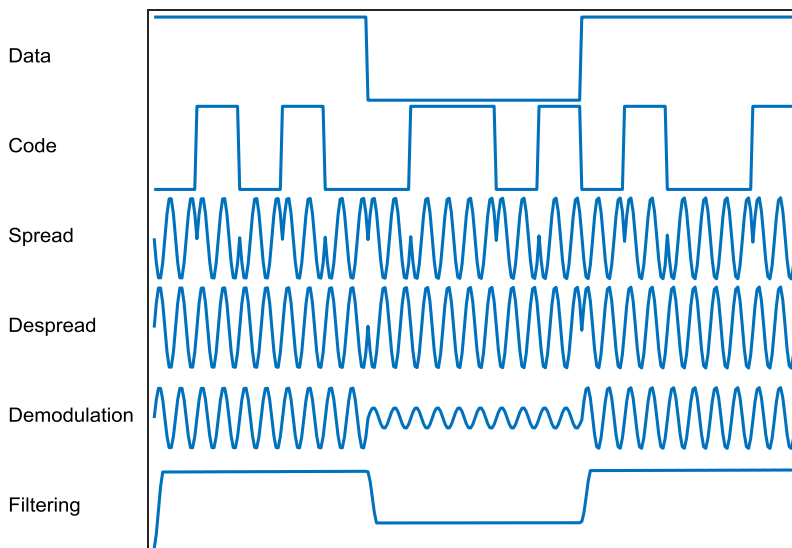


Figure 2.8: The structure of the direct sequence (DS) multi-access method utilizing binary pulse amplitude modulation (PAM) [6, p. 60]

### 2.2.3. Multi-band modulation

The multi-band modulation techniques distribute the dedicated bandwidth of UWB devices into several smaller subbands each with a minimum of 500MHz. This way the available spectrum can be used more effectively by changing the subbands for different devices which eventually results in lower interference rate and scalability of the communication system. Furthermore, the required hardware to receive and transmit signal will be much simpler as lower sampling rate and clock frequencies are required to realize the bandwidth of around 500MHz. This amount of bandwidth is still high enough to benefit from the UWB features such as multi-access capability, interference reduction by having lower energy peaks and avoiding multipath fading problems [6][49].

The modulation of each subband is performed using several analogue carriers tuned to the center of each band. A possible modulation signal is for example, a cosine signal modulating a Gaussian signal as shown in Figure 2.9.

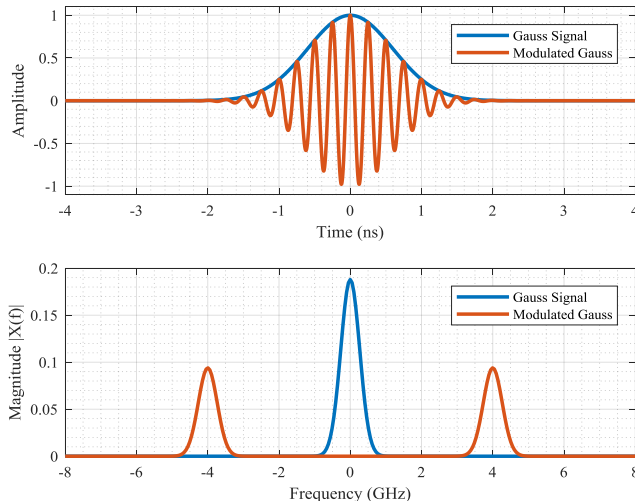


Figure 2.9: Modulation of a Gaussian signal using a cosine signal carrier for the band 2 with center frequency of 3960 MHz in both time and frequency domains

#### 2.2.3.1. Multi-band Orthogonal Frequency Multiplexing (MB-OFDM)

The most common method of multiband modulation is multiband orthogonal frequency division multiplexing (MB-OFDM) defined and standardized by WiMedia Alliance [50]. This method uses a combination of time and frequency domain modulation by switching the carrier frequency in different time slots according to a time frequency code (TFC). This way, multiple users can access the band by changing the selected band without collision and by integrating different TFC for different users.

According to the approach defined by WiMedia, the available spectrum is divided into 14 subchannels each with a bandwidth of 528 MHz located side by side [52, p. 220]. These bands are grouped together and form band group which each device can access based on the applied TFC [50]. In total, 5 groups can be formed with 4 of them including 3 bands and one group containing only two bands. These groups are demonstrated in Figure 2.10. Different regulatory organizations permit usage of only specific groups. As an example, group 1 is only allowed in Europe temporarily [50].

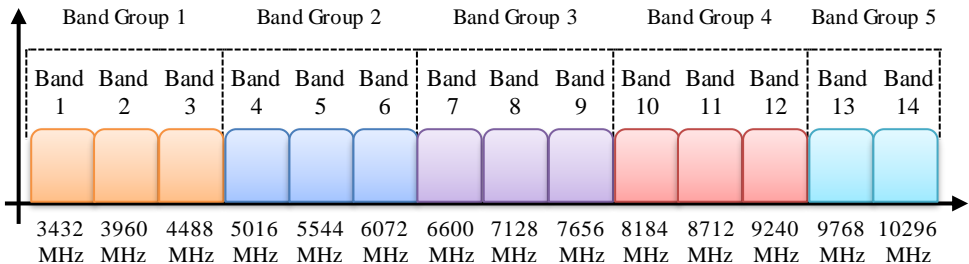


Figure 2.10: Spectrum division and band grouping of MB-OFDM proposed by WiMedia and standardized by ECMA International [44, p. 32]

The transmission of information in each band is modulated according to quadratic phase shift keying (QPSK) on 128 subcarriers which are orthogonally placed for the sake of interference reduction and robustness [52, p. 10]. Additionally, zero padding can be applied which leads to robustness against multipath, higher transmission power and provides enough time for transceivers to alter the subcarrier frequencies. The benefits of such implementation are reduction of clock precision in digital circuits and lower phase noise requirement in the synthesis circuits due to larger subcarrier spaces [52, p. 220]. The procedure of transmission in MB-OFDM technique is illustrated in Figure 2.11.

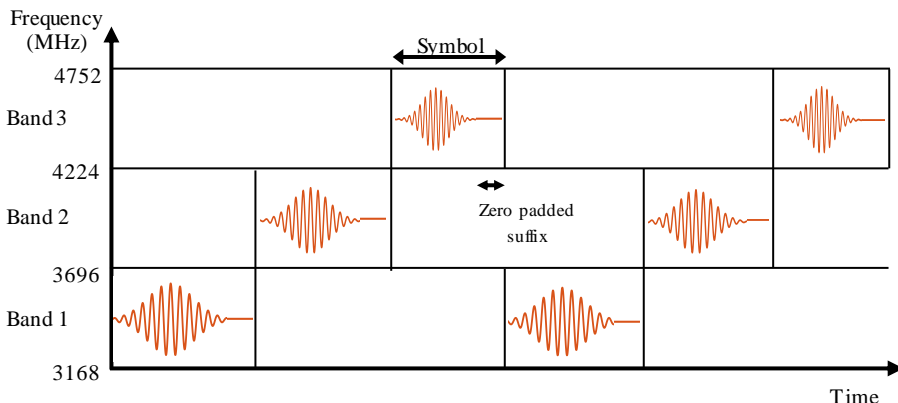


Figure 2.11: Procedure of MF-OFDM modulation implemented on group 1 and according to the sequence code  $\{1,2,3,1,2,3,\dots\}$  [44, p. 35]

## 2.3. UWB Frame Format and IEEE Standard

After regularization of UWB signals by FCC, many efforts have been made to define a specific standard for protocols and frame formats. These efforts led to the extension of the already available IEEE 802.15.4 (2004) standard by the workgroup 4a to include the new requirements. The result was publication of the IEEE 802.15.4a (2007) standard with the focus on high precision ranging and low power consumption based on the UWB devices [2].

According to the standard, two types of physical layers (PHY) are defined namely chirp spread interface (CSI) and impulse radio UWB (IR-UWB). The CSI layer operates in unlicensed 2.4GHz which is less suitable for ranging applications due to the limited bandwidth of 5MHz for 14 channels. In contrast to CSI, IR-UWB utilizes 15 channels, eleven of them with the bandwidth of 499.2 MHz and two channels with the bandwidth of 1331.2 MHz which are more suitable for high accuracy ranging applications [6]. The supported data rates are 110Kbits/s, 851 Kbits/s, 6.81 Mbit/s and 27.24Mbit/s [2].

The IEEE 802.15.4a standard defines a certain frame structure that consists of synchronization header (SHR) preamble, physical layer header (PHR) and a data segment. The role of the SHR preamble is synchronization of the transmitter and receiver, and first path detection. By the end of preamble phase, another segment called start of frame delimiter (SFD) is transmitted to indicate the end of the preamble phase and start of the PHR. The PHR segment contains the frame setting which will be used for transmission of the data including the frame data rate and the length of the data. The last segment is communication data which can carry 127 bytes according to the IEEE standard. Block diagram of the frame structure defined by the IEEE 802.15.4a standard is depicted in Figure 2.12.

SHR		PHY header (PHR)	Data
Preamble 16, 64, 1024, 4096 symbols	SFD 8, 64 symbols		

Figure 2.12: Frame structure of the UWB PHY according to IEEE 802.15.4a [44, p. 159]

Different segments of the frame are modulated using different techniques. The SHR part is modulated according to OOK modulation technique. Three symbol mapping modes are considered namely base mode which contains one chip per symbol, the enhanced mode with four chips per symbol and finally the long range mode with 64 chips per symbol. The first two modes employ a pulse repetition frequency (PRF) of 1 MHz and the last mode has PRF of 2MHz [2]. The PHR and data segments utilize a combination of burst position modulation (BPM) and binary phase shift keying modulation (BPSK) techniques.

The process of BPM/BPSK modulation is defined as follows: in the first step, the data will pass through a Reed-Solomon encoder which is a coding mechanism

used for error detection and correction by oversampling a polynomial, generated from the data itself. These coded data are processed with a convolution encoder with a rating of 1/2 which divides the code into two parts namely parity bit and systematic bit. The first one represents one bit by the polarity of the signal according to the binary phase shift keying modulation (BPSK) concept. The second one represents the bits by the position of the burst signal in the slot similar to PPM modulation. This way of modulation is also called burst position modulation (BPM). Each symbol can optionally have 8, 16, 32, 64 or 128 slots. For each time slot, a guard interval is considered which improves the interference immunity. These two bits are combined together and form a symbol which means each symbol embraces two bits of data with its position representing one bit and its polarity representing another bit of data. The duration of each burst is 2.024 ns corresponding to 500 MHz of bandwidth [2]. Different components of an IR-UWB transmitter according to IEEE 802.15.4a are shown in Figure 2.13.

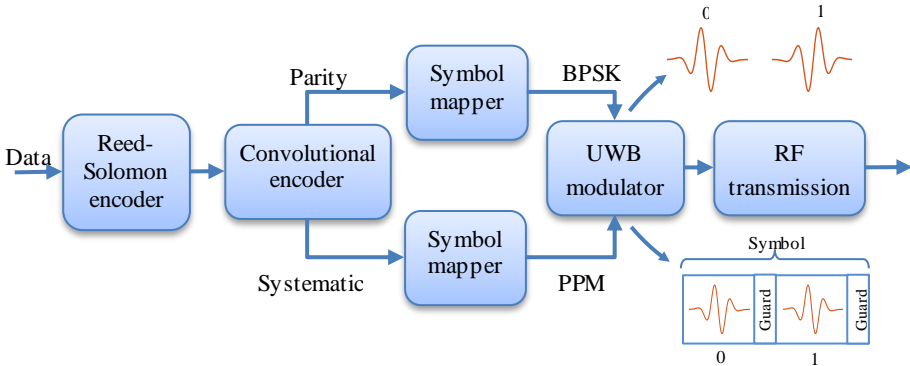


Figure 2.13: Block diagram of an IR-UWB transmitter with BPM modulation [44, p. 40]

Details of the UWB PHY segments are discussed in the following sections.

### 2.3.1. Preamble

This is the part of the frame which is used for ranging as well as channel sounding and data acquisition. Possible lengths of preamble segments are 16, 64, 1024 or 4096 symbols. The length of the preamble field is decided by the application depending on the channel characteristics and receiver capabilities. The longer length of preamble is normally used for non-coherent receivers which results in improvement of SNR and provides the receiver more time for synchronization and signal acquisition. The shorter length of preamble has the advantages of less channel occupation resulting in less interference, lower power consumption and simultaneous channel access of more devices [53, p. 33]. Each preamble symbol is made up of 31 sequential pulses which can have one of the three states namely positive, minus or zero. This sequence is called ternary sequence. In total 8 different possible ternary sequences are defined with ideal periodic

autocorrelation characteristics. This feature results in easier detection of the channel response, the first path as well as possibility of multi-channel access by several devices [6]. If the receiver sequence is exactly lined up with the replica produced by the receiver, then the demodulated signal will have the unity gain. However, if the sequences are not aligned with one pulse width difference, then the result of demodulation will be zero [6]. Each individual pulse of the ternary sequence is separated with a guard interval to improve the signal acquisition at the receiver. List of possible ternary sequences is provided in Table 2.2.

Table 2.2: Ternary sequences of the SHR section defined by IEEE 802.15.4a [6]

Preamble symbol	Pulse sequence
$P_1$	-0000+0-0-++0+-000+-++00-+0-00
$P_2$	0+0+-0+0+000-+0-+-00+00++000
$P_3$	-+0++000-+-++00++0+00-0000-0+0-
$P_4$	0000+-00-00-+++-0++000+0-0++0-
$P_5$	-0+-00+++-000-+0++0+0-0+0000-++
$P_6$	++00+00---+-0++-000+0+0-+0+0000
$P_7$	+0000+-0+0+00+000+0++--0-+00-+
$P_8$	0+00-0-0++0000--+00-+0++-+0+00

The preamble frame can be described mathematically according to [6]:

$$P_i(t) = \sum_{j=0}^{N-1} \psi(t - jT_{pri}) c_i(j) \quad (2.12)$$

where  $P_i(t)$  is the generated preamble frame,  $\psi(t)$  is the burst signal at time  $t$ ,  $N$  is the number of ternary codes equal to 31,  $T_{pri}$  is the time interval of each symbol including the guard interval and finally  $c_i(j)$  is the ternary sequence code which can be one of these states:  $\{+1, 0, -1\}$ .

### 2.3.2. Start Frame Delimiter (SFD)

This part of the frame declares the end of preamble phase and the start of the PHR segment which has a different modulation as described before. Additionally, the field is used for extracting the arrival time of the signal in ranging applications and frame timing. The SFD segment consists of 8 or 64 symbols. The 8 symbols setting is default option which is supported by the standard and is used for baud rates other than 110 Kbits/s. The 64 symbols case is optional and is used for 110Kbits/s mostly suited for long range communication applications. The structure of the symbols is similar to preamble segment with the standard code  $\{0+0-+00-\}$  for 8 symbols sequence. The SFD segment  $f$  is described as [6]:

$$f_i(t) = \sum_{j=0}^{L-1} P_i(t - jT_{syn}) c(j) \quad \text{where } 0 < i < (8 \text{ or } 64) \quad (2.13)$$

where  $L$  is the number of SFD codes which is 8 or 64,  $P_i(t)$  is the preamble frame calculated in Eq. 2.12,  $T_{syn}$  is the length of the basis sync (preamble) symbol and  $c(j)$  is the SFD code with one of these values:  $\{+1, 0, -1\}$ .

### 2.3.3. Physical Header (PHR)

The PHR segment delivers configuration information of the data field. This information includes data rate, data frame length, ranging flag, header extension flag, preamble duration and an error detection and correction mechanism known as single error correction double error detection (SECDED). The length of the PHR frame is 19bits. The modulation concept is BPM/BPSK as described in the introduction of this section. The difference between the modulation of PHR and data segment is that in PHR part no Reed-Solomon encoder is used. The error checking functionality of Reed-Solomon code is replaced with SECDED mechanism. The Details of the bits' number and their functions are listed in Table 2.3 [44, p. 160].

Table 2.3: PHY header (PHR) bit definition and possible field configurations according to IEEE 802.15.4a standard

Data Rate	Frame Length	Ranging Packet	Header Extension	Preamble duration	SECDEC check bits
2 bits	7 bits	1 bit	1 bit	2 bits	6 bits
00: 110Kbps 01: 850Kbps 10: 6.81Mbps 11: 27.24Mbps	Maximum 127 Bytes of data	1: Ranging packet 0: Communication packet	Reserved	00: 16 01: 64 10: 1024 11: 4096	

The data rate of the frame can be set using two bits according to the given block diagram above. The default baud rate is 850 Kbps which is used for the PHR segment as well. For all the other baud rates, the baud rate of PHR stays 850 kbps. The exception is low rate 110 kbps which in that case the baud rate of the PHR frame will be reduced to 110 kbps [44, p. 160]. The ranging flag is used to indicate to the receiver that this packet is used for ranging. The use of header extension flag is reserved for future use. Preamble duration can be configured using two bits to define 4 possible numbers among 16, 64, 1024 and 4096. The last 6 bits are used to embrace the SECDED data which is used for error detection and correction. The SECDED method utilizes five parity bits to code the data and is able to detect two errors or detecting and correcting one error bit. Further information can be found in [54].

## 2.4. First Path Detection

After reception of the preamble section and synchronization of the receiver, the SFD is used to detect the signal time of arrival. This time represents the first path in the channel impulse response of the received signal. Most of the time, when the received signal has high SNR and there is a direct line of sight between the nodes, the first path has the highest amount of energy which is distinguishable from multipath signals easily. However, in noisy conditions, including the non-line of sight cases, the first path is mitigated and sometimes not detectable at all. This different condition and behavior of the first path, demands better detection mechanisms. This section briefly reviews the common first path detection techniques. More details and alternative techniques are provided in [44].

### 2.4.1. Peak detection techniques

The basis of this detection method is to extract the peak of all the components of the channel impulse response and compare them to exclude the peak with the highest energy from the other multipath components (MPC). Three algorithms which operate based on the peak detection concept are single search, search and subtract and finally search, subtract and adjust. The single search approach searches for  $N$  peaks of the strongest MPCs where  $N$  is decided by user. Among the measured peaks, the one which happened at the earliest is selected as the first path. This can be described as [44, p. 133]:

$$\tau = \min(k_1, k_2, \dots, k_N) T_s \quad (2.14)$$

where  $N$  is the number of detected peaks,  $k_N$  is the time index of each MPC and the  $T_s$  is the sample time. An improvement to this technique can be performed in search and subtract method in that the strongest peak of MPC is regenerated using the received pulse shape and subtracted from the original signal. This way the first path will be the second strongest MPC. This process continues iteratively until all the MPCs are subtracted. The result of the algorithm is calculated based on Eq. 2.14 but using the new extracted time stamps. The last technique is based on the joint estimation of channel components at each iteration. In this technique, the channel coefficients calculated in each round of iteration are used in the next round again. This way the performance of the search and subtract method can be even improved however this technique is computationally more expensive compared to other two methods.

### 2.4.2. Two-step ToA estimators

The two-step detection techniques perform the search process in two steps with different sampling rates at each step. At the first step, a search using low sampling rate is performed to make a rough image about the possible position of the paths

and in the second step a search with higher sample rate is performed but only on the area discovered in the first step. This way the high sampling rate requirement of the search mechanism can be released which results in simpler implementation and lower power consumption of the hardware. The first step could be performed using simple detection methods such as maximum peak detection. For the second step, methods with higher sample rates are used which are capable to detect the first path accurately. Examples of these methods are correlation-based techniques or search back algorithm [44, p. 135].

### 2.4.3. Threshold-based techniques

These techniques are a set of algorithms which operate based on defining a threshold level on the absolute amplitudes of the MPCs and detecting the first MPC among the ones which stay higher than the threshold level. The advantages of such techniques are the simplicity of implementation and applicability of the algorithm in analogue form without need of high resolution ADCs [44, p. 138].

The simplest method of this category is to search for the first peak which is exceeding the defined threshold. The level of threshold is decided by evaluating the channel noise floor, received signal characteristics and operating conditions [50, p. 27]. The selection of this parameter is critical as a higher level of threshold may lead to miss-detection of the first path and a lower level of threshold results in detection of the noise as the first path of the received signal.

A better approach compared to the simple threshold method is jump back and search forward algorithm (JBSF). In this algorithm, the strongest MPC is detected as the base point for the search. Then the search index will jump to the leading edge of the received MPCs and from that point on search for the MPC which exceeds the threshold towards the strongest path. This can be represented mathematically in the form of [44, p. 139]:

$$i_{JBSF} = \min(i | x(i) > \lambda) \quad (2.15)$$

where  $i \in \{i_{sb}, i_{sb} + 1, \dots, i_{max}\}$  is the index of the MPC with  $i_{sb}$  as the leading index and  $i_{max}$  as the maximum index denoting where the strongest MPC is detected. The distance between the  $i_{max}$  and  $i_{sb}$  is defined as  $W_{sb} = i_{max} - i_{sb}$ . The parameter  $\lambda$  is the threshold value of detection and the  $x(i)$  is the absolute value of MPC at index  $i$ . The process of jump back and search forward is illustrated in Figure 2.14.

Another similar approach to the previous method is serial backward search algorithm (SBS). This technique also uses the strongest MPC as the reference of search point but unlike JBSF search backwards to the direction of the leading edge. There are generally two types of signals in the channel impulse response (CIR). The signals either carry only noise or MPCs added with noise. If the noisy MPCs are sequentially connected, then we have a single cluster case. However,

if there are noise only blocks between the MPC groups, then it is called multi-cluster scenario. In the case of the latter, the serial backward search method should continue the search until a certain number of consecutive noise block is observed. The mathematical representation of the SBS method for single cluster case is provided in Eq. 2.16 whereas the representation of SBS for multi-cluster is provided in Eq. 2.17 [44, p. 143].

$$i_{SBS-SC} = \max(i | x(i) > \lambda \text{ and } x(i-1) < \lambda) \quad (2.16)$$

$$i_{SBS-MC} = \max(i | x(i) > \lambda \text{ and } \max(x(i-1), \dots, x(\max(i-K, i_{sb}))) < \lambda) \quad (2.17)$$

where  $i \in \{i_{max}, i_{max}-1, \dots, i_{max}-W_{sb}\}$  is the MPC index from the strongest path to the leading edge and  $K$  is the optimum threshold achieved empirically. The rest of parameters are similar to those described in Eq. 2.15. The structure of the SBS method in multi-cluster format is shown in Figure 2.14.

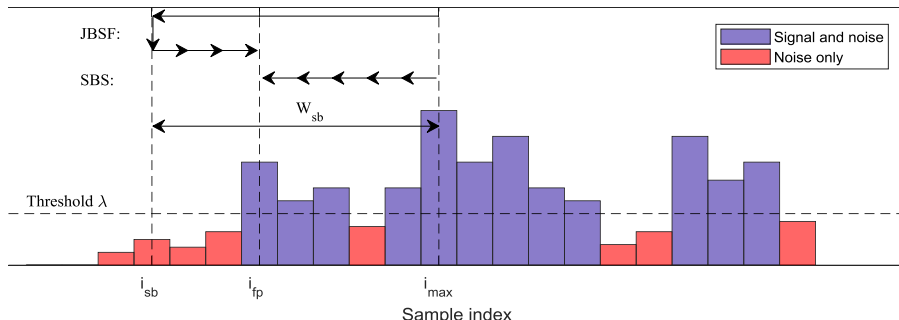


Figure 2.14: The first path detection algorithms based on the jump back forward search (JBSF) or serial backward search SBC for a multi-cluster case

## 2.5. Analysis of Commercial Platforms

Regularization of UWB technology by different regulatory organizations paved the way for development and research in the area of localization and positioning based on this technology. Soon the lack of commercial products in this market was sensed. On the other hand many researches have been carried out in order to apply this technology in localization applications. High market demands from both industry and research laboratories led to appearance of commercial products from many companies with the focus on indoor localization and positioning systems based on UWB technology. Since the hardware module used in this thesis is also one of these modules, it makes sense to provide a brief overview of the possible options and their features to justify our selection. Therefore, in this section, a few of these commercial off-the-shelf (COTS) products are evaluated and compared. These are Ubisense™, Time Domain™, Nanotron™, Zebra™, beSpoon™ and Decawave™.

### 2.5.1. Ubisense

Ubisense Company has been active in the UWB market for a long time. They offer real time localization solutions including hardware nodes, firmware and server-based software. Their current product in the area of UWB is "Dimension 4" which is a location platform designed and developed in the form of turnkey solution mainly for industrial applications. One specific feature of their product is use of an antenna array for localization which has the advantage of using angle of arrival (AoA) topology for localization. This way only two nodes would be enough to extract the range as well as the angle of the two nodes. The power consumption of the nodes is very low which according to the company can be supported by a single battery for 15 years at 1Hz refreshing rate. This distribution unit is a 2U rack-mount device which can support up to 21 tag nodes [55]. The supported position update rate of the node is 134 Hz with the position accuracy of 15 cm. In Figure 2.15 an academic research package from previous products of Ubisense is demonstrated which includes tags, antennas, software and the stationary radios with an approximate price of 10,125.00 € [53].



Figure 2.15: The academic research kit from Ubisense including series of tags, software kit, mechanical holders and antennas (Source: <http://www.rfidstore.it/en/rtls-systems/34-sensore-7000.html>)

### 2.5.2. Time Domain

The Time Domain Company is one of the pioneers in this area who was active even before regularization of UWB took place. Their product series PulsON is famous for its very high accuracy (around 2cm) and flexibility of the modules as these modules can be used either for localization, radar application or data communication applications. One of the current Time Domain's product is P330 which uses Decawave UWB chip as the core but with many additional features and processing power including a USB, Ethernet, CAN or SPI interface to the host device. The dimensions of the modules are 56 mm×103 mm×18 mm with the accuracy of 10cm and maximum range of around 100 m. Another more advanced

product of the company is P440 which is a high accuracy (2cm) sensor suitable for ranging, communication and radar applications simultaneously. This module utilizes two antennas and has position update rate of 125 Hz with maximum range of 300m to 1100 m depending on the antenna and application environment [56]. Time Domain offers a development kit for both of their products including 5 nodes, antennas, accessories and a software package as shown in Figure 2.16.



Figure 2.16: UWB products of Time Domain Company including PulsON440 (left) and PulsON330 (middle) and a development kit (right) [56]

### 2.5.3. Zebra

The Zebra Company is more specialized in accurate asset tracking and personnel visibility solutions mostly based on RFID devices but they also have UWB products known as Dart series. Their products range are Dart Wand which is a table top tag configurator, Dart Hub which is an RTLS system capable of monitoring 1000 tags with accuracy of 30cm up to the range of 200 m, Dart sensor which is an anchor device for monitoring the tag signals and Dart Vision Reader which could be used together with Dart Hub or standalone and finally Dart Tag which will be installed in the assets or carried by personnel. This tag device can run on a small battery for a period of 7 years at 1Hz blink rate [57]. The approximate cost of a demo kit including the tags and anchor devices is around 9,720.0€ [53]. Different products of Zebra Company are shown in Figure 2.17.



Figure 2.17: UWB products of Zebra Company including Dart Tag, Dart Hub (top right), Dart Vision Reader (left). Dart Wand (bottom right) and Dart sensor [57]

## 2.5.4. Nanotron

Another company active in the field of RTLS and indoor positioning is Nanotron which offers two type of technologies. The first one is based on chirp signal in the unlicensed band of 2.4GHz with the bandwidth of 80MHz. This technology has an accuracy of around 1m and a range of up to 500 m. They also offer UWB technology which is based on the chip provided by Decawave which according to their website offers an accuracy of 10cm in the range of 20 m. The API and the software that they offer is the same for both technologies. The range of their products includes the chirp or UWB-based modules, development kits, fixed anchors and RTLS software package [58]. A development kit from Nanotron including 8 anchors and 5 tag devices with a software package would cost around 3.833.5€ [53]. In Figure 2.18 different products of Nanotron are demonstrated.



Figure 2.18: Nanotron chirp (three modules below left) and UWB (the kit on the right) products used for indoor localization and RTLS [58]

## 2.5.5. beSpoon

beSpoon is another company which succeeded in producing cheap price UWB tags. Their products range includes an RTLS positioning solution which is a server-based monitoring system combined with Ethernet or Wi-Fi, a solution so-called Inverted 3D which is a device-based localization technique providing the location information in the tag itself which is suitable for robots, unmanned vehicle or drones navigation and an Indoor GPS solution which is also a device centric technology used for fleet navigation in a network. In addition to these solutions, they offer UWB antennas, modules, development kits, tags and anchors, software packages and it is the only company offering a smartphone which supports the UWB technology [59]. Photos of their products are provided in Figure 2.19.



Figure 2.19: beSpoon series of UWB products including an UWB module, an UWB tag device, a smartphone supporting UWB technology and development kit [59]

### 2.5.6. Decawave

Decawave is one of the most successful companies in the area of UWB devices offering the technology in different form factors including chip level devices, modules, ready to use devices and software packages. Their famous DW1000 chip has been sold more than 30 million times according to the website of the company [60]. The accuracy of the DW1000 chip is around 10 cm with the range of up to 300 m in line of sight and 40m in non-line of sight conditions. Other products of the company based on this chip include DWM1000 and DWM1001 modules. The latter one is a certified module with a host ARM M4 Core microcontroller from Nordic Semiconductor offering Bluetooth and NFC technology in the same package with onboard antennas for both UWB and BLE technologies and an accelerometer which can be used for data fusion purposes. Decawave offers development kits for both modules as well as a complete solution with software for industrial applications. The evaluation kit is available at a low price of 490€, the modules at a price of 22.7€ and the chip at a price of 11.94€ which is currently the cheapest on the market. [60]. Due to low price and extraordinary features of the chip, many companies integrate this chip in their products. A few of them are OpenRTLS [61], eliko [62], radino32 [63] and as mentioned before Time Domain and Nanotron Companies. In Figure 2.20 different products of the Decawave Company are presented.

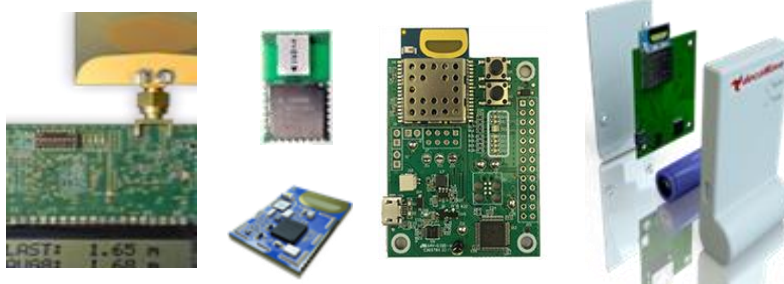


Figure 2.20: Decawave products including the DW1000 development kit (left) and DWM1001 kits (the two on the right) and the modules (in the middle) [60]

### 2.5.7. Comparison of the COTS modules

Many laboratories and research organizations have developed their own hardware for evaluating the UWB characteristics and potentials in localization systems. Such development however demands good knowledge of RF engineering as well as special high frequency equipment and measurement instruments. Preparation of such a laboratory for UWB technology is very costly and most of the time large effort should be invested in hardware design. This results in the fact that less resources could be dedicated to localization algorithms and signal processing part of indoor localization systems. A COTS module can solve this problem by providing a hardware platform which implements the required modulation and analogue signal processing internally hence leaving enough time to research other aspects of localization process. A few of these commercially available modules are introduced in the previous section. Among these module, the PulsOn440 shows the best performance in terms of accuracy (around 2.1 cm) and covering range (up to 1100 m). The performances of Decawave and beSpoon modules seem to be similar however Decawave offers more flexibility in terms of band selection and frame configuration. On the other hand, beSpoon module supports longer range of communication (800m). In the next level Ubisense provides an accuracy of 15cm followed by Zebra which has similar performances in these aspects. The least accuracy belongs to chirp technology of Nanotron but it has longer covering range (500m) which are consequently more suitable for less position sensitive applications. In terms of price, the Decawave and beSpoon products seem to be the best bargain with large distance to other rivals. Parametric comparison of the introduced modules in the previous section is provided in Table 2.4.

Table 2.4: Comparison of different UWB COTS modules available on the market

Module	Company	LOS Accuracy	LOS Range	Position Update Rate	Channel Frequencies	Max Current
DWM1000	Decawave	10cm	290m	200Hz	3.5-6.5GHz	150mA
7000	Ubisense	15cm	160m	20Hz	6-8GHz	NA
PulsON330	Time Domain	10cm	100m	200Hz	4 or 6.5GHz	220mA
PulsON440	Time Domain	2.1cm	300-1100m	153.8Hz	3.1-5.3GHz	395mA
Dart Tag	Zebra	30cm	200m	200Hz	6.3-6.75GHz	NA
Swarm Bee	Nanotron	100cm	10-500m	100Hz	2.4GHz	120mA
UM100	beSpoon	10cm	800m	73Hz	3.99GHz	NA

The modules provided by Zebra and Ubisense are more suitable for industrial applications which are more or less a ready to setup solution and less useful for research oriented projects. The PulsON330 and Nanotron UWB are basically based on the Decawave module. Therefore, for a research project it makes sense to use the Decawave modules directly and add required hardware to customize

the system depending on demands of the project or the research. Although the PulsON440 module of Time Domain provides excellent performances, due to high-tech circuitry and advanced electronics employed, it is often costly for research groups. Among the available options Decawave and beSpoon offer a tradeoff between performance, price and flexibility. A good comparison between Decawave, beSpoon and Ubisense modules in real practical experiments is carried out by Jimenez et al. in the papers [64, 65]. These experiments are performed in similar conditions in indoor as well as outdoor area. According to their results, in terms of measurement error at a certain point, Decawave has a maximum error of 1.3m in comparison to beSpoon with 2m and Ubisense around 30m. The standard deviation (STD) of the measurements in different ranges starting from 0.5m to 25m stays almost constant for Decawave and beSpoon modules which are around 10 to 30 cm with Decawave modules having a superior performance. The Ubisense module however has increasing STD starting from 30 cm and ending at 60cm at the range of 25 m. In general, the measured mean of error for Decawave is 0.49 m, beSpoon 0.71m and 1.93 m for Ubisense modules. Other works based on Decawave module can be found in [66–68], based on Time Domain in [69, 70] and a research based on Ubisense in [71].

To sum up the comparison, it can be seen that Decawave module provides the best in class accuracy with the lowest price offering full flexibility in terms of parameter settings such as baud rate, frame format, payload and it conforms to IEEE standard. Another important factor is the DWM1000 modules are certified for use in many countries which means in case of integration into other products no additional radio certification and licensing is required. Considering the above arguments, we have decided to use DWM1000 in this research project and therefore all the measurements performed and applied algorithms are based on this module.

### 3. Topologies of Localization

This chapter covers the methodologies which are used to estimate the position of a mobile node by exchanging radio signals with other fixed nodes (anchors). In general, the position of a node may be acquired by measuring radio signals directly (direct positioning) or it may be acquired in a two-step process, first by extracting signal characteristics and then calculating the position from the results of the first step (two step positioning) [44, p. 63]. The methods discussed in this chapter are two-step methods due to their simplicity of implementation and their diversity. In terms of radio-based localization techniques three general categories could be named. These are scene analysis, proximity detection and geometrical localization [72]. In the scene analysis approach, the position of the node is calculated by finding the closest match of the measured signal characteristics in database which is holding the statistical information of the signal as well as position information measured in real experiments. The proximity detection method extracts the position from the fixed nodes distributed in the environment (ex. Cell-ID). The geometrical approaches benefit from the range data (lateration) or angle data (angulation) acquired either from signal strength, signal time of travel in air or direction of arriving signal. The first two approaches are simple and cheap to implement however the geometrical approaches provide much higher accuracy and larger covering range compared to other methods. Different radio-based approaches of localization are summarized in Figure 3.1.

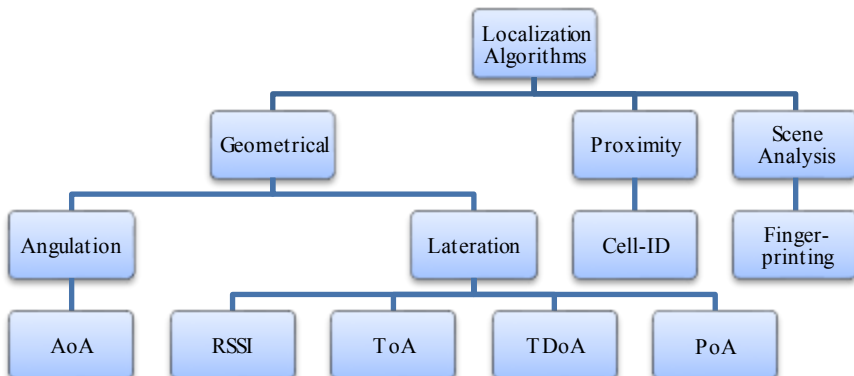


Figure 3.1 Summary of different radio-based localization approaches [73, p. 1329]

The geometrical approaches can be further divided into clock-based and clock-less approaches. The clock-less approaches operate either by measuring the signal strength of the arrived signal (RSS) and extracting the distance information, phase of the arrived signal (PoA) or detecting the angle of arrival (AoA) of the signal. The clock-based approaches include signal time of flight (ToF) also known as time of arrival (ToA) or time difference of arrival (TDoA) between several nodes [73, p. 1329]. The advantages of clock-less methods are their implementation simplicity and hence no need for synchronization of the transmitter and receiver clocks. In the RSS method, the amplitude of the signal is measured and converted to distance data according to propagation model of the radio channel. However, this technique is prone to large variations and uncertainty. The AoA utilizes an array of antennas in order to detect the angle of arriving signal. This leads to higher costs and complexity of the hardware but reduces the minimum number of required nodes for localization. The PoA approach is very accurate in the lower frequency ranges but demands complex algorithms. Both ToA and TDoA approaches calculate the distance between nodes based on the knowledge of the wave speed in air and time stamping the time of arrival of the signal. Different varieties of techniques based on ToA and TDoA exist which are highly accurate but sometimes synchronization and complex hardware are required. The pros and cons of the mentioned methods are summarized in the Table 3.1.

Table 3.1: Comparison of the advantages and disadvantages of different localization approaches [12, p. 251]

Approach	Advantages	Disadvantages
RSSI	Simplicity of implementation, low cost, possible to apply on many radio technologies	Inaccurate and sensitive to noise, multipath fading and environmental conditions
AoA	High localization accuracy, generating angle information, lower number of required nodes	Higher costs and dimensions of hardware, complex algorithms and lower accuracy in longer ranges
PoA	No synchronization, acceptable accuracy in lower frequencies	Low accuracy in non-line of sight, complex algorithms, sensitive to multipath
ToA	Simple and cheap to implement, very high localization accuracy	Sometimes synchronization is required, necessity of high rate clock
TDoA	High accuracy, multi-node support, high position update rate	Several nodes are required, complexity of algorithms, synchronization is needed, necessity of high rate clock

The time-based approaches mostly measure the elapsed time of travelling signal using clock circuitry and therefore in this thesis are categorized under clock-based approaches. Due to wide application of such methods, especially for UWB localization techniques, for each method a separate subchapter is dedicated. The clockless approaches are however discussed only briefly for the sake of completeness in only one subsection.

## 3.1. Clockless Approaches

As discussed in previous part, the clockless approaches are usually simpler to implement but less accurate. In this section, their operation concepts and procedure of distance calculation are discussed briefly.

### 3.1.1. Signal strength

The first technique is signal strength which enquires the distance parameter from the signal strength also known as received signal strength indicator (RSSI). This parameter is available almost in all receivers which is one of the reasons for having less implementation cost. The signal strength however is sensitive to multipath noise, shadowing, scattering and interference which may result in deviation of more than tens of dB [2, p. 85]. Therefore, this technique is usually used either in combination with other techniques or is supported with statistical algorithms such as *fingerprinting* in order to improve the accuracy.

The model between the distance of two nodes and total received power is based on two components namely path loss propagation model which is a constant and a variable component that models range dependent effects such as noise, signal attenuation, shadowing, multipath effect, etc. This model can be presented in the form of [44, p. 65]:

$$d = d_0 \cdot 10^{\left(\frac{P_0 - P(d)}{10n}\right)} \Leftrightarrow P(d) = P_0 - 10n \log_{10} \left( \frac{d}{d_0} \right) \quad (3.1)$$

where  $n$  is the path loss component (changing depends on the environment, as an example 2 for outdoor and 4 for indoor area [74]),  $P_0$  is the amount of received power at distance  $d_0$  which is known mostly from empirical measurements and  $P(d)$  is the measured power at distance  $d$  which we are going to estimate. In the UWB localization systems, the  $P(d)$  can be calculated by summing up the power of all multipath components of the received signal as stated in [44, p. 65]:

$$P(d) = \frac{1}{T} \int_0^T |r(t)|^2 dt \quad (3.2)$$

In this equation,  $r(t)$  is the amplitude of the measured multi-path (MPC) in channel impulse response and the  $T$  is the time span which includes all the MPCs. The power metric  $P(d)$  include shadowing noise which is a zero mean Gaussian variable.

### 3.1.2. Angle of Arrival (AoA)

The AoA technique takes the advantage of antenna array to calculate the direction of the arriving signal using the amplitude of the signal or comparing the carrier

phase of node's antennas [75]. The performance of AoA method is better in short distances however the accuracy of the measurements diminishes with the distance in a way that a short change of angle results in large amount of error [74]. To enquire the position of a node, at least two fixed nodes with known coordinates are required. This point is the intersection point of the lines from anchors (fixed nodes) to the mobile node as demonstrated in Figure 3.2. This localization method is called angulation (triangulation when three nodes are involved).

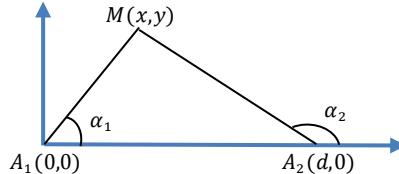


Figure 3.2: Angle of arrival (AoA) localization technique based on trilateration

If one anchor is located at the origin and the other within the distance  $d$  to the first one, then the position of a mobile node at coordinates of  $(x, y)$  with angles  $\alpha_1$  and  $\alpha_2$  to anchor 1 and 2 respectively can be calculated using [6, p. 213]:

$$x = \frac{d \tan(\alpha_2)}{\tan(\alpha_2) - \tan(\alpha_1)}, \quad y = \frac{d \tan(\alpha_1) \tan(\alpha_2)}{\tan(\alpha_2) - \tan(\alpha_1)} \quad (3.3)$$

The AoA approach is less suitable for UWB technology as the implementation of array antennas is too complex and extraction of angle from narrow impulses with multipath will be challenging [75, p. 71]. Therefore, time-based approaches are preferred for UWB localization systems.

### 3.1.3. Phase of Arrival (PoA)

In this approach, the difference of the carrier phase is used to measure the distance between a transmitter and receiver. A common carrier signal in this approach is a continuous sine signal or a modulated tone accurately synchronized in both transmitter and receiver [74]. In this concept, the transmitted signal will be phased lock at the receiver and reflected back to the transmitter. At the transmitter, the difference of the phase between the original signal and the received one will be estimated and converted to distance information according to [6, p. 113]:

$$d = \lambda \left( \frac{\Delta\phi}{2\pi} + n \right) \quad (3.4)$$

where  $d$  is the distance between the two nodes,  $\Delta\phi$  is the phase difference of the received signal with the original transmitted one,  $\lambda$  is the wavelength and  $n$  is the number of cycles passed between the transmission and reception of the signal. In case the signal's wavelength is shorter than the distance, the value of  $n$  should be controlled accurately in order to avoid adding cycles to phase information.

## 3.2. Time of Arrival (ToA)

The main concept of the time of arrival approach is based on measurement of the time that the signal needs to travel from one node to another. If the speed of radio wave in air is known (close to speed of light) then this time is linearly related to the distance between the two nodes. In order to implement this method, high frequency clock rates with high precision and in some cases synchronization between the two nodes are required. A common issue in this technique is the multipath effect which makes the detection of time of arrival challenging. The UWB technology enjoys ultra-narrow pulses which reduce this problem up to some extent. Therefore, the time-based approaches are best suited for localization in UWB devices.

The ToA approach has many variants of implementation [76]. In its simplest form known as one way ranging, only two nodes are required which are synchronized together using the same clock source. At a certain time, known to both transmitter and receiver  $t_{tx}$ , a narrow pulse will be transmitted which arrives at the receiver at time  $t_{rx}$ . Assuming parameter  $c$  which is the speed of radio wave in air, the distance  $d_n$  between the anchor  $n$  and the mobile node can be calculated as:

$$d_n = (t_{rx} - t_{tx})c \quad (3.5)$$

Once the range information between the nodes are calculated, the position of the target node in 2D can be estimated using the Euclidean distance between the fixed nodes with known coordinates and the mobile node according to [3, p. 23]:

$$(x - x_n)^2 + (y - y_n)^2 = d_n^2 \quad (3.6)$$

where  $(x, y)$  are coordinates of the mobile node,  $(x_n, y_n)$  are coordinates of the anchor  $n$  and  $d_n$  is the distance between the anchor  $n$  and the mobile node as stated in Eq. 3.5. In this equation however, we have two unknowns. Although the results of the two equations is enough to lead to an answer but sometimes we have more than a solution which results in ambiguity in the localization process. Therefore, at least three anchors are required to estimate the location of the target node based on three nonlinear equations. The extension of Eq. 3.6 results in:

$$\begin{cases} (x - x_1)^2 + (y - y_1)^2 = d_1^2 \\ (x - x_2)^2 + (y - y_2)^2 = d_2^2 \\ \dots \\ (x - x_n)^2 + (y - y_n)^2 = d_n^2 \end{cases} \quad (3.7)$$

The Eq. 3.6 is nothing but a circle with its center at  $(x_n, y_n)$  and diameter of  $d_n$  which crosses over the point  $(x, y)$ . If we have three equations, then the position of the mobile node can be estimated by finding the intersection point of the three circles as shown in Figure 3.3.

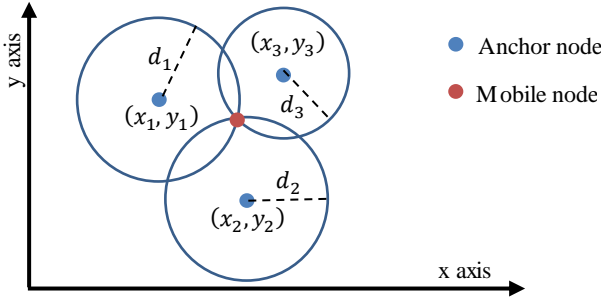


Figure 3.3: Geometrical solution of localization in time of arrival (ToA) approach

In the aforementioned scenario, it is assumed that the nodes are synchronized with the same input with no clock drift or phase difference and there is no delay other than the wave propagation time between transmission and reception of the signal. This is however extremely difficult to realize in practice as the nodes are usually located far away from each other and synchronization using wire connection is costly and inefficient. In order to solve this issue, many other approaches are proposed to relax the synchronization requirement of the case. A few of these techniques are addressed in the rest of this section.

### 3.2.1. Single Sided Two-Way ranging (SS-TW)

The single sided two-way ranging approach is proposed in order to avoid the requirement of synchronization between two nodes. In this method, an UWB impulse signal is transmitted once from mobile node to anchor node and then sent back from anchor node to mobile node after a certain amount of time. This demands that both anchor and mobile node should be able to change their role as transmitter and receiver. Using this technique, each node can run on its own clock without need of synchronization. The time diagram of this approach provided in Figure 3.4 clarifies the process visually:

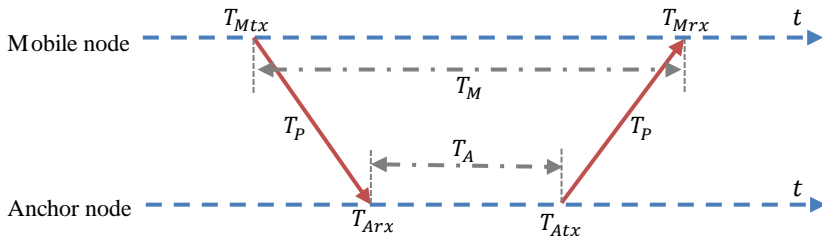


Figure 3.4: Time diagram of range estimation process in single sided two-way ranging (SS-TW) method demonstrating the transmission and receive timing

At the transmission time, the mobile node records its own time stamp as  $T_{Mtx}$ . This signal arrives at time  $T_{Arx}$  at the anchor node. This time will be also time

stamped and recorded in the anchor node. After a certain time interval  $T_A$  which is known to both nodes, the anchor node transmits the signal at time  $T_{Atx}$ . The signal arrives back to mobile node at time  $T_{Mrx}$ . The propagation time  $T_P$  of the signal between these two nodes can be calculated using the following equations:

$$T_A = T_{Atx} - T_{Arx} \quad (3.8)$$

$$T_M = T_{Mrx} - T_{Mtx} = T_A + 2T_P \quad (3.9)$$

$$T_P = \frac{(T_M - T_A)}{2} \quad (3.10)$$

As it can be seen from Eq. 3.10, the values of clocks are calculated differentially which is the reason that synchronization between the values of the two clocks is not necessary. The Time  $T_A$  is usually decided based on the time that the hardware requires to prepare and process the data. This value also determines the location update rate. A shorter delay results in a higher update rate but increases the power consumption. Therefore, this value is a tradeoff between the required location update rate and energy consumption as well as hardware processing capability. In the mentioned scenario, the initiator of the transmission was the mobile node and therefore the ranging information will be available at the mobile node as well. This however can be modified in that the anchor node initiates the process resulting in receiving the range data in the anchor. This is useful in tracking and monitoring applications. In this case, the anchors should be synchronized using either wire-based or wireless methods to avoid signal jamming and interfering of the anchors among each other.

Although synchronization in SS-TW approach is not necessary anymore, still one issue is a point of concern. In this approach, the clock rate of both nodes should have same rate which demands crystals with high accuracy. This is however hard to achieve in practice as crystals have certain deviation in the accuracy window as well as an offset to its nominal value which is evaluated according to parts per million (ppm) unit. This results in the fact that although two crystals have same nominal frequency value, one may run faster or slower than the other according to its defined accuracy range. If we consider the error offset of  $\delta$  in the clock frequency, we can describe the propagation time with inaccuracies as [77]:

$$\hat{T}_P = \frac{1}{2}(T_M(1 - \delta_m) - T_A(1 - \delta_a)) \quad (3.11)$$

The sub-indexes of  $m$  and  $a$  stand for mobile node and anchor node respectively. Using this equation, the error of range measurement is:

$$e = \hat{T}_P - T_p = \frac{1}{2}(T_M(1 - \delta_m) - T_A(1 - \delta_a)) - \frac{1}{2}(T_M - T_A) \quad (3.12)$$

$$e = \hat{T}_P - T_p = \frac{1}{2}(\delta_a T_A - \delta_m T_M) \quad (3.13)$$

Applying  $T_A = T_M + 2T_P$  into previous equation, we can rewrite the Eq. 3.13 into:

$$e = \frac{1}{2}(\delta_a(T_M + 2T_P) - \delta_m T_M) = \frac{1}{2}T_M(\delta_a - \delta_m) + T_P\delta_a \quad (3.14)$$

Knowing the fact that the propagation time  $T_P$  is in the range of nanoseconds and the interval time  $T_M$  in the range of a few milliseconds, we can neglect the last term in the equation and simplify it into [78]:

$$e \approx \frac{1}{2}T_M(\delta_a - \delta_m) \quad (3.15)$$

To enlighten the importance of the clock drift analysis, assume a crystal with accuracy of 10 ppm. This crystal has a drift of  $10\mu s$  in each second. If the total round trip of the signal including interval delays takes 10 ms time, the resulted drift is equal to 100 ns. Considering the speed of the wave which is nearly 30 cm/ns, the distance error is around 30 m which is unacceptable for an accurate localization system [79]. If the bias offset of the clock is constant, this problem can be solved by calibration. But the clock behavior has normally a dynamic part which changes depending on environmental conditions such as temperature and noise. The double sided two way ranging approach (DS-TW) mitigates this effect by averaging the clock inaccuracies of the mobile and anchor nodes clocks.

### 3.2.2. Double Sided Two-Way ranging (DS-TW)

The DS-TW approach benefits from two rounds of signal trip which results in calculating the distance two times. The final outcome will be average of these two distance information. The process can be initiated either in the anchor or mobile node depending on the application. We consider a case where the process starts in mobile node, but the rest of process is more or less the same for the other case. The timing diagram of this approach is demonstrated in Figure 3.5.

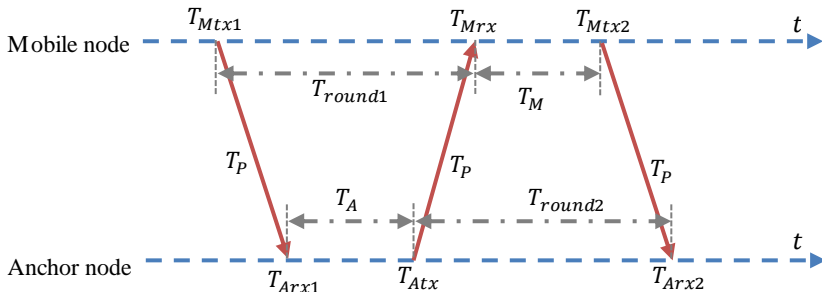


Figure 3.5: Timing diagram of the range estimation process in double sided two-way ranging (DS-TW) method demonstrating the transmission and receive times

The initial part of the process is similar to that in SS-TW method. The difference is an added round of trip after receiving the signal back in the mobile node. The

mobile node starts another round of trip that is time stamped and recorded at  $T_{Mtx2}$  which happens after time interval  $T_M$  after receiving the signal from anchor node. This signal arrives at the anchor node for the second time at  $T_{Arx2}$ . Recall from the Eq. 3.10, the propagation time of the first part is:

$$T_P = \frac{(T_{round1} - T_A)}{2} \quad (3.16)$$

Likewise, the second part of the process can be defined as:

$$T_P = \frac{(T_{round2} - T_M)}{2} \quad (3.17)$$

By combining the Eq. 3.16 and 3.17 together we have:

$$T_P = \frac{(T_{round1} - T_A) + (T_{round2} - T_M)}{4} \quad (3.18)$$

where  $T_{round1}$  is the round time of travel starting from mobile node and returning,  $T_A$  is the interval time in anchor,  $T_{round2}$  is the round time of travel starting from anchor node and returning and finally  $T_M$  is the interval time in mobile node. In order to evaluate the performance of the new method, the propagation time with noise can be calculated similar to the procedure performed in Eq. 3.11-3.13:

$$\hat{T}_P = \frac{1}{4}((1 - \delta_a)(T_{round1} - T_A) - (1 - \delta_m)(T_{round2} - T_M)) \quad (3.19)$$

Replacing  $T_{round1} = T_A + 2T_P$  and  $T_{round2} = T_M + 2T_P$  into previous equation, we can calculate the error of the measurement as:

$$e = \hat{T}_P - T_p = \frac{1}{2}T_p(\delta_a - \delta_m) + \frac{1}{4}((T_M - T_A)(\delta_a - \delta_m)) \quad (3.20)$$

As it was the case in previous method, we can ignore the first term including  $T_p$  as this part is significantly smaller than the second term which yields in:

$$e \approx \frac{1}{4}((T_A - T_M)(\delta_a - \delta_m)) \quad (3.21)$$

As it can be seen, the clock drift error is much less than the one defined in SS-TW due to the fact that the interval errors are subtracted from each other.

The interval delays in this approach can be different leading to asymmetric double sided two way ranging (ADS-TW) [77] or they can be the same which is called symmetric double sided two way ranging (SDS-TW) [53, p. 36] [77]. In the case of the latter, the performance of the method is higher since the error term calculated in Eq. 3.21 will be approximately zero, however practically seen, it is difficult to have two crystals with exactly same clock frequency.

### 3.2.3. Double Response Two-Way ranging (DR-TW)

In this approach two consecutive responses from the anchor node are sent to compensate for clock drift problem. The benefit of this technique is that the distance between the two nodes can be estimated in only one node without need of exchanging information with another node, hence the clock inaccuracy of the second node is irrelevant. The process can be initiated either in mobile or anchor node. Here the case for mobile node is described. After arrival of the mobile node signal in anchor, the sequential signals are transmitted back to mobile node with the same time interval between the transmissions. This way the mobile node is able to measure the time interval of the anchor node according to its own clock and hereby subtract it from the round time of travel directly. Details of the DR-TW range measurement procedure is described in Figure 3.6.

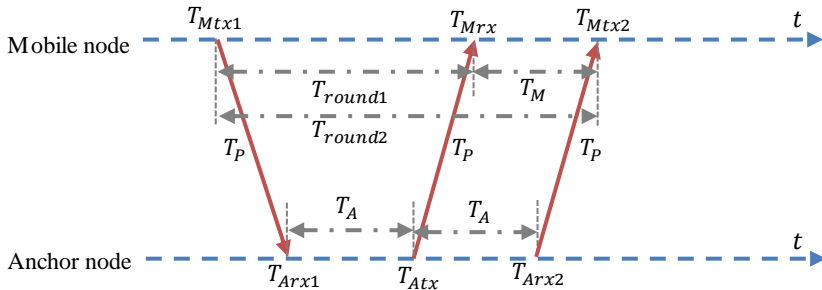


Figure 3.6: Timing diagram of range estimation process in double response two-way ranging (DR-TW) method demonstrating the transmission and receive times

Considering the times  $T_M$  and  $T_A$  to be equal, the propagation time between two nodes can be calculated using [2, p. 245]:

$$T_p = \frac{(T_{round2} - 2T_A)}{2} = \frac{(T_{round1} + T_M - 2T_M)}{2} = \frac{(T_{round1} - T_M)}{2} \quad (3.22)$$

As it can be seen from Eq. 3.22, the propagation time can be calculated without any time stamp knowledge of the anchor node which simplifies the ranging process. The clock drift error can be defined as [2, p. 245]:

$$\hat{T}_p = \frac{(T_{round1}(1 - \delta_m) - T_M(1 - \delta_m))}{2} \quad (3.23)$$

$$e = \hat{T}_p - T_p = \frac{(T_{round1}(1 - \delta_m) - T_M(1 - \delta_m))}{2} - \frac{(T_{round1} - T_M)}{2} \quad (3.24)$$

Knowing the fact that  $T_M = T_A$  and exchanging  $T_{round1} = 2T_p + T_A = 2T_p + T_M$  in the previous equation, we can reach final error result:

$$e = \hat{T}_p - T_p = T_p(1 - \delta_m) - T_p = -T_p\delta_m \quad (3.25)$$

As it can be seen from Eq. 3.25, the final error of the estimation is neither relevant to time delay intervals nor to the clock inaccuracy of the second anchor. The only left term  $T_p \delta_a$  is in the range of femtosecond which can easily be neglected.

### 3.2.4. Double Sided Cascaded Reply (DSCR)

As it was mentioned before, in order to find the location of a mobile node, at least three nodes are required for 2D and 4 nodes for 3D applications. Since each mobile node can only perform one ranging process at a time, the range data should be collected from all the available anchors sequentially. This however is time consuming when a large number of nodes are applied which results in a low rate of location data updates. Double sided cascaded reply (DSCR) method addresses this issue by cascading part of the transmission together and sharing it between all the nodes. The initial point of the process is transmission of a signal packet by mobile node. The signal will be received by all the anchor nodes. But not all of them reply at the same time as this causes signal collision. Instead the anchors reply one after the other with certain time interval between them. This means the first anchor replies after time delay  $d$ , the second anchor after  $2d$  and the anchor  $n$  after  $nd$ . The mobile node performs the ranging calculations as the signals arrive but the final location estimation can only be performed when all the anchors' responses are received. Although this process is explained for the case that the mobile node is the initiator, it is also possible to reverse the process and to start it in the first anchor. This scenario is useful for tracking applications where the location data is required in a centralized server. This process is depicted in Figure 3.7 for both mobile initiator and anchor initiator scenarios.

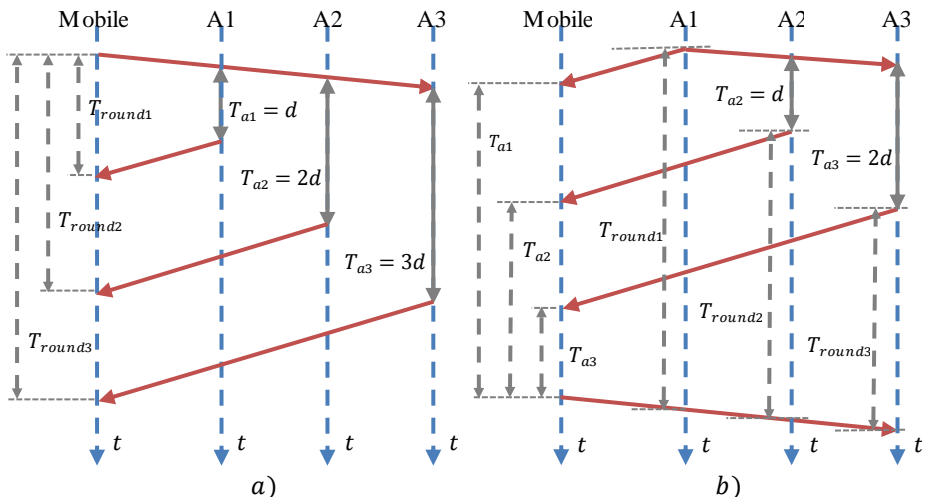


Figure 3.7: Time diagram of localization process in DSCR-TW approach for cases where  
a) the mobile node is initiator and b) the anchor node is initiator

In case the initiator of the ranging process is anchor, it should be noticed that all the anchors should be synchronized to avoid signal collision. In this scenario, the transmission delay of the anchors should not be necessarily the same for all anchors as this information can be transmitted by the anchors to the mobile node in the payload of the packets. The ranging information can be estimated using following equation:

$$T_{P_n} = \frac{(T_{round_n} - T_{a_n})}{2} \quad (3.26)$$

where  $T_{P_n}$  is the propagation time between anchor n and the mobile node,  $T_{round_n}$  is the round travel time of signal from mobile node to anchor n and return back to mobile node and  $T_{a_n}$  is the reply time of anchor n. The error of clock drift is the same as that in the SS-TW algorithm. This could be improved by utilizing the DR-TW approach in cascade form.

### 3.2.5. Comparison of the ToA approaches

The algorithms of ToA mentioned in this section are not covering all the possible solutions. There are still other variations by combining or modifying these methods. To make the selection of a certain approach simpler, in this section we summarize their pros and cons. A detailed comparison of the mentioned methods and many other approaches is provided in the work of Rebel et al. [80] or the work of Pelka et al. [81]. The main advantages and disadvantages of the discussed techniques are listed in the Table 3.2.

Table 3.2: Pros and cons of the most common ToA ranging approaches [80]

Approach	Advantages	Disadvantages
One-Way	Simplicity of algorithm	Synchronization as well as precise clock sources are required
SS-TW	Lower radio traffic, less power consumption, no synchronization	Low accuracy for long reply delays, clock drift problem
ADS-TW	Flexible reply time, less influence from clock drift, no synchronization	Higher radio traffic, higher power consumption, complex role changing
SDS-TW	Zero influence from clock drift, good accuracy, no synchronization	Hard to achieve same reply time in two devices, lower location update rate
DR-TW	No time stamp information from anchor node, simplicity of equations, no clock drift influence	Higher traffic rate compared to SS-TW
DSCR-TW	Lower radio traffic for larger number of nodes, less power consumption	Complexity of the approach, slow update rate for large number of nodes, clock drift issue, synchronization might be required

### 3.3. Time Difference of Arrival (TDoA)

The main idea of the Time Difference of Arrival (TDoA) approach is to estimate the range information by measuring the difference of arrival times of two signals at the receiver. This way no dynamic role exchanging of transmission or reception is required that yields in simpler implementation and lower power consumption. In addition to that, larger number of nodes can be localized either for monitoring or navigation purposes with minimum radio traffic of the network. Since in this technique no time of travel is measured and therefore no data from initial time stamps are required, the common drawbacks of ToA techniques are not relevant anymore. Therefore, this approach is often used for applications implementing a large number of nodes. One disadvantage of this method is the requirement of fully or partly clock synchronization of nodes which could be addressed using different wireless synchronization methods as it is discussed in Chapter 4.

Due to differential structure of the range measurement, the result is a hyperbolic line with its peak located somewhere in between the two anchor nodes and its focus on the closer anchor to hyperbolic line. The distance of the mobile node to a pair of anchors anywhere on the hyperbolic line is constant. The equation of the hyperbola is in the form [6, p. 31]:

$$\frac{x^2}{a^2} + \frac{y^2}{b^2} = 1 \quad \text{where } a = \left(\frac{\Delta d}{2}\right)^2 \quad \text{and } b = \left(\frac{D}{2}\right)^2 - a^2 \quad (3.27)$$

In this equation, the  $(x, y)$  are coordinates of the mobile node,  $\Delta d = d_2 - d_1$  is the difference of the distances between each anchor and mobile node, and  $D$  is the distance between the two anchors used for measurements. In Figure 3.8, details of these dimensions and the shape of the hyperbolic line are demonstrated.

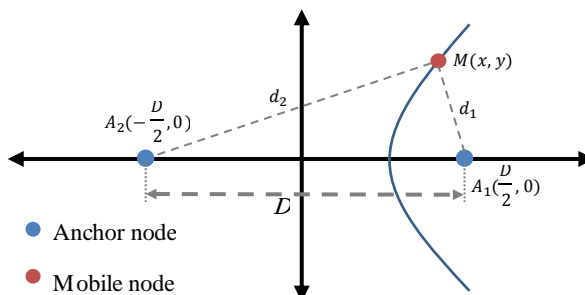


Figure 3.8: Ranging in TDoA localization topology with a hyperbolic line (half of a hyperbola) between the anchors and the mobile node [6, p. 31]

The hyperbola direction is always to the shortest distance side. For example if  $d_1$  in Figure 3.8 is less than  $d_2$  then the hyperbola approaches a point in  $(\infty, \pm\infty)$  whereas if the  $d_1$  is larger than  $d_2$  then the hyperbola tend to  $(-\infty, \pm\infty)$  point. In case both distances are equal, the hyperbolic line is a linear line located at the

middle point of the anchors and approaching to  $(0, \pm\infty)$ . Once the ranging information of the pair nodes are available, the location of the mobile node can be estimated by finding the intersection point of the hyperbolic lines for two dimensions or hyperboloid surfaces in three dimensions. For the 2D case, the intersection point can be estimated using following equations:

$$d_1 = \sqrt{((A_1(x) - M(x))^2 + (A_1(y) - M(y))^2)} \quad (3.28)$$

$$d_2 = \sqrt{((A_2(x) - M(x))^2 + (A_2(y) - M(y))^2)} \quad (3.29)$$

$$d_3 = \sqrt{((A_3(x) - M(x))^2 + (A_3(y) - M(y))^2)} \quad (3.30)$$

$$\Delta d_{2,1} = d_2 - d_1, \Delta d_{3,1} = d_3 - d_1, \dots, \Delta d_{n,1} = d_n - d_1 \quad (3.31)$$

where  $d_n$  is the distance of anchor  $n$ , parameter  $\Delta d_{1n}$  is the difference of the distances between anchor  $n$  and anchor 1,  $A_n(x, y)$  is the coordinates of anchor  $n$  and  $M(x, y)$  is the coordinates of the mobile node. If three anchors are used in the localization system and the coordinates of the anchors are known, then two equations will be available which is enough to extract the value of two unknown variables  $M(x)$  and  $M(y)$ . Geometrical explanation of these equations for two hyperbolic lines are illustrated in Figure 3.9.

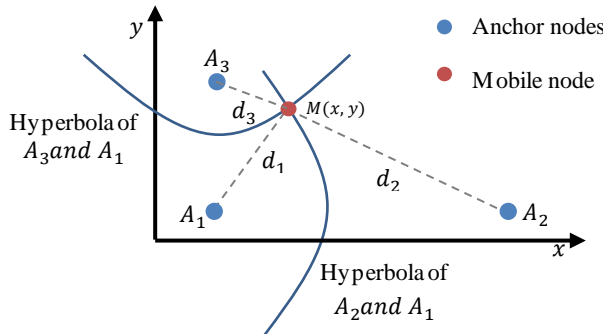


Figure 3.9: TDoA localization principle using two hyperbolas derived from three anchors

The TDoA concept can be applied in two distinct topologies namely unilateral and multilateral [6, p. 192]. In unilateral method, the anchor nodes are transmitter and the mobile nodes are only receiver. Hence the mobile node should localize itself using the received signals. In the multilateral approach the mobile nodes are transmitters and the anchors record the time stamp of the arrived signal. This way the location information is available in a centralized server connected to anchors which can estimate the location by comparing the recorded time stamps of all anchors. In the rest of this section the details of each approach are discussed and a comparison between them is provided.

### 3.3.1. Multilateral TDoA

The working process of the multilateral approach is as follows: The process begins by transmission of a short message known as blink from the mobile node. This blink message arrives at different times at all the anchor nodes in its vicinity. Assuming that the anchors are synchronized and are running with the same clock frequency, the time stamps recorded at each anchor is collected to a central server. The synchronization as well as data communication of the server and anchors can be realized using a wire-based or a wireless media. Difference of the recorded time stamps are calculated pairwise between the anchors. The location of the mobile node can be calculated using the differential range information of each pair and Equations 3.28-3.31. This method also supports multi-node localization. In this case, the blink messages are transmitted randomly but at a short period of time with usually long time intervals between two consecutive transmissions. This is defined in order to avoid signal interference with other nodes which will be inevitable when too many transmitters are utilized in the network. Examples of applications based on this approach are provided in [82, 83]. The structure of a multilateral TDoA localization network and its operational timing diagram is presented in Figure 3.10.

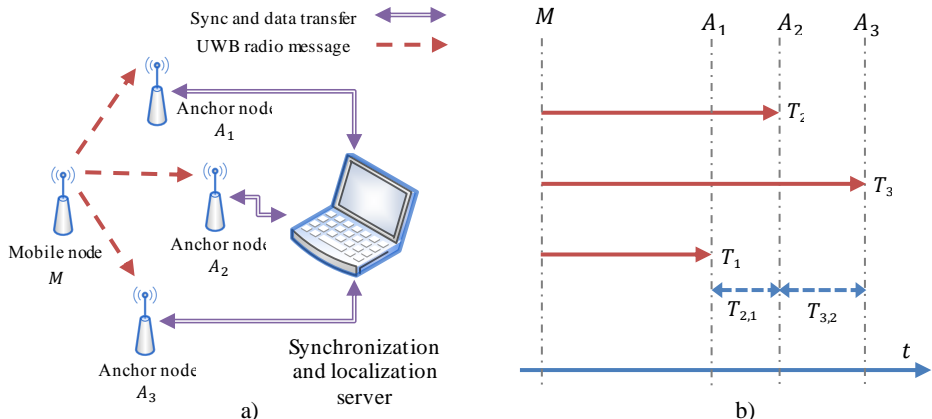


Figure 3.10: The multilateral TDoA approach a) network connection structure b) timing diagram of the communication process [84]

According to the time diagram provided in Figure 3.10.b, the distance of the mobile node to anchors can be calculated using:

$$\begin{cases} \Delta d_{2,1} = cT_{2,1} = \sqrt{(x_m - x_2)^2 + (y_m - y_2)^2} - \sqrt{(x_m - x_1)^2 + (y_m - y_1)^2} \\ \Delta d_{3,2} = cT_{3,2} = \sqrt{(x_m - x_3)^2 + (y_m - y_3)^2} - \sqrt{(x_m - x_2)^2 + (y_m - y_2)^2} \end{cases} \quad (3.32)$$

where  $c$  is the speed of wave,  $(x_m, y_m)$  are coordinates of a mobile node,  $(x_n, y_n)$  are coordinates of the anchor  $n$  and  $d_{2,1}$  and  $d_{3,2}$  are differential distances resulted from subtraction of the time stamps recorded in anchors multiplied by  $c$ .

### 3.3.2. Unilateral TDoA

In the unilateral concept, the roles of the transmitters and receivers are exchanged compared to multilateral method. This means the mobile nodes are only receiver and the anchor nodes are transmitter. The anchor nodes may need to be receiver as well if the clock synchronization of the anchors are performed wirelessly over the same radio channel. The main advantage of this method is the number of utilized mobile nodes in the network is unlimited. This is due to the fact that the mobile nodes are receiver and hence no signal interference can occur by the mobile nodes. This fact, makes the unilateral approach suitable for navigation and self-localizations applications where large number of mobile nodes should be involved with minimum air traffic and implementation cost. All the infrastructure required in this approach is a set of anchors scattered in the area. In some approaches an additional reference node is used with the roles of controlling the clock drift of all the nodes in the network as well as initiating the transmission process. Examples of this approach can be found in ATLAS project [85] or [86]. The approach used in this thesis however employs the first anchor for overtaking this role, since this way the radio traffic can be mitigated and more efficiency can be gained from both cost and performance points of view. A similar work to our approach is performed in the EIGER project [41]. The unilateral approach discussed in this section is mentioned under many other terms in the literature such as asynchronous TDoA (A-TDoA) [87] or Sequential TDoA (S-TDoA) [88]. Application of this approach in vehicle positioning is provided in the work of Kolakowski et al. [89]. The network connection structure of the unilateral method along with a simplified operational time diagram is shown in Figure 3.11.

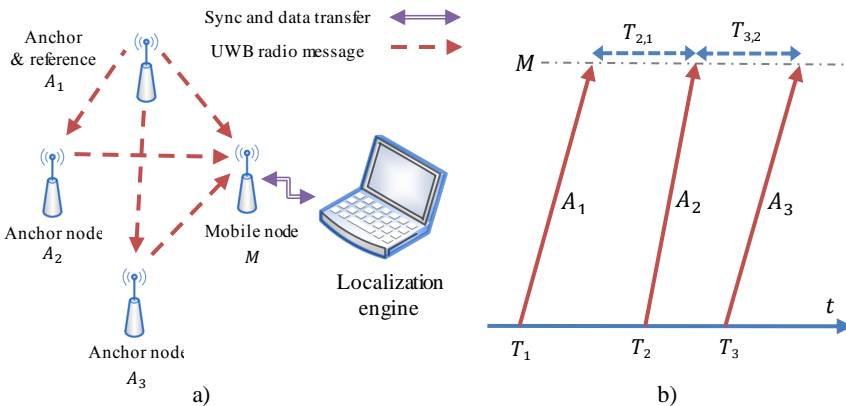


Figure 3.11: The unilateral TDoA approach a) network connection structure b) simplified timing diagram of the communication process [84]

Since the anchors are transmitter in the unilateral technique, a method is required to manage the transmission times to avoid signal interference between the anchor nodes. One solution to this issue is sequential transmission of the anchors with a

constant time delay between transmissions. All the nodes are pre-programmed with the same time delay which will be used for delayed transmission. The mobile nodes use this delay for reconstruction of the time stamps so that only propagation time of the signals are considered and the delays are subtracted. The first anchor is only transmitter sending a signal periodically according to the defined time interval. This time is set to 50 ms in the work performed in this thesis resulting in location update rate of 20Hz. This could be different in other applications with influence on power consumption and radio traffic rate.

At the moment that the first anchor transmits, all the anchors and mobile nodes are receiver waiting for the signal of the first anchor. Each anchor transmits an ID number together with the coordinates of the anchor which is transmitting. All the anchors record the time stamp of the received signal and calculate their next transmission time considering the parameters such as the signal time of flight from the first anchor to the receiving anchor, antenna delays, and defined delay interval according to the anchor ID number. All the mobile nodes record the time stamp of the anchors' received signals and calculate the time difference of arrival between them. Since all the signals are time stamped in mobile node, no synchronization between the anchors and mobile nodes is required. Each mobile node is able to calculate its location utilizing the coordinates of the anchors and their differences of arrival time. A detailed timing diagram of this process is provided in Figure 3.12 for  $n$  number of anchors and  $m$  number of mobile nodes.

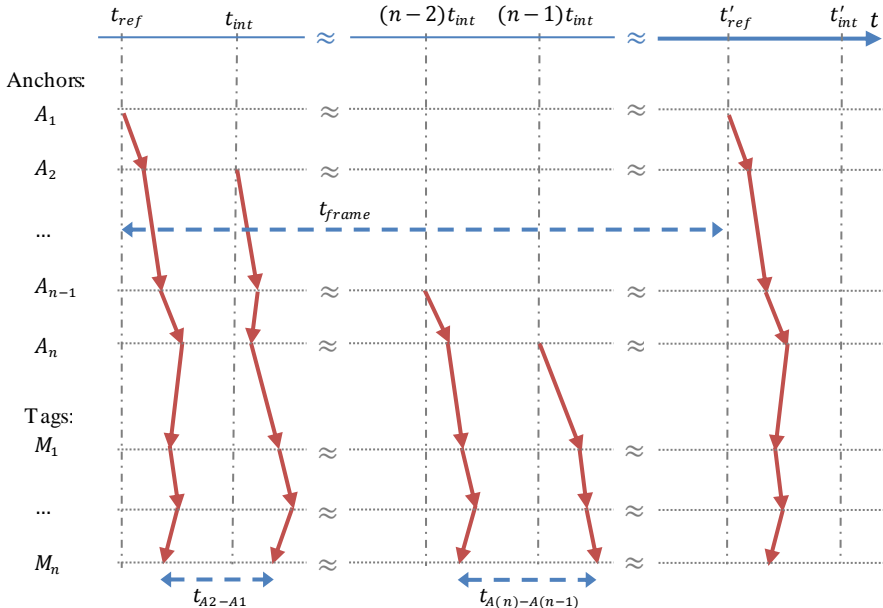


Figure 3.12: Time diagram of unilateral TDoA technique showing  $n$  anchors and  $m$  mobile nodes with details of the time stamps and delay intervals

In the previous graph, the initial transmission time of the first anchor is  $t_{ref}$  and the time interval between the anchors' sequential transmissions is  $t_{int}$ . After all the anchors have transmitted a signal, the process will be repeated starting from anchor 1 at time period of  $t_{frame}$  after the previous transmission has occurred. In order to find out the next transmission time for each anchor, the  $t_{ref}$  should be known. This is however, not available to the anchors and mobile nodes. Each anchor can calculate the reference time using:

$$t_{ref} = t_{A_nrx} - t_{A_1delay} - t_{A_ndelay} - t_{tof} \quad (3.33)$$

where  $t_{A_nrx}$  is the time stamp of the arrived signal in anchor  $n$ , parameter  $t_{A_1delay}$  is the antenna transmission delay in anchor 1,  $t_{A_ndelay}$  is the receive antenna delay in anchor  $n$  and  $t_{tof}$  is the signal time of flight from anchor 1 to  $n$ . The antenna delay of the node is usually provided from the manufacturer or can be measured empirically. Since the locations of all the anchors are known, the  $t_{tof}$  can be calculated using the following equation:

$$t_{tof} = \frac{\|P_1 - P_n\|}{c} \quad (3.34)$$

where  $P_1$  and  $P_n$  are the locations of the anchor 1 and  $n$  respectively, the operator  $\| \dots \|$  is the Euclidean distance between two locations and  $c$  is the speed of wave. The next transmission time for each anchor is calculated according to:

$$t_{A_i tx} = t_{ref} + (i - 1)t_{int}, \quad i = 2, \dots, n \quad (3.35)$$

where  $t_{int}$  is the delay interval between the two consecutive transmissions which in our case is 10 ms and  $i$  is the index of the transmitting anchor. In the mobile nodes, the received signals from all the anchors are time stamped. The differences of two arrivals include the internal delay between the two anchors which needs to be subtracted. Therefore, the difference of arrival between anchor 1 and  $n$  is represented as:

$$T_{i,1} = t_{A_i rx} - t_{A_1 rx} - (i - 1)t_{int}, \quad i = 2, \dots, n \quad (3.36)$$

The 2D location of the node can be calculated using Equation 3.32 when at least two differential time of arrivals are available. Availability of more anchors in the setup results in redundancy of the equations in Equation 3.32 with the effect of having a better accuracy of the location measurement. However, a higher number of anchors lengthens the overall time frame yielding in lower location update rate. Therefore, the number of anchors in this method is a tradeoff between the accuracy of the measurements and location update rate. In our setup, 4 anchors are utilized with interval delay of 10 ms between each anchor and overall time frame of 50 ms resulting in location update rate of 20 Hz. The overall time frame is larger than the required time frame for 4 anchors (40 ms) which is considered

as backup either for adding an anchor in the future or for location estimation algorithms which require longer processing time.

One issue yet to be addressed is the concept of pair selection in TDoA approach. Out of many possible combinations, two of them are the most common one namely star form and chain form. In the star form (Figure 3.13a) the time stamps of anchors from  $(2, \dots, n)$  are compared to the first anchor. The resulted time differences to this anchor can be represented in the form:

$$T_{2,1}, T_{3,1}, \dots, T_{(n-1),1}, T_{n,1} \quad (3.37)$$

The chain form (Figure 3.13.b) considers the pairs sequentially which means the time stamp of each anchor is compared to the next available anchor so that:

$$T_{2,1}, T_{3,2}, \dots, T_{(n-1),(n-2)}, T_{n,(n-1)} \quad (3.38)$$

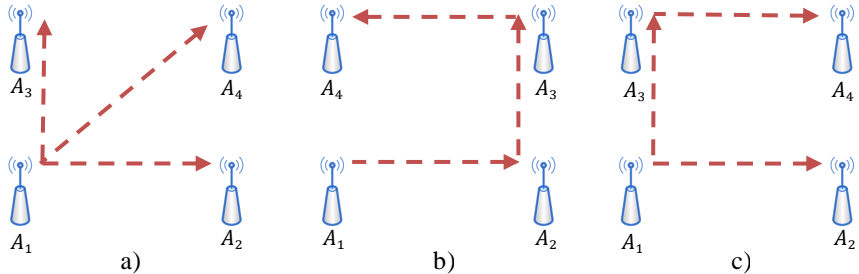


Figure 3.13: Different pair selection approaches for unilateral TDoA topology a) star form, b) chain form, c) hybrid form

The advantage of the star form is that all the anchors are measured to a unique reference time resulting in lower measurement noise. In the chain form however, the measurement noise is accumulated as the new transmission time in each round is based on the previous noisy time stamp. To prove this mathematically, consider  $w$  as an additive Gaussian white noise with zero mean. Then for the case of star form the transmit time can be calculated as:

$$t_{A_2tx} = t_{ref} + t_{int} + w_1 \quad (3.39)$$

$$t_{A_3tx} = t_{ref} + 2t_{int} + w_2 \quad (3.40)$$

$$t_{A_nrx} = t_{ref} + (n - 1)t_{int} + w_n \quad (3.41)$$

At the mobile node, the recorded time stamps are calculated according to Eq. 3.36. Considering the added noise, this equation can be modified as:

$$T_{i,1} = t_{A_i rx} - t_{A_1 rx} - (i - 1)t_{int} + w'_i - w'_1, \quad i = 2, \dots, n \quad (3.42)$$

where  $w'_i = w_{txi} + w_{rxi}$  is the measurement noise of the received signal at the mobile node from anchor  $i$  where  $i = 2, \dots, n$  and  $w_{txi}$  and  $w_{rxi}$  are the noise at the

transmission and reception time in the same anchor respectively. The covariance of the measurement error can be calculated according to the following formula:

$$\mathbf{Q} = E \left[ \left( T_{i,1} - E(T_{i,1}) \right) \left( T_{i,1} - E(T_{i,1}) \right)^T \right] = \sigma^2 \mathbf{I}, \quad i = 2, \dots, n \quad (3.43)$$

where the  $E$  operator is the expectation value of the variable,  $\mathbf{I}$  is the unity matrix and  $\sigma$  is the common standard deviation of the measurement error. This leads to:

$$\mathbf{Q} = E \left[ \begin{bmatrix} (w'_2 - w'_1) \\ (w'_3 - w'_1) \\ \dots \\ (w'_n - w'_1) \end{bmatrix} \begin{bmatrix} (w'_2 - w'_1) & (w'_3 - w'_1) & \dots & (w'_n - w'_1) \end{bmatrix}^T \right] = \quad (3.44)$$

$$E \left[ \begin{bmatrix} (w'_2 - w'_1)^2 & (w'_2 - w'_1)(w'_3 - w'_1) & \dots & (w'_2 - w'_1)(w'_n - w'_1) \\ (w'_3 - w'_1)(w'_2 - w'_1) & (w'_3 - w'_1)^2 & \dots & (w'_3 - w'_1)(w'_n - w'_1) \\ \dots & \dots & \dots & \dots \\ (w'_n - w'_1)(w'_2 - w'_1) & (w'_n - w'_1)(w'_3 - w'_1) & \dots & (w'_n - w'_1)^2 \end{bmatrix} \right]$$

The diagonal terms can be denoted as:

$$E[(w'_i - w'_1)^2] = E[w'_i{}^2] + E[w'_1{}^2] - 2E[w'_i w'_1], \quad i = 2, \dots, n \quad (3.45)$$

Assuming that the noise terms  $w'_i$  and  $w'_1$  are uncorrelated, the term  $E[w'_i w'_1]$  is equal to zero. Therefore, we can rewrite the last equation into:

$$E[w'_i{}^2] + E[w'_1{}^2] - 2E[w'_i w'_1] = \sigma_i^2 + \sigma_1^2 \quad (3.46)$$

For the non-diagonal terms, the expectation value can be calculated according to the following formula which is considering only one element as an example:

$$E[(w'_2 - w'_1)(w'_3 - w'_1)] = E[w'_2 w'_3] - E[w'_2 w'_1] - E[w'_1 w'_3] + E[w'_1{}^2] \quad (3.47)$$

Considering the uncorrelated terms as zero we can rewrite the formula as:

$$E[w'_2 w'_3] - E[w'_2 w'_1] - E[w'_1 w'_3] + E[w'_1{}^2] = \sigma_1^2 \quad (3.48)$$

Therefore, the covariance matrix turns into:

$$\mathbf{Q} = \begin{bmatrix} \sigma_2^2 + \sigma_1^2 & \sigma_1^2 & \dots & \sigma_1^2 \\ \sigma_1^2 & \sigma_3^2 + \sigma_1^2 & \dots & \sigma_1^2 \\ \dots & \dots & \dots & \dots \\ \sigma_1^2 & \sigma_1^2 & \dots & \sigma_n^2 + \sigma_1^2 \end{bmatrix} \quad (3.49)$$

As it can be seen from the covariance matrix, the non-diagonal elements are only dependent on the reference node noise. However, the diagonal terms are affected by the variances of both anchors involved in the measurement. If the hardware used in the setup has almost similar noise characteristics, the diagonal terms present twice the amount of noise measured in each anchor.

In a similar process, the transmission time of anchors for chain form can be estimates based on the following phrases:

$$t_{A_2tx} = t_{ref} + t_{int} + w_1 \quad (3.50)$$

$$t_{A_3tx} = t_{A_2tx} + t_{int} + w_2 = t_{ref} + 2t_{int} + (w_1 + w_2) \quad (3.51)$$

$$t_{A_nrx} = t_{A_{n-1}tx} + t_{int} + w_n = t_{ref} + (n-1)t_{int} + (w_1 + w_2 + \dots + w_n) \quad (3.52)$$

As it can be seen from the above equations, the noise term is cumulating at each step of transmission. Although the mean of the cumulated noise term is still zero, the covariance of it is increasing. In case of chain form the time difference of arrival can be described as:

$$T_{i,(i-1)} = t_{A_i rx} - t_{A_{(i-1)} rx} - t_{int} + w'_{(i-1)} - w'_i, \quad i = 2, \dots, n \quad (3.53)$$

where  $w'_i = w_{txi} + w_{rxi}$  is the measurement noise of the received signal at the mobile node from anchor  $i$  with  $i = 2, \dots, n$  and  $w_{txi}$  and  $w_{rxi}$  are the noise at the transmission and reception time in the same anchor respectively. The covariance matrix can be calculated according to the following process:

$$\mathbf{Q} = E \left[ \begin{bmatrix} (w'_2 - w'_1) \\ (w'_3 - w'_2) \\ \dots \\ (w'_n - w'_{n-1}) \end{bmatrix} \begin{bmatrix} (w'_2 - w'_1) & (w'_3 - w'_2) & \dots & (w'_n - w'_{n-1}) \end{bmatrix}^T \right] \quad (3.54)$$

The diagonal terms can be expressed as:

$$E[(w'_i - w'_{i-1})^2] = E[w'^2_i] + E[w'^2_{i-1}] - 2E[w'_i w'_{i-1}], \quad i = 2, \dots, n \quad (3.55)$$

Assuming that the noise terms  $w'_i$  and  $w'_{i-1}$  are uncorrelated, the term  $E[w'_i w'_{i-1}]$  is equal to zero. Therefore, we can rewrite the last equation into:

$$E[w'^2_i] + E[w'^2_{i-1}] - 2E[w'_i w'_{i-1}] = \sigma_i^2 + \sigma_{i-1}^2 \quad (3.56)$$

For the non-diagonal terms, the expectation value is performed for the sake of simplicity for only one element but the rest of elements can be determined using the same process as star form. This is described as:

$$E[(w'_2 - w'_1)(w'_3 - w'_2)] = E[w'_2 w'_3] - E[w'^2_2] - E[w'_3 w'_1] + E[w'_1 w'_2] \quad (3.57)$$

Since the uncorrelated terms are zero, the previous equation can be transformed into the form:

$$E[w'_2 w'_3] - E[w'^2_2] - E[w'_3 w'_1] + E[w'_1 w'_2] = -\sigma_2^2 \quad (3.58)$$

The amount of the variance for non-diagonal terms tend to be negative which is originated from the common anchor between two equations. The covariance matrix of this case can be summarized as:

$$\mathbf{Q} = \begin{bmatrix} \sigma_2^2 + \sigma_1^2 & -\sigma_2^2 & \dots & -\sigma_n^2 \\ -\sigma_2^2 & \sigma_3^2 + \sigma_2^2 & \dots & -\sigma_n^2 \\ \dots & \dots & \dots & \dots \\ -\sigma_n^2 & -\sigma_n^2 & \dots & \sigma_n^2 + \sigma_{n-1}^2 \end{bmatrix} \quad (3.59)$$

Evaluating the variance of each element in the covariance matrix, it can be realized that the diagonal elements are dependent on the variance of the anchor pairs used for measurement. Referring to Eq. 3.52 the variance of each anchor is involving the variances of the previous anchors which means:

$$\sigma_n^2 = \sigma_1^2 + \sigma_2^2 + \dots + \sigma_{n-1}^2 \quad (3.60)$$

This proves that the total covariance  $\mathbf{Q}$  of the location measurement in the chain form is larger than that defined for star form. Given that the variances of all anchors are the same, the variance of the last anchor is in the scale of  $n$  where  $n$  is the number of anchors utilized in the localization system up to that anchor.

The disadvantage of the star form is that one or more transmissions lines move across the field where the mobile nodes are dynamically moving. This issue leads to non-line of sight (NLOS) situation between the two anchors resulting in large bias errors in the final measurement which is not detectable by the mobile nodes in any way. The chain approach does not suffer from this severe problem as the transmissions lines are on the perimeter of the measurement arena. Our solution to this problem is a hybrid form combining the star and chain forms together as depicted in Figure 3.13.c. In this form the nodes with transmission lines on the perimeter of the arena are paired according to star form to benefit from low measurement noise and those nodes with transmission lines crossing the area are paired according to chain method to avoid NLOS conditions which are almost impossible to detect by the mobile nodes. In this approach, the time stamps of transmission in anchors can be described according to:

$$t_{A_2tx} = t_{ref} + t_{int} + w_1 \quad (3.61)$$

$$t_{A_3tx} = t_{ref} + 2t_{int} + w_2 \quad (3.62)$$

$$t_{A_4tx} = t_{A_3tx} + t_{int} + w_3 = t_{ref} + 3t_{int} + w_2 + w_3 \quad (3.63)$$

These equations are only describing the four anchors scenario which is the case in the work of this thesis. In this scenario, only one anchor is disadvantaged by additional noise but profits from avoiding NLOS problem which often distorts the measurement results even though the anchors and mobile nodes are in direct line of sight condition.

### 3.3.3. Comparison of the TDoA approaches

The advantages of the TDoA techniques compared to the ToA methods are less radio traffic in air, multi-node localization with simple localization algorithm and lower power consumption since the transmissions are occurring once in a while (for example every few seconds) and usually with short message duration.

Considering the defined topologies of the TDoA method, different applications are applicable for each method. The main possible applications of the multilateral approach are tracking and monitoring of dynamic entities such as humans, robots, indoor vehicles, industrial machines etc. where the data needs to be collected in a central server. As it was stated before it is necessary to synchronize anchors to a central clock which is the main challenge of implementation in this method. However, synchronization between anchors and mobile nodes is not required. The transmission time of the mobile nodes are mostly random. If the duration of the transmissions is kept short enough as an example in the range of 1-5ms and the transmission interval of each node is in the range of 1 to 5 seconds, then a large number of nodes (around 100) can be employed with low probability of signal interference (10%). In terms of power consumption the multilateral method performs very well since the mobile nodes only transmit for a short period of the time and in large time intervals between two transmissions. As an example, if a node consumes 100 mA for transmission, and the period of transmission is 2ms with time interval of 1 second, then the average current consumption of the node can be calculated as:

$$I_{avg} = \frac{2 \text{ ms}}{1\text{s}} \cdot 100 \text{ mA} = 200 \text{ uA} \quad (3.64)$$

On the other hand, the application areas of the unilateral method are in navigation or self-localization of robots, vehicles, drones, etc. where the location data is used internally by the device for its navigation and no central monitoring is required. In this approach, clock synchronization between the anchors and mobile nodes is not required. However, pertaining a clock recovery system is necessary to avoid large measurement errors. The number of mobile nodes is unlimited in this approach knowing the fact that the mobile nodes are only listener in the network but the number of anchors which can be utilized in this scope is subject to the desired location update rate. This is mainly for the reason of sequential transmission which results in availability of the location data only after all the anchors have performed the transmission. The power consumption of the mobile node in this approach is generally higher than the other approach as the mobile node needs to activate the receive mode of the transceiver which consumes more power than the transmission mode ( $\approx 150$  mA). In addition to that, the receiver needs to receive the signal of all the anchors sequentially which results in higher power consumption in total. To provide a realistic example, consider a case where the messages of each anchor are 2ms long with an interval delay of 10ms between

anchors. If in total 4 anchors are present in the network, the average current consumption of the node will be:

$$I_{avg} = \frac{2\text{ms}}{1\text{s}} \times 4 \times 150\text{mA} = 1.2\text{mA} \quad (3.65)$$

This amount of current is valid for location update rate of 1Hz. For a higher rate such as 20Hz, this value increases up to  $20 \times 1.2 \text{ mA} = 24 \text{ mA}$ . Other aspects of the differences between the two TDoA approaches are summarized in Table 3.3.

Table 3.3: Comparison of the characteristics of different TDoA approaches [84][89]

Properties	Unilateral approach	Multilateral approach
Number of mobile nodes	Unlimited	Limited (Due to high radio traffic)
Number of anchor nodes	Limited (Due to sequential transmission)	Limited (Due to synchronization and server communication)
Power consumption	Average to high in mobile nodes, low in anchors	Very low in mobile nodes, high in anchors
Processing power	High in mobile nodes, low in anchors	Low in tags, high in anchors
Synchronization	Only clock drift compensation	Required between the anchors
Scalability	The anchors need to be only in the range of the previous anchor.	All the anchors should be in the range of the reference anchor or synchronizer and server
Location data	Available in mobile nodes	Available in central server
Applications	Robots, persons, vehicle navigation, augmented reality	Resource tracking, monitoring, security, fleet management

Considering the advantages and disadvantages of the two approaches and the application area of this thesis which is multi-robot navigation in indoor area, the unilateral method is selected. Therefore, all the algorithms and experiments are based on this topology.

## 4. Clock Management

As it was discussed in the previous chapter, clock-based approaches provide better accuracies than other approaches such as RSSI or AoA. However, in order to achieve the expected level of accuracy, highly accurate oscillators with high level of stability are required. In practice, crystals and oscillators are subject to errors resulting from manufacturing process and environmental conditions such as temperature, jitter noise from other electronic devices in the same circuit, voltage oscillation, electromagnetic fields and many other interfering sources. These factors make it almost impossible to find two identical crystals functioning exactly at the same desired frequency and with no drift. Therefore, it is essential to use a supportive approach to compensate the clock source differences. A main requirement of the most time-based localization especially TDoA methods is synchronization of the anchor nodes. Lack of an efficient synchronization system leads to appearance of a cumulative error which may reach up to a few meters within a short period of time [90]. Jian et al. [77], Djaja-Josko et al. [42] and Zhen et al. [91] have evaluated the effect of clock inaccuracies especially clock drift issue in ToA and TDoA localization approaches in several experiments.

The simplest solution for synchronization of anchors is to connect all the involved anchors using a wire to a central server where a clock is generated and distributed among all the nodes. A mathematical model for wire-based synchronization is provided by Yu et al. in [4, p. 121]. The wired method however raises many other issues such as costs, installation complexity, environmental noise, clock latencies in the wires, etc. Many researches have been carried out to establish a wireless method for synchronization either using same communication channel [92–94] or other supportive wireless technologies [95]. Comparison of a wired and a wireless synchronization technique is provided by Leugner et al. [68]. According to their experiments, the wireless synchronization method achieved the standard deviation of 400ps whereas the standard deviation of the same hardware setup equipped with wired synchronization was 133ps which is more accurate than the wireless approach. But the difficulties of the wired case make the wireless systems the first choice of developers. The synchronization scopes in wireless sensor networks are subject of many research surveys [96–98] which although are different in radio technology, the synchronization algorithms could still be

utilized for localization based on UWB technology. The survey paper provided by Wu et al. [95] provides a detailed comparison of possible synchronization methods as well as clock model analysis. The clock management principle utilized in this thesis is based on monitoring of the clock differences of each anchor with the reference anchor. The reference node is programmed to transmit constantly at certain intervals (in this project 50 ms). This time is measured by all the other anchors and mobile nodes. Using this approaches, each node is able to realize whether it is counting faster or slower than the reference node and accordingly apply required corrective actions. Similar methods of clock management to this idea are also used in projects mentioned in [42][91][99]. In the rest of this chapter, the mathematical model of the clock, as well as details of the proposed approach are explained and practical results are provided.

## 4.1. Clock Time Interval Error (TIE)

The focus of this section is to address the clock management related aspects of the implementation in unilateral TDoA localization technique. As discussed in the previous chapter, the unilateral method does not need a synchronization in the sense that the current clock value of all the nodes be exactly the same because the time stamps are compared locally in differential form and therefore the same clock is used for time stamping. It is however necessary to control the clock rate of all the nodes to avoid clock drift issue between them.

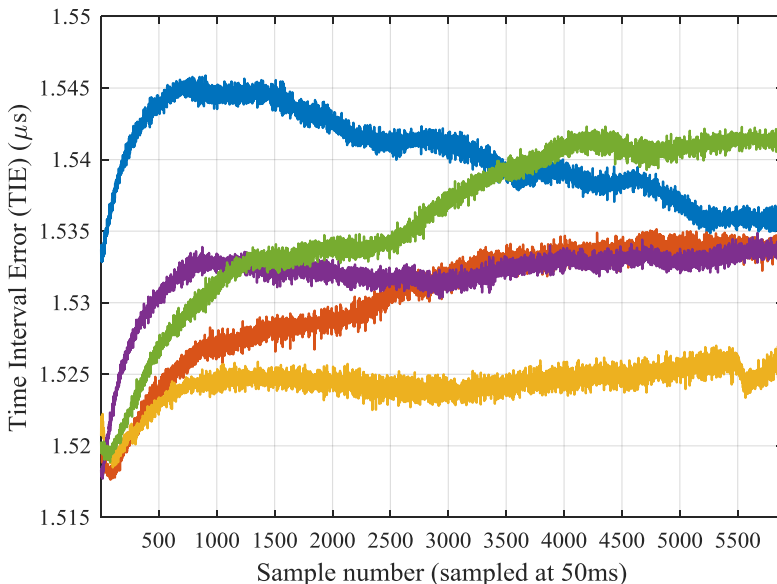


Figure 4.1: Time interval error (TIE) of a crystal oscillator in the same hardware setup recorded in 5 experiments each for the period of 5 minutes

To evaluate this problem in detail, an experiment is performed in that one anchor transmits a signal periodically with a certain interval delay (each 50 ms). At the mobile node, these arrived signals are time stamped and then subtracted from the previous observed time stamp of the same anchor. If both clocks of the anchor and mobile nodes are running with exactly the same frequency, the result of the arrival difference in the mobile node should be the same delay interval used in the anchor. If we subtract this delay from the measured differences in the mobile node, we expect to observe a constant line at zero. This value is called time interval error (TIE). The same experiment is repeated several times in a day using the same hardware setup with same crystal. Each experiment is recorded for the period of 5 minutes. The results of these experiments are shown in Figure 4.1. As it can be seen from the graph, there is a large bias (in average  $1.53\mu s$ ) which is due to different characteristics of the clock elements appeared in manufacturing process. As well as that, the biases are constantly changing as the time pass as a result of environmental changes such as temperature, noise, magnetic and electric fields, etc. The effect of circuit warm-up is clearly visible in the first 500 samples. These results prove that not even the same crystal device is able to keep the clock rate constant and stable within its working period of time. This fact justifies the need for a clock management algorithm in localization systems.

## 4.2. Modeling of the Clock Behavior

The first step in developing a clock management system is to model the clock behavior so that a proper mathematical algorithm for drift compensation can be developed. The clock models proposed in the literature so far are very similar in the sense that they describe the clock model based on a constant part (bias) and a dynamic part (skew) [91, 96, 97]. One commonly used model proposed in [95] is described mathematically as:

$$J_{A_i}(t) = J_{A_1}(t) \cdot C_s(t) + C_b + v_t , \quad i = 2, \dots, n \quad (4.1)$$

where  $C_s(t)$  is the clock skew of the current anchor receiving the signal at time  $t$ ,  $C_b$  is the bias of the clock,  $J_{A_1}(t)$  is the clock time of the reference anchor node and  $J_{A_i}(t)$  is the clock time of the anchor which needs to be synchronized. The parameter  $v_t$  is measurement noise which is treated as a Gaussian white noise with zero mean and variance of  $\sigma^2$  represented as  $v_t \propto \mathcal{N}(0, \sigma^2)$ .

The graphical representation of this clock model is demonstrated in Figure 4.2. According to this graph, the ideal clock has skew of 1 and bias of zero. A slower clock has a skew rate of larger than 1 and a faster clock has skew rate between zero to one. In practice, as it is visible in Figure 4.1 the skew rate is constantly changing however the bias term is fixed which can be estimated empirically or using calibration methods.

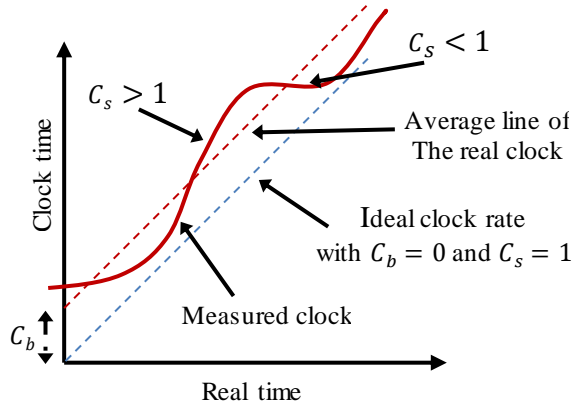


Figure 4.2: Model of the clock in time-based localization systems with bias and skew rate

Applying this model to our localization system, the bias of the clock turns into mean of the time differences between the sequential transmissions of reference anchor measured in receiver anchors which is also called time interval error. This parameter can be calculated once in advance and applied in the equation but the dynamic part of the model the skew rate needs to be calculated for each round of measurement iteratively using:

$$C_s(t) = \frac{T_{fA_i}(t) - C_b}{T_{fA_1}(t)} + v_t , \quad i = 2, \dots, n \quad (4.2)$$

where  $T_{fA_i}$  is the time difference of the two sequential arrival times from reference anchor measured in anchor  $i$  and the  $T_{fA_1}$  is the similar parameter measured in anchor 1 (reference anchor). After the skew rate of the clock is known, the next transmission time stamp of the anchor can be calculated using:

$$t_{txA_i} = t_{ref} + t_{int}.(i - 1).C_s(t) - C_b , \quad i = 2, \dots, n \quad (4.3)$$

This model has been used in some projects as an example in the work of Jiang et al. [77]. There is however a disadvantage in this method which is the noise term in Eq. 4.2 is also multiplied by the delay term in Eq. 4.3 as shown below:

$$t_{txA_n} = t_{ref} + t_{int}.(i - 1).\left(\frac{T_{fA_i}(t) - C_b}{T_{fA_1}(t)} + v_t\right) - C_b \quad (4.4)$$

This results in the fact that the variance of the time of transmission in anchor depends on the drift of the clock which is not desired in an accurate localization system. In order to solve this issue, we propose at the first step a modification in the clock model in a way that we consider the bias term as a part of the dynamic term which needs to be calculated at each iteration and herewith we simplify the process as no advance estimation of the bias term is required. In the second stage, we use following equation for calculating the clock skew:

$$C_{s_i}(t) = T_{fA_1} - T_{fA_i} + v_t \quad , \quad i = 2, \dots, n \quad (4.5)$$

This way the difference of the two sequential transmissions is calculated and used to correct the transmission time of the next signal. As it can be seen, the bias term is not relevant any more. The next transmission time can be calculated using:

$$t_{txA_i} = t_{ref} + t_{int} \cdot (i - 1) - \frac{(i - 1)}{n} \cdot C_{s_i}(t) \quad (4.6)$$

where  $t_{txA_i}$  is the next transmission time in anchor  $i$ ,  $i$  is the number of the current anchor and  $n$  is the total number of anchors available in the localization system. This model does not increase the variance of the noise as it was the case for the previous model. Moreover, the variance of the noise is even decreased due to the fraction term multiplied to it which is always less than 1. This model should also be applied in all the mobile nodes to adjust the time differences of arrivals according to the correct drift which is dictated by the reference anchor. Since all the anchors synchronize themselves to the reference anchor, no adjustment of the time stamps of the signal arrivals in mobile nodes is required. It should be noticed that this model is developed for the star form pair selection style and in case other forms are desired, the model should be adapted correspondingly.

### 4.3. Clock TIE Filtering Methods

In order to estimate the parameters of the clock model mentioned in the previous section and to filter the measurement noise, many algorithms are proposed in the literature. McElroy et al. [100] have discussed a few of these methods thoroughly which are linear interpolation, PI control, PID control, PII control and Kalman filter. According to their results, the best performance has been achieved by utilizing a Kalman filter. Selection of a filtering method and its corresponding parameters should be performed carefully as a heavily damping filter results in a lazy localization system that reacts in response to quick motions of the mobile node slowly. On the other hand a low damping filter reacts to noises of the clock time interval error impulsively resulting in higher noise variance of the distance measurements, inaccurate measurements, appearance of outliers and in some worse cases divergence of the localization engine with the consequences of numerical issues in microcontroller. In this section, we discuss two common filters which are a zero order model low pass filter and a first order model Kalman filter with two states. Please note that the low pass filter itself is a first order filter but the dynamic of the signal model has only one parameter which is therefore called a zero order model. From structure point of view, these two filters have many similarities but their reactions to dynamics of the signal are quite different. For the sake of better comparison, both algorithms are applied in practice and the results are provided and discussed in this section. A zero order model low pass filter is mathematically described as:

$$\hat{C}(t) = \hat{C}(t-1).(1-k) + C(t).k \quad (4.7)$$

where  $\hat{C}(t)$  is the filtered estimated clock noise,  $\hat{C}(t-1)$  is the previous output of the filter,  $C(t)$  is the current measurement which is the difference of the last two time stamps of arrival from the reference anchor and  $k$  is the error gain of the filter with ranges between  $0 \leq k \leq 1$ . Small values of error gain close to zero results in higher damping effect which means lower noise but it may represent a bias to the mean of the signal when a signal is rising or falling as it is visible in Figure 4.3 for  $k = 0.1$ . In contrary, the larger values of  $k$  have lower damping effect or higher noise but does not have deviation issue from the mean value. The error gain equal to 1, does not filter the input signal at all. The recommended range of  $k$  for this application achieved through practical results is  $0.1 \leq k \leq 0.3$ .

The Kalman filter describes the model of the clock noise in the form of state space using the first order Newtonian equations with two state variables. This results in the fact that this filter offers optimum level of noise reduction without presenting any biases from the real mean value of a noisy and dynamically changing signal. The equations of a Kalman filter for this application are as follows:

$$\begin{bmatrix} C(t) \\ \dot{C}(t) \end{bmatrix} = A \begin{bmatrix} C(t-1) \\ \dot{C}(t-1) \end{bmatrix} + Bu(t) + \psi_t \quad (4.8)$$

$$A = \begin{bmatrix} 1 & \Delta t \\ 0 & 1 \end{bmatrix}, \quad Bu(t) = 0, \quad \psi_t \sim \mathcal{N}(0, Q) \quad (4.9)$$

$$y = H \begin{bmatrix} C(t) \\ \dot{C}(t) \end{bmatrix} + v_t \quad (4.10)$$

$$H = [1 \ 0], \quad v_t \sim \mathcal{N}(0, R) \quad (4.11)$$

In this equations,  $C(t)$  and  $\dot{C}(t)$  are the state variables representing the clock TIE and the change rate of the clock TIE respectively,  $A$  is the fundamental matrix describing the transition model of the system,  $B$  is the input matrix which is not considered in the equation due to the fact that  $u(t)$  the input of the system is zero,  $\Delta t$  is sampling rate and  $\psi_t$  is the system noise with white additive Gaussian characteristics with mean of zero and variance of  $Q$ . The output of the filter is  $y$  which is resulted as multiplication of observation matrix  $H$  with the state variable and measurement noise with the same characteristics of the system noise but with covariance of  $R$ . The Kalman filter has two stages of deployment. In the first step which is called prediction, the state variables are propagated through the defined model to make an estimation about the next value of the states. In addition to that, the estimate error covariance  $P$  needs to be propagated which can be expressed as:

$$P_t = P_{t-1}AP_{t-1}^T + Q \quad (4.12)$$

Using the estimate error, covariance matrix and observation matrix, the gain of the Kalman filter can be calculated as:

$$\mathbf{K} = \mathbf{P}_t \mathbf{H}^T (\mathbf{H} \mathbf{P}_t \mathbf{H}^T + \mathbf{R})^{-1} \quad (4.13)$$

The value of the Kalman gain is in between 0 to 1 with the same characteristics as the damping factor used for the low pass filter. The next step of the Kalman filter is update phase in that the estimate of the filter is updated by considering the Kalman gain and the amount of the observed error. This can be presented as:

$$\begin{bmatrix} \mathcal{C}(t+1) \\ \mathcal{C}(t+1) \end{bmatrix} = \begin{bmatrix} \mathcal{C}(t) \\ \mathcal{C}(t) \end{bmatrix} + \mathbf{K} \left( \mathbf{y} - \mathbf{H} \begin{bmatrix} \mathcal{C}(t) \\ \mathcal{C}(t) \end{bmatrix} \right) \quad (4.14)$$

In addition to the state variables, the estimate error covariance matrix should be updated according to the following formula:

$$\mathbf{P}_{t+1} = (\mathbf{I} - \mathbf{K} \mathbf{H}) \mathbf{P}_t \quad (4.15)$$

where  $\mathbf{I}$  is the identity matrix and  $\mathbf{P}_{t+1}$  represents the *a posteriori* value of the estimate error. The performance of the two filters are compared in Figure 4.3. As it can be seen, the low pass filter does not follow the changes when the signal is varying with a high rate (samples 0-60), but Kalman filter (KF) follows these changes immediately without being sensitive to noise. At the stationary moments a constant offset is visible in low pass filter output as this filter cannot integrate small errors. Better performance of KF is also partly originating from the higher order of the model which can better track the dynamics of the signal.

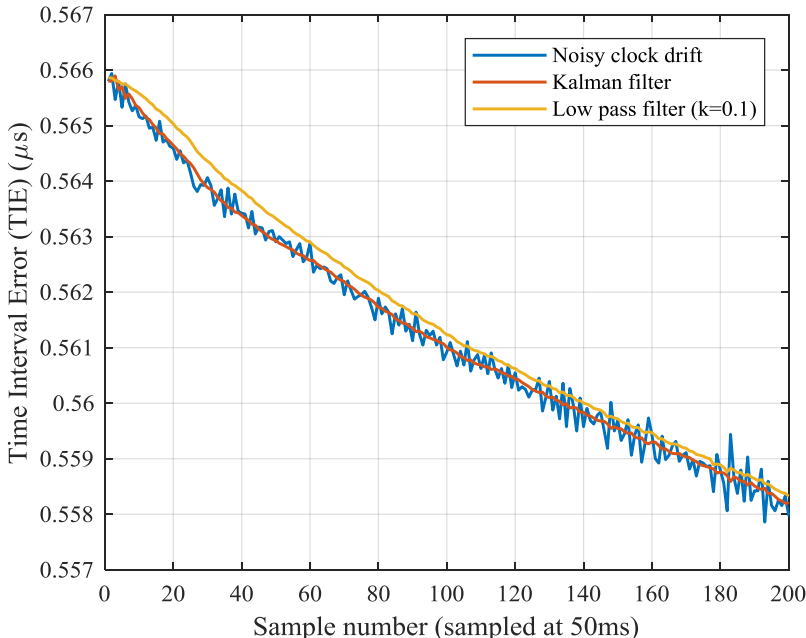


Figure 4.3: Performance comparison of low pass (zero order model) vs. Kalman (second order model) filtering techniques on the measurement noise of the TIE

## 4.4. Implementation Aspects

Although the clock recovery methods discussed previously have straight through implementation procedures, there are many aspects which should be taken into account to avoid instability of the localization engine and undesired inaccuracies. This section addresses a few of these issues and provides a practical solution for each of them. These problems are time rounding issue, appearance of the missing packets and occurrence of outliers in the clock TIE.

### 4.4.1. Time rounding issue

The time rounding problem is always a hardware issue which occurs either due to digitalization or casting variables to smaller dimensions. The hardware module used in this thesis DWM1000, performs most of the analogue to digital signal conversion, signal time stamping, first path detection, etc. in the chip level. There are two basic hardware parts involved in this process. The first part is an ASIC which is running on high frequency of 64GHz responsible for analogue to digital conversion as well as preliminary signal processing and time stamping of the arrived signal. This clock speed brings the advantage of time stamping with the accuracy of 15.62ps. The second part of the hardware is a processor running with a slower clock frequency of 125MHz responsible for interaction with host over SPI bus, updating register values, storing the configuration values, etc. which are not sensitive enough to be driven with high speed clock [79]. This way, large section of the hardware can be made for lower frequency which leads to lower overall costs of the module. Another useful feature which is provided in this module is the possibility of programming the next transmission time which is of great help for implementation of the unilateral method. Using this feature, it is possible to calculate the next time stamp based on the last time of arrival and the required delay between two transmissions and program it into corresponding register. The module automatically starts the transmission as soon as the time of the clock is equal to the programmed time. At this point, a critical drawback in the hardware exists that is the lowest 9 bits of the register holding the delayed transmission time are ignored. Therefore, the time resolution of the register used for delayed transmission is only time gaps of  $\sim 8\text{ns}$  ( $512 \times 15.65\text{ps}$ ). This happens because this part of the process is handled by the processor of the chip which runs on the clock of 125MHz resulting the clock steps of 8ns. In case the desired transmission time is between the two possible transmission slots, the hardware round down the value and performs the transmission earlier than the planned time of transmission. Since the clocks of the other nodes are not synchronized in value, it is impossible to estimate this value in the receiver node without having an additional knowledge about the clock condition of the transmitter node. The rounding transmission problem of the hardware is demonstrated in Figure 4.4.

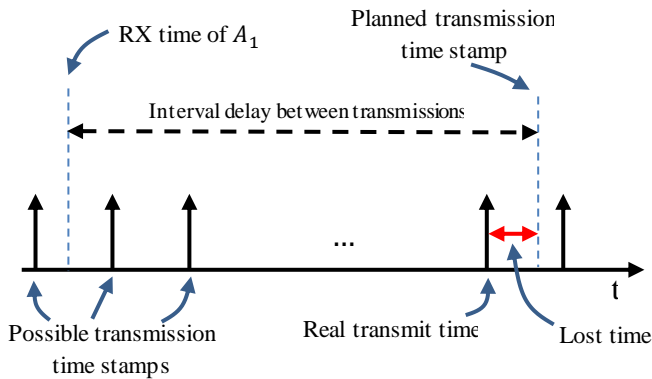


Figure 4.4: The rounding effect of the delayed transmission in DW 1000 module resulting from lower clock frequency (125 MHz) of processing unit

In order to evaluate the effect of this rounding on the clock recovery in the receiver node, the same experiment as defined before is performed in that an anchor is programmed to transmit a signal periodically with the period of 50 ms and a receiver anchor receives these signals and time stamps them. After receiving a signal, the receiver anchor turns its role to transmitter and arranges a delayed transmission for the time period of 10 ms after the moment the signal of the first anchor has arrived. A mobile node is used to receive the signal of both anchors and to calculate the difference of arrival between two signals. The results are shown in Figure 4.5.

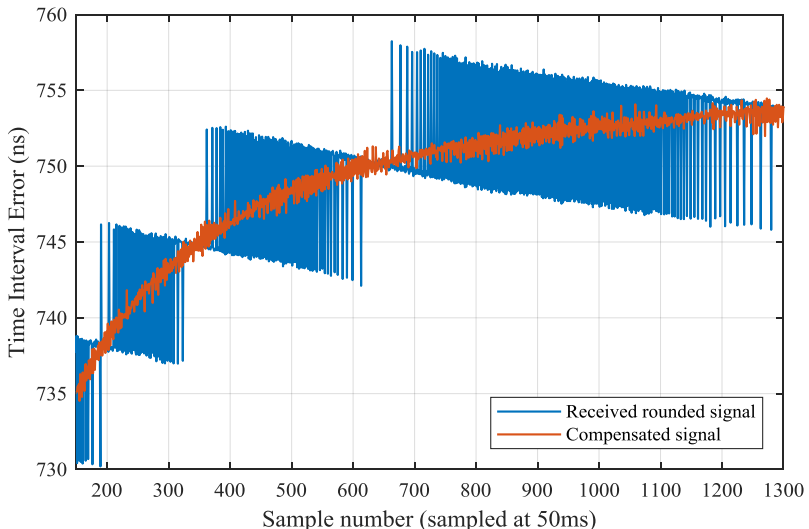


Figure 4.5: The rounding effect of the signal received from anchor 2 in mobile node showing the 8ns gaps and the signal before and after reconstruction

As it can be seen from this graph the transmission time of anchor 2 has jumps between the 8 ns gaps of possible transmission time. This jumps are managed by

the hardware in the form of a modulated PWM signal which provides the user the possibility of reconstruction of the signal at the target using different filtering techniques. This however demands the collection of large amount of samples to enable the filter to estimate the mean value accurately. This solution raises an accuracy issue in the distance results as the desired accuracy is only achieved after collecting certain amount of data. If an accurate measurement is required at each round of iteration, another approach should be applied. In our proposed approach, the amount of lost time of each signal is calculated by the transmitter anchor in advance before the transmission occurs and it is attached to the payload of the same packet. At the receiver node, the data in the payload section is extracted and the recorded time stamp of arrival is modified by adding the lost section of the time. The lost time can be calculated using following formula:

$$T_{los} = T_{pl} - \rho \left[ \frac{T_{pl}}{\rho} \right] \quad (4.16)$$

where  $T_{los}$  is the time that will be lost as a result of ignoring the lowest 9 bits of the time stamp,  $T_{pl}$  is the planned time which we would like the transmission happens,  $\rho$  is the resolution of lost time which in our case is 512 and the operator [...] truncates the fraction part of the division leaving only the integer part of it. The results of the successful compensation are demonstrated together with the original received time stamps in Figure 4.5.

#### 4.4.2. Detection of missing packets

One of the main challenges of any communication system is detection of missing packets which often happens due to large amount of noise, low signal strength, signal interference and many other factors. This issue is more serious in the localization systems as missing one packet results in the lack of enough data for calculating the locations but also results in disturbance of the clock management method which basically operates based on the difference of each time stamp with the previous signal of the same anchor. Lack of one or more of the pulses, leads to large incorrect clock TIE. If this issue is not prevented, unrealistic results may be expected or in the worst case the localization engine may stop functioning due to divergence issue. Sometimes the hardware itself is able to recognize that a packet is transmitted but the quality of the data was not high enough to demodulate and decode it properly. This can be spotted by monitoring the flags of the checksum control unit or error detection mechanisms. However, the hardware is not always able to recognize such a condition as it may happen that the sent packet does not arrive at all. To tackle this problem, a software solution is utilized in that the reference node dedicates a number to each packet and stores this number in its payload. This number is increased sequentially as the packets are transmitting. In the anchor nodes, the received packet is processed and the same number is used in the other anchors for transmission. Using this method,

the mobile node is able to recognize all the packets which belong to the same round of transmission. If one or more packets are missing, it is not only possible to detect it, but also it is possible to recognize the number of missing packets and to apply proper actions to calculate the right amount of clock TIE. The difference of the sequence number of each packet with its previous one should be always 1. Higher value than 1 indicates loss of one or more packets according to the achieved number. This can be formulated as:

$$\begin{cases} \Delta s = Seq(t) - Seq(t-1) & \text{if } (Seq(t) > Seq(t-1)) \\ \Delta s = N_s - (Seq(t) - Seq(t-1)) & \text{if } (Seq(t) < Seq(t-1)) \end{cases} \quad (4.17)$$

In this equation,  $\Delta s$  is the difference of two consecutively received sequence numbers,  $Seq(t)$  is the sequence number of the packet transmitted at time  $t$  and  $N_s$  represents the maximum value of sequence counter register which in our case is a one byte register capable of counting up to 255. The reason of having two equations in Eq. 4.17 is the fact that the counter may overflow and generate a case in that the value of current sequence number is smaller than the previous sequence number. For this reason, the lower term checks the two sequence numbers before applying the values into equations. The effect of packet loss on the drift clock is illustrated in Figure 4.6 where the packet loss is not controlled. The large created spikes are clearly visible which emphasize the importance of packet loss management.

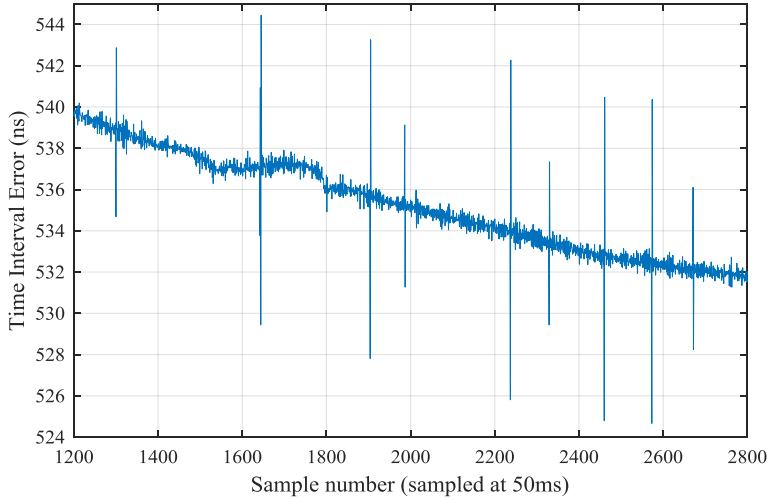


Figure 4.6: Effect of the packet loss on the clock TIE which results in large deviation

Since a new parameter is defined to recognize the number of missing packets, the formula provided in Eq. 4.5 needs to be modified into:

$$C_{s_i}(t) = \frac{(T_{fA_i}(t - \Delta s) - T_{fA_1}(t))}{\Delta s} + v_t , \quad i = 2, \dots, n \quad (4.18)$$

### 4.4.3. Outlier detection and filtering

Another issue which is often arising in the signal processing of the sensor data as well as communication systems is appearance of outliers. These are in principle data with large deviation from the mean which is happening due to influence from noise, non-line of sight cases, low signal to noise ratio of the received signal, packet loss as discussed in the previous section or signal interference with other communication devices to name a few. A simple solution is to apply a filter as discussed in Section 4.3. But in order to filter an outlier effectively, a high damping ratio is required otherwise the effect of outlier will still be perceivable in the filtered clock TIE signal. A higher damping ratio on the other hand makes the filter to not react or slowly react to normal changes of the skew rate which is important to track if an accurate localization system is desired. Our solution to this problem is a modified filter which dynamically updates the damping factor of a low pass filter or covariance matrix of the measurement in a Kalman filter. To implement this technique, the deviation of the current sample in clock TIE is measured at each iteration and is used to detect the outlier case. The deviation can be calculated using:

$$\Sigma(t) = |C(t) - \hat{C}(t)| \quad (4.19)$$

where  $\Sigma$  is the deviation of the clock TIE for current sample,  $C(t)$  is the clock TIE of the current sample and the  $\hat{C}(t)$  is the estimate of the filter applied to the signal. Once the deviation is known, the following conditions can be applied to the error gain of the low pass filter  $k$ :

$$\begin{cases} k = 0.2 & \Sigma(t) \leq \lambda_{th} \\ k = 0.01 & \Sigma(t) > \lambda_{th} \\ \lambda_{th} = 5\sigma^2 & \end{cases} \quad (4.20)$$

In this equation, the  $\lambda_{th}$  is a threshold that is used to compare with the deviation. In case the deviation is higher than this threshold, the outlier case is detected and treated with higher damping factor otherwise normal gain value is used. The threshold is chosen to be five times larger than the current value of the filter estimate. In case a Kalman filter is utilized, these changes are applied to the covariance of the observation variable  $R$  as described below:

$$\begin{cases} R = 5 & \Sigma(t) \leq \lambda_{th} \\ R = 50 & \Sigma(t) > \lambda_{th} \\ \lambda_{th} = 5\sigma^2 & \end{cases} \quad (4.21)$$

For the case of values below the threshold, the variance is determined to be 5 whereas for the values higher than the threshold, value 50 is chosen to emphasize more on the value of the state and to down weight the amount of the current measurement. These values are selected empirically from experiments.

The output of this filter recorded in an experiment is depicted in Figure 4.7.

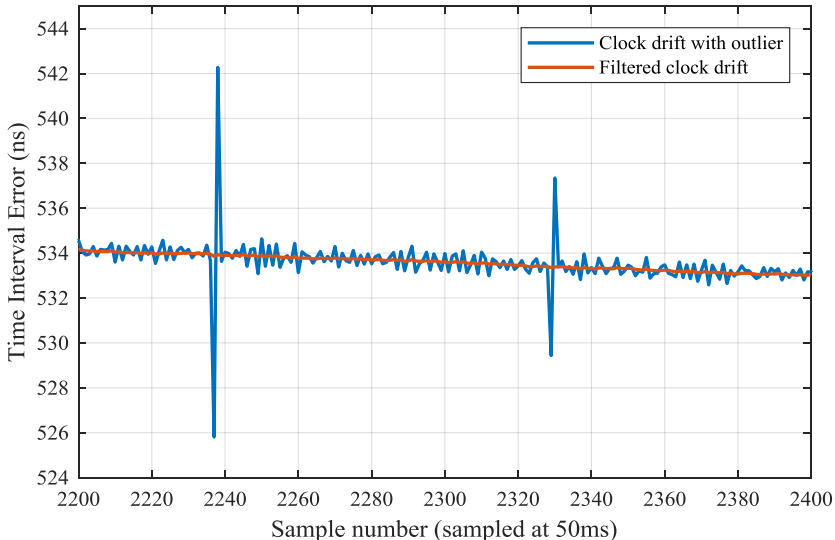


Figure 4.7: Output of the modified low pass filter operating with and without outliers. No perceivable changes in the output of the filter is visible in outlier cases.

## 4.5. Clock Source Analysis

The basis of the clock management in the unilateral approach is to synchronize the clock rates of all the nodes involved in the system with the clock dictated by the reference anchor. This means the clock source of the reference node is the base of the measurements and therefore it should be very accurate and stable. Any inaccuracies introduced in the clock of the reference anchor (first anchor) scales up or down the whole distance measurements which is critical for location estimation engine. The consequences of these inaccuracies are nonlinear shift of the measurement points or divergence of the algorithms to their numerical saturation limits. One solution to this problem is to calibrate the reference node's clock but as we experienced before, these deviations are not constant and are environment dependent. A better solution is to benefit from temperature compensated oscillators or even oscillators with voltage compensation feature which provides better accuracies in the range of 1ppm or better. This way, although there are still clock inaccuracies but they are limited to very low amount and more importantly the influence of the environment is compensated up to some extent. To evaluate the influence of these compensated oscillators on the measurement performance and their characteristics such as noise variance, stability, temperature effect, tolerance area, etc. several experiments are performed involving different crystals and oscillators. In all the experiments,

same hardware setup is used in order to exclude the influence of the other hardware components from the results. List of the clock sources including their specification and manufacturer information is provided in Table 4.1.

Table 4.1: List of different clock sources used for the clock evaluation experiments

Part number	Manufacturer	Supply voltage	Technology	Accuracy	Stability
CX2520DB	Kyocera	Passive	Quartz	15ppm	15ppm
LFTCXO070898	IQD	3.3v	TCXO	1ppm	0.5ppm
TYEAACSANF	Taitien	1.8-3.3v	VCTCXO	2ppm	0.2ppm

The first device used in the experiments is a crystal with an accuracy of 15ppm. This type of crystal is a passive device which resonates in combination with two external capacitors with the value of 8pF. This crystal is purchased for 0.64€. The second device is a temperature compensated oscillator (TCXO) with a high accuracy of 1ppm. This device needs separate power supply with the voltage of around 3.3V and consumes 2.5mA of current. This oscillator is acquired for 2.05€. The last device is a voltage-controlled, temperature compensated oscillator (VCTCXO) providing a high level of stability and accuracy which is obtained for 2.67€. This is an active device, operating in the voltage range of 1.8-3.3 V and consuming 2.5mA current. The frequency of operation in all the cases is 38.4 MHz as requested by the manufacturer to drive a DW1000 chip. Compensated oscillators get advantage from sensory devices integrated inside the chip which can modify the operation point of the frequency according to environmental changes such as temperature or supply voltage. The results of the experiments and comparison of these clock sources are categorized and provided into four segments namely frequency accuracy analysis, stability analysis, noise analysis and thermal dependencies. These are discussed in detail in the following sections.

### 4.5.1. Frequency accuracy analysis

In the experiments used to evaluate the frequency of different clock sources, the TIE of the reference anchor is measured in a mobile node. According to the accuracy provided by the manufacturer which is given in the parts per million unit (ppm), one may expect certain level of bias in the TIE recorded in the mobile node. Assuming that the mobile node has zero deviation in its clock rate, the estimated clock TIE in mobile node represents the accuracy of the reference node. This is for example 1us of TIE for a given accuracy of 1ppm. In practice however, it is hard to find a clock source with such level of accuracy. Therefore, we have measured the amount of clock offset achieved from the mobile node using precise instruments and subtracted it from the observed bias in the mobile node. This can be presented as:

$$C_A = C_o - C_m \quad (4.22)$$

where  $C_A$  is the clock TIE resulted from inaccuracies of the clock in reference anchor,  $C_o$  is the observed clock TIE in mobile node and  $C_m$  is the clock TIE resulted from the inaccuracies of the clock in mobile node itself.

For evaluation of the clock TIE offset of each clock source, several experiments are performed each for the period of 5 minutes and at different times of a day. The results are shown in Figure 4.8 for all the three applied clock sources but the experiments are extended to two other devices with the same technologies. The demonstrated results are the average of all the recorded data for that specific clock device.

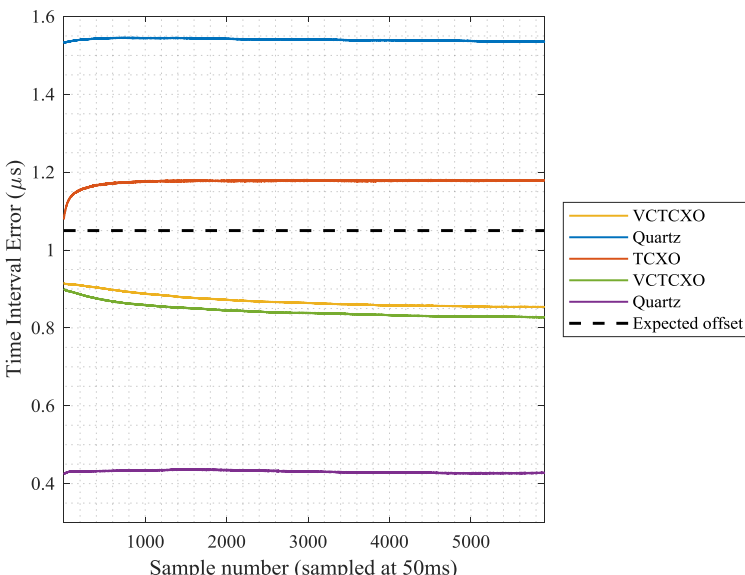


Figure 4.8: Clock TIE of different clock source technologies including crystal, TCXO and VCTCXO representing the bias of each device relative to the desired line

The ideal clock TIE which is expected from all the clock sources is  $1.07\mu s$  which is resulted from the frequency tolerance of the mobile node. This value is plotted in Figure 4.8 together with the real clock drifts observed from different clock sources. The deviation of the quartz crystals are the highest from the expected line. As an example the clock TIE of the first crystal is estimated to be  $1.53\mu s$  which yields in deviation of  $460\text{ ns}$ . In order to calculate the accuracy of this crystal according to ppm unit, we should remind that 1ppm speaks for  $1\mu s$  of drift in each second. Since the measurements are recorded with the delay interval of  $50\text{ ms}$ , the expected drift in the clock is  $1/20$  of this  $1\mu s$  which leads to  $50\text{ ns}$  of bias seen at each transmission frame. Given that the current crystal has bias of  $460\text{ ns}$ , we can deduct the amount of crystal accuracy according to:

$$\text{Accuracy} = \left( \frac{\text{observed bias}}{\text{update rate/s}} \right) \times \left( \frac{1\text{ ppm}}{1\mu s} \right) = \left( \frac{460\text{ ns}^2}{50\text{ ms}} \right) \times \left( \frac{1\text{ ppm}}{1\mu s} \right) = 9.2\text{ ppm} \quad (4.23)$$

This result is in the range of minimum accuracy given in the datasheet (15 ppm). For the case of the TCXO this value is measured to be  $1.17\ \mu s$  which is equal to 2 ppm and for both VCTCXO devices this value is around 860 ns equal to an accuracy of 4 ppm. These two values are larger than what is stated in their datasheet (1 ppm for TCXO and 2 ppm for VCTCXO). This higher tolerance might occur due to overheating in the soldering process, mechanical stress, long storage time, etc. According to this test, it is also visible that two crystals from the same company and even from the same reel tape, may have two diverse points of operation. This diversity is however minimized for the two VCTCXO devices.

### 4.5.2. Frequency stability analysis

The frequency stability is defined as deviation of the frequency around its operation point after stabilization process is performed. In other words, it is expected that the frequency of oscillator does not change when encountered to environmental changes. The results achieved through experiments performed in the previous section are evaluated in this section in terms of stability of the frequency. For each clock device, the TIE parameters are measured and recorded five times at different times of a day and at each round for the period of five minutes. The reason of performing the tests at different times of a day is to evaluate the effect of temperature on the performance of oscillators. The results are provided in Figure 4.9.

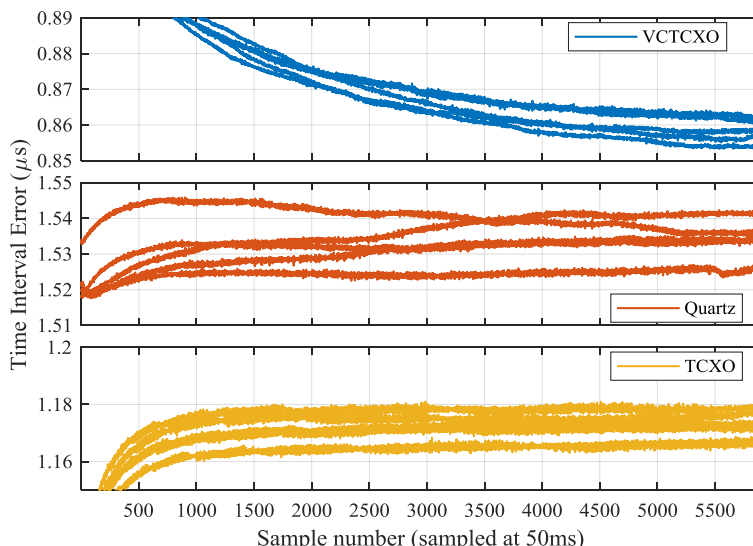


Figure 4.9: Clock stability of different oscillator devices after warm-up phase

As it can be seen from Figure 4.9, there are two main stages in the stabilization process of the clock devices. At the first stage which is short in time, there is a high rate of changes. This occurs due to warm-up effect of the electronic devices

as well as the oscillator itself. The second stage is a relatively constant phase in that the oscillator tries to keep their output constant. The highest amount of deviation is visible in crystal case as no electronic compensation is performed in this type of devices. The visible deviation is around 20ns which is equivalent to stability rate of 0.4 ppm. This value is far better than expected as the value stated in the datasheet of the crystal is around 15 ppm. The TCXO oscillator has almost the same range of deviation which is 20ns for different experiments but once the signal is stabilized, there is almost no change in the frequency. This performance is achieved through the temperature control unit and frequency compensation. The value of stability rate in the datasheet is mentioned to be 0.5 ppm which in this case is true. In case of VCTCXO device, the deviation of the frequency is the best in group with 10ns equivalent to 0.2 ppm which is also equal to what the manufacturer has declared in the datasheet.

### 4.5.3. Clock noise analysis

The results of the same experiment as before is also used in this section to evaluate the amount of noise presence in the output of each clock source. The distribution of the noise in all three cases is measured to be white Gaussian. Therefore, it may appear that the effect of the noise can be filtered out using the filter techniques introduced before. In practice however, it could be observed that the clock noise directly influences the distance measurement noise in that a higher clock noise results in a higher distance data noise. Figure 4.10 depicts the amount of observed noise for all the three cases. As it can be seen, the smoothest clock TIE belongs to VCTCXO oscillator which has the lowest amount of noise with peaks around 700 ps.

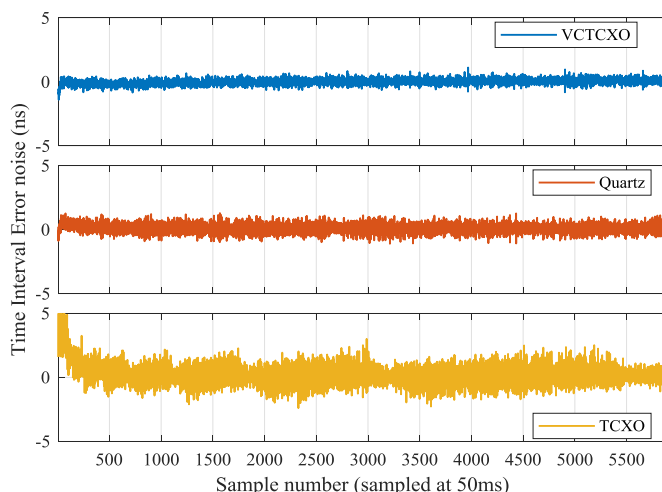


Figure 4.10: Clock TIE noise of difference clock sources. The strange behavior of the noise in TCXO is visible.

The noise level of the crystal is slightly higher than the VCTCXO oscillator with its peaks measured to be around 1100 ps. To our astonishment the TXCO proves to be the noisiest among the three devices showing variations of up to 2.1 ns. Additionally, strange behavior of noise is visible with dynamic changes of the variance. It seems the amount of noise in the output is a function of other variables resulting in periodic behavior of the noise. To evaluate the generated noise in each clock device, the probability distribution function (PDF) of each device is calculated and plotted in Figure 4.11. According to this diagram, the TCXO has standard deviation of 55ps, the VCTCXO has the best standard deviation of 21ps and this value for the crystal device is 23 ps. The reason of appearing spikes in the histograms is low sampling rate which is around 15.65 ps.

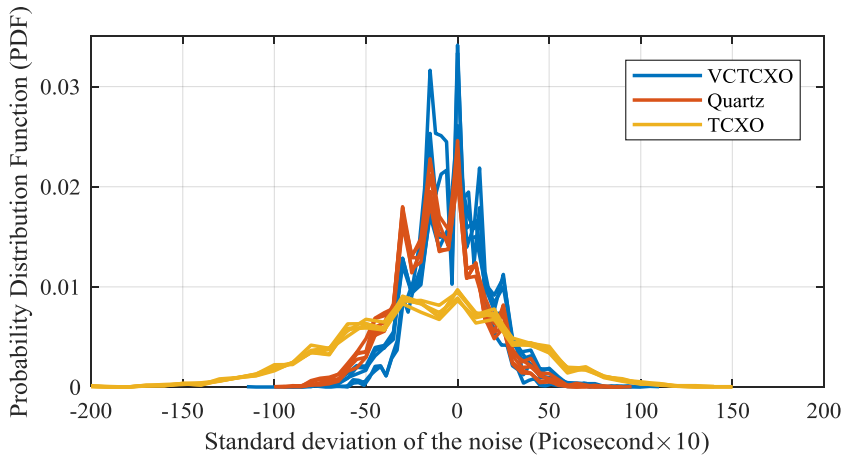


Figure 4.11: Probability distribution function (PDF) of the noise monitored on the drift clocks for three different clock devices

### 4.5.4. Thermal dependencies and warm-up

As it was discussed before and observed in the experiment results, temperature has dominant influence on the performance of the oscillators and crystals. This problem is highly apparent at the start phase of the operation due to the fact that the electronic circuits as well as the clock source device itself warm up. The temperature differences may reach up to 10 degrees which have huge influence on the frequency output. This startup period was observable explicitly in Figure 4.9. It was noticed that, different clock generators require different time to reach to their steady state. This is for example 250 seconds for VCTCXO which is a long time compared to TCXO with 45 seconds and crystal with minimum time of 15 seconds. This long time is required by oscillator's feedback loop to converge to its final state. This feedback loop is normally tuned to react slowly to environmental changes to avoid instability issues. The warm-up period of the oscillator causes nonlinearity in the distance measurement in a way that although

the clock TIE is compensated, still a noticeable amount of error in the distance measurement is visible. As the oscillator reaches its steady state phase the error mitigates and eventually vanishes. This situation is graphically depicted in Figure 4.12. In the experiments performed for measuring this effect, the mobile node is located on the location where the difference of the distances to both anchors is zero. Therefore, plotting the range difference information, we are expecting to see a constant line at zero. In this graph, the difference range of the mobile node is shown against the clock TIE of the TCXO oscillator. The deviation of distance at warm-up phase which is around 15cm is clearly noticeable.

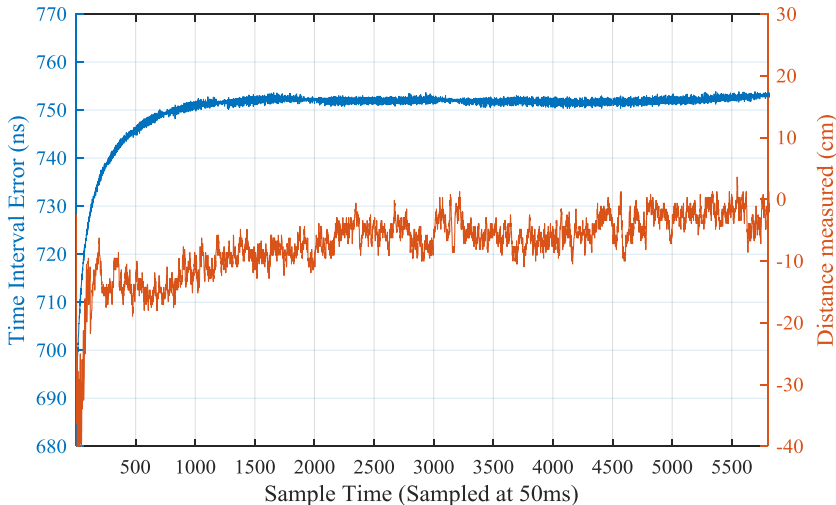


Figure 4.12: Warm-up effect of the TCXO oscillator on distance measurement accuracy

## 4.6. Performance Comparison

Concerning the achieved results so far, it was comprehensible that different clock sources have distinctive behavior in localization systems. In one hand, the crystal devices are less accurate in terms of stability as well as frequency tolerance compared to active oscillators, but they produce less noise and are remarkably cheaper. On the other hand oscillators offer higher stability and tolerance but with higher power consumption and price. It was also evident that not all the oscillators could propound high quality results as in the case of TCXO higher accuracy compared to the others achieved but with extremely high noise and nonlinearity in the startup phase. This means if a high precision and accurate oscillator is desired, the specifications in the datasheet would not guarantee to achieve the best results, instead the quality of the product and in-field measurement results should be considered for selection of a certain clock source device. As a conclusion, it seems the selection of a suitable clock source device is a tradeoff between simplicity and price versus accuracy and stability. It is necessary to

mention that only the reference anchor needs to be equipped with high precision and accurate clock and the other nodes could be supplied with any type of clock devices preferably with low noise and small jitter. All the other anchor nodes synchronize their clock with the reference node and therefore their accuracy and stability is not influencing the distance measurement results. The achieved results of the experiments are summarized in Table 4.2.

Table 4.2: Summary of the clock sources characteristics achieved from the experiments

Parameter	Quartz Crystal	VCTCXO	TCXO
Mean of the frequency bias (ns) including bias of the mobile node	1532	859	1170
Mean of frequency bias (ns) when bias of the mobile node is removed	452	211	100
Frequency stability between different experiments (ns)	$\pm 10$	$\pm 5$	$\pm 10$
Clock noise standard deviation (ps)	$\pm 23$	$\pm 20.9$	$\pm 54.7$
Frequency fluctuation in long run after stability (ns)	$\pm 1.93$	$\pm 0.33$	$\pm 0.48$
Stability time (seconds)	15	250	45
Bias deviation after start up (ns)	10	40	62

Once the clock TIE of each anchor is calculated, the differential distance data achieved in the mobile node should be compensated. In our experiments, we have selected three pair of anchors in the star form namely anchor 1 and 2, anchor 1 and 3 and anchor 1 and 4. The anchors are located in the corner of a square surface and the mobile node exactly in the middle of the area where the differential distance to each anchor is zero. According to the star pairing style and recall from Eq. 4.6, the second anchor transmits after 10ms, the third one after 20ms and the last one after 30ms when the signal of the first anchor is arrived. Imagine the case that the anchors have synchronized their clock rate with the reference anchor. The mobile node measures clock TIE of its crystal and estimates average offset of 550 ns with the reference node. This is achieved for the period of 50 ms between the two sequential transmissions of the reference anchor. This means the clock TIE of the time for the first anchor pair is 110 ns, for the second 220 ns and for the third pair 330 ns. Knowing the fact that the radio wave travels at 30cm/ns, the delay of 10ms should yield an offset of about 33 meters in the ranging results. This value is 66 m for the second pair and 99 m for the third pair. The results of the ranging are demonstrated in Figure 4.13. As it can be seen from the first three plots, the error of the measured distance before compensation match to those calculated theoretically. The results of the compensation are also shown in the same graph but in the bottom window. As it can be seen, the compensation process effectively cancels out the large created offsets and hence all the plots are indicating distance of zero where the node truly is locating. Moreover, the skew

rate of the clocks is compensated as well resulting in a flat line during the measurement period. The available fluctuation of the signal is originating from the measurement noise and other uncertainties such as radio noise, etc.

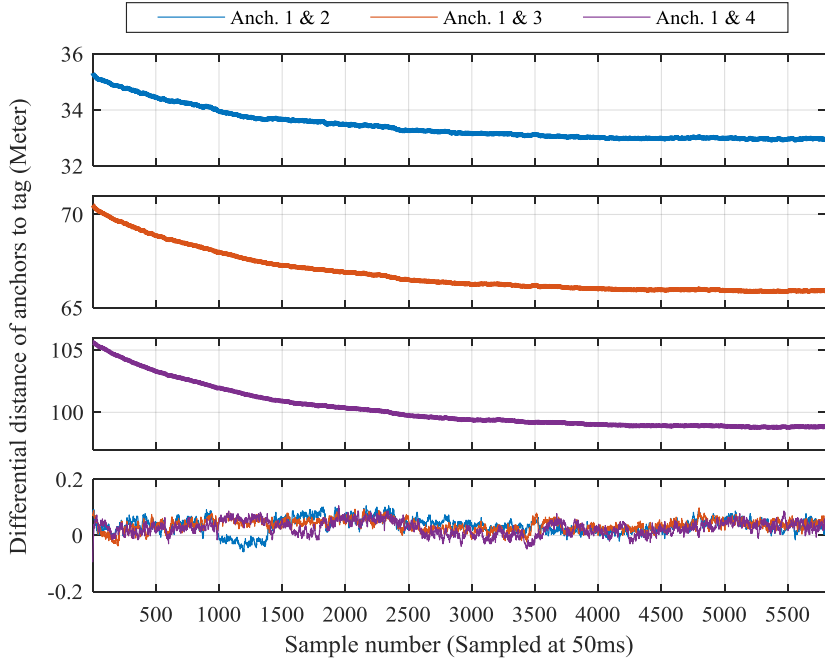


Figure 4.13: Results of differential ranging for three anchor pairs before (the first three plots) and after (the last plot) compensation.

In another experiment, the effect of different clock source devices on the accuracy of distance data is evaluated. For this purpose, different location data of the same hardware setup is collected while equipped with different clock source devices as described before. The mobile node is located at the middle of the test arena where the differential range of all anchor pairs is zero. Then the probability distribution function (PDF) of the results are plotted for all the experiments and clock sources. Assuming a very accurate localization system, the PDF graph should look like a Gaussian distribution with its mean located at zero and representing small range of standard deviation. The result of this experiment is illustrated in Figure 4.14. According to this figure, the best location accuracy among the group is achieved by VCTCXO device with the mean of 2.9cm in average and standard deviation of  $\pm 1.6\text{cm}$ . The maximum deviation in this case is measured to be in the range of  $\pm 8\text{cm}$ . In the case of quartz crystal, the mean is around  $-14.22\text{cm}$  with standard deviation of  $\pm 4\text{cm}$  and maximum deviation range of  $\pm 15\text{cm}$ . These parameters for the case of TCXO device are  $-5.8\text{cm}$ ,  $\pm 3.9\text{cm}$  and  $\pm 14\text{cm}$  for mean, standard deviation and maximum deviation respectively. As it can be seen, the quartz crystal has the highest deviation of the mean which is resulted from high deviation

range of the frequency in this type of device. The variance of the error in this case is slightly larger than the VCTCXO but better than that from TCXO devices. As it was discussed before, the noise issue of TCXO devices has influence on the distance error. This is clearly visible in the PDF graphs as the variance of the distance error is the highest among the three devices. The mean of the distance error however is better than the crystal as this is controlled by the temperature control unit of the oscillator.

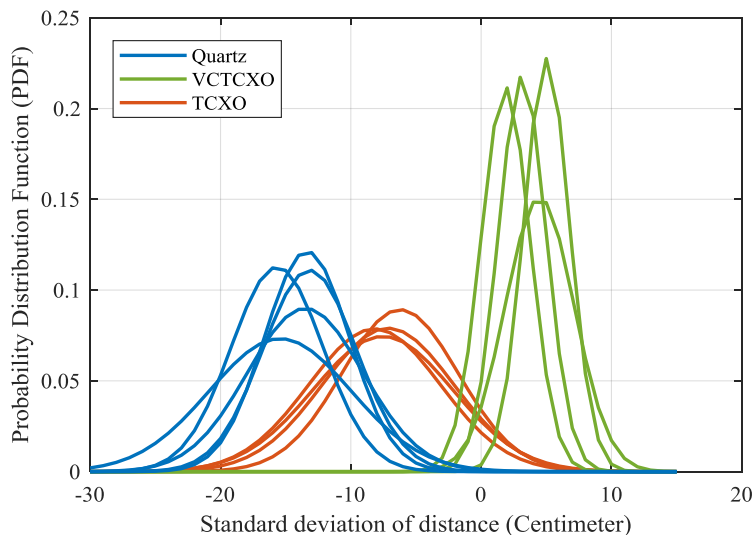


Figure 4.14: Accuracy analysis of the error of distance measurement for different experiments performed on all the clock sources repeatedly

For the sake of comparison, the achieved results of accuracy analysis are listed in Table 4.3.

Table 4.3: Summary of the clock sources variance analysis achieved from experiments

Parameter	Quartz Crystal	VCTCXO	TCXO
Standard deviation of distance measurement (cm)	$\pm 4.05$	$\pm 1.62$	$\pm 3.98$
Mean of the distance between 5 rounds of measurements (cm)	-14.22	2.90	-5.81
Maximum range of deviation (cm)	$\pm 17$	$\pm 10$	$\pm 14$

## 5. Localization Algorithms

The localization techniques are defined to be a set of algorithms which are used to extract the location of an entity (human, object, etc.) either relative to another entity (e.g. robots) or in absolute form from a reference point (landmarks, anchors, etc.). The information of location can be presented in 2D by indicating the point in the form of  $(x, y)$  for Cartesian or  $(r, \phi)$  for polar coordinates. In case of 3D localization, an additional axis will be added in the form  $(x, y, z)$  and  $(r, \phi, \theta)$  for Cartesian and polar coordinates respectively. In Figure 5.1, the block diagram of the required signal processing components in TDoA topology of localization is demonstrated. The process of extracting data from radio nodes and converting them to pseudo-ranges is described in Chapter 3. These pseudo-ranges are the differential time of arrival of signals multiplied by the speed of light. Details of the synchronization and filtering methods are presented and discussed in Chapter 4. This chapter discusses the last segment of localization chain which is an algorithm that extracts the location information of the mobile node by fusing the pseudo-ranges together. Model description of the TDoA localization system, introduction of algorithms used for localization of static and dynamic systems and evaluation and comparison of these techniques are subjects of this chapter.

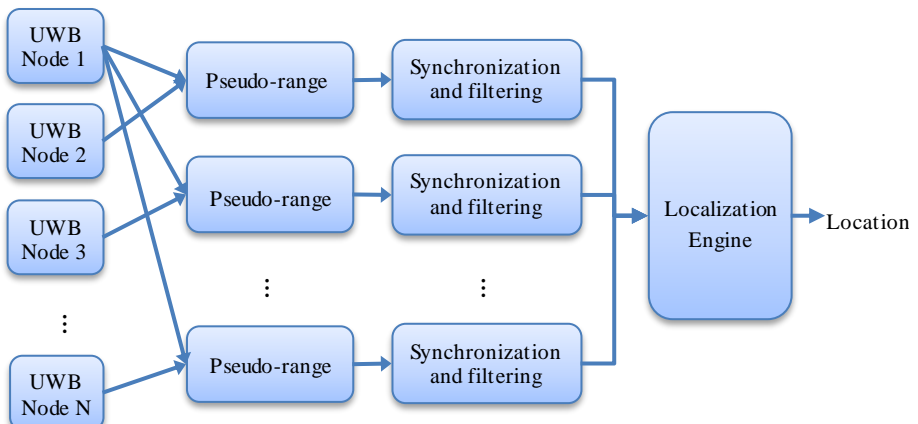


Figure 5.1: Block diagram of the processing units in a TDoA localization system

## 5.1. Modeling of the TDoA Topology

The main part of a localization algorithm is to define a set of mathematical equations which describe the relation of pseudo-ranges achieved from the nodes to the location of the node we would like to localize. In this section a model is defined which describes these relations. As another fact, it should be considered that the goal of the localization system is to estimate the coordinates of a target object such as a robot which is usually dynamic. This means the location of the robot may change from sample to sample. Therefore, in order to find an accurate estimation of the location, it is necessary to consider this dynamic behavior of the mobile nodes by realizing a model describing the dynamics of the target node and merging it with the model of the observed range data from the radio nodes. These models are described in the following subsections in detail.

### 5.1.1. Measurement model of the TDoA

Recall from Eq. 3.32, a mathematical relation between the location of a mobile node and the differential range estimates is defined. This equation is extended for  $n$  anchors resulting in a system of  $(n - 1)$  equations:

$$\begin{cases} d_{2,1} = \sqrt{(x_m - x_2)^2 + (y_m - y_2)^2} - \sqrt{(x_m - x_1)^2 + (y_m - y_1)^2} \\ d_{3,1} = \sqrt{(x_m - x_3)^2 + (y_m - y_3)^2} - \sqrt{(x_m - x_1)^2 + (y_m - y_1)^2} \\ \vdots \\ d_{n,1} = \sqrt{(x_m - x_n)^2 + (y_m - y_n)^2} - \sqrt{(x_m - x_1)^2 + (y_m - y_1)^2} \end{cases} \quad (5.1)$$

As it was mentioned before, the solution of these equations in geometry is the intersection point of the hyperbolas. However, for the sake of implementation in digital systems, an algebraic solution is required. These equations are in quadratic form and therefore nonlinear. Closed-form technique is a way to represent these equations in linear form [6, p. 195]. The closed-form technique starts with declaring the differential distances by their distance components as:

$$d_{i,1} = D_i - D_1 \quad , \quad \text{where } i = 2, \dots, n \quad (5.2)$$

where  $D_i$  is the distance of the mobile node to anchor node  $i$ , and  $D_1$  is the distance of the mobile node to anchor 1 (reference anchor). Given that the coordinates of the mobile node in 2D is  $(x_m, y_m)$  the distance  $D_i$  can be described in squared form as:

$$D_i^2 = (x_m - x_i)^2 + (y_m - y_i)^2 \quad (5.3)$$

If we subtract this term of anchor  $i$  from the same term of anchor 1, we have:

$$D_i^2 - D_1^2 = (d_{i,1} + D_1)^2 - D_1^2 = d_{i,1}^2 + 2d_{i,1}D_1 \quad (5.4)$$

Therefore, the differential equation in squared form is:

$$d_{i,1}^2 = D_i^2 - D_1^2 - 2d_{i,1}D_1 \quad , \quad \text{where } i = 2, \dots, n \quad (5.5)$$

By extending the Eq. 5.3 and replacing in Eq. 5.4 we have:

$$D_i^2 = x_m^2 + x_i^2 - 2x_m x_i + y_m^2 + y_i^2 - 2y_m y_i \quad (5.6)$$

$$\begin{aligned} d_{i,1}^2 &= x_m^2 + x_i^2 - 2x_m x_i + y_m^2 + y_i^2 - 2y_m y_i \\ &\quad -(x_m^2 + x_1^2 - 2x_m x_1 + y_m^2 + y_1^2 - 2y_m y_1) - 2d_{i,1}D_1 \end{aligned} \quad (5.7)$$

By reorganizing the known variables on one side and unknown variables on the other side, a linear relation can be defined as:

$$(x_1 - x_i)x_m + (y_1 - y_i)y_m - d_{i,1}D_1 = \frac{1}{2}(d_{i,1}^2 - x_i^2 - y_i^2 + x_1^2 + y_1^2) \quad (5.8)$$

In this equation, the coordinates of anchor 1 ( $x_1, y_1$ ) and anchor  $i$  ( $x_i, y_i$ ) are known. The differential distance between two anchors  $d_{i,1}$  is available from the measurements. Therefore, the unknown variables are coordinates of mobile node ( $x_m, y_m$ ) and  $D_1$  the distance of mobile node to anchor 1. This means at least three equations are required to calculate the three unknowns in the form:

$$\begin{bmatrix} (x_1 - x_2) & (y_1 - y_2) & -d_{2,1} \\ \dots & \dots & \dots \\ (x_1 - x_i) & (y_1 - y_i) & -d_{i,1} \end{bmatrix} \begin{bmatrix} x_m \\ y_m \\ D_1 \end{bmatrix} = \begin{bmatrix} \delta_2 \\ \dots \\ \delta_i \end{bmatrix} \quad (5.9)$$

$$\delta_i = \frac{1}{2}(d_{i,1}^2 - x_i^2 - y_i^2 + x_1^2 + y_1^2) \quad (5.10)$$

This form of equation is a common representation of  $\mathbf{Ax} = \mathbf{b}$  in which the matrix  $\mathbf{A}$  is the left hand side of Eq. 5.9 and parameter  $\mathbf{b}$  is the right hand side of the same equation. This equation set has an answer if only there is no error in the measurement and the data are quite close to real given setup. However, this is almost never the case in practice. This means the parameter  $d_{i,1}$  includes an additional noise term which should be considered in the model. The result is, there is an area between the curves instead of an intersection point. This is shown in Figure 5.2. In this case, there is not a unique solution for the given equation set. Therefore, algorithms should be used which consider this error in the model and calculate the point where the residual error of the estimate is minimized. The model of the system including the model error can be represented as:

$$\mathbf{Ax} + \mathbf{e} = \mathbf{b} \quad (5.11)$$

where  $\mathbf{e}$  is the added error term in the model including the measurement noise as well.

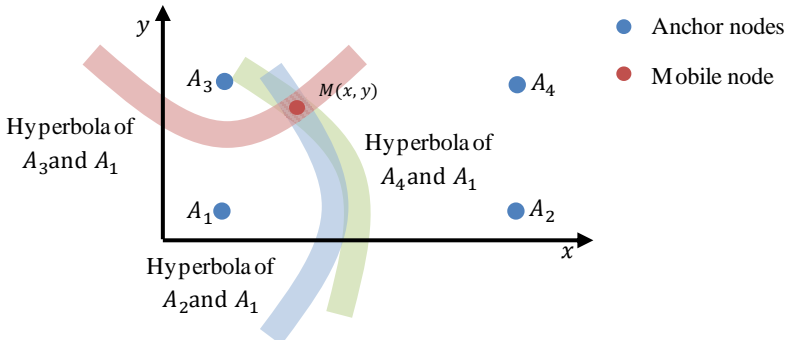


Figure 5.2: Effect of the measurement noise and model inaccuracies on the localization of TDoA topology where the area of the intersection is formed

The localization algorithm in this case should find a value for  $x$  in that the error term is minimized. This can be described in the form:

$$J = \hat{\mathbf{e}}^2 = \hat{\mathbf{e}}^T \hat{\mathbf{e}} = (\mathbf{b} - \mathbf{Ax})^T (\mathbf{b} - \mathbf{Ax}) \quad (5.12)$$

This problem is commonly solved using least square technique which defines the solution as defined below [101, p. 187] if matrix  $A$  is a full rank matrix:

$$\mathbf{x} = (\mathbf{A}^T \mathbf{A})^{-1} \mathbf{A}^T \mathbf{b} \quad (5.13)$$

Other variations of the least square (LS) technique are also available which perform better than the LS. A pioneer work in this area is the work of Smith et al [102] by proposing three different variations of the closed-form in combination with LS under the names spherical interpolation method, spherical intersection method and plane intersection method. Other works based on the implementation of the closed-form can be found in [103] where a total least square solution is provided, or the work of Gillette et al. [104] which extends the closed-form equations for larger number of anchors. Khalaf-Allah [105] has also applied these approaches in differential UWB localization systems. Other approaches for solving Eq. 5.9 are Weighted Least Square (WLS) in that measurements are weighted based on the variances of data, Bayesian least square which benefits from the prior information or probability density function of data or finally probabilistic approaches such as maximum likelihood or maximum *a posteriori* which treat the state (location of the target) as a fixed and unknown value and try to estimate a value which maximizes the probability of happening [106, p. 128]. The least square technique is a batch processing method which is used offline. Another variation of LS method is Recursive Least Square (RLS) which estimates the unknown variables online by introducing a memory effect holding only a certain number of past samples [107, p. 290]. Iterative approaches are also commonly utilized for solving this problem. A few of these methods are addressed in the following sub-sections. More details about these approaches can be found in [107–109].

### 5.1.2. Model of the system's dynamics

The location of a static device is a time invariant state which can be achieved from the measurement model as described in the previous section. The mobile device however changes its state as the time passes by and therefore the model of such systems should consider the mobility characteristics. In total, three general form of models can be defined as  $P$  (position),  $PV$  (Position and Speed) and  $PVA$  (Position, speed and acceleration). Although the only measurable parameter in defined localization system is ranging distance between anchor and node, still it is possible to estimate the speed and acceleration of the mobile node by differentiating the location measurements. The base of the equations used for defining these models is Newtonian kinematic equations as defined below:

$$\text{P model: } x = x_0 \quad (5.14)$$

$$\text{PV model: } x = vt + x_0 \quad (5.15)$$

$$\text{PVA model: } x = vt + \frac{1}{2}at^2 + x_0 \quad (5.16)$$

where  $x$  is position,  $v$  is speed and  $a$  is defined as acceleration of the entity. The subscript zero indicates the initial condition of the corresponding parameter. For the case of a  $PVA$  model, these equations can be presented in the state space form derived from the following equations [106, p. 31]:

$$\dot{x} = \frac{d}{dt}x, \quad \ddot{x} = \frac{d}{dt}\dot{x}, \quad \ddot{x} = q, \quad y = x \quad (5.17)$$

$$\begin{bmatrix} \dot{x} \\ \ddot{x} \\ \ddot{x} \end{bmatrix} = \begin{bmatrix} 0 & 1 & 0 \\ 0 & 0 & 1 \\ 0 & 0 & 0 \end{bmatrix} \begin{bmatrix} x \\ \dot{x} \\ \ddot{x} \end{bmatrix} + \begin{bmatrix} 0 \\ 0 \\ 1 \end{bmatrix} q \quad (5.18)$$

$$\dot{x} = Fx + Bu \quad (5.19)$$

$$y = Hx \quad (5.20)$$

In the given state space form,  $q$  is the process noise which is normally added to the state with the highest derivative order but it could also be present in other states. The parameter  $y$  is the output of the system which is related to states over observation matrix  $H$ . In order to predict the value of the states for the next sample time, the transition matrix also known as fundamental matrix  $\Phi(t)$  should be calculated. This can be performed using two techniques. The first one is based on the Taylor series described in the form:

$$\Phi(t) = e^{Ft} = I + Ft + \frac{(Ft)^2}{2!} + \cdots + \frac{(Ft)^n}{n!} \quad (5.21)$$

Considering only the first three terms of the Taylor series and replacing the  $\mathbf{F}$  by matrix from Eq. 5.18 in the previous equation, the fundamental matrix  $\Phi(t)$  can be calculated as [110, p. 34]:

$$\Phi(t) \approx \begin{bmatrix} 1 & 0 & 0 \\ 0 & 1 & 0 \\ 0 & 0 & 1 \end{bmatrix} + \begin{bmatrix} 0 & 1 & 0 \\ 0 & 0 & 1 \\ 0 & 0 & 0 \end{bmatrix} t + \frac{\left( \begin{bmatrix} 0 & 1 & 0 \\ 0 & 0 & 1 \\ 0 & 0 & 0 \end{bmatrix} t \right)^2}{2} \quad (5.22)$$

$$\Phi(t) \approx \begin{bmatrix} 1 & t & 0.5t^2 \\ 0 & 1 & t \\ 0 & 0 & 1 \end{bmatrix} \quad (5.23)$$

The second technique benefits from the inverse Laplace transform in the form of [110, p. 35]:

$$\Phi(t) = \mathcal{L}^{-1}(s\mathbf{I} - \mathbf{F})^{-1} \quad (5.24)$$

$$\Phi(t) = \mathcal{L}^{-1} \left[ \left( s \begin{bmatrix} 1 & 0 & 0 \\ 0 & 1 & 0 \\ 0 & 0 & 1 \end{bmatrix} - \begin{bmatrix} 0 & 1 & 0 \\ 0 & 0 & 1 \\ 0 & 0 & 0 \end{bmatrix} \right)^{-1} \right] = \mathcal{L}^{-1} \left[ \left( \begin{bmatrix} s & -1 & 0 \\ 0 & s & -1 \\ 0 & 0 & s \end{bmatrix} \right)^{-1} \right] \quad (5.25)$$

$$\Phi(t) = \mathcal{L}^{-1} \left[ \begin{bmatrix} s^{-1} & s^{-2} & s^{-3} \\ 0 & s^{-1} & s^{-2} \\ 0 & 0 & s^{-1} \end{bmatrix} \right] = \begin{bmatrix} 1 & t & 0.5t^2 \\ 0 & 1 & t \\ 0 & 0 & 1 \end{bmatrix} \quad (5.26)$$

Once the fundamental matrix is calculated, the transitional model of the system in the state space form can be written as:

$$\begin{bmatrix} x(t+1) \\ \dot{x}(t+1) \\ \ddot{x}(t+1) \end{bmatrix} = \begin{bmatrix} 1 & \Delta t & 0.5\Delta t^2 \\ 0 & 1 & \Delta t \\ 0 & 0 & 1 \end{bmatrix} \begin{bmatrix} x(t) \\ \dot{x}(t) \\ \ddot{x}(t) \end{bmatrix} + \begin{bmatrix} 0 \\ 0 \\ 1 \end{bmatrix} q \quad (5.27)$$

where  $x$  is the location in axis  $x$ ,  $\dot{x}$  is the speed and  $\ddot{x}$  is the acceleration of the mobile node. Parameter  $\Delta t$  is the inverse of sampling rate. This equation can be extended in the same way for 2D or 3D space localization.

The process noise  $q$  added in Eq. 5.27 is for the sake of transferring the equations from a deterministic system to a stochastic system. This time varying errors of the system in discrete form is called random walk which is often used to model random processes [106, p. 31]. Another common method of modeling random processes is Markov model also known as colored noise. This model can be continuous or discrete and defines the probability of the current state to be dependent only on the current state and not on the previous samples up to the current sample [111, p. 64]. Other modeling methods are Brownian-motion model (continuous form of random walk) or random waypoint walk model which are described in detail in [2, p. 139].

Considering that the process noise  $q$  is only applied on  $\ddot{x}$ , the covariance matrix of the process noise is defined as  $\mathbf{Q}$ . This can be represented in the form:

$$\mathbf{Q} = E \begin{bmatrix} 0 \\ 0 \\ q \end{bmatrix} [0 \quad 0 \quad q] = \begin{bmatrix} 0 & 0 & 0 \\ 0 & 0 & 0 \\ 0 & 0 & \phi_s \end{bmatrix} \quad (5.28)$$

$\phi_s$  is scalar value of the variance. The matrix of a random walk process model is defined according to the following equation [110, p. 131]:

$$\mathbf{Q}(t) = \int_{\tau=0}^{\tau=t+T} \mathbf{\Phi}(\tau) \mathbf{Q} \mathbf{\Phi}^T(\tau) d\tau \quad (5.29)$$

After replacing the variables with the given matrices in Eq. 5.26, we have:

$$\mathbf{Q}(t) = \int_{\tau=0}^{\tau=T} \begin{bmatrix} 1 & \tau & 0.5\tau^2 \\ 0 & 1 & \tau \\ 0 & 0 & 1 \end{bmatrix} \begin{bmatrix} 0 & 0 & 0 \\ 0 & 0 & 0 \\ 0 & 0 & \phi_s \end{bmatrix} \begin{bmatrix} 1 & 0 & 0 \\ \tau & 1 & 0 \\ 0.5\tau^2 & \tau & 1 \end{bmatrix} d\tau \quad (5.30)$$

which results in:

$$\mathbf{Q}(t) = \phi_s \begin{bmatrix} \frac{T^5}{20} & \frac{T^4}{8} & \frac{T^3}{6} \\ \frac{T^4}{8} & \frac{T^3}{3} & \frac{T^2}{2} \\ \frac{T^3}{6} & \frac{T^2}{2} & T \end{bmatrix} \quad (5.31)$$

This means for calculating the covariance of the estimates, the sampling rate is required as a parameter as well as constant value of  $\phi_s$  which is the variance of the process noise. The achieved results of matrices for different orders of the system model are provided in Table 5.1.

Table 5.1: Stochastic models of dynamic systems in the form of state space [110, p. 135]

Model type	Dynamic matrix $\mathbf{F}$	Fundamental matrix $\mathbf{\Phi}$	Covariance matrix $\mathbf{Q}$
P	1	1	$\phi_s$
PV	$\begin{bmatrix} 0 & 1 \\ 0 & 0 \end{bmatrix}$	$\begin{bmatrix} 1 & \Delta t \\ 0 & 1 \end{bmatrix}$	$\phi_s \begin{bmatrix} \frac{T^3}{3} & \frac{T^2}{2} \\ \frac{T^2}{2} & T \end{bmatrix}$
PVA	$\begin{bmatrix} 0 & 1 & 0 \\ 0 & 0 & 1 \\ 0 & 0 & 0 \end{bmatrix}$	$\begin{bmatrix} 1 & \Delta t & 0.5\Delta t^2 \\ 0 & 1 & \Delta t \\ 0 & 0 & 1 \end{bmatrix}$	$\phi_s \begin{bmatrix} \frac{T^5}{20} & \frac{T^4}{8} & \frac{T^3}{6} \\ \frac{T^4}{8} & \frac{T^3}{3} & \frac{T^2}{2} \\ \frac{T^3}{6} & \frac{T^2}{2} & T \end{bmatrix}$

## 5.2. Static Iterative Techniques

We define static localization methods as algorithms which do not need to know the previous status of the states to estimate the current states. Therefore, only the results of the current measurement is used to calculate the position of a node. As it was discussed in Section 5.1.1, the relation of the pseudo-ranges to location of a node is a set of nonlinear equations. It is not always possible to reach to an answer in closed-form for such nonlinear problems especially when the data are noisy and inaccurate. In addition to that, the mathematical equations of closed-form and LS technique are complex and involved matrix inversion which may result in divergence of the localization engine when the data are not plausible or the model is to some extent inaccurate. Iterative approaches address this problem by making an initial guess and evaluate the error between the outcome of the model based on this guess and real measurements. Then in an iterative process, the initial guess is optimized in a way that smaller error is achieved. The process ends when the error between model outcome and measurement is minimum. The general algorithm of iterative optimization is described below [112]:

---

### Iterative localization Algorithm

---

$\mathbf{x}(0)$  = initial guess

$\mathbf{e}(0) = \mathbf{0}$

Loop:

$$\mathbf{x}(t+1) = \mathbf{x}(t) + \alpha \cdot m \cdot \mathbf{e}(t)$$

$$e^2(t+1) = (\hat{\mathbf{y}} - \mathbf{g}(\mathbf{x}(t+1)))^T (\hat{\mathbf{y}} - \mathbf{g}(\mathbf{x}(t+1)))$$

If  $e^2(t+1) == e^2(t)$  or  $e^2(t+1) < \delta$

if the squared error  $e^2$  is not decreasing or a minimum of squared error is achieved then end the loop

End of Loop

In this algorithm,  $\mathbf{e}(t)$  is the error of the model prediction and measurement at time  $t$ ,  $\mathbf{x}(t)$  is the estimated location of the node,  $\hat{\mathbf{y}}$  is the measured pseudo-ranges and  $\mathbf{g}$  is the nonlinear function relating the pseudo-ranges to location of a mobile node based on the measurement model. Parameter  $\alpha$  determines the direction and  $m$  the amount of improvement in the initial guess which is estimated differently based on the applied algorithm.  $\delta$  is a minimum threshold for error at which the algorithm will stop to avoid too many unnecessary iterations.

The iterative approaches do not need to linearize the model equations which is a great advantage. Furthermore, the iterative approaches always lead to an answer even if the model is badly selected or data are very noisy. It is also possible to establish a metric for evaluating the quality of data by measuring the residual error. These algorithms are very simple and easy to implement even in limited microcontrollers. There are however some critics to these iterative approaches as

the algorithms are normally time consuming (due to iteration process), need a good initial guess and may find a local minimum instead of a global one. The last one is however irrelevant to our localization application as the equations are quadratic and therefore there is only one minimum either in 2D or 3D cases. High speed microcontrollers have solved the long estimation time problem of these algorithms. The initial guess is still an issue but only for the first round of calculation, since once the first round of measurement is performed the previous point of the node can be used as initial guess for the next round. This way it is assured that we always make a guess in the vicinity of the location of the mobile node. There are many iterative optimization approaches such as secant, Fibonacci search, quasi-Newton, steepest descent, Newton, Gauss-Newton, Levenberg-Marquardt, to name a few. Details of these approaches can be found in [101, 109, 112–114]. This section briefly reviews a few of these methods and provides a comparison of them based on their results from real localization experiments.

### 5.2.1. Gradient-Descent (G-D) method

This algorithm uses the gradient operator to find the direction of the search and the step of improvement in the initial state estimate in order to minimize the error. Imagine  $y$  as the measured data and  $x$  as the estimate of the model based on an initial guess. Given that  $g(x)$  is the estimate of the system,  $y$  is the measured values and  $f(x)$  is the error of the measurements compared to estimates, we are trying to find an optimum  $x$  which minimize the sum square of residuals  $r(x)$ :

$$\hat{x} = \underset{x}{\operatorname{argmin}} r(x) = \underset{x}{\operatorname{argmin}} (f_x^T f_x) = \underset{x}{\operatorname{argmin}} \left( (y - g(x))^T (y - g(x)) \right) \quad (5.32)$$

The gradient-descent method starts from an initial guess and tries to improve the state in order to minimize the error. This can be described as [112]:

$$\hat{\alpha} = \underset{\alpha}{\operatorname{argmin}} r(x + \alpha h_d) \quad (5.33)$$

where  $\alpha$  is the amount of improvement in order to minimize the error function  $r$  and the  $h_d$  is the search direction which is opposite of the gradient sign. Using the Taylor series, the term  $r(x + \alpha h_d)$  can be extended into [112]:

$$r(x + \alpha h_d) = r(x) + \alpha h_d^T \nabla r(x) + O(\alpha^2) \quad (5.34)$$

The last term of the equation, summarizes the higher order segments of the Taylor series which can be ignored for small values of  $\alpha$ . The next step of improvement in the initial state is estimated by considering a small value for  $\alpha$ , direction of the search in transpose form  $h_d^T$  and gradient of the error function  $\nabla r(x)$ . The algorithm of the gradient-descent equation is defined as [112]:

$$x_{k+1} = x_k + \alpha J^T(x)(y - g(x)) \quad (5.35)$$

where  $\mathbf{J}(\mathbf{x})$  is the Jacobian matrix of the error function. Based on this equation, the algorithm of gradient-descent is defined below:

---

Gradient-descent Algorithm

---

$\mathbf{x}(0)$  = initial guess

$\mathbf{f}(0) = \mathbf{y} - \mathbf{g}(\mathbf{x}(0))$

Loop:

$$\mathbf{J} = \frac{\partial}{\partial \mathbf{x}} \mathbf{g}(\mathbf{x}_t)$$

$$\mathbf{x}_{t+1} = \mathbf{x}_t + \alpha \cdot \mathbf{J}^T \cdot \mathbf{f}(t)$$

$$r_{t+1} = (\hat{\mathbf{y}} - \mathbf{g}(\mathbf{x}_{t+1}))^T (\hat{\mathbf{y}} - \mathbf{g}(\mathbf{x}_{t+1}))$$

If  $r_{t+1} == r_t$  or  $r_{t+1} < \delta$

if the residual error  $r$  is not decreasing or a minimum of error is achieved then end the loop

End of Loop

As an example, consider a localization system with three anchors at coordinates  $A_1(x_1, y_1)$ ,  $A_2(x_2, y_2)$ , and  $A_3(x_3, y_3)$  and a mobile node located at  $(x_m, y_m)$ . The distance of the anchors to the mobile node in ToA topology extracted from the model is represented as  $d_1, d_2$  and  $d_3$  and the measured data  $d'_1, d'_2$  and  $d'_3$  for anchor 1, 2 and 3 respectively. In this case, the optimization equation of the gradient-descent method can be described as:

$$d_i = \sqrt{(x_i - x_m)^2 + (y_i - y_m)^2} , \quad i = 1, 2, 3 \quad (5.36)$$

$$\begin{bmatrix} x_m \\ y_m \end{bmatrix}_{k+1} = \begin{bmatrix} x_m \\ y_m \end{bmatrix}_k + \alpha \begin{bmatrix} \frac{\partial d_1}{\partial x_m} & \frac{\partial d_2}{\partial x_m} & \frac{\partial d_3}{\partial x_m} \\ \frac{\partial d_1}{\partial y_m} & \frac{\partial d_2}{\partial y_m} & \frac{\partial d_3}{\partial y_m} \end{bmatrix} \left[ \begin{bmatrix} d'_1 \\ d'_2 \\ d'_3 \end{bmatrix} - \begin{bmatrix} d_1 \\ d_2 \\ d_3 \end{bmatrix} \right] \quad (5.37)$$

$$\begin{bmatrix} x_m \\ y_m \end{bmatrix}_{k+1} = \begin{bmatrix} x_m \\ y_m \end{bmatrix}_k + \alpha \begin{bmatrix} Jx_1 + Jx_2 + Jx_3 \\ Jy_1 + Jy_2 + Jy_3 \end{bmatrix} \quad (5.38)$$

$$Jx_i = \frac{(x_i - x_m)(d'_i - d_i)}{d_i} , \quad Jy_i = \frac{(y_i - y_m)(d'_i - d_i)}{d_i} , \quad i = 1, 2, 3 \quad (5.39)$$

The gradient functionality of this method brings the initial state guess within a few iterations to the vicinity of the target value but then it improves linearly resulting in long number of iterations to get closer to the final state [112]. A solution to this problem is Barzilai-Borwein method [115] which reduces the number of iterations by updating the  $\alpha$  parameter as it gets closer to the final state. This method for one dimensional and scalar case can be described as:

$$\alpha_k = \frac{(x_k - x_{k-1})^T (f'(x_k) - f'(x_{k-1}))}{\| (f'(x_k) - f'(x_{k-1})) \|^2} \quad (5.40)$$

## 5.2.2. Newton method

The newton approach benefits from the gradient and Hessian of the cost function for determining the amount of state's improvement in each iteration. To extract the formula of this method, the sum of residuals  $r(\mathbf{x})$  is used as cost function which is defined in Eq. 5.32. This function can be modelled as a quadratic function  $q$  according to Taylor series defined as:

$$q(\mathbf{x} + \mathbf{h}) = r(\mathbf{x}) + (\nabla r(\mathbf{x}))^T \mathbf{h} + \frac{1}{2} \mathbf{h}^T \mathbf{H}(\mathbf{x}) \mathbf{h} \quad (5.41)$$

If we would like to minimize this model at the current iteration, we can calculate the gradient of the quadratic function and equalize it to zero:

$$\nabla q(\mathbf{h}) = (\nabla r(\mathbf{x}))^T + \mathbf{H}(\mathbf{x}) \mathbf{h} = \mathbf{0} \quad (5.42)$$

Using this equation, we can define the amount of improvement in each iteration:

$$\mathbf{h} = -\mathbf{H}(\mathbf{x})^{-1} \nabla r(\mathbf{x}) \quad (5.43)$$

The function  $\nabla r(\mathbf{x})$  is gradient of the cost function and  $\mathbf{H}(\mathbf{x})$  is Hessian of the cost function. Knowing the amount of increment step  $\mathbf{h}$ , the Newton optimization algorithm can be described as:

$$\mathbf{x}_{k+1} = \mathbf{x}_k + \mathbf{h} = \mathbf{x}_k - \mathbf{H}(\mathbf{x})^{-1} \nabla r(\mathbf{x}) \quad (5.44)$$

The Newton approach has quadratic form at the end of its process close to final state which results in faster convergence to the final point. If the objective function is also in quadratic form, only one iteration is required to reach to the final answer [101, p. 103]. One of the disadvantages of Newton approach is the Hessian matrix which is difficult and time consuming to calculate and may also result in matrix singularity if the model is ill-conditioned [112]. For the case of the experiment described in the previous section, the gradient and Hessian matrices are required. The gradient matrix is defined in Eq. 5.38-39. Accordingly the Hessian matrix for a two dimensional system is:

$$\begin{aligned} \mathbf{H}(1,1) &= \sum_{i=1}^n \left( \frac{(d_i(x_i - x_m) - 2(d'_i - d_i)d_i^2 + (d'_i - d_i)(x_m - x_i)^2)}{d_i^3} \right) \\ \mathbf{H}(2,2) &= \sum_{i=1}^n \left( \frac{(d_i(y_i - y_m) - 2(d'_i - d_i)d_i^2 + (d'_i - d_i)(y_m - y_i)^2)}{d_i^3} \right) \\ \mathbf{H}(1,2) &= \mathbf{H}(2,1) = \sum_{i=1}^n \left( \frac{2(x_m - x_i)(y_m - y_i)}{d_i^2} \left[ 1 + \frac{(d'_i - d_i)}{d_i} \right] \right) \end{aligned} \quad (5.45)$$

As it can be seen from this equation, the process of calculating the Hessian matrix is complicated. The Gauss-Newton method provides similar characteristics as the Newton method but avoids the requirement of calculating the Hessian matrix.

### 5.2.3. Gauss-Newton (G-N)

This is also a very common optimization technique used for many problems. In some special cases, this technique can also provide quadratic convergence [114]. The benefit of this approach to the Newton method is calculation of the second derivative is not required. To derive the equation of this method, the Taylor expansion of the cost function  $f$  as described in Eq. 5.32 is used:

$$f(\mathbf{x} + \mathbf{h}) \approx f(\mathbf{x}) + \mathbf{J}(\mathbf{x})\mathbf{h} = \mathbf{q}(\mathbf{h}) \quad (5.46)$$

In this equation, a new function  $\mathbf{q}$  is introduced which models the cost function for each iteration based on the amount of improvement  $\mathbf{h}$ . We can describe this function in quadratic form and find the minimum of the function based on  $\mathbf{h}$ :

$$Q(\mathbf{h}) \equiv \mathbf{q}^T(\mathbf{h})\mathbf{q}(\mathbf{h}) = (\mathbf{f}^T(\mathbf{x})\mathbf{f}(\mathbf{x}) + 2\mathbf{h}^T\mathbf{J}^T(\mathbf{x})\mathbf{f}(\mathbf{x}) + \mathbf{h}^T\mathbf{J}^T(\mathbf{x})\mathbf{J}(\mathbf{x})\mathbf{h}) \quad (5.47)$$

$$\nabla Q(\mathbf{h}) = 2\mathbf{J}^T(\mathbf{x})\mathbf{f}(\mathbf{x}) + 2\mathbf{J}^T(\mathbf{x})\mathbf{J}(\mathbf{x})\mathbf{h} = \mathbf{0} \quad (5.48)$$

$$\mathbf{h} = -(\mathbf{J}^T(\mathbf{x})\mathbf{J}(\mathbf{x}))^{-1}\mathbf{J}^T(\mathbf{x})\mathbf{f}(\mathbf{x}) \quad (5.49)$$

Therefore, the algorithm of Gauss-Newton method uses only the Jacobian in the form of Eq. 5.49 and hence no Hessian is required. The equation of this technique in iterative form is:

$$\mathbf{x}_{k+1} = \mathbf{x}_k - (\mathbf{J}^T(\mathbf{x})\mathbf{J}(\mathbf{x}))^{-1}\mathbf{J}^T(\mathbf{x})(\mathbf{y} - \mathbf{g}(\mathbf{x})) \quad (5.50)$$

The process of the algorithm of the Gauss-Newton method in iterative form is as follows:

---

#### Gauss-Newton Algorithm

---

$\mathbf{x}(0)$  = initial guess

$\mathbf{f}(0) = \mathbf{y} - \mathbf{g}(\mathbf{x}(0))$

Loop:

$$\mathbf{J}(t) = \frac{\partial}{\partial \mathbf{x}} \mathbf{g}(\mathbf{x}(t))$$

$$\mathbf{x}(t+1) = \mathbf{x}(t) - (\mathbf{J}^T(\mathbf{x})\mathbf{J}(\mathbf{x}))^{-1}\mathbf{J}^T(\mathbf{x})\mathbf{f}(t)$$

$$r_{t+1} = (\hat{\mathbf{y}} - \mathbf{g}(\mathbf{x}_{t+1}))^T(\hat{\mathbf{y}} - \mathbf{g}(\mathbf{x}_{t+1}))$$

If  $r_{t+1} == r_t$  or  $r_{t+1} < \delta$

if the residual error  $r_{t+1}$  is not decreasing or a minimum of error is achieved

then end the loop

End of Loop

### 5.2.4. Levenberg-Marquardt (L-M)

The main advantage of the Gauss-Newton method is its fast convergence but it needs a good initial guess. Otherwise the process at the beginning may take too long or may not converge at all if the model is ill-conditioned [114]. Unlike the Newton or Gauss-Newton method, the gradient-descent converges quickly at the beginning but then turns into a linear function and has a very slow convergence close to the final target. The Levenberg-Marquardt solution solves this problem by combining the two techniques in a way that at the initial phase, the gradient-descent method is applied and once the state is close enough to the final target changes to Gauss-Newton method. This is done by dynamically updating the improvement term depending on the current iteration number. In order to realize this, a new parameter  $\lambda$  is introduced with modification in the Gauss-Newton method defined below [116]:

$$\mathbf{x}_{k+1} = \mathbf{x}_k - (\mathbf{J}^T(\mathbf{x})\mathbf{J}(\mathbf{x}) + \lambda\mathbf{I})^{-1}\mathbf{J}^T(\mathbf{x})(\mathbf{y} - \mathbf{g}(\mathbf{x})) \quad (5.51)$$

For a large values of  $\lambda$ , the denominator of the improvement term turns into a constant which resembles the gradient-descent algorithm. This can be described mathematically in the form:

$$(\lambda\mathbf{I})^{-1}\mathbf{J}^T(\mathbf{x})(\mathbf{y} - \mathbf{g}(\mathbf{x})) = \alpha\mathbf{J}^T(\mathbf{x})(\mathbf{y} - \mathbf{g}(\mathbf{x})) , \text{ if } \lambda\mathbf{I} \gg \mathbf{J}^T(\mathbf{x})\mathbf{J}(\mathbf{x}) \quad (5.52)$$

Likewise, if the value of  $\lambda$  is significantly smaller than the squared of Jacobian matrix, the modification variable  $\lambda$  can be ignored. This results in Eq. 5.50 which is Gauss-Newton method. The general idea of Levenberg-Marquardt method is to choose large  $\lambda$  at initial phase to turn the improvement term into gradient-descent method and as the iterations are progressed, the value of  $\lambda$  is decreased gradually to convert the algorithm into Gauss-Newton to benefit from faster convergence properties of this method at final iterations [116].

Different approaches are proposed for determining the value of  $\lambda$ . Two simple methods proposed in [112, p. 48] are based on defining a gain factor defined as below for one dimensional case:

$$r = \frac{f(x_{k+1}) - f(x_k)}{x_{k+1} - x_k} \quad (5.53)$$

In the first technique, the value of  $\lambda$  is defined by specifying a value for certain region of gain factor  $r$ . This is realized by developing a series of "if" conditions and controlling the amount of  $r$  such as: "if  $r > 0.5$  then  $\lambda = \lambda/2$ ". This however disrupts the convergence process due to discontinuity created by the  $\lambda$ . In another approach the value of  $\lambda$  is gradually updated as [112, p. 49]:

$$\lambda = \begin{cases} 1 - (2r - 1)^3 & \text{if } r > 0 \\ 2\lambda & \text{if } r < 0 \end{cases} \quad (5.54)$$

The algorithm of the Levenberg-Marquardt approach is provided below:

---

### Levenberg-Marquardt Algorithm

---

$\mathbf{x}(0)$  = initial guess

$\mathbf{f}(0) = \mathbf{y} - \mathbf{g}(\mathbf{x}(0))$

$\lambda=100$

Loop:

$$\mathbf{J}(t) = \frac{\partial}{\partial \mathbf{x}} \mathbf{g}(\mathbf{x}(t))$$

$$\mathbf{x}(t + 1) = \mathbf{x}(t) - (\mathbf{J}(t) \mathbf{J}^T(t) + \lambda \mathbf{I})^{-1} (\mathbf{J}(t) \cdot \mathbf{f}(t))^T$$

$$\mathbf{r}(t + 1) = (\hat{\mathbf{y}} - \mathbf{g}(\mathbf{x}(t + 1)))^T (\hat{\mathbf{y}} - \mathbf{g}(\mathbf{x}(t + 1)))$$

$$\lambda = \lambda/10 \text{ (simple approach of changing per iteration)}$$

If  $r(t + 1) == r(t)$  or  $r(t + 1) < \delta$

if the residual error  $r$  is not decreasing or a minimum of error is achieved

then end the loop

End of Loop

Another solution is to start the iteration with large value for  $\lambda$  (ex. 10-100) and constantly decrease the value per each iteration. Alternative variations of the Levenberg-Marquardt are provided in [117].

### 5.2.5. Performance comparison

As it was discussed in the previous sections, the gradient-descent method is a simple and straightforward method which converges reliably to a minimum point with higher convergence rate at initial steps and with slower rates at final steps. The Newton and Gauss-Newton approaches benefit from the second derivative and squared derivative respectively which improve the convergence in quadratic steps but needed a good initial point. The Levenberg-Marquardt is a hybrid method which benefits from both gradient-descent and Gauss-Newton by dynamically adjusting the state improvement parameter. To evaluate the performances of these optimization methods, an experiment is defined in that a mobile node is localized in a 2D arena equipped with three anchors. Details of this test is the same as the one described in Section 5.2.1. The ToA localization topology is applied with the anchors located at points (0,0), (0,400), (400,0), (400,400) all with centimeter unit. The evaluation criteria are number of required iterations for different initial guesses, convergence test for different mobile node locations, level of accuracy, tolerance of the algorithms against added noise or non-line of sight conditions, computation complexity and computation speed. All of the algorithms in this section are implemented in MATLAB environment in the form of script code and performed on a PC with 8 CPU cores and Windows 7 operating system. The results are provided in the rest of this section.

For the first test, the mobile node is positioned at coordinates of (200,-50). The reason that the mobile node is located outside of the arena is to provide two different directions of optimization to the algorithms. The initial state is selected at the origin (0,0). The iteration process is stopped once an error of less than 0.01cm is achieved. The state matrix has two variables for each axis. The results of convergence for the discussed algorithms are shown in Figure 5.3.

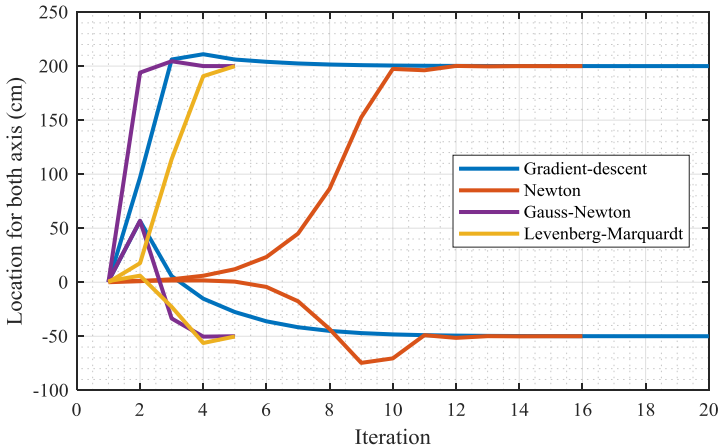


Figure 5.3: Convergence of different optimization algorithms to the position of the mobile node for both  $x$  (located at 200) and  $y$  (located at -50) axis.

As it can be seen from the graph, the gradient-descent method although has a good convergence at the initial phase, has the largest number of iterations with 20 rounds. As it was discussed before this method improves very slowly closer to final state. Unlike the gradient-descent method, the Newton method improves slowly in the beginning but finally converges faster to final state. This algorithm needed 17 iterations to reach to desired level of accuracy. The best algorithm in this test seems to be the Gauss-Newton method which has both rapid advances in initial and final states. This algorithm needed 5 iterations versus 6 iterations for Levenberg-Marquardt (L-M) method. The L-M method has demonstrated similar performances as the Gauss-Newton approach. In this graph, different rates of convergence resulted from different applied techniques in L-M method is obvious. Considering the final residual error, the Gauss-Newton method has nearly zero squared error achieved within a few iterations. In terms of running time, the gradient-descent method has the shortest runtime although it needed 20 rounds of iteration. This is mainly due to simplicity of this algorithm. Summary of the results for this experiment is provided in Table 5.2. Unlike the gradient-descent method, the L-M method has the longest running time as a result of several matrix multiplications in spite of having 7 iterations. These iterative processes are demonstrated for 2D space in Figure 5.4.

## 5 Localization Algorithms

---

Table 5.2: Location estimation with different optimization algorithms for initial point at (0,0) and mobile node position at (200,-50)

Parameter	G-D	Newton	G-N	L-M
Number of iterations	20	17	5	6
Final sum of squared error (m <sup>2</sup> )	0.0352	0.0122	≈ 0	0.0553
Run time (ns)	14.82	32.69	48.27	74.12

As it is visible, the gradient-descent and Gauss-Newton approaches take a zigzag path to reach to the final location whereas the L-M method goes straightly towards the location of the node. The zigzag behavior of Gauss-Newton method is the reason of divergence in some applications as the first move may go too far from the ideal point which may not return towards the target again. Fortunately in localization applications, this situation rarely happens as the model of these systems are quadratic and with only one minimum. In complex applications the L-M method offers better stability in the iteration process with minimum additional iteration required to converge.

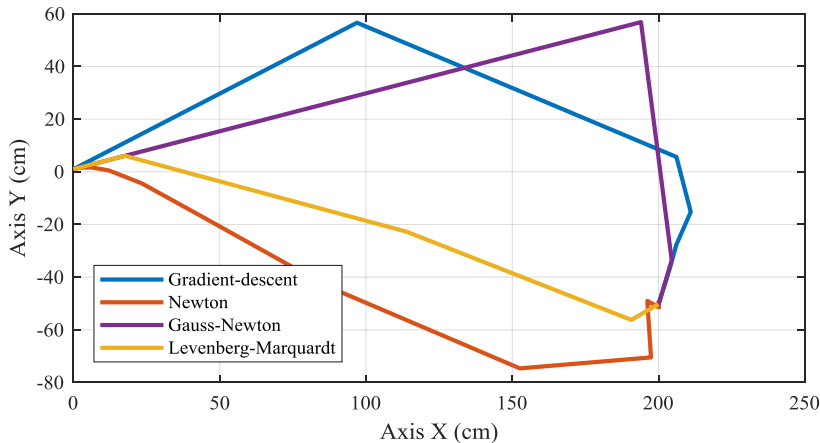


Figure 5.4: Progress of iteration for different optimization approaches in 2D with initial point at the origin of 2D Cartesian coordinates and mobile node at (200, -50)

In order to test the effect of the initial guess on the iteration process, the same experiment is repeated with different initial points.

Table 5.3: Location estimation with different optimization algorithms for initial point (200,500) and mobile node position of (200,-50)

Parameter	G-D	Newton	G-N	L-M
Number of iterations	18	10	7	7
Final sum of squared error (cm)	0.0496	0.0150	≈ 0	0.0565
Run time (ns)	19	22.80	68.04	102.25

The result of one of the experiments with initial point located at (200,500) is shown with the anchor positions and the structure of the nodes in Figure 5.5.

According to this graph, the smoothest path to target belongs to the gradient-descent and L-M methods although the L-M method needed a lower number of iterations. With this initial point, the gradient-descent method had 18 iterations, Newton method 10, Gauss-Newton and L-M both 7 iterations. According to these results, the lowest number of required iterations belongs to the Gauss-Newton and L-M method. However, the running time of the L-M method in this case is 5 times (102 ns) longer than the gradient-descent method. In terms of the final achieved residual error, the Gauss-Newton method still provides the best result with nearly zero residual error. These results are summarized in Table 5.2.

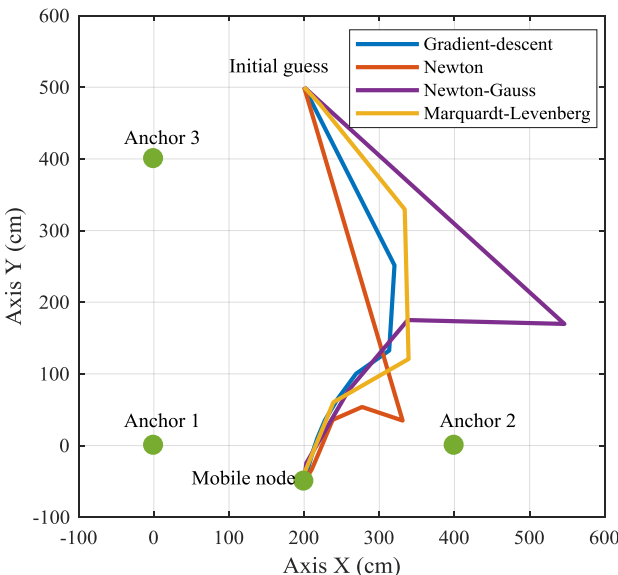


Figure 5.5: Progress of iteration for different optimization approaches in 2D with initial point at (200,500)

The data provided so far for the experiments were ideal data achieved from the models with no noise. This is however not the case in practice. Therefore, the final experiment is performed in order to study the behavior of the algorithms in presence of noise and system model inaccuracies. For this purpose, the data are mixed with the normal distributed white noise. This way, there is no unique answer for the equation set of localization model and therefore the optimization algorithms should continue to improve until the minimum error is achieved. In this case, it is expected that the estimated location is not exactly the point where the mobile node is located rather somewhere in the vicinity of it. Due to additional noise the algorithms needed higher number of iterations to narrow down to the final solution. In this case, 36 iterations were needed for gradient-descent method, 30 for Newton, 16 for L-M and only 14 for Gauss-Newton method which is the

least among the four. This number of iterations slightly increased the overall time of all the algorithms but the relation of maximum time to number of iterations stayed almost the same for all the algorithms in a way that in spite of higher number of iterations compared to other methods, still the gradient-descent method is the fastest. The result of residual error in all the cases is the same ( $541\text{cm}^2$ ) as the minimum possible optimization point is reached by all the algorithms. The results of this experiment are summarized in Table 5.4.

Table 5.4: Location estimation with different optimization algorithms for initial point (150,-40) and mobile node position of (200,-50) in presence of the noise

Parameter	G-D	Newton	G-N	L-M
Number of iterations	36	30	14	16
Final sum of squared error ( $\text{cm}^2$ )	541.4	541.4	541.4	541.4
Run time (ns)	44.4	44.8	115.9	174.8

The result of the test in 2D area in presence of the noise is provided in Figure 5.6. As it was expected, the estimated point differs from the mobile node's location.

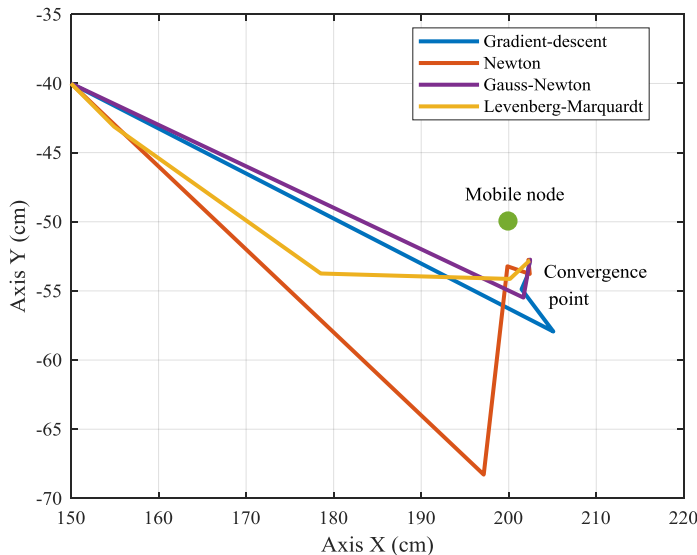


Figure 5.6: Behavior of different optimization approaches in 2D with presence of the noise and initial point at (150,-40)

As a conclusion it can be mentioned that the number of iterations in a method is not necessarily a factor for speed of an algorithm. Other than that, stability of the algorithm in presence of noise and model errors, simplicity of implementation and efficiency of the method should be considered according to the conditions of a certain application.

### 5.3. Dynamic Iterative Techniques

In this section, we introduce and discuss other iterative algorithms which consider the previous states of the node's location up to the previous sample for deciding about the current location of the node. Using this information, one may generate a database holding the probability distribution pattern of the system model as well as statistic characteristics of the measured data. Therefore, these algorithms are probabilistic processes which use the stochastic and dynamic behavior of the localization system for estimating the location of a node. The estimation methods which will be discussed in this section are all members of Bayesian filters family which benefit from all the previous measurements including the current one in order to estimate the PDF of the current state. This means the filters are trying to construct the PDF of  $p(x_k | (y_1, y_2, \dots, y_{k-1}, y_k))$  where  $x_k$  is the current state and  $y_1$  to  $y_{k-1}$  are the previous measurement from time 1 to  $k - 1$  and  $y_k$  is the current measurement of data. The Bayes estimation theory addresses this problem in two steps. At the first phase called prediction, the model of the state is formed using previous observed states and measurements. This is presented as [3, p. 103]:

$$p(x_k | (y_1, \dots, y_{k-1})) = \int p(x_k | x_{k-1}) p(x_{k-1} | (y_1, \dots, y_{k-1})) dx_{k-1} \quad (5.55)$$

The Bayes theorem defines the joint probability of the two random variables  $x, y$  based on the conditional probability of the two variables in the form [106, p. 117]:

$$p(x, y) = p(x|y)p(y) = p(y|x)p(x) \quad (5.56)$$

Using the Bayes theorem, the second phase of the state estimation which is called prediction, can be formed according to the following formula:

$$p(x_k | (y_1, \dots, y_k)) = \frac{p(y_k | x_k) p(x_k | y_1, \dots, y_{k-1})}{p(y_k | y_1, \dots, y_{k-1})} \quad (5.57)$$

The term  $p(y_k | x_k)$  defines the probability of measuring  $y_k$  given that the current state of the system is  $x_k$ . This is called observation model or measurement model which is achieved from the statistics of the measurement noise. The other term in the numerator  $p(x_k | y_1, \dots, y_{k-1})$  defines the probability of witnessing the current state  $x_k$  considering the previous observations. This is prior distribution model of the system. The term  $p(x_k | (y_1, \dots, y_k))$  is posterior estimation model which estimates the current state of the system considering the observation model and prior estimation model of the system. The denominator of the equation  $p(y_k | y_1, \dots, y_{k-1})$  is the normalization constant which is achieved by integrating the product of the two PDF models and is defined as [3, p. 103]:

$$p(y_k | y_1, \dots, y_{k-1}) = \int p(y_k | x_k) p(x_k | (y_1, \dots, y_{k-1})) dy_k \quad (5.58)$$

According to the definition, the integral of the area under PDF function is equal to 1. After calculating the two products namely observation and prior estimate, the value should be normalized again to produce a PDF with integral value of 1. One of the assumptions of the Bayes estimation method is that the distribution of the noise in measurement model and prior state is Gaussian. This is due to the fact that the product of two Gaussian distributions is also a Gaussian distribution. The proof of this fact is provided in Appendix A1. This feature is important as the posterior state is used again in the next iteration as prior state and therefore this assumption stays true throughout the whole estimation process. If this assumption is not true then the optimality of the estimator is not guaranteed and even divergence is expected. Two Gaussian distribution models and the result of their products are visually demonstrated in Figure 5.7.

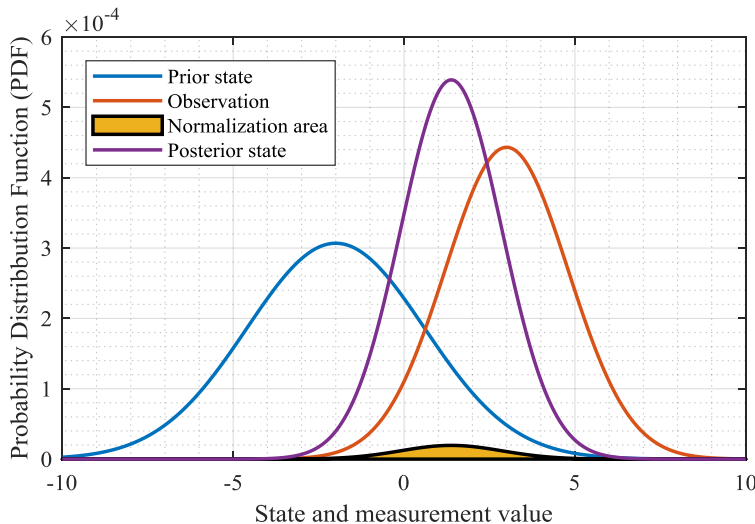


Figure 5.7: Process of Bayesian estimation based on Bayes theorem demonstrating the mean and variance of prior state, observation model and posterior state

The Bayesian estimation algorithms are widely used for localization applications. The discussed algorithms in this thesis are extended Kalman filter, unscented Kalman filter and  $H_\infty$  filter. However, there are many other variations available as example iterated Kalman filter, indirect Kalman filter [118], ensemble Kalman filter [119] and particle filter [120]. Comparison of Kalman filter with heuristic approaches such as neural network is provided in [121]. The particle filter method is based on Monte Carlo estimation theory [122] which has been also widely applied for localization as well as SLAM applications. Example implementations are provided in [122–124]. Details of the theory and implementation of these algorithms are provided in theoretical books written by Brookner [111], Gibbs [106], Frank et al. [125], van Handel [126], Zaknich [127] and Zekavat [128].

### 5.3.1. Extended Kalman Filter

The extended Kalman filter (EKF) is a very common variation of Bayesian filter which is developed by modification of Kalman filter so that it can be applied to nonlinear system models. Same as the Kalman filter, it is assumed that the noise has zero mean Gaussian distribution and the measurement and process noise are independent. It is a very simple though powerful estimator capable of predicting the future states of the system based on the system model, knowledge of the noise and last measurements. This filter benefits from the state space format for presenting the value of states and the process noise. The filter process includes two development stages namely prediction and update. In the prediction phase previous estimates of the states are propagated to the next sample time through the system model. According to definition of the extended Kalman filter, this can be described as:

$$\dot{\mathbf{x}} = \mathbf{f}(\mathbf{x}, u, t) + \mathbf{w}(t) \quad (5.59)$$

$$\mathbf{y} = \mathbf{h}(\mathbf{x}, t) + \mathbf{v}(t) \quad (5.60)$$

where the function  $f$  is a nonlinear model of the system and a function of states ( $\mathbf{x}$ ), time ( $t$ ) and system input ( $u$ ). The function  $h$  is the nonlinear observation model which relates the states to the output of the system  $y$ . The  $\mathbf{w}(t)$  is the process noise and  $\mathbf{v}(t)$  is the measurement noise. Both of these noise parameters are independent random variables (zero cross-correlation) with zero mean and Gaussian distribution with covariances of  $\mathbf{Q}$  and  $\mathbf{R}$  for the process noise and measurement noise respectively. This is described as follows [108, p. 144]:

$$\mathbf{E}[w_n w_m^T] = \begin{cases} \mathbf{Q} & , n = m \\ \mathbf{0} & , n \neq m \end{cases}, \mathbf{E}[v_n v_m^T] = \begin{cases} \mathbf{R} & , n = m \\ \mathbf{0} & , n \neq m \end{cases}, \mathbf{E}[wv^T] = \mathbf{0} \quad (5.61)$$

The functions  $h$  and  $f$  are defined in nonlinear form in Eq. 5.60, but they are not necessarily nonlinear. In localization applications, usually the dynamic model of the system is linear but the observation model is nonlinear. The EKF linearizes this model using the truncated Taylor series around the current estimate point. In this method, only the first derivative of the Taylor series is considered to derive a linear relation between the state and measurements. This approximation is performed using Jacobian of the nonlinear function around the estimation point. The Taylor series and Jacobian matrix can be represented as [6, p. 365]:

$$\mathbf{h}(\mathbf{x}) \cong \mathbf{h}(\mathbf{x}_t) + \frac{\partial \mathbf{h}(\mathbf{x})}{\partial \mathbf{x}} \Big|_{x_t} (\mathbf{x} - \mathbf{x}_t) \text{ where } \frac{\partial \mathbf{h}(\mathbf{x})}{\partial \mathbf{x}} = \begin{bmatrix} \frac{\partial h_1}{\partial x_1} & \dots & \frac{\partial h_1}{\partial x_n} \\ \vdots & \ddots & \vdots \\ \frac{\partial h_n}{\partial x_1} & \dots & \frac{\partial h_n}{\partial x_n} \end{bmatrix} \quad (5.62)$$

Along with the projection of the estimates, the error estimate of the system should be propagated to the next step. The error estimate  $\mathbf{P}$  is the covariance of the state estimated at the current iteration. This propagation is performed according to:

$$\mathbf{P}_{k+1}^- = \mathbf{A}\mathbf{P}_k\mathbf{A}^T + \mathbf{Q} \quad (5.63)$$

where  $\mathbf{A}$  is the fundamental matrix of states. The noise covariance  $\mathbf{Q}$  is added to estimate error at each iteration to avoid  $\mathbf{P}_k$  converging to zero otherwise the filter permanently converges to final estimate. Once this happens the filter is not following the changes of the measurements anymore. After the error estimate is propagated, the Kalman gain can be calculated as:

$$\mathbf{K}_k = \mathbf{P}_{k+1}^-\mathbf{H}_k^T(\mathbf{H}_k\mathbf{P}_{k+1}^-\mathbf{H}_k^T + \mathbf{R})^{-1} \quad (5.64)$$

where  $\mathbf{H}_t$  is the Jacobian approximation of function  $\mathbf{h}(\mathbf{x})$  at time  $t$  and  $\mathbf{K}_t$  is the Kalman gain at time stamp  $t$ . The covariance of measurement  $\mathbf{R}$  is added to gain in denominator to determine how much weight should be dedicated to the error estimate and how much weight to the measurements. The maximum value of gain is 1 which means the measurement is very accurate and has covariance of zero. In this case any changes in the measurement influence the states directly. If the  $\mathbf{R}$  parameter is too large compared to  $\mathbf{P}$ , then the gain will be close to zero which means more value is dedicated to the current state. This process, is applied in the update phase of the filter which has following equation:

$$\mathbf{x}_{k+1}^+ = \mathbf{x}_{k+1}^- + \mathbf{K}_k(\mathbf{y} - \mathbf{h}(\mathbf{x})) \quad (5.65)$$

In this equation, the  $\mathbf{x}_k^-$  is the *a priori* estimate of the system resulted from the propagation of the previous state into system model as described in Eq. 5.59 and  $\mathbf{x}_k^+$  is the *a posteriori* estimate of the state after applying the correction. It should be noticed that the  $\mathbf{h}(\mathbf{x})$  in this equation is the original nonlinear equation of the model and should not be linearized. The difference of the measured data  $\mathbf{y}$  and the output of the observation model  $\mathbf{h}(\mathbf{x})$  represents the error of the estimated state which will be added to or subtracted from the last estimate after applying the Kalman gain. From Eq. 5.65, it can be noticed that for gain value of one, all the error will be applied to the propagated state whereas for value of zero no change to the previous state will occur and therefore the error of the estimate will be ignored.

Likewise, the error estimate  $\mathbf{P}$  should be updated to the next iteration using the Kalman gain as follows:

$$\mathbf{P}_{k+1}^+ = (\mathbf{I} - \mathbf{K}_k \mathbf{H}_k) \mathbf{P}_{k+1}^- \quad (5.66)$$

In this equation,  $\mathbf{I}$  is the identity matrix,  $\mathbf{P}_k^-$  is the prior estimation of the error covariance resulted from Eq. 5.63 and  $\mathbf{P}_k^+$  is the posterior of the same parameter after correction is performed.

The process of the EKF algorithm is provided in Fig. 5.8 graphically.

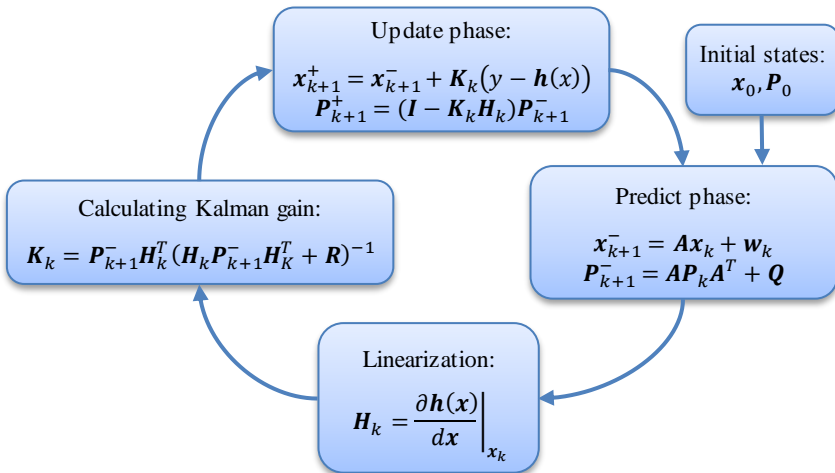


Figure 5.8: The iterative process of EKF algorithm with prediction and update phases

The EKF method has many advantages such as estimation of the measurement accuracy during the run time, flexibility of handling non-periodic data sampling rates and missing data by changing the covariance parameter of the measurement, optimal use of *a priori* information and providing additional side products such as velocity and acceleration of the nodes in context of localization applications. It is however, a suboptimal solution for highly nonlinear systems due to the fact that higher order terms of the Taylor series are ignored. Therefore, for complex nonlinear systems, other approaches such as unscented Kalman filter or particle filter are recommended. This non-linearity is most of the time the reason of divergence in the filter as the defined model is not always matching to the behavior of the system. In addition to that, problems such as round off errors, singularity of the matrices and observability of the states are issues which need to be considered at the design time to avoid divergence. A few solutions for divergence problem are application of high precision arithmetic, excluding deterministic processes from the models and symmetrizing the covariance matrix at each iteration as follows [108, p. 181]:

$$P_k = \frac{P_k \cdot P_k^T}{2} \quad (5.67)$$

Other remedies of divergence problem such as memory fading, square root filtering, noise covariance updating, monitoring of error estimate, etc. are stated in the books written by Simon [129, p. 140], Brown et al. [108, p. 259], Groves [1, p. 76], Grewal, et al. [130, p. 204] and Lewis [125, p. 226]. Examples of the applications of the EKF in localization systems can be found in the works of Hartman et al. [131], Maceraudi et al. [132], Ledergerber et al. [43], Tiemann et al. [85], Sharif and Zhu [133] and in the thesis of Negenborn [134].

### 5.3.2. Unscented Kalman Filter

This method is another variation of the Bayes filter applicable on nonlinear state estimation proposed initially by Julier in 1995 [106, p. 475]. This technique determines the nonlinear characteristics of the model by propagating a series of deterministically selected samples called sigma points through the state model of the system. The sigma points are distributed around the current state with known covariances and propagated through the nonlinear system transfer function. This helps the filter to estimate the mean and covariance of the random variable by evaluating the transformed sigma points. This way no derivation and Jacobian matrix is required which is one drawback of EKF method as it is not always possible to calculate the Jacobian analytically [135, p. 136]. In this technique, the first and second moments of the model are maintained which results in more accuracy and robustness of the estimator [136, p. 198].

The first step of this algorithm is to determine the sigma points. The number of required sigma points depends on the dimension of the states and is calculated as:

$$x \in \mathbf{R}^n \Rightarrow \sigma = 2n + 1 \quad (5.68)$$

where  $x$  is the states vector,  $\sigma$  is the number of required sigma points and  $n$  is the degree of the dimension. As an example, for 2D localization we need 5 and for 3D we need 7 sigma points. Since this method determines the distribution of states through the transfer model statistically, each sigma point is defined with a mean and a weight parameter. The mean parameters are determined as defined below [136, p. 200]:

$$x_i = \begin{cases} \mu & \text{for } i = 0 \\ \mu + (\sqrt{(n + \lambda)\Sigma})_i & \text{for } i = 1, \dots, n \\ \mu - (\sqrt{(n + \lambda)\Sigma})_{i-n} & \text{for } i = n + 1, \dots, 2n \end{cases} \quad (5.69)$$

where  $n$  is the dimension of the states,  $\Sigma$  is the covariance of the process noise and  $\lambda$  is the scaling parameter. One issue here is the square root of the covariance which is standard deviation is required. This will be a matrix if the dimension of the state is larger than 2. However, we need a scalar variable for determining the position of each sigma point. One solution to determine the standard deviation in matrix form is Cholesky method which defines the covariance as:

$$\Sigma = \mathbf{q}\mathbf{q}^T$$

$$\begin{bmatrix} \Sigma_{11} & \cdots & \Sigma_{1n} \\ \vdots & \ddots & \vdots \\ \Sigma_{n1} & \cdots & \Sigma_{nn} \end{bmatrix} = \begin{bmatrix} q_{11} & \cdots & 0 \\ \vdots & \ddots & \vdots \\ q_{n1} & \cdots & q_{nn} \end{bmatrix} \begin{bmatrix} q_{11} & \cdots & q_{1n} \\ \vdots & \ddots & \vdots \\ 0 & \cdots & q_{nn} \end{bmatrix} \quad (5.70)$$

Therefore, the Cholesky method decomposes the matrices into two triangular matrices in transpose form. By multiplying the elements of the matrices and

solving the equations one row after another we can find all the unknown variables as follows:

$$\begin{aligned}\Sigma_{11} &= q_{11} \cdot q_{11} \Rightarrow q_{11} = \sqrt{\Sigma_{11}} \\ \Sigma_{1n} &= q_{11} \cdot q_{1n} \Rightarrow q_{1n} = q_{n1} = \frac{\Sigma_{1n}}{\sqrt{\Sigma_{11}}} \\ \Sigma_{nn} &= q_{n1} \cdot q_{1n} + \dots + q_{nn} \cdot q_{nn} \Rightarrow q_{nn} = \sqrt{\left( \Sigma_{nn} - \left( \frac{\Sigma_{1n}}{\sqrt{\Sigma_{11}}} \right)^2 - \dots \right)}\end{aligned}\quad (5.71)$$

The standard deviation parameter in Cholesky method is still a matrix. However, the position of each sigma point should have a scalar mean. To solve this issue, in Eq. 5.69 an index  $i$  is introduced which represents the number of corresponding column in the standard deviation matrix. This way for each sigma point one scalar value is extracted. After the mean of the sigma points are determined, the weights of each point should be calculated. In general, two sets of weights are defined one for calculating the mean  $\omega_m$  and the other one for estimating the covariance  $\omega_c$ . The process of calculating is described as follows [108, p. 265]:

$$w_{m_i} = \begin{cases} \frac{\lambda}{n + \lambda} & \text{for } i = 0 \\ \frac{1}{2(n + \lambda)} & \text{for } i = 1, \dots, 2n \end{cases} \quad (5.72)$$

$$w_{c_i} = \begin{cases} w_{m_0} + (1 - \alpha^2 + \beta) & \text{for } i = 0 \\ \frac{1}{2(n + \lambda)} & \text{for } i = 1, \dots, 2n \end{cases} \quad (5.73)$$

$$\lambda = \alpha^2(n + k) - n \quad (5.74)$$

The parameter  $\alpha$  determines the spread of the sigma points around the mean point, the parameter  $\beta$  is determined based on the knowledge of distribution, (optimal value of  $\beta$  for Gaussian distribution is 2) and  $k$  is the scaling factor which is usually a positive number and equal to  $3n$ . The influence of these parameters on the position of the sigma points are provided in Appendix A2. One important characteristic of the weight is normalization constraint which states the sum of all weights should be 1. Each weight however can be positive, negative, smaller or larger than 1. This can be defined as:

$$\sum_{i=0}^{2n} \omega_{m_i} = 1 , \quad \sum_{i=0}^{2n} \omega_{c_i} = 1 \quad (5.75)$$

The first sigma point is always in the center of the ellipse which embraces the distribution area of the covariance. The other sigma points are positioned on the perimeter of the ellipse to mark the extent of the distribution in each direction. The goal is to model the characteristics of the original distribution using these

points so that after propagating through the nonlinear process, the statistics of the distribution can be determined by analyzing the changes happened to these sigma points [136, p. 200]. This process is shown graphically in Figure 5.9.

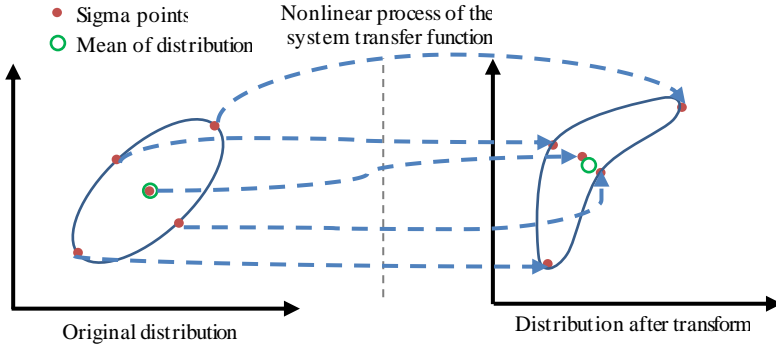


Figure 5.9: Propagation of sigma points in 2D Gaussian distribution through nonlinear process and determination of the new mean and covariance after transform

The process of the unscented Kalman filter (UKF) continuous to the next step with propagation of the sigma points through the system model and observation model. This is defined as:

$$\boldsymbol{x}_k = (\mu_k, \mu_k + \gamma q, \mu_k - \gamma q, \dots) \quad (5.76)$$

$$\boldsymbol{x}_{k+1}^- = \mathbf{f}(u, \boldsymbol{x}_k) \quad (5.77)$$

$$\boldsymbol{y}_{k+1}^- = \mathbf{g}(\boldsymbol{x}_{k+1}^-) \quad (5.78)$$

where  $\boldsymbol{x}_k$  is the current set of sigma points,  $\gamma$  is equal to  $\sqrt{n + \lambda}$  and  $q$  is the standard deviation of the process noise,  $u$  is the input of the system which in localization applications is considered as zero and  $f$  is the dynamic system model. After the propagation,  $\boldsymbol{x}_{k+1}^-$  is *a priori* estimate which is transferred through nonlinear observation model  $g$ . After the weights and locations of sigma points are determined, the statistics of the distribution function which are mean and covariance should be extracted from the sigma points. This is done by calculating the overall mean of the sigma points and covariance of the sigma points using the following equations:

$$\boldsymbol{\mu}_x = \sum_{i=0}^{2n} \omega_{m_i} \boldsymbol{x}_i \quad (5.79)$$

$$\boldsymbol{\Sigma}_{xx} = \sum_{i=0}^{2n} (\omega_{c_i} (\boldsymbol{x}_i - \boldsymbol{\mu}_x)(\boldsymbol{x}_i - \boldsymbol{\mu}_x)^T) + \mathbf{Q} \quad (5.80)$$

The same procedure is performed in order to transfer the sigma points through the observation model. This results in:

$$\boldsymbol{\mu}_y = \sum_{i=0}^{2n} \omega_{m_i} \mathbf{y}_i \quad (5.81)$$

$$\boldsymbol{\Sigma}_{yy} = \sum_{i=0}^{2n} \left( \omega_{c_i} (\mathbf{y}_i - \boldsymbol{\mu}_y) (\mathbf{y}_i - \boldsymbol{\mu}_y)^T \right) + \mathbf{R} \quad (5.82)$$

Likewise the cross-covariance can be calculated according to:

$$\boldsymbol{\Sigma}_{xy} = \sum_{i=0}^{2n} \left( \omega_{c_i} (\mathbf{x}_i - \boldsymbol{\mu}_x) (\mathbf{y}_i - \boldsymbol{\mu}_y)^T \right) \quad (5.83)$$

This means at this stage we have an estimate for system states  $\boldsymbol{\mu}_x$ , an estimate for *a priori* of the observation model  $\boldsymbol{\mu}_y$  and *a priori* estimate of the process error  $\boldsymbol{\Sigma}_{xx}$  and measurement error  $\boldsymbol{\Sigma}_{yy}$  as well as estimate of cross-covariance of the two error models  $\boldsymbol{\Sigma}_{xy}$ . This knowledge is enough to derive the Kalman gain according to the following relation:

$$\mathbf{K} = \boldsymbol{\Sigma}_{xy} \boldsymbol{\Sigma}_{yy}^{-1} \quad (5.84)$$

The rest of the process is very similar to the update phase of EKF in that the state estimate as well as the error estimate are updated based on the measurement error observed. These processes can be represented mathematically as:

$$\boldsymbol{\mu}_x^+ = \boldsymbol{\mu}_x^- + \mathbf{K}_k (\mathbf{y} - \boldsymbol{\mu}_y) \quad (5.85)$$

$$\boldsymbol{\Sigma}_{xx}^+ = \boldsymbol{\Sigma}_{xx}^- - \mathbf{K}_k \boldsymbol{\Sigma}_{yy}^- \mathbf{K}_k^T \quad (5.86)$$

The process of sigma point selection and their applied parameters which are described here are not the only way to describe the statistics of the distribution. Other variations of the UKF filter are described for example in the book of Simon [129, p. 446] or Gibbs [106, p. 475]. Julier has presented the scaling version of sigma point selection in his paper in [137] which according to his results provide better accuracies in describing the statistics of the distribution without additional calculation burden and slowing down the estimation process. Simon believes that the UKF filter greatly improves the accuracies of the estimate compared to EKF method in nonlinear conditions [129, p. 457]. Further practical comparisons of EKF and UKF in localization application are provided in the work of Pelka et al. [138], Konatowski et al. [139], Yang et al. [140] and Umamageswari et al. [141]. Features such as no need of Jacobian matrix or analytical form of defining distribution as well as requiring only a few sample points compared to algorithms such as ensemble Kalman filter (EnKF) or particle filter makes this approach an attractive option for many applications.

### 5.3.3. H-infinity Filter

The main requirements of the EKF and UKF filters are the distribution of the noise should be Gaussian with zero mean and the characteristics of the noise should be known. If these two conditions are not met, the filter may diverge or turn into a suboptimal estimator. In the reality however, it is not always possible to extract the statistics of the noise. As well as that, it is not guaranteed that these characteristics stay unchanged. One solution to this problem is H-infinity ( $H_\infty$ ) filter which does not take any assumption about the distribution and mean of the noise. Also no initial knowledge about the characteristics of the noise is required [142]. The structure of the Kalman filter is based on the variance or mean of the power of the estimation error whereas the  $H_\infty$  filter is designed based on deterministic noises with the goal of bounding the energy of the noises to a certain limit. Therefore, the  $H_\infty$  filter is specifically designed for robustness and tolerance of noise model inaccuracies [143]. The general equations of the  $H_\infty$  filter are defined for linear systems but the same extension as EKF can be applied to derive the extended  $H_\infty$  filter or according to unscented transform to derive unscented  $H_\infty$  filter which are suitable for nonlinear systems. There are many variations of the  $H_\infty$  filter defined which are slightly different in definitions. The implemented filter used in the projects of this thesis is based on the definition given by Dan Simon [129, p. 343].

Consider a nonlinear system represented in the state space format as:

$$\begin{aligned} \dot{\mathbf{x}}_{k+1} &= \mathbf{A}\mathbf{x}_k + \mathbf{w}_k \\ \mathbf{y}_{k+1} &= \mathbf{h}(\mathbf{x}_{k+1}) + \mathbf{v}_k \\ \mathbf{z}_k &= \mathbf{L}_k \mathbf{x}_{k+1}^- \end{aligned} \tag{5.87}$$

Unlike the definition given for  $\mathbf{w}_k$  and  $\mathbf{v}_k$  before, these noises may be non-zero and non-Gaussian distributed. The  $H_\infty$  filter defines a new parameter  $\mathbf{z}_k$  which is a linear function of states. The new matrix  $\mathbf{L}_k$  is a user defined matrix which relates the states to the new defined parameter  $\mathbf{z}_k$ . If we find an estimate for states this can be presented as  $\hat{\mathbf{x}}_k$  which results in  $\hat{\mathbf{z}}_k$ . The error of the estimate is defined as  $\tilde{\mathbf{x}}_k = \mathbf{x}_k - \hat{\mathbf{x}}_k$  and likewise we have  $\tilde{\mathbf{z}}_k = \mathbf{z}_k - \hat{\mathbf{z}}_k$ . The  $H_\infty$  filter is trying to minimize the error by choosing the best value for state  $\hat{\mathbf{x}}_k$ . The process of minimization is according to the game theory in that the nature tries to maximize the error by choosing the worst case condition for the initial state  $\mathbf{x}_0$ , process noise  $\mathbf{w}_k$  and measurement noise  $\mathbf{v}_k$  and on the other side the filter is trying to minimize the error by opting for the best value of the state  $\hat{\mathbf{x}}_k$ . This process can be described mathematically by defining the cost function  $J$  as [106, p. 471]:

$$J = \frac{\sum_{k=0}^{N-1} (\tilde{\mathbf{z}}_k \mathbf{S}_k \tilde{\mathbf{z}}_k^T)}{\tilde{\mathbf{x}}_0 \mathbf{P}_0^{-1} \tilde{\mathbf{x}}_0^T + \sum_{k=0}^{N-1} (\mathbf{w}_k \mathbf{Q}_k^{-1} \mathbf{w}_k^T + \mathbf{v}_k \mathbf{R}_k^{-1} \mathbf{v}_k^T)} \tag{5.88}$$

where parameters  $\mathbf{S}_k$ ,  $\mathbf{Q}_k$ ,  $\mathbf{R}_k$  and  $\mathbf{P}_0$  are symmetric, positive definite weighting matrices determined experimentally based on the application,  $\tilde{\mathbf{x}}_0$  is the initial error of the state estimate and  $N$  is the number of current iteration. The difference of this cost function compared to the criteria used in Kalman filter is that, this cost function considers the sum of all measurements from beginning up to the previous sample but KF considers only the expected value of current estimate. In other words, the effect of the deterministic matrices in  $H_\infty$  filter are calculated at horizon which is why this filter is called  $H_\infty$  [106, p. 472]. Since it is difficult to find an optimum value for  $J$ , we define a bound for the cost function as:

$$\min_{\tilde{\mathbf{z}}} \max_{w, v, \tilde{\mathbf{x}}_0} J < \left(\frac{1}{\gamma}\right) \quad (5.89)$$

where  $\gamma$  is a threshold defined by us to bound the cost function which is normally a small value close to zero. This is a constraint optimization problem which can be solved using Lagrangian functions [144]. Details of the calculation process is provided in [129, p. 343]. The solution of this problem results in the following Riccati inequality which must be true at each iteration:

$$\mathbf{P}_k^{-1} - \gamma \mathbf{\bar{S}}_k + \mathbf{H}_k^T \mathbf{R}_k^{-1} \mathbf{H}_k > 0 \quad (5.90)$$

In this equation,  $\mathbf{\bar{S}}_k = \mathbf{L}_k^T \mathbf{S}_k \mathbf{L}_k$  in that the  $\mathbf{L}_k$  and  $\mathbf{S}_k$  parameters are user-defined matrices and matrix  $\mathbf{H}_k$  is Jacobian of the nonlinear function  $h$  linearized at the operating point  $k$  as defined in Eq. 5.87. This condition should be checked at each iteration and if the condition is not true, smaller values of  $\gamma$  should be selected. Care must be taken as too small values of the  $\gamma$  results in divergence of the filter. Therefore, a suitable value of  $\gamma$  is a tradeoff between the mean squared error of the noise and maximum gain of the error which should be selected based on the practical results [145].

The gain of the  $H_\infty$  filter is calculated according to the following formula:

$$\mathbf{K}_k = \mathbf{P}_k \left( \mathbf{I} - \gamma \mathbf{\bar{S}}_k \mathbf{P}_k + \mathbf{H}_k^T \mathbf{R}_k^{-1} \mathbf{H}_k \mathbf{P}_k \right)^{-1} \mathbf{H}_k^T \mathbf{R}_k^{-1} \quad (5.91)$$

Once the gain of the filter is evaluated, the update phase of the filter can be performed in order to estimate the *a posteriori* of the states' estimate and the error estimate  $P_{k+1}$ . This can be performed as follows:

$$\hat{\mathbf{x}}_{k+1} = \mathbf{A}_k \hat{\mathbf{x}}_k + \mathbf{A}_k \mathbf{K}_k (\mathbf{y}_k - \mathbf{h}(\hat{\mathbf{x}}_k)) \quad (5.92)$$

$$\mathbf{P}_{k+1} = \mathbf{A}_k \mathbf{P}_k \left( \mathbf{I} - \gamma \mathbf{\bar{S}}_k \mathbf{P}_k + \mathbf{H}_k^T \mathbf{R}_k^{-1} \mathbf{H}_k \mathbf{P}_k \right)^{-1} \mathbf{A}_k^T + \mathbf{Q}_k \quad (5.93)$$

As it can be seen from the last equations, for  $\gamma = 0$  the  $H_\infty$  filter turns into EKF [106, p. 474]. The  $H_\infty$  filter is however computationally more expensive than EKF. In addition to that, the EKF outperforms the  $H_\infty$  in normal conditions when the noise characteristics are ideal. Another disadvantage of the  $H_\infty$  filter is in difficulties of parameter tuning. There are many matrices such as  $\mathbf{S}_k$ ,  $\mathbf{Q}_k$ ,  $\mathbf{R}_k$ ,  $\mathbf{P}_0$

and  $\gamma$  which should be selected based on the scenario and user experiences [129, p. 344]. Therefore, the application of  $H_\infty$  filter is only sensible when either the conditions of the system such as unknown characteristics of the noise or model inaccuracies (e.g. non-line of sight condition in localization) are expected. Summary of the  $H_\infty$  filter process is graphically demonstrated in Figure 5.10.

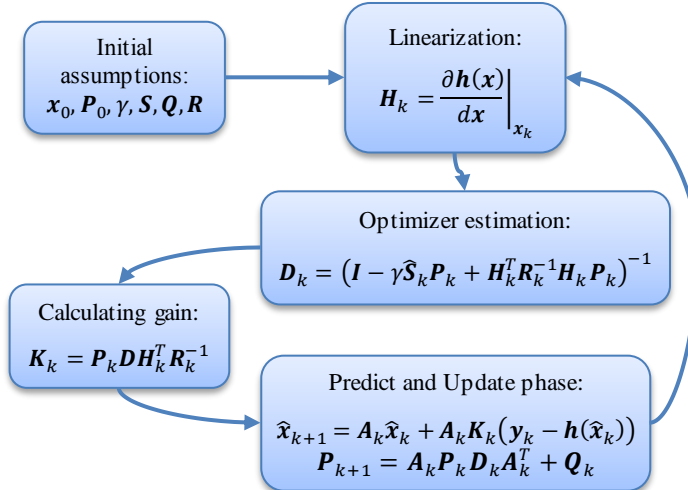


Figure 5.10: Workflow of the  $H_\infty$  filter algorithm

As it can be seen from the algorithm, the  $H_\infty$  process includes the Jacobian which means only the first moment of the nonlinear system is extracted. More accurate estimation of the nonlinear systems can be achieved using approaches such as unscented  $H_\infty$  filter, second order extended Kalman filter (SOEKF), Gauss-Hermite Kalman filter (GHKF), cubature Kalman filter (CKF), central difference Kalman filter (CDKF), etc. as discussed in [146, 147]. Examples of the work based on  $H_\infty$  filter are provided in the paper of Batista et al. [148] and Poveda et al. [146] with comparison between KF filter. Use of  $H_\infty$  for detection of NLOS condition is proposed in [149] with combination of EKF and maximum likelihood method. Application of  $H_\infty$  in GPS/INS navigation systems is provided by Jiang et al. in [150]. In their paper, they have proposed an adaptive version of EKF and  $H_\infty$  as (AKF) and (AHF) which are able to manage the effect of measurement outliers on the filter. They have compared their results with normal version of the filters with the conclusion that the adaptive version of  $H_\infty$  filter can improve the robustness against the outliers better than other approaches. A modified  $H_\infty$  filter is proposed by Kiriakidis et al. [151] which guarantees the stability of the filter locally. P. Rawicz [152] compares in his PhD thesis the three filters  $H_\infty$ ,  $H_2$  and KF together with the focus on the target tracking applications. Application of  $H_\infty$  in robot localization and tracking is addressed in the papers listed in [153–156]. Zhang et al. [157] has applied a mixed  $H_\infty/H_2$  filter on nonlinear stochastic systems with examples from real experiments.

### 5.3.4. Performance comparison

In the previous sections, three different types of nonlinear system estimator namely EKF, UKF and extended  $H_\infty$  were introduced. It was mentioned that the EKF is a suboptimal estimator in nonlinear cases as it uses only the first moment of the Taylor series whereas UKF estimates the nonlinearities of the system up to the second moment of the series and therefore is more accurate. Both of the systems however are sensitive to noise model and model inaccuracies. The assumption of the noise for both EKF and UKF filters is zero mean Gaussian distribution. As well as that, the covariance of the noise should be known. On the other side, the  $H_\infty$  filter releases these assumptions and deterministically defines weighting matrices which minimize the cost function in the worst case noise scenario. The summary of the features and characteristics of the three filters are provided in Table 5.5.

Table 5.5: Feature comparison of nonlinear iterative filters from Kalman family

Parameter	EKF	UKF	Extended $H_\infty$
Assumption about the noise	Zero mean Gaussian	Zero mean Gaussian	No assumption
Knowledge of noise	Covariance	Covariance	Not needed
Linearization technique	Deterministic (Jacobian)	Statistic (Sigma points)	Deterministic (Jacobian)
Order of linearization	1	2	1
Tolerance of model inaccuracies	Unstable	Unstable	Robust
Divergence issue	Probable	Probable	Rarely
Complexity of implementation	Low	High	Medium

In order to evaluate the performance of the introduced filters, several experiments are defined and the efficacies of the filters are assessed in similar conditions. In the first experiment, a small arena with the dimensions of  $60 \times 42\text{cm}^2$  is selected with four anchors mounted at each corner of the area. One mobile node is utilized for applying different localization algorithms. This node has been placed at five different locations. At each location, the node stayed stationary for roughly 30 seconds and then moved to the next point while the samples are still recorded. The points are selected in a way that one point is in the center of the arena and the other 5 points are in the vicinity of each anchors. This is a useful technique for evaluating the localization system as well as calibrating the ranging data. The node at the center has differential distance of zero with respect to all anchor pairs. This point can be used as a reference to adjust the biases of the ranging data to compensate for antenna delays and other probable delays appearing in ranging

data. The plan of the arena including the outcomes of the localization algorithms are demonstrated in Figure 5.11. According to this diagram, it is expected that the measurement of point 3 (middle point) is accurately matched to coordinates of (30,22.5). If this is not the case, an offset may be added to the ranging data in order to calibrate the system.

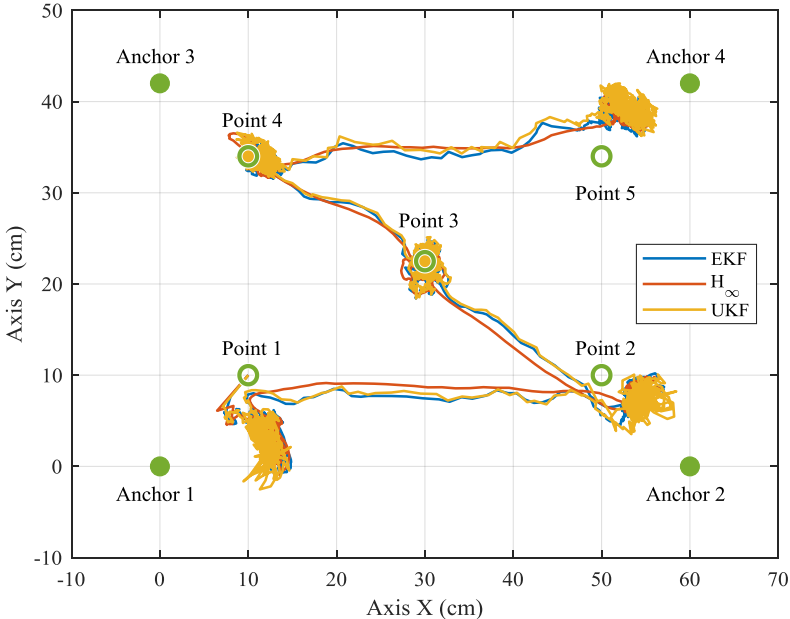


Figure 5.11: Small localization setup with 4 anchors and 5 points measurement technique with results of three different localization algorithm

In this setup, it can be noticed that the results of measurements on points other than the center are not exactly matching to the expected point and a deviation of up to 5 cm is visible. This is happening for two main reasons. The first one is Fresnel zone [158] which defines a certain radius around antenna which should be free area otherwise the signal may get distorted. In case of this experiment, the mobile node is located in the distance of nearly 10 cm to the anchors and therefore the mobile node experiences signal distortion. The second reason is correlation of the range data to signal strength reported by the hardware module manufacturer as well as un-accumulated preamble sequence which usually happens in short distances [79]. This relation affects the distance measurements in short distances where the signal strength is strong and decreases nonlinearly as the distance of the two nodes increases. Empirical compensation methods are proposed by manufacturer [159] but according to our witnesses, this problem occurs only within distances of 10-15 cm in our setup as the antenna gains are less than assumption defined in data sheet. In order to evaluate the performances of the localization algorithms, the distance error of each method compared to reference in each iteration is calculated and demonstrated in Figure 5.12. According to this

graph, all the three algorithms perform similarly with only minor differences. As it was also visible in Figure 5.11 the  $H_\infty$  performs slightly better in filtering the measurement noises as the transition lines between the measurement points are linear with minimum deviations. According to Figure 5.12, it can be seen that the maximum of the error is 17 cm which happens only in one overshoot and majority of the measurement errors were below 5cm.

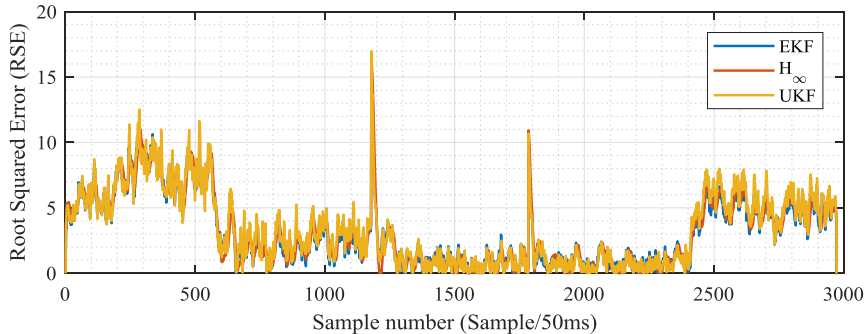


Figure 5.12: Measured error of three localization algorithms (EKF, UKF and  $H_\infty$ ) at each iteration collected in the small scale experiment

To develop a metric for the amount of error, the cumulative distribution function (CDF) of the error is calculated and illustrated in Figure 5.13. According to this graph, 80% of the measurements are within the accuracy level of 5 cm and the maximum of the error is 17 cm. As another metric, circular error probability (CEP) [2, p. 106] can be named which defines a radius around the node in that 50% of the measurements are below the maximum level of error. In case of this experiment the CEP is equal to 2cm in average. Referring to this graph, the error of UKF method is less at short distances of 1 cm but for large distances EKF and  $H_\infty$  seem to be more accurate with almost identical localization errors.

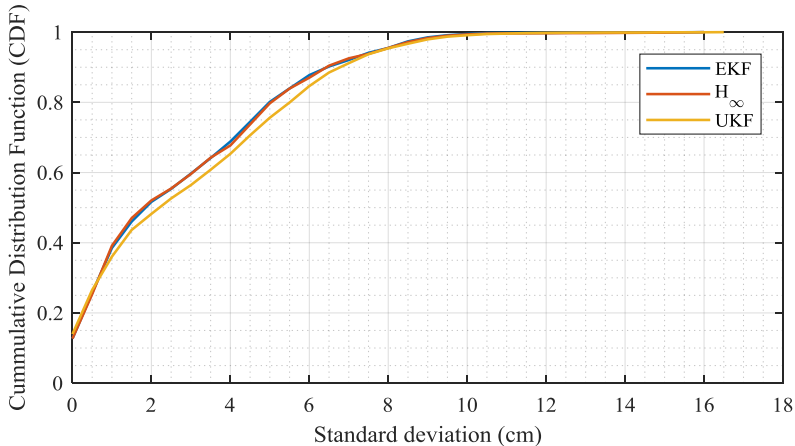


Figure 5.13: Cumulative distribution function of the error observed in small-scale setup

## 5 Localization Algorithms

---

As another metric for measuring the error, the root mean squared error (RMSE) is used. The results are the root mean error of 4.11 cm for EKF method, 4.36 cm for UKF method and 4.15 cm for  $H_\infty$ . The run time of each algorithm is calculated using MATLAB platform running scripts on a PC with 8 CPU cores, clock speed of 2.7 GHz and Windows 7 operating system. The results are presented in Table 5.6. The UKF algorithm is more than 3 times slower than the EKF and less than 2 times slower than  $H_\infty$  approach.

Table 5.6: Error analysis and performance results of different localization algorithms

Parameter	EKF	UKF	Extended $H_\infty$
Run time in each iteration	19.38 $\mu$ s	65.76 $\mu$ s	34.91 $\mu$ s
RMSE	4.1192 cm	4.3662 cm	4.1592 cm
CEP	1.8 cm	2.2 cm	1.8 cm
Maximum error	16 cm	16.5 cm	16 cm

In another experiment, the localization performance of the aforementioned filters are evaluated in a larger scale arena with dimensions of 240 cm  $\times$  120 cm. Same as previous setup, 4 anchors are deployed at each corner of the arena but this time 9 measurement points are selected for mobile node as it is depicted in Figure 5.14. The measurement point number 5 is used for calibration as in this points the differential ranges of anchor pairs are all zero so that the offset of the delays can be recognized and compensated easily. During the time that the mobile node was recording the location data, it is moved to the next point so that the accuracies can be evaluated at dynamic moments of the node as well.

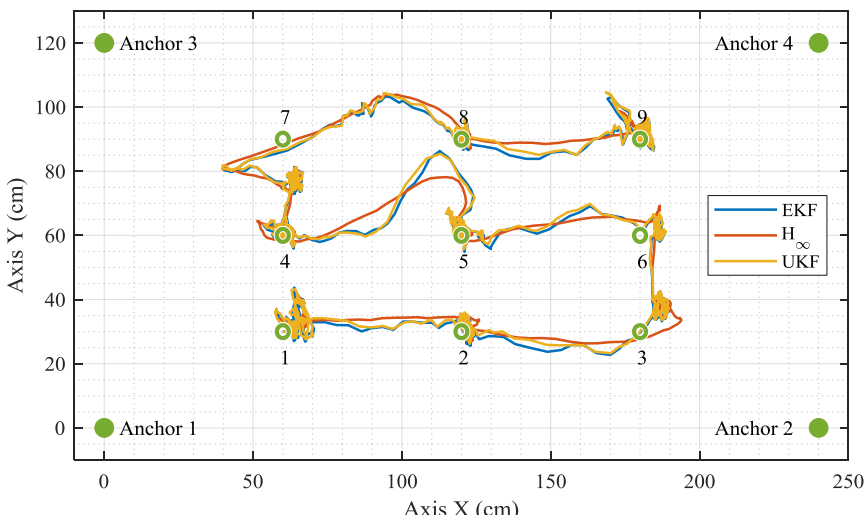


Figure 5.14: Large-scale measurement arena with 9 measurement points and 4 anchors presenting the outcomes of EKF, UKF and  $H_\infty$  the filters

Referring to Figure 5.14, it can be seen that the tracks between the point 4 and 5 as well as point 4 and 7 are distorted heavily in a way that the measurement point 7 is completely deviated from the expected point. In order to find the reason, the differential range of anchor pairs are inspected. The result is depicted in Figure 5.15. At the sample numbers around 600, a spike point can be observed where all the range data are deviated together downwards. This effect typically happens when a barrier between the mobile node and the anchor 1 (reference node) exists. Since the pairing topology of the system is star form, all the anchors are paired with the reference node, hence a barrier between the anchor 1 and mobile node influences the ranging data of all the anchor pairs. Another NLOS case is spotted at sample 900 but this time only between anchor 2 and the mobile node. These NLOS cases are the reason of localization distortions which have happened due to presence of human hand in the vicinity of the antenna nodes.

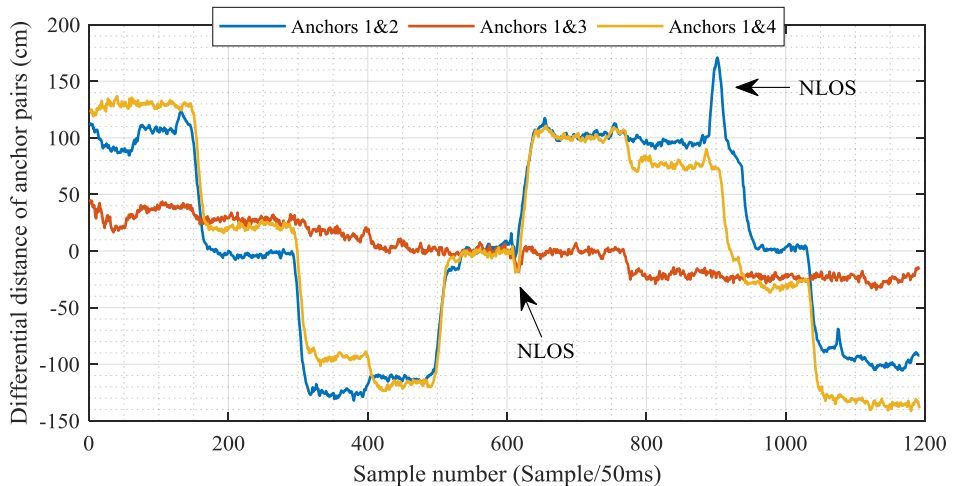


Figure 5.15: Differential distance of the anchor pairs recorded in the large-scale arena. The NLOS cases due to presence of hand are visible in the measurements

Considering the accuracies of the measurement, it is observed that the  $H_\infty$  filter is filtering the NLOS cases more smoothly and turns to the right track faster than the other methods when the NLOS effect is not present anymore. This is due to robust characteristics of this filter which is designed to tolerate such conditions. The evaluation of the error results proves this fact, as the error of this filter at the area where the NLOS cases happen is the least among the other two approaches. These are for example at the sample number 620 and 1070 as shown in the Figure 5.16. In LOS cases where the noise condition is white Gaussian, the performance of EKF is better but the differences are in the order of centimeter. In general, the performances of all the three techniques are almost identical with maximum observed distance error of 26 cm for EKF, 25 cm for UKF and 18 cm for  $H_\infty$  method and majority (90%) of the samples have less than 10cm error. In this trial, the error of Fresnel zone was not influential.

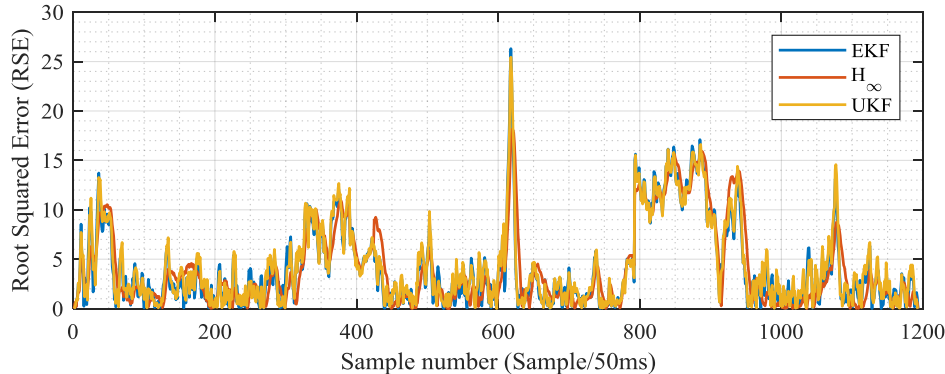


Figure 5.16: Measured error of the three localization algorithms (EKF, UKF and  $H_\infty$ ) at each iteration collected in large scale experiment

The run-time of all the three algorithms is measured for this trial as well. The run times are almost identical as the previous experiments since the structure of the algorithms and parameters have not changed. The results of this test as well as error metrics are summarized in Table 5.7.

Table 5.7: Error analysis and performance results of different localization algorithms in large scale experiment with 9 measurement points

Parameter	EKF	UKF	Extended $H_\infty$
Run time in each iteration	20.96 $\mu$ s	71.842 $\mu$ s	36.491 $\mu$ s
RMSE	5.85 cm	5.98 cm	5.83 cm
CEP	1.66 cm	1.87 cm	1.42 cm
Maximum error	26 cm	25 cm	18 cm

Another similar test is performed to evaluate the efficiencies of the algorithms when the target node is dynamically moving. For this test, the mobile node is moved with altering speed according to the reference path demonstrated in Figure 5.17. Other than the distortion experienced at the initial phases of the movement which has happened due to presence of a hand, the rest of the path is in small error range of 5 cm. It can be seen that as the mobile node is farther than the anchors and the arena is larger, the distortions and deviations are less observed. Since all the three localization methods are tuned with identical parameters, the differences of the measured locations are almost negligible. As in this case, the severe cases of NLOS were not present, the performance of EKF filter was slightly better than the other approaches. This can be seen in the CDF diagram of the error provided in Figure 5.18. The maximum observed error in this test was 14 cm with 90% of the data having less than 7 cm error and CEP of 1.9 cm in average. The RMSE values measured in this experiment are 4.58 cm, 5.98 cm and 5.83 cm for EKF, UKF and  $H_\infty$  respectively.

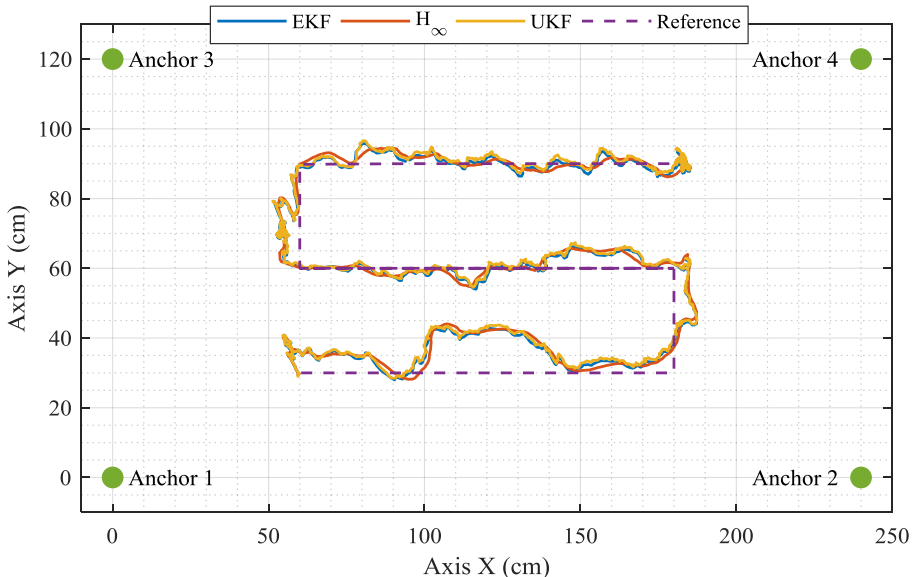


Figure 5.17: Sample trajectory of the mobile node with dynamic alteration of the speed performed in the large scale arena

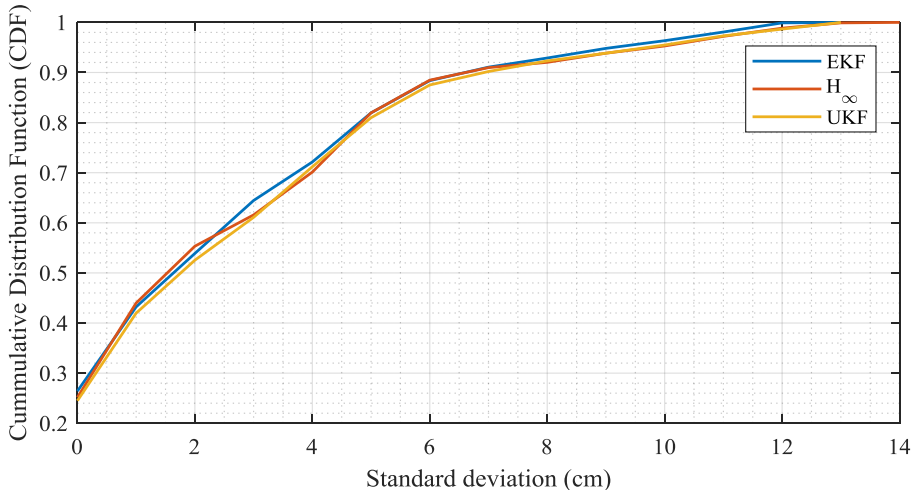


Figure 5.18: The cumulative distribution function of the error results from the experiment performed in the large-scale arena with dynamic speed

In the PV model of the system (Eq. 5.15) which is used in this experiment, both the location and velocity of the mobile node can be estimated. In order to evaluate the dynamics of the system, the speed of the node in  $x$  axis is demonstrated in Figure 5.19 estimated by different localization algorithms. According to this graph, the speed of the node is varying between  $\pm 20$  cm/s. The sign of the speed shows the direction of the movement which in the initial phase is from left to the

right hence positive, then it is from left to right which is represented as negative and finally from left to the right with positive speed. As the acceleration of the node is not estimated in this model, the velocity data are noisy. Surprisingly the speed result of the  $H_\infty$  filter is very smooth and as accurate as the other methods. The major reason of this effect is the deterministic parameters of this filter namely matrices  $S_k, Q_k, R_k$  defined in Eq. 5.88 which are tuned for smoother behavior of the filter.

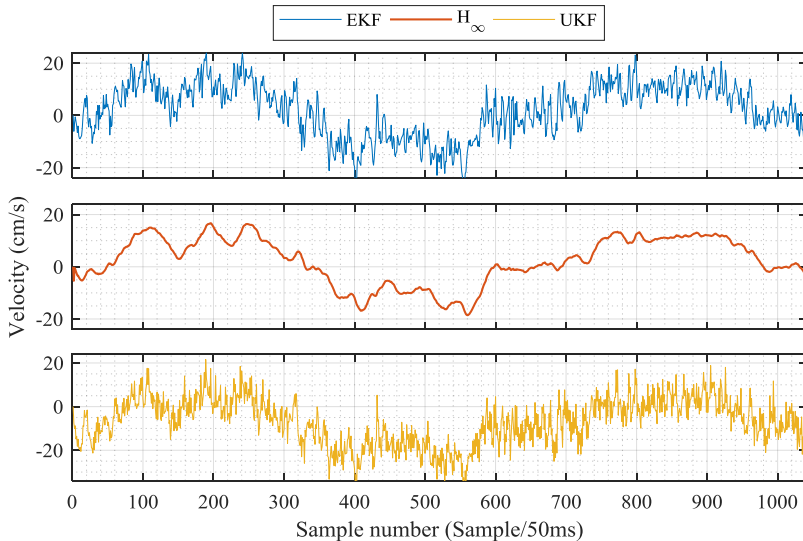


Figure 5.19: Velocity of the mobile node in direction of  $x$  axis acquired using different localization techniques

In the next round of the experiments, variances of the distance measurements at a stationary point are evaluated. For this purpose the target node is located at coordinate of (30,10) and the location data is recorded for the period of 5 minutes at the rate of 20 samples per second. The idea behind this experiment is to extract the distribution model of the measurement noise and its mean if there is any bias in the measurements. In terms of accuracy of the measurement, all the three algorithms seem to be identical as it was also the case in the previous trials. The range of the location measurements as well as the probability distribution function of the error is demonstrated in Figure 5.20. As it can be seen from the PDF, the distribution of the noise is not Gaussian. This is due to the fact that the differential ranging data are filtered before feeding to the localization engine in order to improve the accuracy of the localization. Using fitting tool, the noise distribution is estimated to be Weibull with mean of 1.88cm and variance of 1.26. The Weibull distribution equation and its estimated parameters are as follows:

$$Y = \frac{b}{a} \left(\frac{x}{a}\right)^{b-1} e^{-\left(\frac{x}{a}\right)^b} \text{ where } a = 2.11 \text{ and } b = 1.73 \quad (5.94)$$

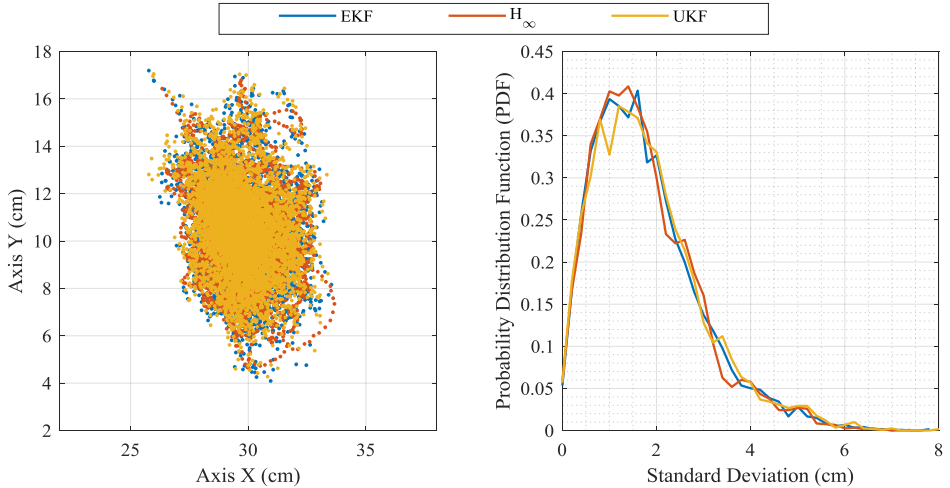


Figure 5.20: Variance of the localization data (left) and the PDF of the measurement error (right) with its Weibull distribution

In the last experiment of this chapter, the convergence speed of the localization algorithms and the influence of the initial point on the convergence and stability of the filters are evaluated. For this purpose, the same setup of the previous experiment with stationary node is used. For all the algorithms, different initial points are chosen with coordinates as follows: (1,1), (80,50), (-10,80) and (-1,-5). The result of this experiment is presented in Figure 5.21. In this graph only the result of axis  $x$  is demonstrated which has the location of 30. Using the first initial values, all the three filters converge within 2 to 3 iterations to the vicinity of the final value however the  $H_\infty$  needs around 30 more iterations to completely converge to the final value. In the second case where the initial point is selected somewhere outside of the arena, the EKF filter has difficulties in convergence at the initial phase but eventually after 20 samples converge to the desired location. The other two approaches converge to the target within 4 iterations with no issues. For the next points, one negative value is selected but the other value is still outside of the arena to challenge the filters. This situation is slightly challenging for the filters at the initial phase but finally all the filters converge within 20 iterations. For the last case both initial points are negative. Although these values are only a few centimeters far away from the first case, the negative sign of the values results in initial instability especially for UKF filter. In this case, the  $H_\infty$  has very smooth behavior and converge immediately in 5 iterations in spite of challenging condition of the initial points. The reason is, this filter is optimized for extreme cases of the noise inaccuracies and worse case initial point as discussed in Section 5.3.3. There have been other initial points such as (80,100) which resulted in total divergence of all the filters. This shows the importance of the initial point for this type of localization systems. A solution to this problem is to store the last position of the system and use it as initial point

in the next round of the measurements but again there is no guarantee that the mobile node is not moved when it was not in service. Another solution is to use static iterative techniques introduced in section 5.2 to find out a suitable start point and then use the point in the desired dynamic approach.

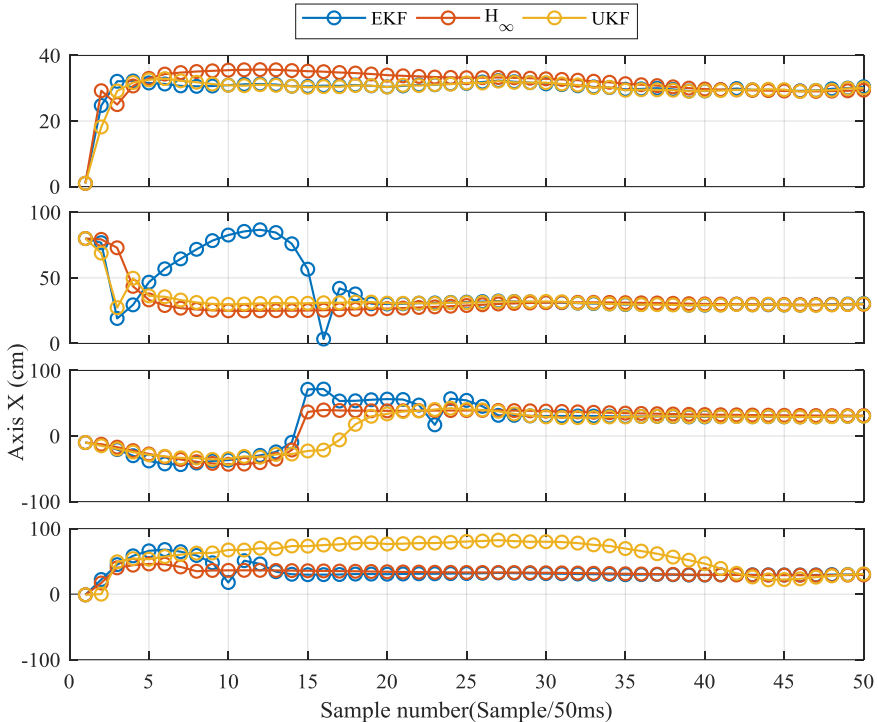


Figure 5.21: Convergence rate of different localization system with different initial point with coordinates from top to bottom diagram as follows: (1,1), (80,50), (-10,80) and (-1,-5)

It can be concluded that the EKF approach is a simple and effective method which has optimum estimate when the characteristics of the noise are known and the model of the system is almost exact. The UKF approach seems to be more accurate for highly nonlinear systems but for localization applications it is too slow and too complex to implement. The  $H_\infty$  filter approach although is slower and more complex than EKF, but promises smooth behavior of the system in NLOS cases and other model inaccuracies which happen often in localization applications. Hence use of this filter is recommended if the computational complexity of the system is not a burden and non-optimal conditions are expected.

## 6. NLOS Identification and Mitigation

One major challenge of the indoor localization and navigation systems is lack of direct line of sight between the transmitter and receiver. This may happen when the transmission path between the two radio devices is blocked by an object such as furniture or wall or even presence of humans. In addition to this problem, high level of signal reflections in indoor area results in multipath effect which can falsify the measurements severely. In general, three scenarios of non-line of sight (NLOS) can be defined. The first one, is a barrier between the two radio devices blocking the direct path but with no reflection signals. In this case, the signal will arrive at the receiver with delay which is the result of lower travel speed of the wave in the barrier compared to air. Furthermore, in such a condition the energy of the arrived signal is less than the direct line of sight scenario. In the second case, although the direct path is blocked, the transmitted signal is reflected by the environment resulting in the arrival of several signal's replicas at the receiver over different paths. Bearing in mind that the blocked direct path has a delay in transmission, it may occur that the reflections arrive faster at the receiver than the direct path. This case is really hard to detect as the time stamp of the first detected path in the response channel is not corresponding to the shortest path between the nodes. Moreover, these reflections result in multipath effect which could ruin the signal of the direct path by overlapping it. The last scenario is the worst case in that the direct path signal does not arrive at the receiver due to high attenuation of the signal. In this case, the reflection signals are the only arrived signals which do not deliver any information about the shortest distance between the two communicating nodes. These scenarios are demonstrated in Figure 6.1.

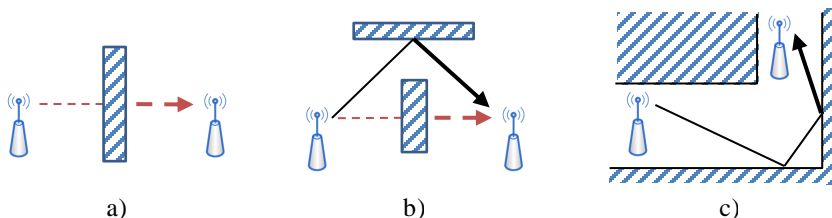


Figure 6.1: Different non-line of sight (NLOS) scenarios in indoor localization systems, a) delayed direct path, b) delayed direct path and reflection, c) only reflection

The NLOS conditions create an error bias in the distance measurement. The previously mentioned scenarios are not the only reasons of observing this error bias. In general, parameters such as multipath effect, channel propagation delay, lack of line of sight between transmitters and receivers, false recognition of first path in channel impulse response and differences of wave propagation speed in different materials could be the reasons of observing the bias error in the measurements [160]. The NLOS error is usually much larger than the noise available in the signal in a way that in some severe NLOS cases, errors of up to few meters may be expected [52, p. 166]. This shows the necessity of developing algorithms which are able to detect these conditions and reduce the error as much as possible to have an optimized estimator even in non-ideal conditions.

Many algorithms and solutions are proposed so far for detection and mitigation of the NLOS cases. Zekavat et al. [128, p. 523] categorize these algorithms into cooperative and non-cooperative methods. The cooperative methods consider the measurements from several nodes which are scattered in the area in different directions and compare the quality of the measurements achieved from these nodes in order to spot out the node with NLOS conditions. Once the node with the NLOS condition is recognized, its measurement is ignored if the network is redundant (having more nodes than the minimum required). This is a practical way if NLOS conditions happen only between one or two nodes. However, for a larger number of NLOS cases, the efficiency of such algorithms decreases. Examples of the criteria used in this category are residual error of the localization as it is used in the work of Li et al. [161] and Schröder et al. [162] or variance or standard deviation of the data as it is presented in the papers in [163–165].

In non-cooperative methods, each node is evaluated independently based on the quality of the data received at that node. These signal quality metrics do not reflect the error in the measurements directly but once certain features are extracted and combined, it is possible to deduct the LOS or NLOS condition of the received signal. Therefore, the algorithms of this category are more diverse and mostly based on statistical methods or machine learning algorithms. The usual metrics used for detection of NLOS conditions in these methods are extracted mainly from the channel impulse response (CIR) which reflects channel conditions based on different aspects of the received signal quality. A detailed analysis of the CIR for LOS and NLOS conditions is provided by Decarli et al. [70]. A few of commonly used features for evaluation of the channel conditions are energy of the received signal as it is used by Alsindi et al. [166], skewness of the elements in CIR as proposed by Abbasi, et al. [167], kurtosis of the CIR elements applied in the papers presented in [168–170], root mean square of CIR elements as it is used in the projects [168–170] and mean excess delay which is proposed and applied in [167–170]. Depending on the number and quality of the collected data, condition of the measurement environment and effectiveness of the applied algorithm, different level of accuracies are reported which makes it difficult to judge about the effectiveness of a certain approach.

## 6.1. Problem Definition

The first step of handling the NLOS scenario is to define a mathematical model for the NLOS error. Considering the fact that the NLOS case results in a delay in time of arrival, many sources in the literature define this error as a positive additive term [167, 168, 171]. Therefore, the NLOS error is an additional variable which is added to the distance measurement in the form of [172]:

$$\begin{cases} z_i = r_i + v_i & \text{LOS condition} \\ z_i = r_i + v_i + b_i & \text{NLOS condition} \end{cases} \quad (6.1)$$

where  $z_i$  is the observed distance at each iteration including the errors,  $r_i$  is the real distance between two nodes in ToA case or differential distance between the mobile node and two anchors in TDoA topology,  $v_i$  is the measurement noise assumed to be Gaussian in the form of  $\mathcal{N}(0, \sigma^2)$  and  $b_i$  is the bias error of anchor  $i$  appeared as a result of NLOS condition.

As the distance of the nodes in ToA structure is directly related to the time of signal propagation from transmitter to receiver, the positivity of the bias error is guaranteed. This is however not the case in TDoA structure as the distance here is in differential form and resulted from subtraction of two time of arrival signals. In case of unilateral topology this can be defined as:

$$\Delta t_{m,n} = t_m - t_n - t_{interval} \quad (6.2)$$

where  $\Delta t_{m,n}$  is the difference of the time of arrival,  $t_m$  is the signal time of arrival from the anchor  $m$  to the mobile node, and  $t_n$  is a similar parameter for anchor  $n$ . Considering this equation, if NLOS case is happening between the mobile node and the anchor  $m$ , the term  $t_m$  is larger than its usual value and therefore  $\Delta t_{m,n}$  is positive. However, if the NLOS case is happening between the anchor  $n$  and the mobile node, then  $t_n$  is larger which results in the fact that  $\Delta t_{m,n}$  could get negative or even zero in certain circumstances. This can get even worse if the NLOS condition with similar severity occurs between the mobile node and both anchors. In this case, there will be an offset in both time of arrival data but they cancel out each other in differential form. This means although there is NLOS condition between both two pair nodes, the distance result may not get influenced from it at all. In order to evaluate this problem, we define an error metric which describes the observed bias error in the form:

$$e = \Delta t'_{m,n} - \Delta t_{m,n} \quad (6.3)$$

where  $e$  is the observed measurement error,  $\Delta t'_{m,n}$  is the measured difference of arrival in different channel conditions and  $\Delta t_{m,n}$  is the same parameter but in

ideal LOS condition. Assuming that the error is evaluated in different NLOS conditions, the possible values of the observed error  $e$  can be summarized as:

$$\begin{cases} e = b_m & \text{NLOS between anchor } m \text{ and target node} \\ e = (b_m - b_n) & \text{NLOS between both pairs} \\ e = -b_n & \text{NLOS between anchor } n \text{ and target node} \\ e = 0 & \text{LOS} \end{cases} \quad (6.4)$$

These complex conditions yield in the fact that the positivity assumption of the NLOS error is not guaranteed in TDoA structures. To evaluate this problem in practice, an experiment is designed in that two anchors and one target node are used in unilateral TDoA setup. All the nodes are considered stationary but a movable barrier is used to block the direct path between the anchors and the target node. The barrier is applied for a certain amount of time and then removed to provide the LOS condition between the nodes. The target node is located at a point that is exactly between the two anchors where the expected differential distance of the two pairs is zero. The result of the test is depicted in Figure 6.2.

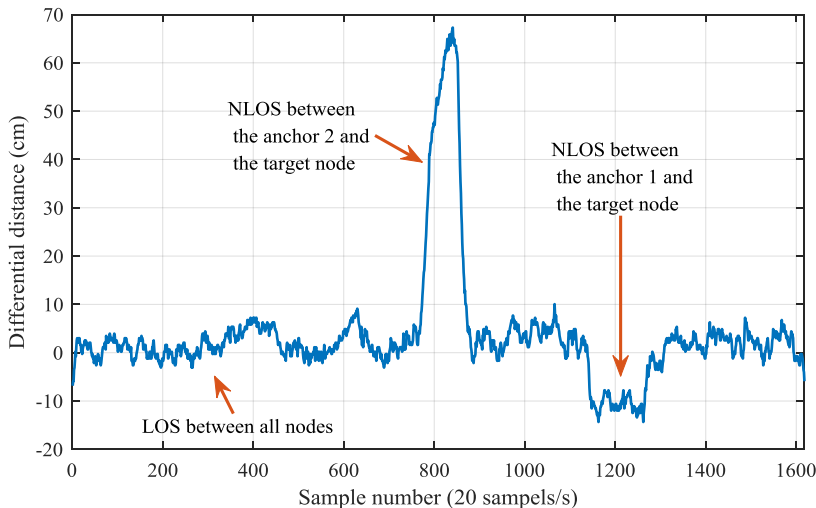


Figure 6.2: Differential distance of a target node with anchor pairs in a TDoA structure with positive and negative bias error created as a result of NLOS conditions

As it can be seen from this graph, the initial phase of the measurement is LOS condition where the differential distance is zero as expected. By blocking the path between the anchor 2 and the target device, a positive error is appeared which is as high as 70 cm even though all the nodes were stationary. The same condition happens when the barrier is located between the anchor 1 and the target node but this time the error is negative. It should be noticed that the target node in TDoA configuration compares all the signal time of arrivals with the reference node. This means if the NLOS case occurs between the target node and the reference node, the results of all the anchors will be influenced with a negative bias. This

condition leads immediately to divergence of the localization algorithm if suitable actions are not taken to compensate these errors in advance. The majority of the researches in the literature address only the NLOS identification of ToA setups and therefore the problem of the TDoA configurations is rarely covered. The idea of this chapter is to address the NLOS identification problem of such setups by defining a quality metric of NLOS condition for each anchor and applying the difference of these metrics on the detection system. This way, the severity of NLOS condition at each anchor is used to determine the sign of the bias error and the amount of mitigation required to compensate the created bias error. The rest of this chapter describes the details of the algorithms used for detection of NLOS case and mitigation of the error according to the described idea.

## 6.2. Data Collection and Preparation

As it was discussed previously, the aim of the NLOS identification method is to extract signal quality metrics from each anchor and decide about the channel condition based on either statistical methods or machine learning algorithms. For this purpose, *a priori* statistical information of the channel features is required. One way of dealing with this problem is to use already available models such as those provided by IEEE 802.15.4a channel modeling subgroup [173]. This task group has performed several experiments in different environments and recorded the channel characteristics of both LOS and NLOS conditions. In total, 8 different models are developed which are described in Table 6.1.

Table 6.1: Channel models defined by IEEE 802.15.4a channel modeling subgroup

Test area	Residential	Indoor office	Outdoor	Industrial
LOS	CM 1	CM 3	CM 5	CM 7
NLOS	CM 2	CM 4	CM 6	CM 8

These models provide the ground knowledge required for developing features and evaluating the channel conditions based on the received signal. Example of the researches based on these models are the work of Güvenc et al. [169] or Abbasi et al. [167]. Another model is proposed in [174]. One major problem of these models is that the effects of the hardware especially the antenna is not considered in these models [173, p. 2]. Moreover, the definition of an industrial or indoor environment is too general and cannot be applied exactly to all the use cases. These issues make the application of the models in different areas suboptimal. Therefore we decided to perform a measurement campaign with the aim of first developing a model which includes the hardware characteristics and the second producing a dataset which could be used for training the machine learning algorithms as well. The measurement campaign is carried out in different areas including classrooms, offices, laboratories, open areas and corridors.

### 6.2.1. Details of the measurement setup

In all the experiments, unilateral TDoA configuration is applied with 4 anchors located at each corner of a rectangular arena. One target node is used for recording the measurements. During the measurement, the target node was stationary but the recordings are performed with many possible positions of the target node in different angles. This way the position of the target node is known and is encoded in the name of the file holding the data which can be used later to extract the error of measurement. The anchor pair selection concept is according to the hybrid form that is explained in Chapter 3. The reason of placing the target node in different angles is to evaluate the effect of antenna gain on the accuracy of the measurements. The dimensions of the measurement arenas as well as coordinates of the measurement points are provided in Appendix A3.

DWM1000 modules are used in the hardware setup which is used for both anchor and target nodes. For the reference node specifically a circuit is designed which contains a DW1000 chip from Decawave and a VCTCXO crystal as described in Chapter 4. The structure of the setup is very similar to the 9 points test presented in Section 5.3.4 and demonstrated in Figure 5.14.

For simulating the NLOS conditions, different objects made up of metal, wood and even human body is used. Since the target node is stationary, the barriers are inserted temporarily between the nodes and moved along this line towards the nodes and eventually removed to provide the LOS condition again. This process is repeated for each anchor pairs separately and the data are stored in different files. This is performed with the aim of simplifying data referencing as well as improving the quality of the data by providing only relevant data to learning algorithms. In total, more than one million samples are recorded which are enough to clearly model the measurement area. The process of analyzing this data and extraction of the relevant features are subject of the next section.

### 6.2.2. Features selection

The idea of feature identification is to find a set of parameters from the received signals which represent correlation to the desired target. The desired target in our case is detection of channel condition specifically NLOS error. The feature identification is a very complex process as sometimes these features are not available directly and need to be extracted by combining other features. Examples of such parameters are signal to noise ratio (S/N) which uses energy of the signal and recorded level of the noise to define a new metric or frequency analysis which needs a period of data for evaluating the frequency range of data. The process of feature selection is based on extracting as many features as possible and evaluating the correlation of each feature to the channel conditions. For this purpose correlation analysis such as Pearson, Kendall or Spearman [175, p. 59] or correlation diagram can be used which represents the correlation of two

parameters in the form of a geometrical shape. In this case, two parameters are plotted with each parameter in each axis. If the result is a circle, this means no or low amount of correlation between the parameters, however an oval shape located diagonally demonstrates higher correlation between the two parameters. The correlations of four features are illustrated in Figure 6.3, two of them with low correlation and two others with higher correlation.

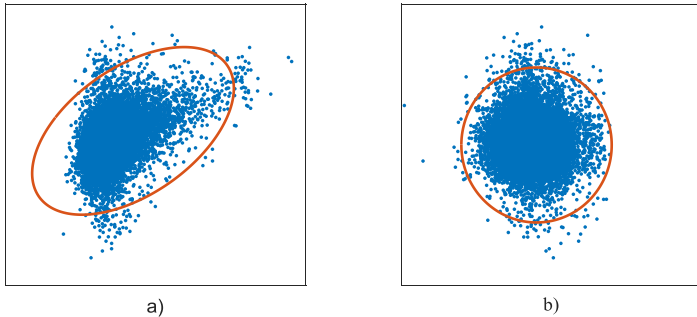


Figure 6.3: Comparison of the features correlation with a) good correlation (diagonal oval) and b) no correlation (circle)

Care must be taken in the selection of the features to choose parameters which provide useful information to the learning system otherwise the learner may get either overfitted when too many correlations between the data and the target exist or it may not improve as the data is not related to the target class. One solution for evaluating the effectivity of the features is wrapper approach [175, p. 119] in that a subset of features are formed and a model based on that is extracted. Then at each round, one feature is removed from the subset and the accuracy of the model is reevaluated. If the removed feature has not led to degradation of the accuracy of the model, it is permanently removed otherwise it is kept. Data reduction approaches such as principal component analysis (PCA) could also be applied to remove data redundancies before the model is extracted. Other than the selection criteria mentioned before, we are interested in features which fulfil the implementation constraints of the localization system running on a 32-bit microcontroller. These constraints are listed as follows:

- The desired location update rate is 20 samples/s or faster. For a setup with unilateral TDoA configuration and 4 anchors, this rate will be 4 times faster as the data of each anchor arrives sequentially. Therefore, the expected time between each signal reception is 10ms or faster.
- The algorithms for localization, NLOS identification and mitigation should be simple enough to be implemented in a microcontroller with single precision float unit and clock frequency of maximum 80 MHz.
- Features should be instantly available at each iteration so that the NLOS identification algorithms can be run online within the given time limit.
- Maximum memory dedicated for this purpose is set to 10 KB. Therefore, algorithms which demand large amount of memory could not be utilized.

One of the typical sources of extracting signal quality metrics is evaluating the channel impulse response of each received signal. A few examples of the features which could be extracted from CIR are kurtosis, skewness, mean excess delay, root mean square delay (RMS), etc. as it is applied in the works of [70, 167, 176]. The channel impulse response is simply an array of signal amplitudes and phases started from end of preamble phase and recorded for a certain period of time as discussed in Chapter 2. This can be represented as [168]:

$$h(t) = \sum_{k=0}^{K-1} f_k \delta(t - k) \quad (6.5)$$

where  $h(t)$  is the channel impulse response,  $f_k$  is the amplitude of each bin in the array, parameter  $\delta(t - k)$  is the time shift of each bin and  $K$  is the maximum number of recorded samples. The DWM1000 module is able to record this information and provide it to user, however this data is stored in a register with the size of 4KB which needs to be transferred to microcontroller over the SPI bus. Moreover, the recorded values are in complex form with separated real and imaginary parts which need to be converted to amplitude and phase values. The total amount of time required for such a process is reported by different research groups to be around 2-5 seconds depending on the applied processor [168, 177]. This cumbersome process is too heavy for a microcontroller and hence the defined constraints cannot be met. Therefore, only attributes are selected that are provided by the module directly or can be extracted from simple mathematical processes. Keeping these constraints in mind, more than 25 different attributes are extracted either directly or by combining other signal characteristics together. Among them, 10 features are selected which show good amount of correlation to channel conditions namely LOS and NLOS. There have been other features which still could be used but we decided to keep a balance between the complexity and accuracy of the model. Therefore, only the best 10 attributes in the ranking are selected. These features are introduced in detail as follows:

- *Peak path power*: If the elements of the recorded CIR are considered in discrete form, the bin with the highest amount of energy represents the peak path power. This can be described mathematically as:

$$P_{max}(t) = \max|h(t)|^2 \quad (6.6)$$

This feature is related to the maximum amplitude recorded in the CIR which is provided by the hardware module directly. Considering the fact that the signal in NLOS condition is either passed through a barrier or it is arrived over reflections or even a combination of these situations, less energy of the signal is arrived at the transceiver and therefore the peak path power in NLOS is generally lower than in LOS conditions. In case of having reflections in the area, the received energy of the signal is more distributed over the time rather than concentrating in the first path.

- *First path power:* This attribute defines the energy level of the first bin observed in the CIR which has higher energy than a defined threshold. This threshold is selected at a level where the noise can be clearly separated from the arrival signals. This is represented in the form:

$$P_f(t) = \max \left( h(t)^2 \mid_{t=0}^{t=\tau_f} \right), \text{ where } P(\tau_f) > \lambda_{th} \quad (6.7)$$

In this equation,  $\tau_f$  is the time index of the first detected signal with higher energy than the threshold,  $P(\tau_f)$  is the energy of the signal in that index and  $\lambda_{th}$  is the noise threshold. In LOS cases, this feature has usually the highest amount of energy as the signal passes through the shortest path and the energy is not wasted by reflections. Therefore, this feature is useful for distinguishing between different channel conditions. The Decawave module does not provide this feature directly, however the manufacturer has provided a mathematical solution to calculate this parameter based on other available parameters [168, 178]. These parameters are the number of preambles  $N_p$ , the amplitude of the first path measured at three sequential points called  $F_1, F_2$  and  $F_3$  and a constant  $A$  which is defined by the manufacturer based on pulse repetition frequency (PRF) settings of the module. The applied settings in our project is PRF of 64 MHz resulting in the constant of  $A = 121.74$ . The equation of calculating the first path power is defined as:

$$P_f(t) = 10 \log_{10} \left( \frac{F_1^2 + F_2^2 + F_3^2}{N_p^2} \right) - A \quad (6.8)$$

- *Received signal strength (RSS):* This parameter declares the total amount of signal energy received and recorded in CIR. This can be presented as:

$$P_{rss} = \sum_t h(t)^2 \quad (6.9)$$

This attribute is commonly used for evaluation of signal quality even in other radio technologies such as Wi-Fi and therefore it is provided by many radio devices. It is believed that this parameter is subject to environmental changes and noise so that the observed values have high variance and hence are less reliable. However, in UWB radio systems, this feature is more stable due to the fact that the signal is constructed by accumulating the signal over longer period of time. Same as previous attribute, this feature is not provided by the hardware directly and needs to be estimated using other parameters. These parameters are the number of recorded preambles  $N_p$ , a constant  $A$  as defined before and a parameter  $C$  which is channel impulse response power value. The given relation between these parameters is [168]:

$$P_{rss} = 10 \log_{10} \left( \frac{C \cdot 2^{17}}{N_p^2} \right) - A \quad (6.10)$$

- *Peak path index:* We define this attribute as  $\tau_m$  which is the index of the bin in the CIR array where the maximum energy of the signal  $P_{max}(t)$  is observed. This parameter is demonstrated in Figure 6.4 and can be defined as:

$$t = \tau_m, \text{ where } P_{max} = \underset{t}{\operatorname{argmax}}(h(t)^2) \quad (6.11)$$

In LOS conditions, usually either the first path has the maximum energy and therefore it is equal to the maximum power path or the maximum power path is very close to the first path. In NLOS conditions however, the first path is strongly attenuated and therefore the maximum power path will be one of the reflected signals arrived later. Therefore, the index of the maximum power path could be a good indicator for recognizing channel conditions. This feature is provided in the registers of the hardware module directly.

- *Difference of peak to first path index:* This is also one of the features which is achieved by combining other attributes namely index of the first path and the index of the maximum power path as it is shown visually in Figure 6.4. The mathematical relation of the features is as follows:

$$T_d = \tau_m - \tau_f \quad (6.12)$$

As it was mentioned for previous feature, the  $\tau_m$  is a good measure of channel condition. However, the indexes of the CIR elements changes depending on the point where the first path is recognized. Therefore, considering the indexes in differential form provides a more stable parameter independent of the index numbers recorded in CIR. As it can be seen, this parameter has correlation with the peak path index. So for the sake of simplicity of the model, one of these could be removed. But according to our observations, better prediction performances are achieved when both features are utilized. This feature is commonly used by the researchers due to its distinctive correlation to channel conditions. Examples of the work based on this feature are [177, 179].

- *Power difference:* This attribute is achieved by subtracting the energy of the first path  $P_f$  from the total energy of the signal  $P_{rss}$  as defined below:

$$P_d = P_{rss} - P_f \quad (6.13)$$

As it was discussed before, the first path amplitude in NLOS case is usually attenuated compared to the amplitude of the maximum path. In LOS cases, the difference of the two parameters are very small or even zero when the first path is the maximum power path itself. This means, the difference of these two parameters is higher in NLOS cases compared to the LOS scenarios. According to practical experiments performed in [158, 168, 177], this difference is larger than 10 dB for NLOS conditions whereas in the LOS cases the difference is measured to be less than 5 dB in most of the cases. Therefore, this feature provides a good criterion which is widely used in the literature to distinguish between different channel conditions as shown in Figure 6.4.

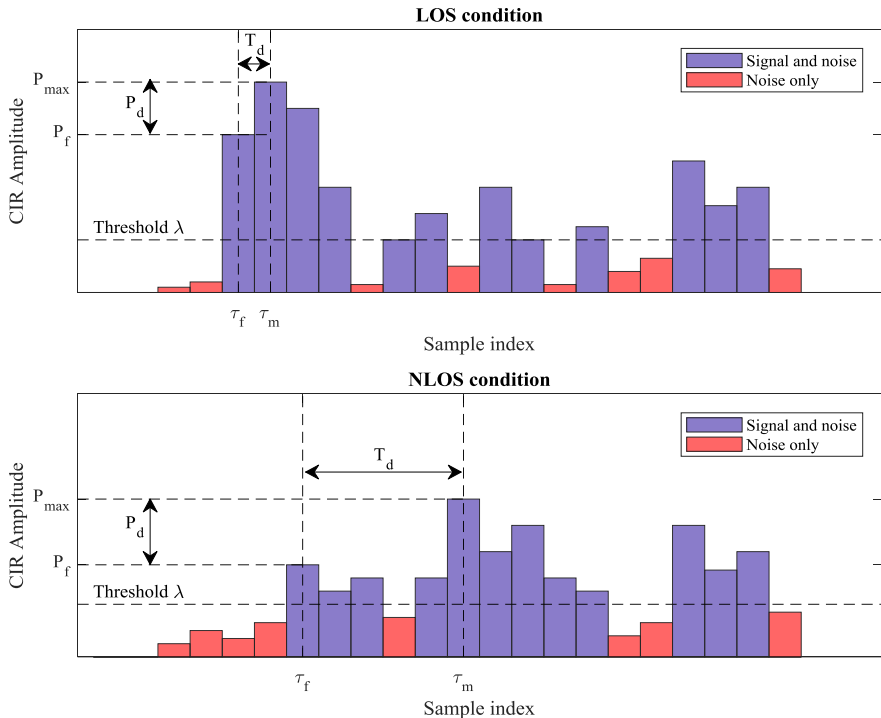


Figure 6.4: Different characteristics of the signal in LOS and NLOS channel conditions.  
Higher level of noise, wider difference of index and larger power difference in NLOS condition compared to LOS case is visible

- **Noise:** It has been observed that the level of the measured noise in LOS conditions is relatively lower than the NLOS conditions. As this metric is provided in the registers of the hardware directly, it could be easily used as an attribute for detection of the corresponding channel condition. It is assumed that the measurement noise follows the Gaussian distribution with zero mean and variance of  $\sigma$  which can be represented in the form:

$$N = \frac{1}{\sigma\sqrt{2\pi}} e^{\frac{-t^2}{\sigma^2}} \quad (6.14)$$

- **Skewness:** The skewness parameter  $S$  is a term used in statistics that generally describes the symmetry of the received signal around the mean point. This feature can be calculated by estimating the third moment of the expectation value around its mean point which can be formulated as:

$$S = \frac{E[(h(t)^2 - \mu)^3]}{E[(h(t)^2 - \mu)^2]^{\frac{3}{2}}} \quad (6.15)$$

where  $E$  operator is the expectation value,  $h(t)$  is the CIR array and  $\mu$  is the mean value of the CIR elements. The skewness of a signal is zero if the signal is completely symmetrical around its mean point. If the signal is leaned to left side, the skewness is positive and if it is leaned to right side, the skewness is negative as demonstrated in Figure 6.5.

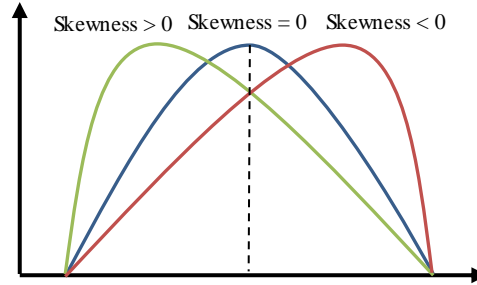


Figure 6.5: Representation of the symmetry of a signal through skewness parameter

The LOS condition has the majority of the signal energy concentrated in the initial part of CIR where the first path and maximum path are located, whereas the NLOS condition has a wider spectrum of energy with the maximum path located at the middle or even the end part of the CIR. Therefore, the symmetry of the CIR around the mean point can be used to determine the focus of the energy in different segments of the CIR and correspondingly the channel conditions. As it is clear from the description of the skewness, for calculating this parameter, all the elements of the CIR are required. However, we would like to avoid extracting the CIR elements due to the issues mentioned before. Our solution is to apply the skewness function only on the three measurement points around the first path  $F_1$ ,  $F_2$  and  $F_3$  as introduced before. As these points are provided by the module directly, extraction of the CIR elements is not required anymore. The result of experiments shows that use of these three points delivers enough information about the channel condition. In Figure 6.6, different combinations of the measurement points as well as the skewness and predicted channel condition are demonstrated.

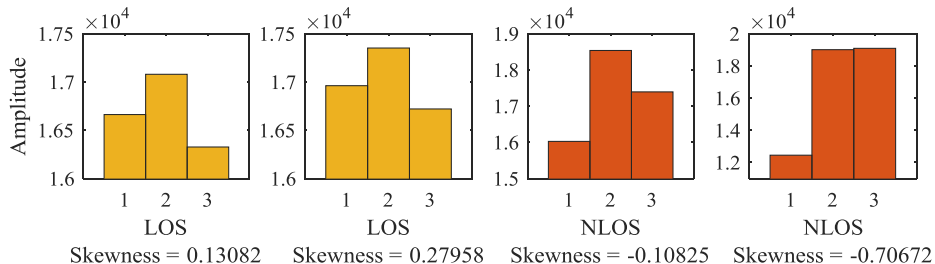


Figure 6.6: Skewness of four samples, two of them taken in LOS and two in NLOS cases based on the three measurement points around the first path  $F_1$ ,  $F_2$  and  $F_3$

Considering the defined solution, Equation 6.15 can be summarized as:

$$S = \frac{\frac{1}{3} \sum_{k=1}^{k=3} (F_k - \bar{f})^3}{\sqrt{\left(\frac{1}{3} \sum_{k=1}^{k=3} (F_k - \bar{f})^2\right)^3}} \quad \text{where} \quad \bar{f} = \frac{F_1 + F_2 + F_3}{3} \quad (6.16)$$

- *Peak path to mean power ratio (PMR)*: This attribute also benefits from the three measurement points  $F_1, F_2$  and  $F_3$  as introduced before but this time the ratio of the peak path energy to mean of these three points are considered. It has been observed that in LOS conditions, the value of these three points are in the same range as the first path and its side lobes have usually higher energy than other bins. However, in NLOS conditions, the signal of the peak power bin has larger energy than these measurement points. Therefore, this feature could also be used for determining the channel conditions. The mathematical relation of the parameters are described as follows:

$$PMR = \frac{P_{max}}{mean(F_1, F_2, F_3)} \quad (6.17)$$

- *Signal to noise ratio (SNR)*: This feature is also commonly used as a metric for determining the quality of the received signal. Higher values of SNR represents a clear gap between the amplitude of the signal and the noise level. This normally happens when direct line of sight between the nodes is available and the environment is not noisy. In NLOS conditions, the energy level of the signal is either at the same level of the noise or even below the noise floor. Based on these parameters, the SNR feature can be defined as:

$$SNR = \frac{P_{rss}}{N} \quad (6.18)$$

### 6.2.3. Data cleaning and labeling

After the features are selected, the data of the features need to be prepared for training or extraction of the statistical information. The major issues which need to be addressed here are identification and removal of outliers, noise, missing data and other forms of inconsistencies [180, p. 85]. The outliers are data samples that are located far from the nominal range of the rest of data. Many different methods exist for detection of outliers. Among them, visualization approaches such as histogram, scatter plots, box plot, etc. are the most common way to recognize the common range of the data and to remove the samples which are located outside of these ranges [180, p. 544]. As an example, the histogram of peak path index is plotted in Figure 6.7. As it can be seen, the majority of the data are located in the range of 746 to 756 but the histogram is much wider due to availability of the outliers far from the common range. The recommended range of limiting outliers are marked on the graph for lower limit as  $u_l$  and for upper limit as  $u_h$ .

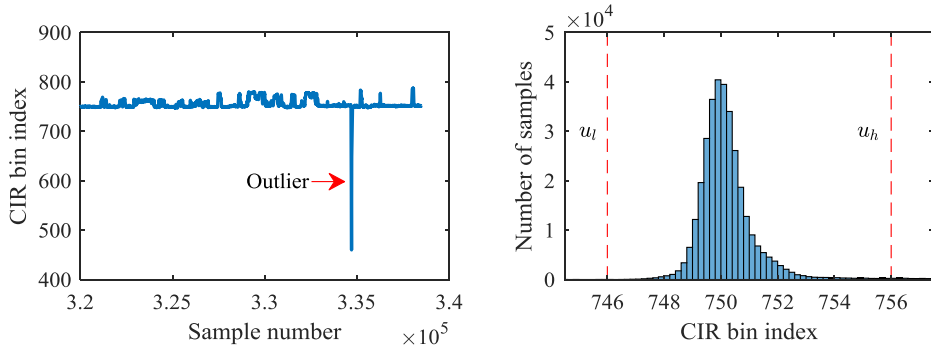


Figure 6.7: Outlier detection process performed on the peak path index parameters with determination of data range using histogram plot

The process of outlier detection is repeated for all of the features and an upper and lower limit is defined. An iterative filtering process, goes through all the elements of the database and removes the samples that either locate outside of the defined region or do not hold a data according to the desired format. The next aspect which needs to be considered is the noise of attributes. It is observed that filtering the data before training the classification system, improves the accuracy of predictions. In order to avoid a complex filtering mechanism, a simple zero order iterative filter is defined according to the following equation:

$$\bar{x}(t) = \bar{x}(t - 1) + k(y - \bar{x}(t - 1)) \quad (6.19)$$

where  $\bar{x}(t)$  is the current estimate of the filtered attribute,  $y$  is the recorded sample at each iteration, and  $k$  is the filtering coefficient which is a number between 0 and 1. In case of our application, it is selected as 0.2 which is a moderate value and not too smooth to destroy the useful information of the features.

Once the database holding the attributes is processed, each sample should be labeled either as LOS or NLOS condition. This is required to provide an output to the supervised learning approaches. It is impossible to perform labeling manually for such a large database. Therefore, we extract the labels by defining a threshold on the error of the measurements. Defining this threshold is not an easy task as the data collection experiments are performed in different arena sizes ranging from  $40 \times 60 \text{ cm}^2$  to  $6 \times 8 \text{ m}^2$ . An error of 30 cm in the case of the latter arena, is still acceptable and should be labeled as LOS whereas the same amount of error for the smallest arena is a case of severe NLOS condition. To solve this problem, a lookup table is created holding different threshold values for each experiment. In an iterative process, the measurement error of each sample is compared with the threshold and based on the results labeled either as 1 for NLOS or as 0 for LOS conditions. After filtering process, 100000 samples are kept, half of it holding the LOS samples and the other half holding the NLOS samples which are used for model analysis and training.

### 6.3. NLOS Identification Algorithms

Considering the structure of the algorithms used for LOS/NLOS identification, the proposed algorithms could be categorized into parametric and non-parametric approaches [181, p. 737]. The parametric methods treat the NLOS identification problem statistically by defining a hypothesis model based on either an already available statistical model or extracting such a model from the experiments [128, p. 524]. In this case, the model of the system is extracted by fitting the training data to a certain predefined function and extracting the best values of the parameters of that function which minimize the model error. This way a model is created that requires only certain parameters to describe the system and therefore once the training process is finished, the training dataset is not required anymore. Examples of such methods are naive Bayes classifiers, linear regression or discriminant analysis. The non-parametric methods instead do not limit the model by any predefined functions. This way, the generated model can be more accurate and can be fitted to more complex models according to what the training data is representing. In this case, the whole or majority of the training data is retained for prediction phase. Examples of these methods used for NLOS identification applications are k-th nearest neighbors (KNNs) as suggested by Zhang et al. [182], least square support vector machines (SVM) as proposed in the papers [170, 183–185], SVM regression proposed by [186], relative vector machines introduced by Nguyen et al. [187] or decision trees [188] to name a few.

Most of the research performed in the area of channel condition recognition are in the form of supervised training systems using binary classification (detection of LOS or NLOS) or in some rare cases multi-class identification and regression (representing the NLOS error numerically). Our efforts to develop a model in regression or multi-class form, that is able to represent the severity of the NLOS conditions with the given features, were not effective. The experimental results have shown that, there is a poor correlation between the level of NLOS severity and signal quality aspects. However, these attributes are still useful enough to develop a binary classifier which can detect the class only. This approach might be useful in ToA configurations where the only involved parameter is the distance between two nodes. However, in TDoA configurations, the distance error is treated differentially and it cannot be extracted by considering only one anchor. Our solution to this problem is to keep the binary classifier, but use the methods which are able to provide additional information such as probability of the final outcome of the predictor or the confidence level of predictions. These types of classifiers are also called rankers [189] because they provide a ranking metrics for the output class instead of providing a yes or no answer. This way, a threshold can be defined to classify the predictor outcome based on the error of the cost function [190]. Many sources in the literature have addressed the structure of rankers and probability estimators in different projects. Examples of these works can be found in [191–193].

The idea proposed in this thesis is to extract the probability of the channel condition for each anchor separately and then compare the results of the two involved anchors differentially. We define the differential probabilities of the conditions in the form of weights  $W_i \in R[-1,1]$  which will be used later in error mitigation process. These weights are calculated from the following equation:

$$W_d = P(\text{NLOS})_n - P(\text{NLOS})_{ref} \quad (6.20)$$

where  $W_d$  is the differential probability metric or weight and  $P(\text{NLOS})_n$  and  $P(\text{NLOS})_{ref}$  are the probability of NLOS condition for the anchor  $n$  and the reference node respectively. Based on the probability value acquired from each anchor, different scenarios are expected which are summarized below:

$$\begin{cases} W_d < 0 & \text{NLOS between reference anchor and target} \\ W_d \approx 0 & \text{LOS or same level of NLOS between the nodes} \\ W_d > 0 & \text{NLOS between anchor } n \text{ and target} \end{cases} \quad (6.21)$$

Since we are interested in extracting the probability metric from the features, we should use the machine learning algorithms that are able to provide the probability of the predictions as side product. Among the common parametric approaches, naive Bayes, binary classifier and logistic regression could be mentioned which will be introduced in the next sections. The non-parametric approaches are not generally designed for such a purpose, but with some modifications it is possible to extract the confidence metric of classes. Possible approaches of this type are decision trees, SVM and KNN.

### 6.3.1. Naive Bayes method

Naive Bayes is a statistical learning approach which constructs a probabilistic model based on the conditional probability distribution of the provided dataset [194]. The base of this method is the Bayes theorem which defines the conditional probability distribution of a feature as follows:

$$P(y|x) = \frac{P(x|y)P(y)}{P(x)} \quad (6.22)$$

where  $P(y|x)$  is the conditional probability of  $y$  given that  $x$  is occurred. Applying this formula on the case of prediction of channel conditions based on the features, we can describe two conditional probabilities for each channel condition as:

$$P(\text{los}|f_i) = \frac{P(f_i|\text{los})P(\text{los})}{P(f_i)} \quad \text{and} \quad P(\text{nlos}|f_i) = \frac{P(f_i|\text{nlos})P(\text{nlos})}{P(f_i)} \quad (6.23)$$

where  $P(\text{los}|f_i)$  is the probability of observing LOS conditions given that feature  $f_i$  is observed. The index  $i$  indicates the number of attribute in the database that is under evaluation and is in the range of 1 to 10. The two parameters  $P(\text{los})$  and  $P(\text{nlos})$  are the probabilities of observing LOS or NLOS in general. These values

are not random variables as the situation is created either by user or as a result of target node's mobility. Therefore, we assume the probability of 0.5 for both parameters. The next parameter  $P(f_i)$  is the marginal probability of each feature defined according to the following equation:

$$P(f_i) = P(f_i|los)P(los) + P(f_i|nlos)P(nlos) \quad (6.24)$$

The most important part of the equation 6.23 is  $P(f_i|nlos)$  which describes the probability distribution function of each feature based on each channel condition. In order to find this conditional distribution, first the data are separated into two groups namely LOS and NLOS according to the label of each sample. At the next step the PDF of each feature is extracted using histogram on each group separately. These PDFs demonstrate the statistical distribution of each feature in different channel conditions. The PDF of the 10 previously defined features are shown in Figure 6.8 for both channel conditions. As it can be seen from this graph, some features such as skewness (S) or noise, represent clear distribution between each channel condition whereas other features such as peak path power ( $P_{max}$ ) have a larger overlapping area between the LOS and NLOS distributions.

At the feature selection stage, care must be taken to have the same number of samples in each class otherwise the algorithm will be trained with bias as in one class more data are trained than in the other class. In addition to that, the range of data and the number of bins for each histogram should be equal for both LOS and NLOS classes to avoid scaling issues of PDFs.

The naive Bayes algorithm is the best estimator when its constraint is fulfilled which is conditional independency of the attributes [175, p. 218]. This is however in reality hard to achieve. This assumption simplifies the process of calculating the final probability of observing a class when multiple features are involved. A common practice for this problem is to use joint probability distribution (JPD) in the form defined below:

$$JPD = \frac{P_{nlos}(f_1)}{P_{los}(f_1)} \cdot \frac{P_{nlos}(f_2)}{P_{los}(f_2)} \cdot \dots \cdot \frac{P_{nlos}(f_n)}{P_{los}(f_n)} \quad (6.25)$$

In order to determine the class result, the JPD is compared with a threshold which is defined by the system designer empirically. Based on the result of this comparison, following scenarios are expectable:

$$\begin{cases} JPD < 1 & \text{LOS} \\ JPD = 1 & \text{Equal probability} \\ JPD > 1 & \text{NLOS} \end{cases} \quad (6.26)$$

The naive Bayes algorithm is a very effective method for detection of channel conditions due to its simplicity and low amount of required processing power. As an example of this algorithm in channel detection applications the work of Abassi et al. [167] can be mentioned which uses 4 features for detection of NLOS cases. Güvenc et al. [169] also use likelihood ratio test similar to the one defined in Eq.

## 6 NLOS Identification and Mitigation

6.25. Another work based on the likelihood ratio test can be found in the work of Maali et al. [179] where  $P_f$  and  $T_d$  are used as features for predicting the NLOS.

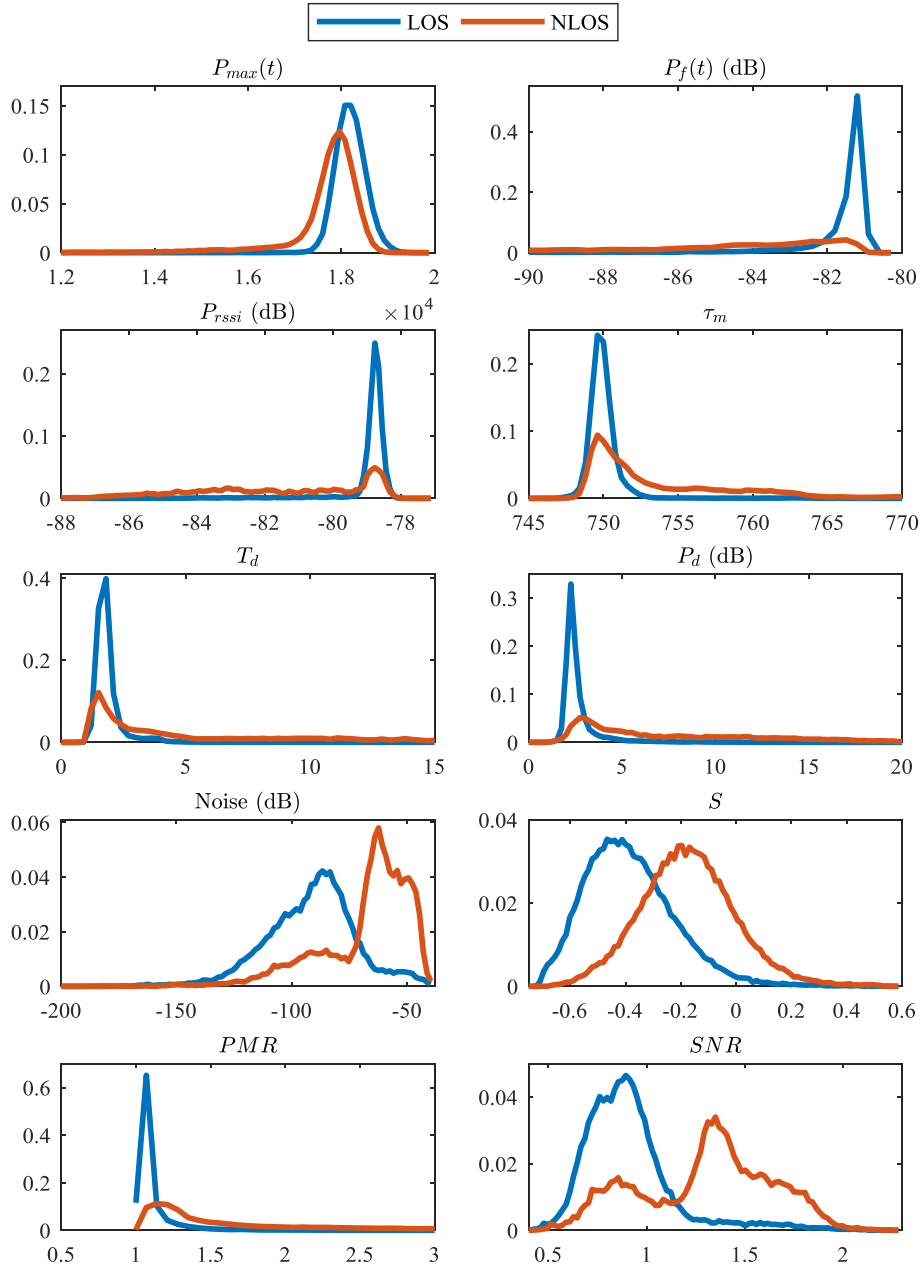


Figure 6.8: Probability distribution function (PDF) of the collected attributes for both LOS and NLOS channel conditions which the x axis scaled according to the range of each attributes

### 6.3.2. Binary classification method

This approach is another parametric classification method which benefits from the PDF of the features as underlying *a priori* statistical information of the model. The decision about the class that the features are belong to, is made by comparing the value of each feature with a certain threshold. This threshold is defined at the point where the two PDFs of the LOS and NLOS cases are intersecting. Therefore, the process of decision making can be defined as:

$$f_i \stackrel{H_1}{\leq} \lambda_i \Rightarrow H_{1,2} = \begin{cases} \text{LOS} & \text{if } P(f_i|los) > P(f_i|nlos) \\ \text{NLOS} & \text{if } P(f_i|los) < P(f_i|nlos) \end{cases} \quad (6.27)$$

where  $H_1$  and  $H_2$  are hypothesis which determine the class based on the PDF form of the feature,  $f_i$  is the value of the feature and  $\lambda_i$  is the defined threshold. An example of selected threshold for signal to noise ratio (SNR) is illustrated in Figure 6.9. According to this graph, the probability of observing LOS condition is higher if the value of SNR is less than the defined threshold. Likewise if this attribute is larger than the threshold, the decision is taken for NLOS class. The list of different values for the selected thresholds is provided in Table 6.1.

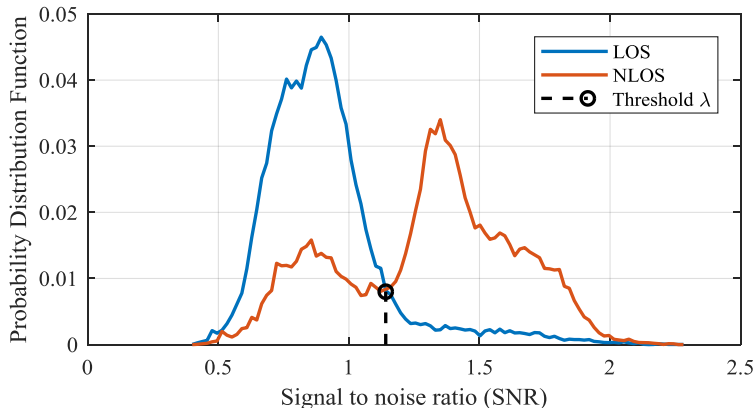


Figure 6.9: Threshold selection of the feature in binary classification approach for the signal to noise ratio (SNR)

Table 6.2: Defined thresholds for different attributes based on the binary classification

Attribute	$P_{max}$	$P_f$	$P_{rss_i}$	$\tau_m$	$T_d$
Threshold	18100	-81.8 dB	-79 dB	750.9	2.14
Attribute	$P_d$	$N$	$S$	$PMR$	$SNR$
Threshold	2.87	-72 dB	-0.29	1.16	1.12

This algorithm is simpler compared to naive Bayes approach and demands less processing power. The reason is only the threshold values are required as model parameters and once the thresholds are known, the PDF values are not required anymore. One disadvantage of this method up to this point is the fact that this method is a classifier and does not provide the probability of each prediction. We can address this issue by utilizing the mean of features voting (MFV) method and represent the final class decision based on the average of the votes in the form of:

$$W_j = \frac{1}{N} \sum_{i=1}^N C_i \quad (6.28)$$

where  $C_i$  is the class output of the feature  $i$ , parameter  $N$  is the maximum number of features which in our case is 10 and  $W_j$  is the confidence metric extracted from anchor  $j$ . If the output of the predictor is 0 for LOS and 1 for NLOS, then the average of the votes will be a number in the range of  $W_j \in R(0,1)$ . If all the features vote for 1 (NLOS), then the output will be also one meaning NLOS with 100% confidence. Likewise if all the features vote for 0 (LOS), then the decision is made for LOS with 100% confidence. Considering the output of this method, it can be realized that the resolution of the predictions depends on the number of features involved which in our case is 0.1. This yields in a stepwise prediction of the output which may be inappropriate. This problem can be tackled in that the confidence value of the output is filtered iteratively to smooth out the prediction signal considering the results of the previous predictions. In order to evaluate the performance of this predictor, the training set is applied to the system and the outcome of the predictor is evaluated. The results are demonstrated in Figure 6.10. In the left diagram in this figure, the output of the classifier based on the confidence level is depicted for each class separately.

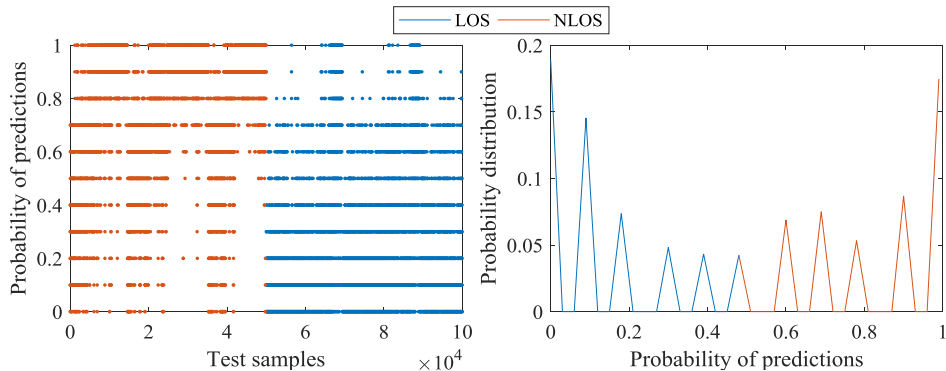


Figure 6.10: The confidence level of the predictions for each sample (left) and the probability distribution of the predictions (right) based on the outcome of the binary classification approach after applying the collected training data set

The first 50000 samples hold the NLOS data which are expected to be in the confidence range of 0.5 to 1. Similarly the second segment holds the LOS data

which is expected to be observed in the range of 0 to 0.5. As it can be seen, there are also misclassifications which are common in many classifiers. The right diagram shows the probability distribution of the outcome. As it is visible in this graph, the majority of predictions are with maximum confidence of 1 for NLOS or 0 for the LOS conditions. After extracting the thresholds from the PDF analysis of each feature, the whole training dataset is fed to the predictor in order to evaluate the accuracy of the predictions. The accuracy of each feature is evaluated separately using MATLAB platform and is provided in Table 6.3.

Table 6.3: Feature performance evaluation in the binary classification method

Attribute	$P_{max}$	$P_f$	$P_{rss_i}$	$\tau_m$	$T_d$
Accuracy (%)	67.7	86.2	81.5	74.3	74.7
Attribute	$P_d$	$N$	$S$	$PMR$	$SNR$
Accuracy (%)	82.1	79.6	75.17	83.8	80

As it can be seen from the table, the most accurate feature is the first path power ( $P_f$ ) with the accuracy level of 86.2%. The weakest feature according to the result is the peak path power ( $P_{max}$ ) with the accuracy of 67.7%.

### 6.3.3. Logistic regression method

This is a very popular method for the sake of its structure's simplicity, prediction performance and the fact that the confidence levels of the predictions are provided for each class [195, p. 286]. This method is also a parametric approach which extracts model parameters from the training dataset and therefore storage of the training data is not required after the model is extracted. The base of this method is the logistic function also called sigmoid function which is defined as:

$$f(x) = \frac{1}{1 + e^{-x}} \quad (6.29)$$

This function is an S-shape signal which converges to 1 when  $x$  tends to infinity and it converges to 0 when  $x$  goes to infinity in negative direction. Therefore, this function effectively maps the range of the input data into the limited range of 0 to 1. The logistic regression method is best suited for binary classification cases where the probability of the outcome is required [196]. This approach in its simplest form when only one feature is available, is defined as:

$$P(y|f) = \frac{1}{1 + e^{-(b_0 + b_1 f)}} \quad (6.30)$$

where  $P(y|f)$  is the probability of observing a certain class given the feature  $f$  is happened,  $b_0$  is the bias of the model and  $b_1$  is the weight of the feature  $f$ . The

two parameters  $b_0$  and  $b_1$  are model parameters that need to be learned from the training dataset. The training process finds an optimum value for the parameters using the gradient descent approach by minimizing the cost function which is the error between the estimation and the target data in the training dataset [181, p. 726]. Examples of the trained models using three different attributes are provided in Figure 6.11.

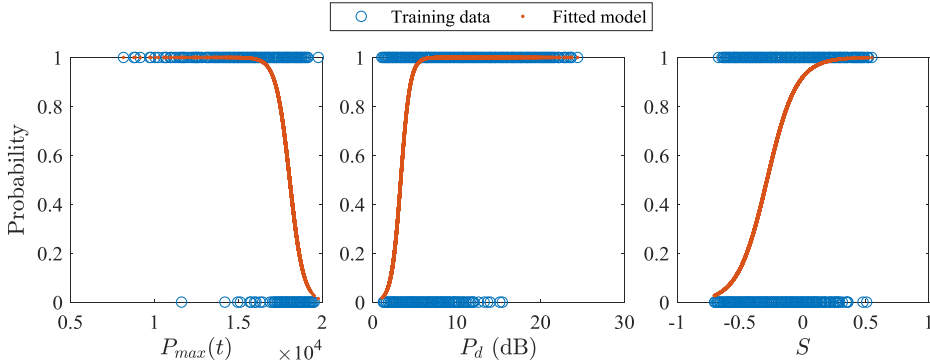


Figure 6.11: The logistic regression fitted model on the three different attributes namely peak path power (left), power difference (middle) and skewness (right)

In case of a multi-feature application, the formula provided in Eq. 6.30 can be extended to multi-feature using the following equation:

$$P(y|(f_1, \dots, f_N)) = \frac{1}{1 + e^{-w}} \text{ where } w = b_0 + \sum_{i=1}^N b_i f_i \quad (6.31)$$

The  $b_0$  parameter defines the position of the midpoint in the logistic function where the data experience a turnover in the output class and  $b_1, \dots, b_N$  are the parameters that define the direction and increase rate of the logistic function. The block diagram of the logistic regression algorithm is demonstrated in Figure 6.12.

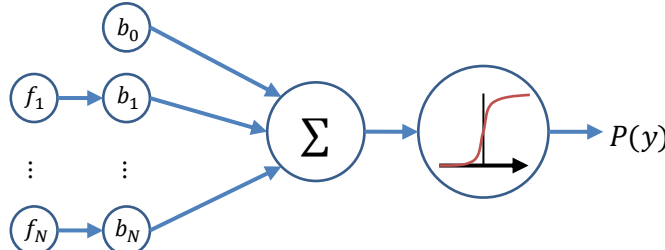


Figure 6.12: Block diagram of the logistic regression algorithm

As it can be seen, the logistic regression method is indeed similar to a single perceptron neuron with a sigmoid function.

### 6.3.4. Non-parametric algorithms

There are a few non-parametric algorithms which could be used for extracting the probability of the classification results. This is however not the main purpose of these approaches and therefore some modifications are required in order to achieve a confidence metric. The first technique is the decision tree which models the data based on a series of conditional sets that form a tree with the initial point on the top, and the leaves representing the target classes. The probability of the final prediction in its simplest form is the number of positive samples in one leaf divided by the number of all the samples dedicated to that leaf. One issue here is, as we go through the stems towards a leaf, the number of available samples decreases which results in a lower accuracy of the probability estimations. The classification process of a decision tree is demonstrated in Figure 6.13.

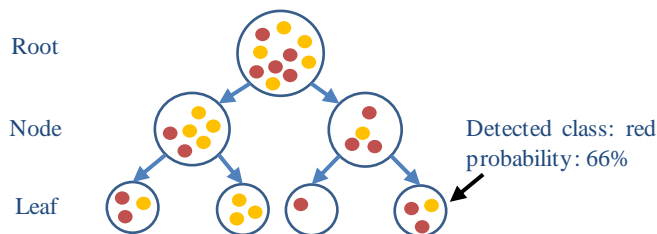


Figure 6.13: Classification process in decision tree algorithm

More advanced modifications of the decision tree approach for the purpose of improving the accuracies of the class probability are provided in [192, 194, 197].

Another popular approach for classification is Support Vector Machine (SVM) which defines a hyperplane in the feature space in order to separate two classes [181, p. 744]. Unlike other non-parametric approaches, the SVM method only retains a small portion of the training dataset that includes the most important supporting vectors representing the dimension of the hyperplane. According to the proposed idea in [197] the probability of the predictions can be extracted by calculating the distance of each sample from the defined decision boundary between the two classes. Classification process of SVM is shown in Figure 6.14.

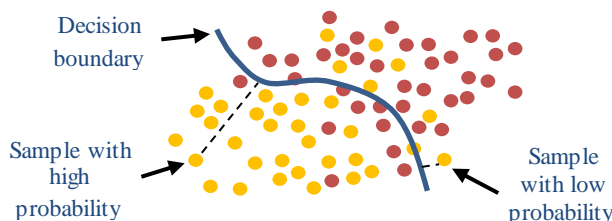


Figure 6.14: Classification process of the SVM algorithm

Another powerful algorithm for classification is k-th nearest neighbor (KNN) that determines the class of an input sample based on the mean of the classes of the  $N$  closest samples in the training dataset. The algorithm procedure is as follows: once an input feature is provided, the algorithm calculates the distance of this input sample with all the samples available in the training dataset and sorts out the first  $N$  data which have the shortest distance to this input. The decision about the class of this input sample is taken based on the average of the class of the  $N$  samples that are sorted out. Since we are considering the shortest distance as a parameter, the majority of selected samples are in the vicinity of the input sample. This algorithm has many variations depending on the formula used for calculating the distance such as Euclidean, city block, Mahalanobis, Chebyshev, cosine, etc. The formula of the Euclidean method is as follows [195, p. 159]:

$$D = \left( \sum_{i=1}^N (x_i - f_i)^2 \right)^{\frac{1}{2}} \quad (6.32)$$

where  $x_i$  is the feature  $i$  of the input sample provided for classification,  $N$  is the total number of features and  $f_i$  is the feature  $i$  from the database and  $D$  is the Euclidean distance between the input sample and the sample in the database.

Although the KNN approach is very simple and powerful, it needs to retain the whole training dataset for prediction. In other words, the extracted model in the KNN method is the training data itself. This issue limits the implementation of the KNN method for the systems with large memory and high processing power.

One method to extract the probabilities of the predictions is to count the number of matching samples to the determined class in the given neighborhood and divide it by the total number of defined neighbors. This can be formulated as follows:

$$P(y) = \frac{N_p}{N_n + N_p} \quad (6.33)$$

As an example, if the number of neighbors is defined as 10,  $N_p$  is the number of samples with the same class as the final detected class, and  $N_n$  is the number of samples holding the opposite class. This is visually illustrated in Figure 6.15.

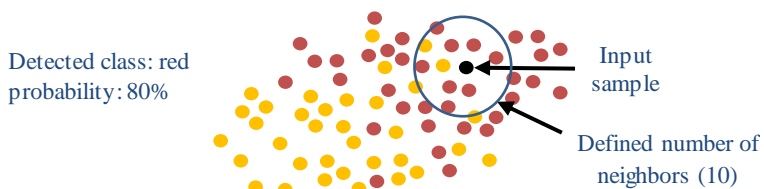


Figure 6.15: Classification process in k-th nearest neighbor (KNN) algorithm with 10 neighbors and probability estimation feature

### 6.3.5. Performance evaluation and comparison

In this section, performance of the introduced NLOS identification algorithms are evaluated and compared. For validation process, usually a portion of collected data is preserved for evaluation and the rest of data is used for training and model extraction. A common metric for evaluating the results is confusion matrix which represents the percentage of the successfully determined samples in class 1 as true positive rate (TPR) versus the number of successfully determined samples in class 0 as true negative rate (TNR). The unsuccessful predictions of each class is false positive (FPR) and false negative (FNR) rates for class 1 and 0 respectively.

The first algorithm under investigation is naive Bayes with JPD classification technique. The prediction result of this algorithm for the same dataset used in training is provided in Figure 6.16. In the left diagram of this figure, the output of the method for each sample is shown. In ideal case, all the NLOS samples (red dots) should show probability of 1 and all the LOS samples (blue) should indicate zero. As it can be seen from the right diagram, the distribution of the probability is nonlinear and mostly condensed around the decision line (0.5). As the NLOS mitigation algorithm is designed based on the probability metric, this issue reduces the accuracy of the mitigation method and also introduces a bias towards the class with higher probability.

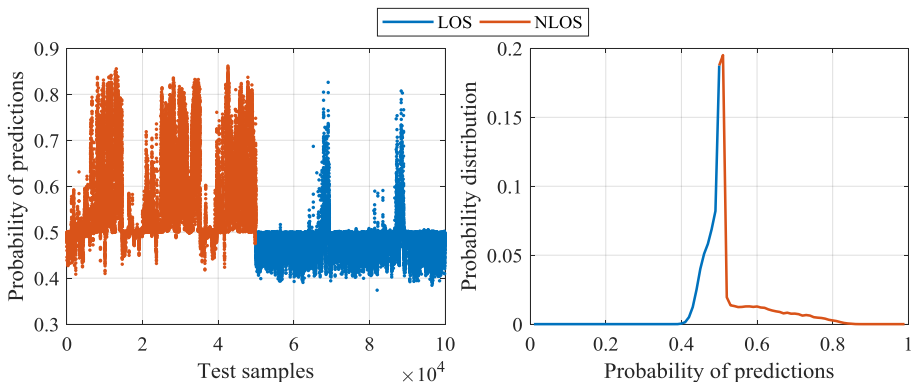


Figure 6.16: The prediction results of the naive Bayes algorithm using JPD for each sample (left) and the probability distribution of the predicted results (right)

The nonlinear prediction of the naive Bayes approach, can be addressed by applying the averaging technique MFV on the predicted probability of attributes. The result of prediction for this combination is demonstrated in Figure 6.17. As it can be seen from the left graph, the predictions are distributed to the whole range of the probability and therefore can be effectively integrated in mitigation algorithm in differential form. The probability distribution of the predicted results that is depicted in the right diagram, confirms that majority of the predictions are shifted to maximum or minimum probability and fewer samples are condensed around the decision boundary.

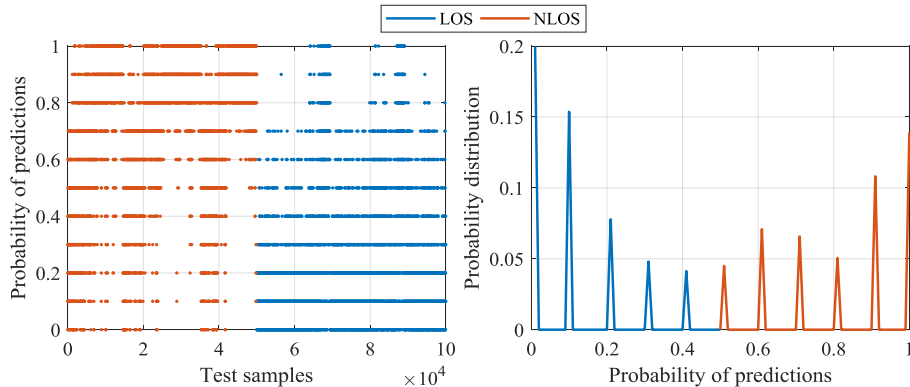


Figure 6.17: The prediction results of the naive Bayes algorithm using MFV for each sample (left) and the probability distribution of the predicted results (right)

The accuracies of both variations of the naive Bayes (NB) methods are provided in the confusion matrices shown in Figure 6.18. The green boxes describe the number of successful predictions versus the red boxes describing the number of wrong predictions. The overall performances of both variations shown in the blue boxes are identical with a slight advantage of MFV classification case. The TPR for NB with JPD is 82.5% and the TNR is 89.1%. These parameters for NB with MFV are 83.9% and 88% for TPR and TNR respectively. The structure of the NLOS mitigation algorithm is designed in a way that it is less sensitive to false alarms or FNR. Therefore, the most important criterion is the TPR parameter which is expected to have high rate for the sake of avoiding the filter divergence. In other words, if the predictor detects a LOS case wrongly as NLOS, the localization engine can still continue without any problem as the real data are in ideal LOS case. However, in reverse scenario, the risk of filter divergence exists.

		Naive Bayes with JPD			Naive Bayes with MFV		
		Target Class			Target Class		
		LOS	NLOS	TNR/FPR	LOS	NLOS	FPR/TNR
Output Class	LOS	<b>44571</b> 44.6%	<b>8756</b> 8.8%	<b>83.6%</b> <b>16.4%</b>	<b>43998</b> 44.0%	<b>8058</b> 8.1%	<b>84.5%</b> <b>15.5%</b>
	NLOS	<b>5429</b> 5.4%	<b>41244</b> 41.2%	<b>88.4%</b> <b>11.6%</b>	<b>6002</b> 6.0%	<b>41942</b> 41.9%	<b>87.5%</b> <b>12.5%</b>
TPR/FNR	<b>89.1%</b> <b>10.9%</b>	<b>82.5%</b> <b>17.5%</b>	<b>85.8%</b> <b>14.2%</b>	<b>88.0%</b> <b>12.0%</b>	<b>83.9%</b> <b>16.1%</b>	<b>85.9%</b> <b>14.1%</b>	

Figure 6.18: Confusion matrix of the naive Bayes approach with JPD (left) and MFV (right) including the TPR, TNR, FPR, FNR and overall accuracy

At the next step, the efficiencies of the binary classification approach is evaluated. This approach benefits from the MFV classification technique in its last stage as it was described before. Therefore, the performance of this method is very similar to NB with MFV with the same overall accuracy level of 85.9%. The results of prediction are provided in Figure 6.19. In this method however, the TPR and TNR values are more balanced resulting in a better separation of classes. As the TPR value is more important for the mitigation approach, this method provides a better confidence metric for NLOS identification compared to the NB methods.

		Binary Classification		
		Target Class		
		LOS	NLOS	TNR/FPR
Output Class	LOS	42893 42.9%	7033 7.0%	85.9% 14.1%
	NLOS	7107 7.1%	42967 43.0%	85.8% 14.2%
	TPR/FNR	85.8% 14.2%	85.9% 14.1%	85.9% 14.1%

Figure 6.19: Confusion matrix of the binary classification method presenting the final accuracy rate, TNR and FPR (1<sup>st</sup> row) and TPR and FNR (1<sup>st</sup> column)

The next algorithm is logistic regression which provides probability metric as well as classification result. The prediction results of this method for the samples used in the training dataset are depicted in Figure 6.20. Unlike the methods based on the MFV classification, the distribution of the results is not stepwise and it is dispersed in the whole range with the most focus on the extreme points.

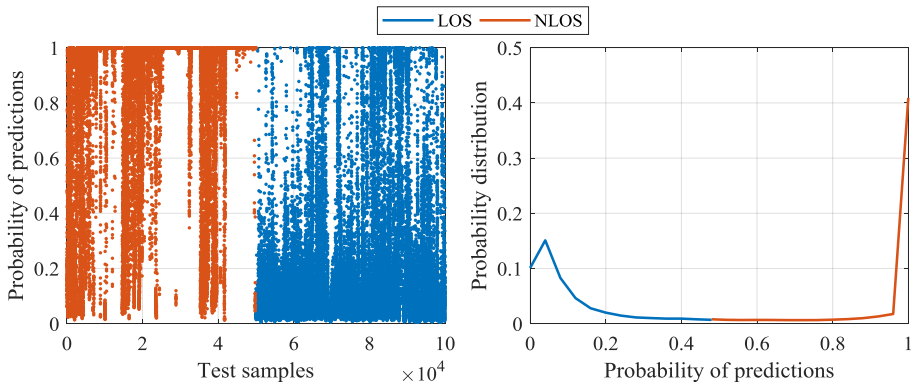


Figure 6.20: The prediction results of the logistic classification algorithm for each sample (left) and the probability distribution of the predicted results (right)

Although the distribution of the NLOS and LOS cases are not symmetrical (right graph in Figure 6.20), the fact that the detection of NLOS cases is more weighted than the LOS is desired in mitigation approach for the reasons explained before. According to the confusion matrix provided in Figure 6.21, the overall achieved accuracy of this approach is 87.2% which is higher than the other two approaches introduced before. Another advantage is having almost similar rate of TPR and TNR parameters which leads to a better quality of NLOS predictions.

Logistic Classification			
Output Class	Target Class		
	LOS	NLOS	TNR/FPR
LOS	43249 43.2%	6084 6.1%	87.7% 12.3%
NLOS	6751 6.8%	43916 43.9%	86.7% 13.3%
TPR/FNR	86.5% 13.5%	87.8% 12.2%	87.2% 12.8%

Figure 6.21: Confusion matrix of the logistic classification method presenting the final accuracy rate, TNR and FPR (1<sup>st</sup> row) and TPR and FNR (1<sup>st</sup> column)

Although the non-parametric approaches are not suitable for the implementation in a low memory processor with low processing power, the prediction results of a few of them are provided here using a PC for the sake of comparison. The training and evaluation process in these algorithms are performed using the MATLAB classification toolbox. The confusion matrix of the decision tree and KNN techniques are provided in Figure 6.22. According to the results, the decision tree method has an accuracy of 89% versus the KNN approach which provides a superior accuracy of 91% with similar TPR and FNR rates.

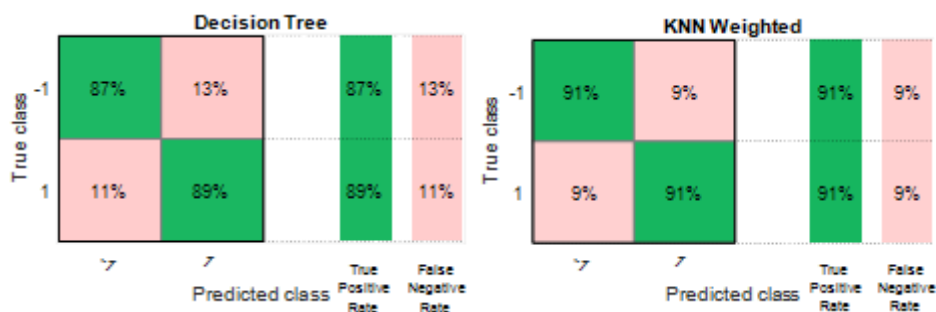


Figure 6.22: The confusion matrix of decision tree approach (left) and the weighted KNN (right) representing the TPR and FNR values for each

The same training process explained before, is also performed on SVM algorithm with its confusion matrix demonstrated in Figure 6.23. This method has achieved an accuracy of 87.5% in average with TPR of 86%.

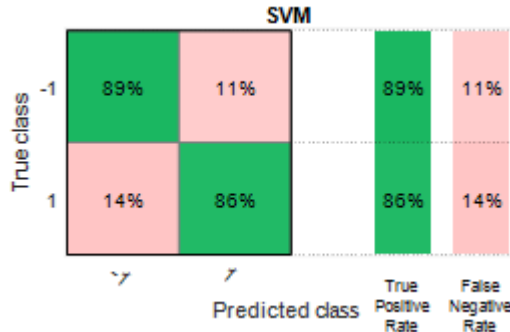


Figure 6.23: The confusion matrix of the supported vector machine (SVM) representing the TPR and FNR values

The decision tree approach used for the classification, resulted in generating 8519 conditional If-Else sentences which are very extensive to implement in a small microcontroller. Likewise, the KNN approach needs to retain the whole dataset which in our case demands 10MB of storage space. The SVM method used in this experiment utilized a Gaussian kernel with scaling factor of 3.2 and resulted in generating 29374 vectors for each feature. This represents almost one third of the whole training dataset. As it can be seen from the results, the performances of non-parametric approaches are only slightly better than parametric methods. Keeping in mind that the parametric approaches only need a few parameters to store and have a very simple calculation process, it can be deducted that they offer reasonably better options for constrained processing systems. The achieved performance results of all the discussed approaches are summarized in Table 6.4.

Table 6.4: Summary of the prediction results using different classification algorithms

Algorithm	NB+JPD	NB+MFV	Binary	Logistic	DT	KNN	SVM
Overall %	85.8%	85.9%	85.9%	87.2%	88.5%	90.5%	87.3%
TPR	82.5%	83.9%	58.9%	87.8%	89%	91%	89%
TNR	89.1%	88%	85.8%	86.5%	88%	91%	86%
Prediction Runtime <sup>1</sup>	449ns	2.32μs	2.03μs	1.86μs	1.1ms	6.5ms	4.4ms

In order to evaluate the performances of these algorithms in real experiments, a test setup is used with a stationary target node and 4 anchors. As the localization engine was recording the distance measurements, several NLOS conditions are

<sup>1</sup> Performed in MATLAB on a PC with 8 CPU cores with frequency of 2.7GHz and Windows 7

deliberately created by blocking the transmission path between the nodes. The differential distances of the nodes with visible NLOS error are plotted together with the probability output of different determination approaches in Figures 6.24 and 6.25. In these trials, only parametric approaches are applied. Due to nonlinear outcomes of the NB-JPD method, the results of this method are not included. As it can be seen from these graphs, all the techniques are able to successfully determine the NLOS conditions. Among the three methods, the performance of logistic regression is outstanding and in some severe NLOS cases reaches up to maximum probability which is desired. The performance of the naive Bayes and the binary classification are similar. Although both methods benefit from MFV approach, in case of the binary classification, the output results are filtered but the result of the NB method is provided without filtering. This is the reason that the probability prediction of naive Bayes has step jumps. If the filtering is not applied, the result of both techniques will be stepwise with the resolution of 0.1.

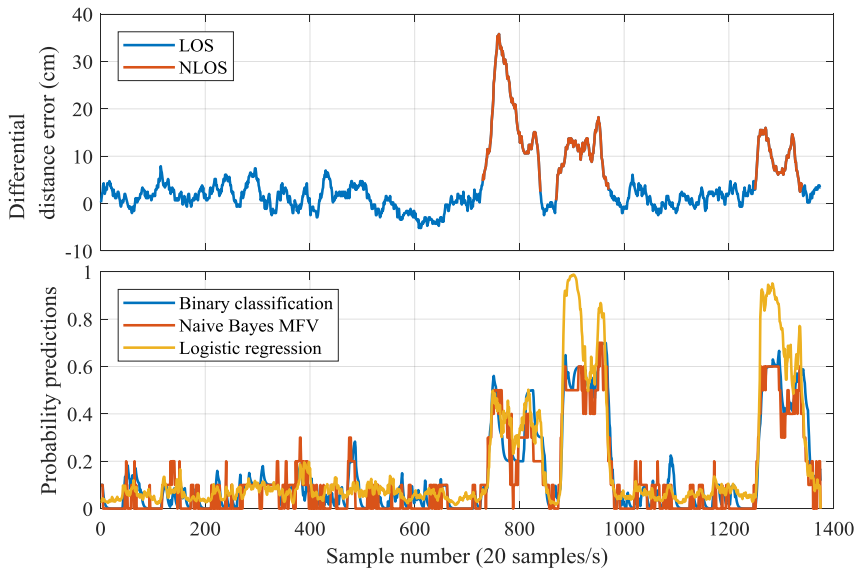


Figure 6.24: Differential distance error of the anchor pair 1 and 2 with the output of the three different NLOS identification approaches

As conclusion, it has been observed that the performance of the non-parametric approaches are better than the parametric ones but with the cost of large required memory and heavy computation power. The parametric approaches require only a few parameters to describe the model with simpler mathematical process and provide almost similar performances. Among the parametric approaches, the logistic regression method has better accuracy and relatively short prediction time. In terms of simplicity of implementation, binary classification is the easiest method with slightly better performance compared to the traditional naive Bayes algorithms. Keeping these results in mind, the logistic regression approach is selected as the base system to be implemented in error mitigation algorithms.

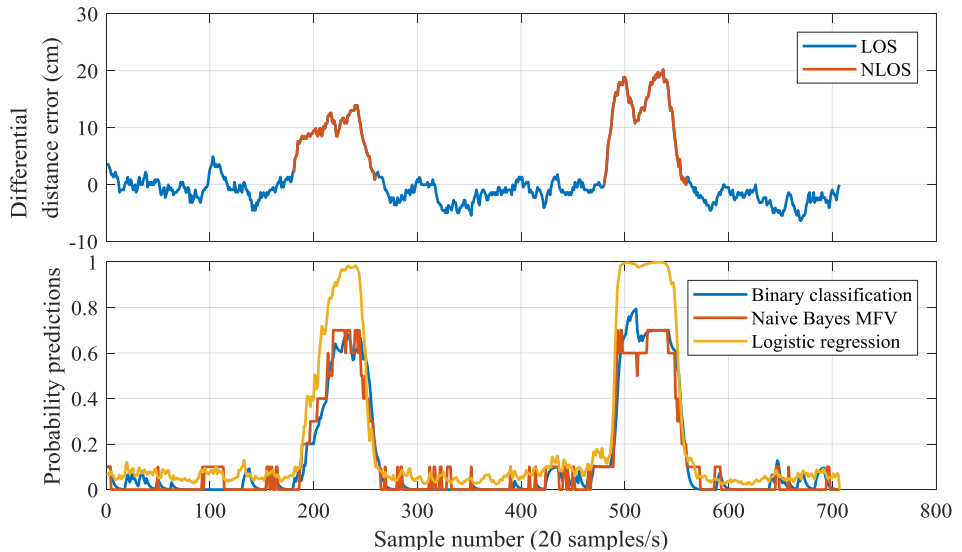


Figure 6.25: Differential distance error of the anchor pair 1 and 3 with the output of the three different NLOS identification approaches

## 6.4. Mitigation Techniques

There are many approaches proposed in the literature for mitigation of the NLOS error. One trivial solution when the number of anchors is redundant is to remove the samples of the anchor with NLOS condition and consider only those with LOS conditions [198]. This is however not effective as the predictions may not be accurate and therefore good results are dismissed. Use of the weighted least square (WLS) is a common solution proposed in many papers [166, 167, 169, 199]. In this method, the nodes with NLOS conditions are less weighted so that their influence on the final results is suppressed. Güvenc et al. [198] provide and compare many approaches such as WLS, maximum likelihood (ML), Cramer-Rao lower bound (CRLB), etc. Vaghefi et al. [200] propose another mitigation technique based on the semi-definite programming.

The NLOS mitigation methods based on the extended Kalman filter are discussed extensively in the literature. These filters are mostly known under the name of biased EKF (BEKF) or modified EKF (MEKF). Principally, there are two common ways of mitigating the NLOS error based on the EKF filter. The first one increases the variance matrix of the measurement  $\mathbf{R}$  for the results with NLOS error. This way the effect of the error is less weighted by the Kalman gain. As an example, Garcia et al. increase the variance of the noise for 3m once the NLOS condition is detected [176]. In other works presented in [163, 164, 201], the authors extract some weighting metrics such as residual of the distance error or variance of the ranging data to determine the amount of additional variance to be

added in the measurement noise variance (matrix  $\mathbf{R}$ ). In the second technique, either the innovation term of the update phase is reduced or the error estimation covariance (matrix  $\mathbf{P}$ ). An example of this type is provided in the work of Yu et al. [202]. A combination of these two scopes is also practiced. Examples of this hybrid type are presented in the following papers [171, 172, 203].

In chapter 5, different localization mechanisms namely EKF, UKF and  $H_\infty$  are introduced. The NLOS mitigation methods addressed in this section are based on the modifications applied to these algorithms for two purposes. The first goal is to stabilize the localization method against unrealistic inputs created due to the NLOS error and the second is to suppress the influence of the created NLOS error on the final location estimates. The first goal can be achieved by modification of the measurement noise variance and the second goal with the manipulation of the innovation term in the update phase. These two techniques are described in detail in the next subsections.

### 6.4.1. Measurement noise variance manipulation

It is known that in the NLOS cases, the distance measurements are biased. The easiest way to reduce the effect of the NLOS error is to increase the covariance of the measurement noise, so that the Kalman gain dedicates less weight to erroneous inputs. In NLOS identification phase, a confidence metric is developed which represents the probability of the NLOS case in the range of 0 to 1. Since we have two anchors involved in each differential distance data, the sum of these weights as an added value is considered. This way, it is not important which node pairs have experienced the NLOS conditions. The sum of the weight represents the erroneous data which should be less weighted in the matrix. The measurement noise covariance matrix can be adjusted according to the following equation:

$$\mathbf{R} = \begin{bmatrix} r + (W_2^2 + W_1^2)M & 0 & \dots & 0 \\ 0 & r + (W_3^2 + W_1^2)M & \dots & 0 \\ 0 & 0 & \dots & r + (W_n^2 + W_1^2)M \end{bmatrix} \quad (6.34)$$

where  $W_n$  is the confidence metric of the anchor  $n$ , parameter  $M$  is a constant acquired empirically based on the worst case NLOS error observed which is estimated to be around 80 cm and parameter  $r$  in case EKF or UKF is applied is the variance of differential distance for each anchor pair and for case  $H_\infty$  is applied is the positive weight defined deterministically for LOS cases.

In order to evaluate the effectiveness of this modification, a set of experiments are performed with NLOS conditions created between the nodes. The logistic regression is applied for detection of the NLOS cases. For error mitigation case, the noise variance modification matrix is utilized using different filters. The results of one of these experiments are shown in Figure 6.26 providing the results

of all the discussed filters compared with the biased filters named as biased EKF (BEKF), biased  $H_{\infty}$  (BH $_{\infty}$ ) and biased UKF (BUKF).

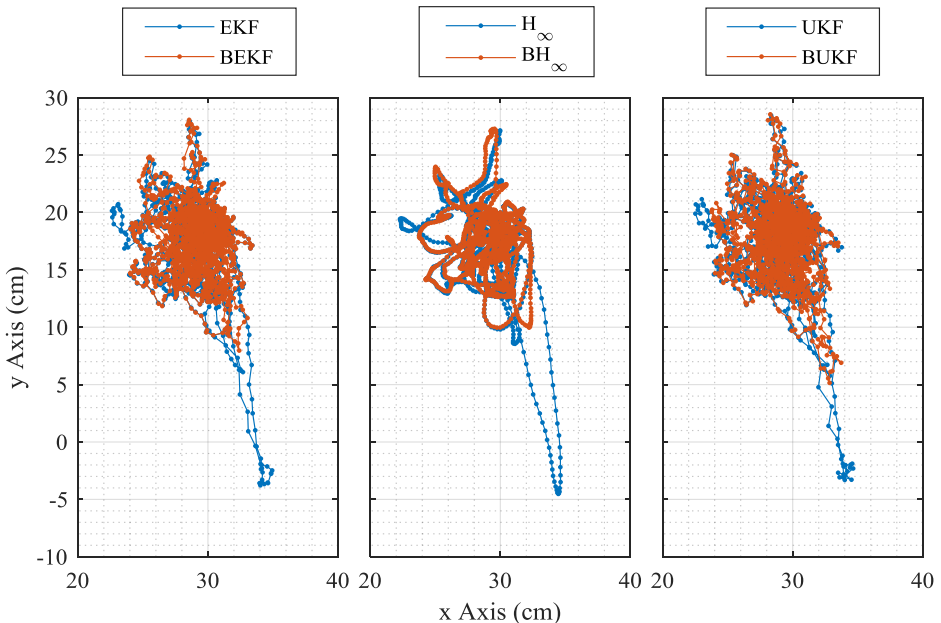


Figure 6.26: Localization results of the EKF, UKF and  $H_{\infty}$  filter before and after the new modified variance term is applied on the stationary node located at (30, 20)

The target node in this experiment was a stationary node located at coordinates of (30, 20). The results shown in the graph indicate the amount of improvement achieved through modification of the variance term. All the three filters show significant sensitivity to NLOS noise in their original form. The large deviation visible at bottom direction is the result of the NLOS error. When the modification is applied, this error is largely reduced so that the effect of the NLOS error is hardly detectable. To evaluate the amount of improvement, the localization error of the estimated locations are calculated. The results for each sample are depicted in Figure 6.27. As it is visible in this graph, there is not any noticeable change in the results of the filters before and after modification when LOS condition is available. However, once the NLOS condition is appearing, the original filter deviates up to 17cm whereas the modified filter reduces it down to less than 5cm. The amount of reduction based on this mitigation technique for EKF method is 55%, for  $H_{\infty}$  is 77% and for UKF method is 45%. Better results of the  $H_{\infty}$  filter is due to more robust structure of this filter compared to others as well as tighter settings of the filter's parameters. It is also visible that, in all cases, there is an offset in the error which is around 15 cm. This is due to the filtering of the range data before feeding the data to the localization system as well as transmission delays of the antennas which could be improved by calibrating the nodes. If the

nodes are stationary, another method can be applied in that another state parameter is added to the model known as bias. This bias will be updated during the iteration process and eventually converges to the mean value of the bias. Details of this process is provided in the work proposed by Najar et al. [204].

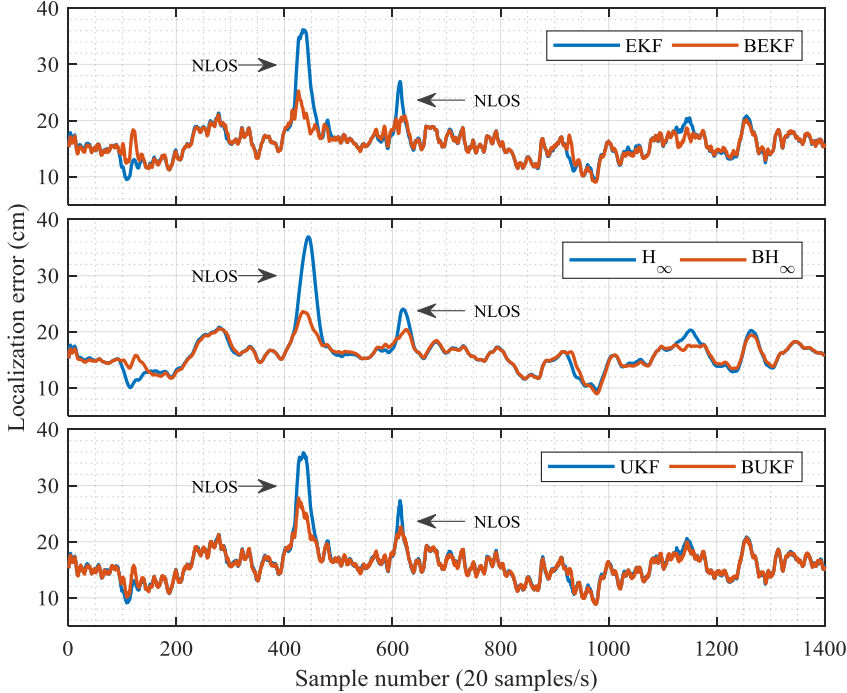


Figure 6.27: Localization error of different filters for a fixed node evaluated before and after applying the modification in variance term

### 6.4.2. Innovation term manipulation

The second step of the mitigation with the goal of reducing the NLOS error before applying in the localization system is to modify the innovation term in the update phase of the filters. The innovation term is defined to be the error between the estimate of the filter based on the model prediction and the real measurement received from the sensors. The update equation of the EKF and  $H_\infty$  filters with their innovation term highlighted are presented as follows:

$$\hat{x}_{k+1} = A_k \hat{x}_k + A_k K_k \underbrace{(y_k - h(\hat{x}_k))}_{\text{Innovation term}} \quad (6.35)$$

The similar term applied for unscented Kalman filter (UKF) is:

$$\mu_x^+ = \mu_x^- + K_k \underbrace{(y - \mu_y)}_{\text{Innovation term}} \quad (6.36)$$

The proposed modification term is a bias which is achieved from the confidence metrics estimated by the NLOS identification method. The equations of the new bias term is described below for different filters:

$$\hat{\mathbf{x}}_{k+1} = \mathbf{A}_k \hat{\mathbf{x}}_k + \mathbf{A}_k \mathbf{K}_k (\mathbf{y}_k - \mathbf{h}(\hat{\mathbf{x}}_k) - \mathbf{B}) \quad (6.37)$$

$$\boldsymbol{\mu}_x^+ = \boldsymbol{\mu}_x^- + \mathbf{K}_k (\mathbf{y}_k - \boldsymbol{\mu}_y - \mathbf{B}) \quad (6.38)$$

$$\begin{cases} \mathbf{B} = (\mathbf{W}_n - \mathbf{W}_1) (\mathbf{y}_k - \mathbf{h}(\mathbf{x}_{k+1})) & \text{Star form} \\ \mathbf{B} = (\mathbf{W}_n - \mathbf{W}_{n-1}) (\mathbf{y}_k - \mathbf{h}(\mathbf{x}_{k+1})) & \text{Chain form} \end{cases} \quad (6.39)$$

As it can be seen from the last equation, the weight terms  $\mathbf{W}_n$  that are achieved from the identification phase are applied differentially to compensate the error based on the direction of the NLOS bias error. As an example, if the NLOS case is observed between the target node and the anchor 1, then the bias term will be negative and if it is observed between the anchor 2 and the target node, a positive bias will be applied in the innovation term. In Eq. 6.39, different bias terms are defined depending on whether the star pairing selection method is applied or the chain form. In case there is LOS condition, both weight terms will be close to zero which result in a very small value of the bias. This means in LOS cases, almost no changes in the innovation term will occur. Similar situation can happen when both sides of the transmission paths are blocked so that the weights of both anchor pairs are similarly large and indicating NLOS conditions. In such cases, large weights cancel out their effects and hence no or little amount of corrective bias will appear. This differential weighting concept in determination of positive or negative error in the case of a practical experiment is shown in the Figure 6.28.

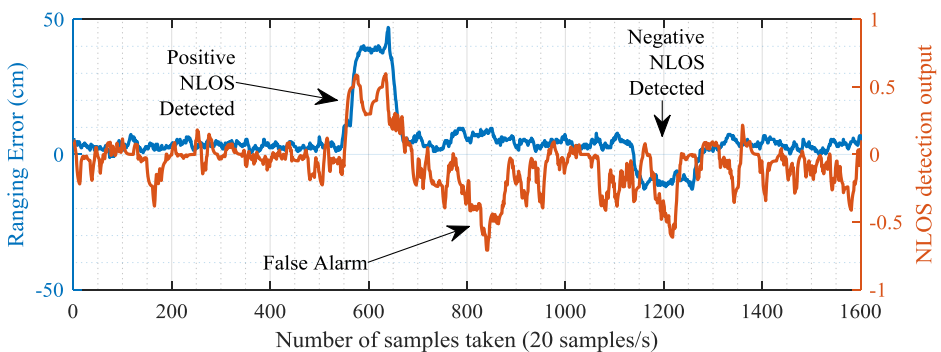


Figure 6.28: Differential NLOS identification mechanism based on the comparison of the weights achieved from each anchor

In the experimental setup, two systems are compared. These are the filters which are modified with only variance term and the filters modified in variance as well as innovation term. This is performed for the sake of evaluating the amount of

improvement that can be achieved when all the modification terms are applied. The results of this experiment are provided in Figure 6.29 for different filters.

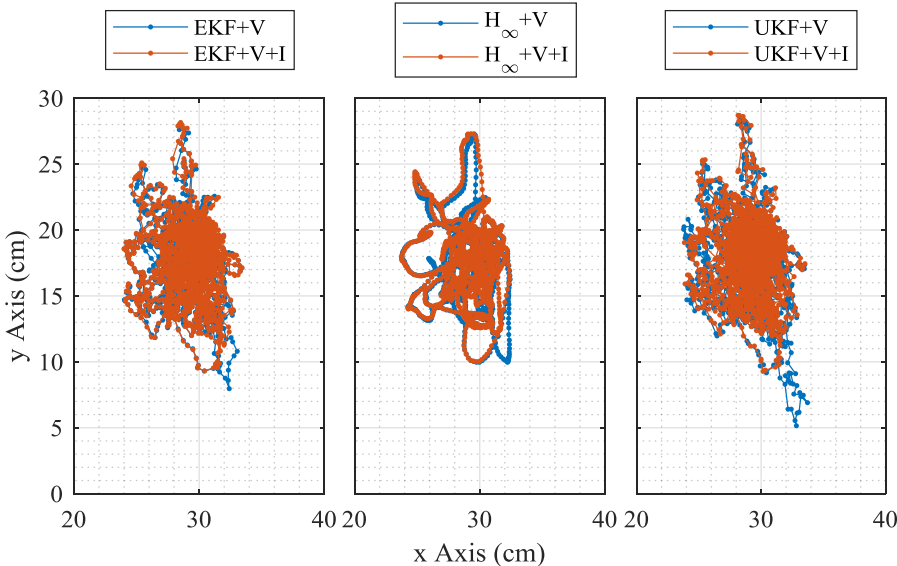


Figure 6.29: Localization comparison of the EKF, UKF and  $H_{\infty}$  filters with variance modification and filters with variance and innovation term modification

According to the results, modification that is applied to the innovation term further reduces the NLOS error which yields in more stability of the filters against biased erroneous measurements. To evaluate the amount of the improvement, the localization error of the estimated locations is calculated and illustrated in Figure 6.30. Further improvements are 3cm for EKF, 2cm for  $H_{\infty}$  and 6cm for UKF filter with both modifications applied. As it was also observed in the previous trial, these improvements are achieved only when the NLOS cases where observed and for the LOS cases no perceptible changes exist. In case of this experiment, the amount of NLOS error was not large enough to diverge the filters. In another experiment, more severe NLOS conditions are created which produce NLOS errors in the range of up to 3m. This condition leads to divergence of EKF filter. The proposed methods not only stabilize the filters, but also reduce the introduced NLOS error down to 35cm for EKF and  $H_{\infty}$  filter and 50cm for UKF. The localization results of this experiment are demonstrated in Figure 6.31 for different filters. In this graph, it was not possible to plot the results of the original EKF filter due to divergence issue. The localization error of these filters are provided in Figure 6.32. Here the robustness of the  $H_{\infty}$  filter is noticeable which could resists against the non-ideal and erroneous input data and keep the error below 100 cm. As a conclusion, the efficiency of the proposed mitigation approach is proved which is useful in reduction of the NLOS error without impelling the performances of the filters in LOS conditions.

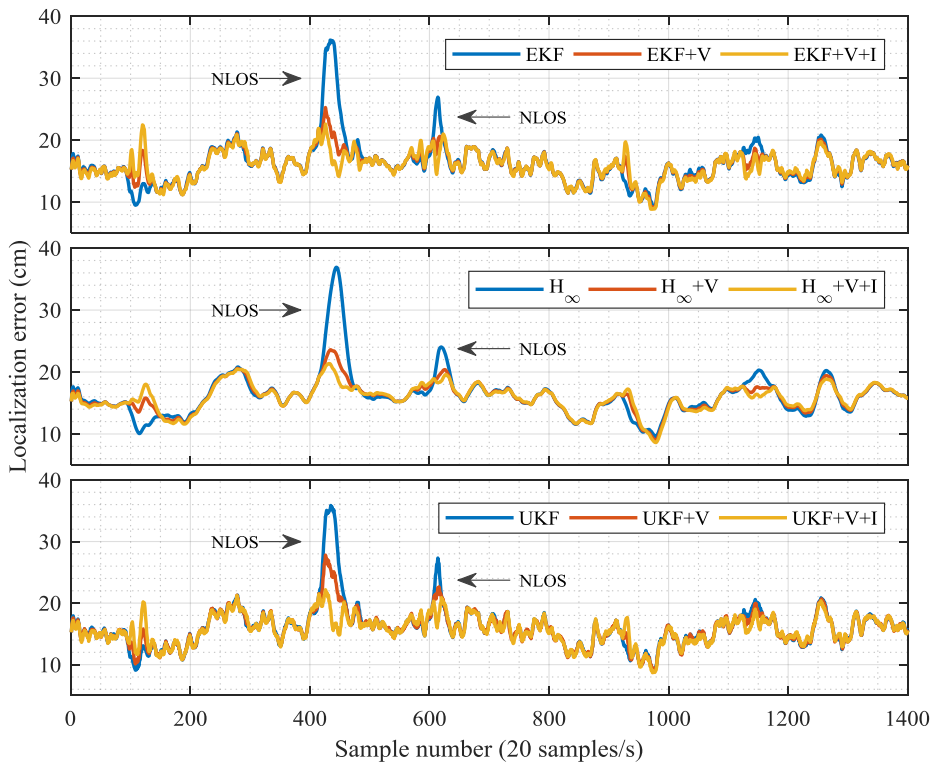


Figure 6.30: Localization error of different filters before applying the modification and after applying with variance and finally including both modifications

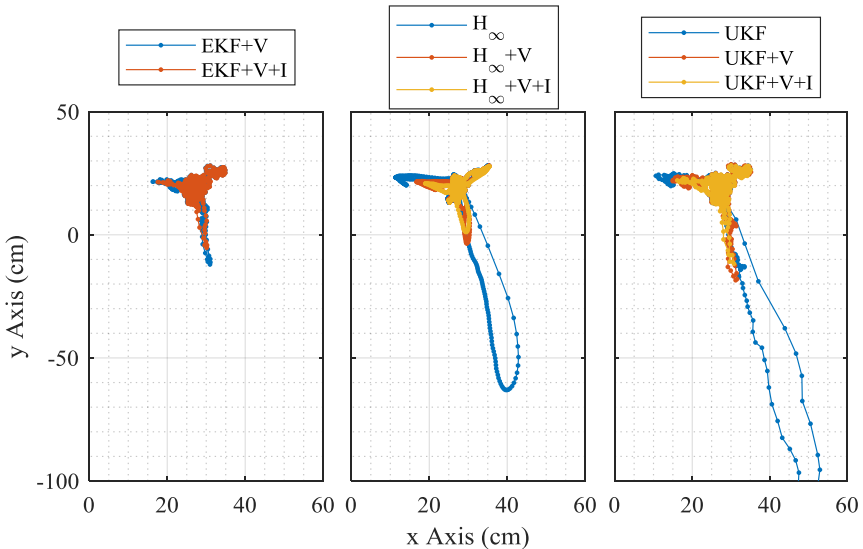


Figure 6.31: Localization results of EKF,  $H_{\infty}$  and UKF filters in severe NLOS conditions

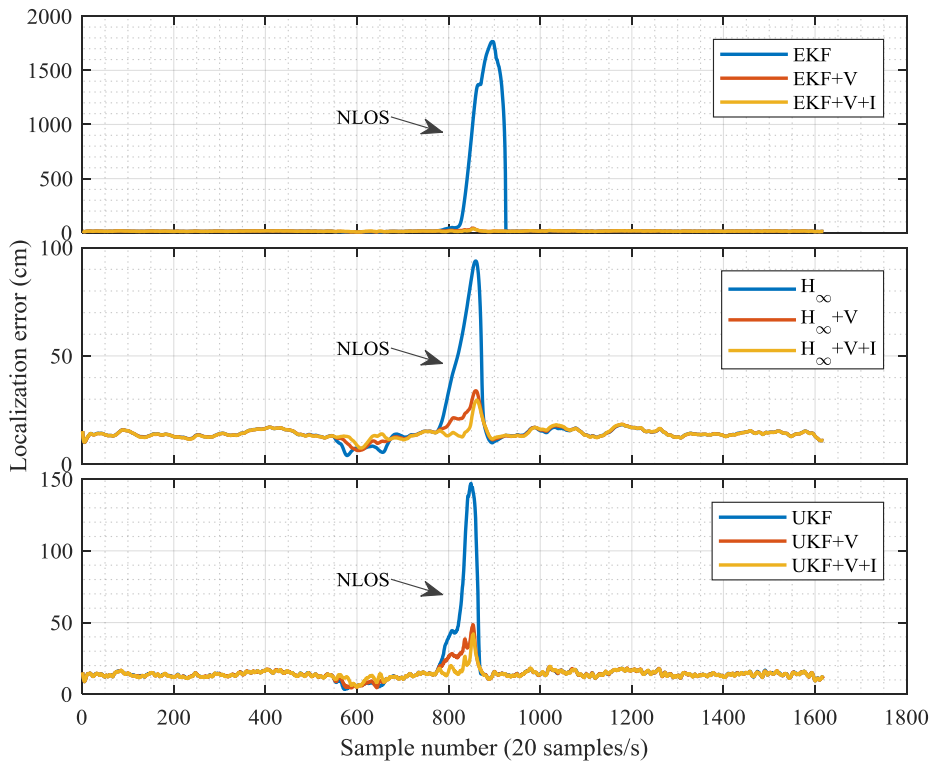


Figure 6.32: Localization error of different filters in case of severe NLOS conditions with different modification techniques applied

# **7. System Implementation Aspects**

This chapter covers the development of the hardware and software parts of the nodes used in the localization system. As it was discussed briefly in Chapter 2, the base of the designs for implementation of UWB technology is the DW1000 chip from Decawave which is used in both integrated chip as well as in module form containing an integrated chip. In the first section, details of the hardware including the development process of the prototypes are provided. Second section explains the details of software components used for the experimental trials.

## **7.1. Hardware Design**

The DW1000 chip is not a standalone chip and needs to be served by an external processor. The tasks of this processor are setting up the registers of the module based on the requirements of the application, triggering the data transmission or reception, handling the data transfer to and from the module and managing different energy saving modes of the module. As the host of the UWB modules, a microcontroller from STMicroelectronics is used which is benefiting from an ARM Core processor with floating point unit, hardware multiplier and plenty of other useful integrated peripherals such as UART, DMA, SPI, I<sup>2</sup>C, etc. which are necessary in complex localization applications demanding high computational power. For developing the hardware, different aspects are considered. The main idea was to develop one circuit in very small form factor which can be carried by small robots or drones or even humans. As these devices are considered for self-navigation applications, they are equipped with a portable battery, a charging circuit and highly energy efficient components to have a standalone device capable of running for a long time. The microcontroller of the module acts as an interface between the UWB module and the host that carries the system. For the projects of this thesis, two prototypes are developed which are introduced in the next section. In addition to the hardware required for UWB implementation, many other supportive components are integrated which are power supply, data storage and communication units, inertial and motion sensory devices, etc. Details of these components are provided in subsection 7.1.2.

### 7.1.1. Prototype development

The first developed prototype is based on the DW1000 chip as frontend chip providing UWB communication and a microcontroller from STM32L101 series of STMicroelectronics as the main organizer of the circuit which handles the data communication between the nodes and extracts the location data. The dimensions of this circuit are  $5 \times 2 \text{ cm}^2$  including an SMA connector for an external antenna. The antenna used for this project is a printed circuit board antenna but other types of antennas suitable for UWB technology can be used as well. This board also contains other additional components such as voltage regulators, quartz crystal or oscillator, and the antenna matching circuit. The connection of this board to a host PC is either over USB or UART interface. The block diagram of the elements involved in the design of the first prototype is illustrated in Figure 7.1.

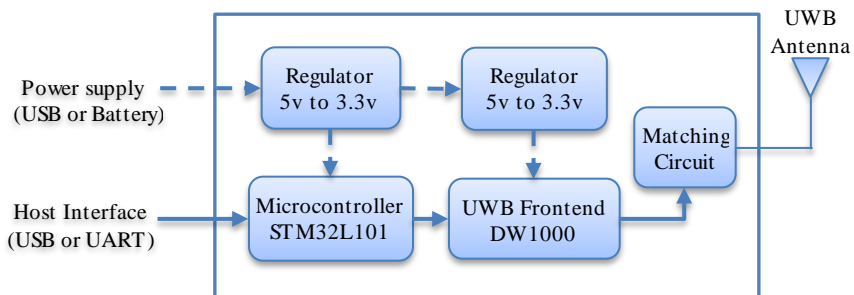


Figure 7.1: Block diagram of the hardware components used in the first prototype

The designed hardware module itself is capable of being used as either mobile target or anchor node since this is determined by the software of the module. However for the case of anchor devices, additional holding stand is considered that integrates a large capacity backup battery which guarantees long time operation of the stationary nodes. Photos of an assembled module used as target node and another module used as anchor device are provided in Figure 7.2.

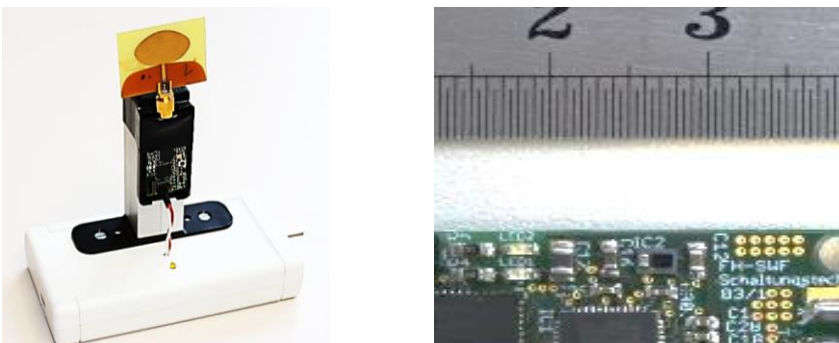


Figure 7.2: Hardware platform used for both anchor module (left) with module holder and additional backup battery and a tag module (right)

The second prototype is designed based on the DWM1000 module which benefits from an onboard chip antenna. All the required side components such as matching circuit, regulator and oscillator are integrated in the module so that no other additional components are required. This module is shielded against the noise and EMC problems and it is certified in many countries which means it can be easily integrated in a product without further licensing issue. The microcontroller used in this version, is STM32L433 which is more powerful than the first prototype as it is based on M4 family of ARM processors with floating point unit and hardware multiplier. The dimensions of this board are  $4.5 \times 2.5 \text{ cm}^2$  which is slightly larger than the first prototype, but it includes the antenna as well. In this prototype, a small size Li-Po battery is used which could be integrated in the enclosure of the board. Photos of the second version of the prototype are provided in Figure 7.3.

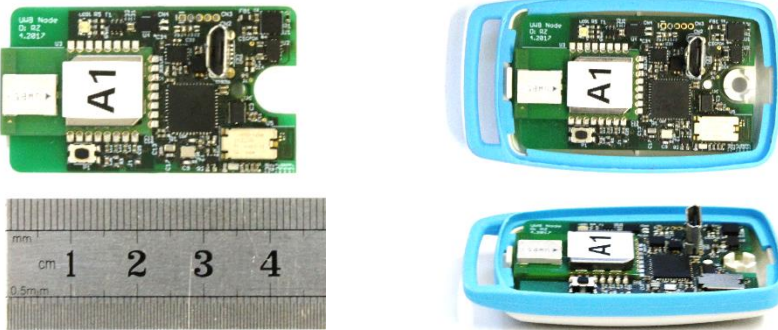


Figure 7.3: Photos of the second prototype with and without enclosure designed based on the DWM1000 module from Decawave

In this prototype, many other supportive components such as battery charging circuits and power supply, IMU units, communication units and a large data storage unit are integrated which are introduced in the next section.

### 7.1.2. Peripheral components

One of the design criterion for this prototype was to equip the board with IMU sensors for the sake of improving the localization results using data fusion techniques. For this purpose, two hybrid sensors are selected. The first chip is a sensor which integrates an accelerometer and a gyroscope sensor with the part number LSM6DSM. The second chip has an accelerometer and a magnetometer integrated in the chip with the product number LSM303C. Both of these sensors are low power components with very low current consumption in sleep and standby modes provided by STMicroelectronics. Although there are other hybrid sensors on the market which offers all the three sensors in the same package, we have decided to use these two sensors for many reasons as an example the sum of the power consumption of these two sensors together is less than a triple sensor chip and the second reason is these sensors offer higher accuracy and resolution

## 7 System Implementation Aspects

compared to other devices that were available at the design time. Another reason is in the selected scenario we have two accelerometers onboard which could be fused together for the sake of improving the accuracy of the measurements. Important characteristics of these two sensors are provided in Table 7.1.

Table 7.1: Important characteristics of the selected IMU sensors [205, 206]

Part number	First sensor			Second sensor			Current	
	Type	Range	Accuracy	Type	Range	Accuracy	Active	Standby
LSM6DSM	Accel.	$\pm 16\text{g}$	$\pm 40\text{mg}$	Gyro.	$\pm 2\text{kdpS}$	$\pm 2\text{dpS}$	$650\mu\text{A}$	$3\mu\text{A}$
LSM303C	Accel.	$\pm 8\text{g}$	$\pm 40\text{mg}$	Magn.	$\pm 16\text{G}$	$\pm 1\text{G}$	$450\mu\text{A}$	$6\mu\text{A}$

For communication purposes, one Bluetooth module from Taiyo-Yuden with the product number EYSGJNAWY is considered which could be used for inter-communication or transferring the localization data to a host PC in either nodes. As another way of interacting with user, a NFC memory chip (M24LR16E) is provided which could be used for storage of the settings or other parameters such as coordinates of anchors or the role of the nodes as anchor or target node. These parameters can be transferred to the memory of this chip either using smartphone or a NFC reader device which is practical in dynamically changing setups as no cable-based connection or a PC is required. This chip requires a NFC coil antenna which is available on the market in the form of flexible PCB and can be integrated inside the device enclosure. For the sake of storing the localization data in offline mode or logging of the system states for debugging purposes, a NOR flash is utilized with a capacity of 1MByte. The block diagram of the components used in the second prototype including their product numbers is provided in Figure 7.4.

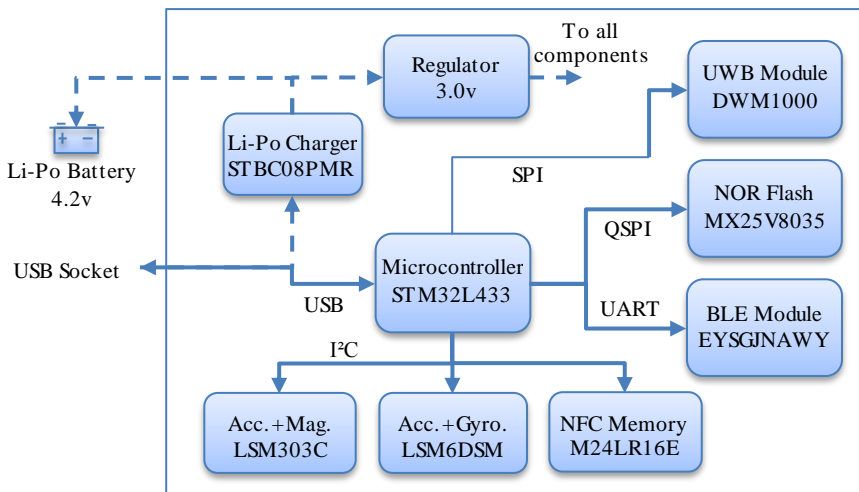


Figure 7.4: Block diagram of the hardware components used in the second prototype

### 7.1.3. Energy efficiency constraint

As the modules are aimed to run on a battery, it is important to consider low energy components in the design and apply the energy efficient modes in the program wherever applicable to reduce the total amount of consumed power. Almost all the components used in this circuit have such an energy saving mode. The Decawave module defines 5 operation modes as listed in Table 7.2 [207].

Table 7.2: Different operation modes of Decawave chip DW1000 and module DWM1000

Mode	Deep Sleep	Sleep	Initial	Idle	TX	RX
Maximum current	50-100nA	1μA	4mA	12mA	130mA	150mA

As it can be seen from the table, the highest amount of current is consumed when the module is receiving data. This depends naturally on the settings of the module such as preamble length, payload size, baud rate, PRF rate and number of packets transmitted per second. The provided values in this table are the results of real measurements carried out based on the settings in our project which are preamble length of 1024, PRF of 64 MHz, baud rate of 110 Kbps, payload size of 8 Bytes and packet transmission rate of 80 packets/s. The amount of current that is consumed during the receive part is around 150 mA which is very high for a battery operated device. This can be however reduced if the receive mode is enabled only shortly before the signal is arrived and turned off again when the receive phase is complete. As it was discussed before, the unilateral TDoA localization system utilizes the first anchor as only transmitter, the other anchors as both receiver and transmitter and the target nodes as only receiver. In case of the first anchor, the device needs only to activate the transmitter when the signal is going to be transmitted and after that switch to the initial mode to save power. Here, care must be taken not to choose sleep or deep sleep mode as in these modes the main clock is off and therefore periodical transmission with the fixed time interval is not possible. In case of other anchors, the nodes must first activate the receive mode, then wait for a defined time interval and finally activate the transmit mode. During signal receive and transmit time, the device can switch to the initial mode, however for the first listening phase, the node must be in the receive mode until a signal is detected. The same issue exists for the target nodes as these nodes should wait for a signal to arrive which is not known in advance. To reduce the power consumption in receive mode, Decawave provides sniff feature which turns the receiver unit on and off within definable tiny time slots. This way the module turns on the receiver circuitry (analogue and digital) only for a short period of time and in case no signal activity is detected, it deactivates it again to save power. Further improvements can be achieved by enabling this mode only once in a long time or just shortly before the signal is expected. This is for example the case when the signal of the reference node is already detected, so that the target node knows the next signal is expected 10ms after the reference

## 7 System Implementation Aspects

---

signal is time stamped. Details of the energy saving modes and the applied modes in operation time of a unilateral TDoA system is provided in Figure 7.5.

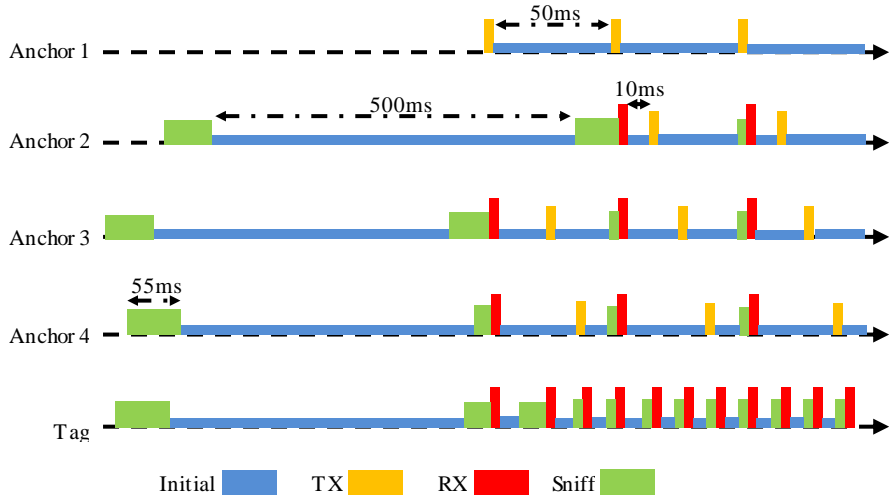


Figure 7.5: Timing diagram of the unilateral TDoA localization system with 4 anchors demonstrating the applied energy modes and related power consumption

Once the nodes are activated, the target nodes and anchors other than the first node, performs sniffing mode only once in each 500ms and for the period of 55ms. Since the interval time of transmissions are 50ms, this 5ms additional time guarantees recognition of a packet once the transmission is started.

In an experiment, the current consumption of a target node in a unilateral TDoA is measured using an oscilloscope which is measuring the voltage of a  $1\Omega$  shunt resistor differentially. The results are illustrated in Figure 7.6. This graph shows different phases of device operation which are as follows: In the first phase the target device is in sniff mode, altering the activity of the receiver circuit. This phase has peak current of 150mA but since the reception mode is active only for a short period of time, the average of the current decreases down to 50mA. As soon as an arriving signal is detected, phase 2 begins which is data reception and demodulation. This phase has the highest current consumption of up to 180 mA. Once the reception of the signal is completed, phase 3 begins in that the module starts analyzing the signal, filling the corresponding registers and transferring the data to the microcontroller. This stage consumes up to 130 mA. The stage 4 is the last phase when the device switches to the initial mode to save power. At this phase the consumed current is as low as 15 mA. The amount of current stated here includes the consumption of all the elements in the circuit board including the microcontroller. The sniffing process is performed for the anchor 1 for a long time since the arrival of this signal is not predictable. For other anchors however the sniffing mode is very short as it is activated only 2 to 3 milliseconds before arrival of the signal since the arrival of the signal at that time is expected. The

anchor 1 repeats the process every 50ms. This time is enough for 4 other anchors to send a signal sequentially with interval delay of 10 ms. In this project however only 3 other anchors are utilized leaving some space for one backup anchor which could be utilized additionally in the future.

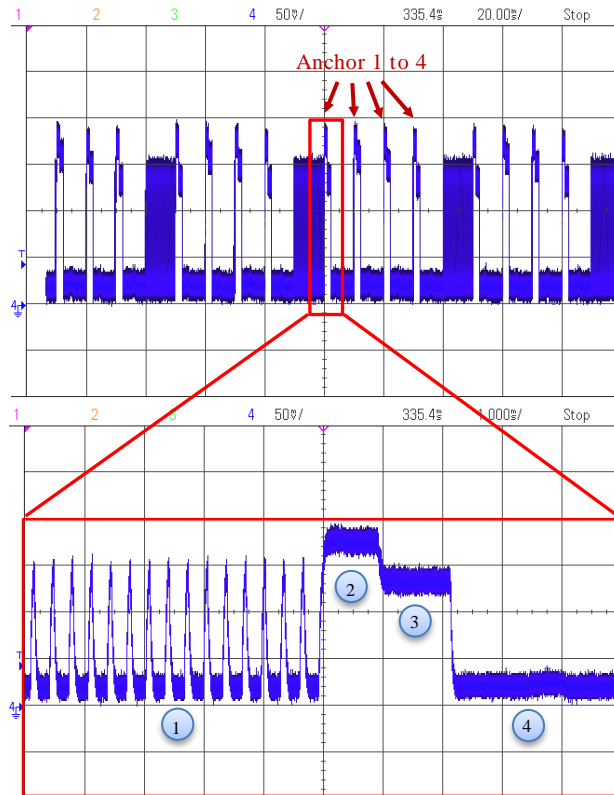


Figure 7.6: Voltage of the shunt resistor representing the current consumption of a target node in a unilateral TDoA system with different phases of operation modes

The microcontroller used in this project also benefits from different operating modes. These are active mode, low power run mode, sleep, shutdown, and several stop modes. The power consumption of each of these modes with their transition time is provided in Table 7.3.

Table 7.3: Different operation modes of STM32L433 stating current consumption [208]

Mode	Run	Sleep	Shutdown	Stop 0	Stop 1	Stop 2
Current	4.6mA	1.3mA	130mA	108 $\mu$ A	4.63 $\mu$ A	1.3 $\mu$ A
Transition time	-	6 cycles	6 cycles	4.1 $\mu$ s	7.8 $\mu$ s	8.2 $\mu$ s

The amount of current consumed in microcontroller in normal run mode is measured to be around 4.5mA and in sleep mode sinks down to 1.5mA.

## 7.2. Software Design

This section describes the structure of the software developed for a standalone localization system which is implemented in this thesis. The software includes many components including the drivers, hardware related libraries and several user applications developed for different purposes. Besides the main tasks of the node circuit board which are interaction with the UWB module and extracting the location data, many other applications are developed for interaction with user, debugging and logging the data and different states of the program as well as collecting sensory data for improvement of the localization performance. In addition to the software developed for microcontroller of the node devices, an application is developed for PC in Java language for interacting with the module, data storage in PC and demonstrating the localization results graphically. Details of these software components are described in the following sections.

### 7.2.1. Communication and user interaction

For demonstration and data recording purposes, an application is developed which simplifies monitoring and configuration of the distance measurement module. This software accesses the measurement module over virtual COM port which is generated by communications device class (CDC) profile of the USB driver of the module. With the help of this software, users are able to setup the configuration parameters of the module, operation modes, coordinates of anchors, and finally read and demonstrate the measurement data and its related parameters. In addition to that, it is possible to show the location of the anchors and target node graphically during the operation.

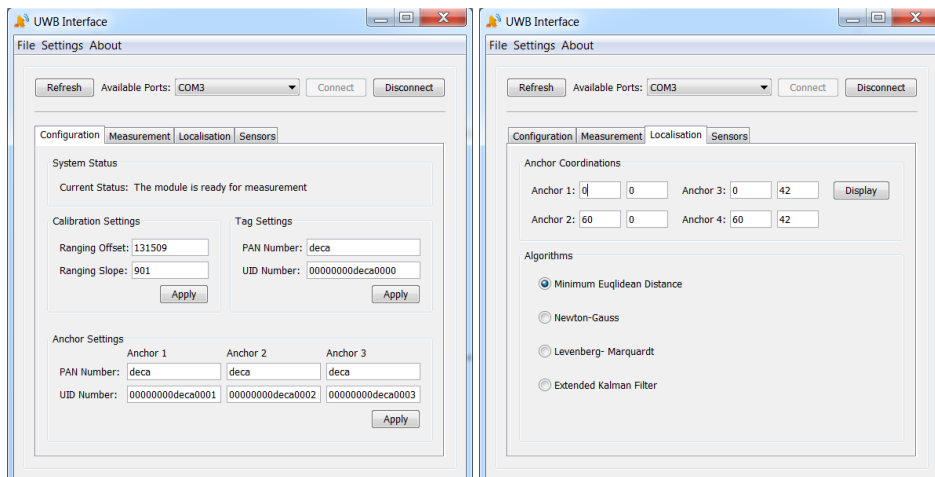


Figure 7.7: Screenshots of the Java program designed for monitoring, configuration and data logging showing the configuration tab (left) and localization tab (right)

The screenshots of the GUI of this program are demonstrated in Figure 7.7. Once the program is started, the user can choose the COM port which is dedicated to the device from a drop down list. In total, there are four tabs in this program which are used for configuration as it is depicted in the left screenshot of Figure 7.7, measurement tab, localization (right picture in Fig. 7.7) and sensor tab. The configuration tab is used for applying calibration parameters, node and network IDs and monitoring the last operation mode of the module. In the measurement tab, general status of each anchor is shown such as availability, error codes, etc. In addition to that, the data of the measurements are provided both in distance and time stamp for each anchor pairs. The localization tab is used for graphical demonstration of the anchors as well as target node in 2D space. For this purpose, user should provide coordinates of the anchors and choose a localization algorithm. A screenshot of the graphical plot is presented in Figure 7.8.

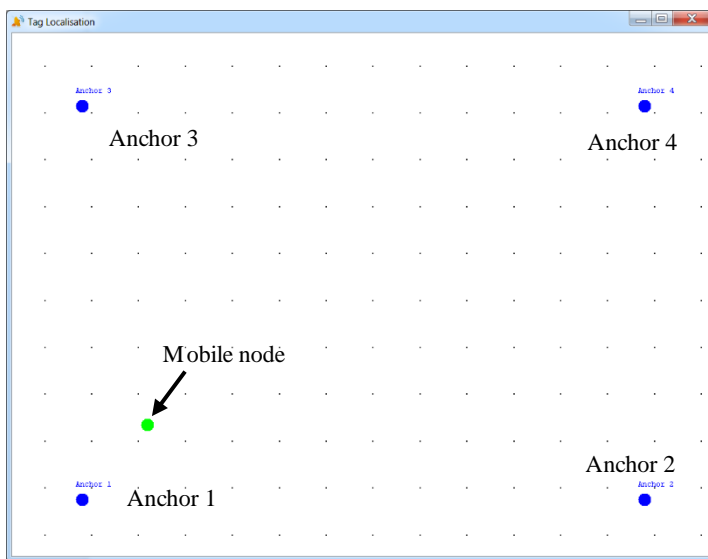


Figure 7.8: Graphical presentation of the anchors' and node's locations in 2D space

In the graphical presentation, a grid with the dimensions of  $5 \times 5\text{cm}^2$  is defined in order to provide a clear visual distance estimation. The connection status of the anchors are coded in the color of the nodes in a way that the blue color indicates connection availability and the red color shows an anchor with missing data. The node with green color represents the target node which can move dynamically based on the latest location information received from the node.

In the sensor tab, the data of each IMU sensor is demonstrated in its raw form. There are in total 4 windows which represent the latest data of each sensor with the possibility of enabling or disabling the sensor. All the received data of the modules are logged in a text file which are used later for signal analysis in the MATLAB program. The structure of this text file as well as the description of the logged parameters are provided in Appendix A4.

## 7.2.2. Debugging and data storage

During the implementation phase of the software routines, as well as localization algorithms, it was necessary to store the results of all the calculations in a database which could be used later in offline mode by MATLAB program for further analysis or simulation of the algorithms. One way of transferring the data from microcontroller was to transmit the data over USB port using the CDC profile which simulates a virtual COM port in PC. As the speed of this type of data transfer is high (115200 bps), many parameters are defined to be transferred to PC as defined in the previous section. The problem of this method is that a PC is required with a USB connection during the node operation time. This is however not always possible to realize as the nodes are dynamic and should be carried by small robots. To solve this problem, the external NOR-Flash is used to store the data during the localization process. As well as that, the address of the anchor nodes are stored in this memory. These data can be transferred to PC over USB port after the experiments are over. To simplify the process of data transfer in a way that no additional program is required, the mass storage device (MSD) class of USB is applied that treats the device as a general storage device which appears as an additional partition in PC. The recorded data in the memory are shown in the form of text files which can be easily copied to the computer. Likewise the setting data of the anchors are compiled in a text file which could be simply copied to the memory from the PC using drag and drop feature. The simultaneous implementation of two USB classes namely CDC and MSD demands a new class in the form of composite device which abstracts both classes in hybrid form. This way both functionality of virtual COM port and additional partition are available in parallel. A mechanism is developed which automatically detects the way data should be treated by scanning the USB port status. If a USB cable is connected, the data will be transferred over CDC class and if the cable is not available, the data are stored in the flash. The flowchart of this mechanism is demonstrated in detail in Figure 7.9.

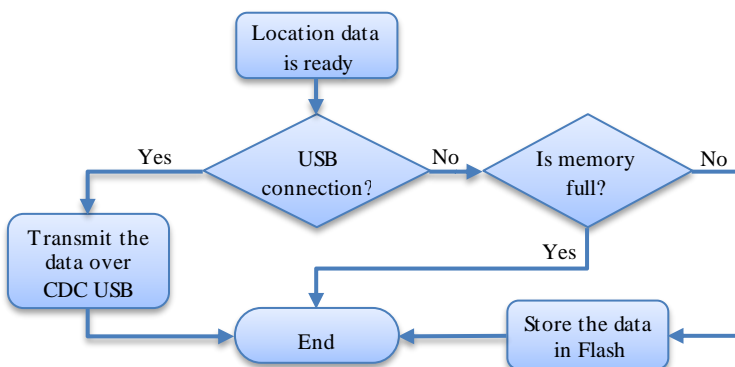


Figure 7.9: Flowchart of the data route selection between online and offline recording

The main purpose of the NOR-Flash memories is to hold data that will be read often and should be available immediately. But they have a limited number of write cycles (100000 times) and the process of writing is time consuming (5 ms per page). As well as that in the read process, the data are accessible for each addressed word but in case of writing only a page of data (512 Bytes) are addressable [209]. This means it is not possible to write a byte of data in a certain address and for each write command at least 512 bytes should be programmed. In case of erase command, it is only possible to erase a block of data (4096 Bytes) which takes 50ms to perform. These limitations arise two problems. The first one is that the data need to be collected until the minimum required data is available otherwise the maximum number of write cycles will be reached immediately. The second problem is the erase and write time is pretty large which yields in losing arriving localization packets. To solve these problems, double buffering method is implemented in that two buffers with the capacity of 4 KB are utilized. One of the buffers is dedicated for data reception and collects the data as soon as they are available. Once this buffer is full, the index of the buffers are swapped so that the last buffer can be dedicated to memory write process and the new buffer starts to collect the data. This way the race effect of buffers is avoided as the writing process of a buffer in that size is finished sooner than the filing process. This process is shown graphically in Figure 7.10.

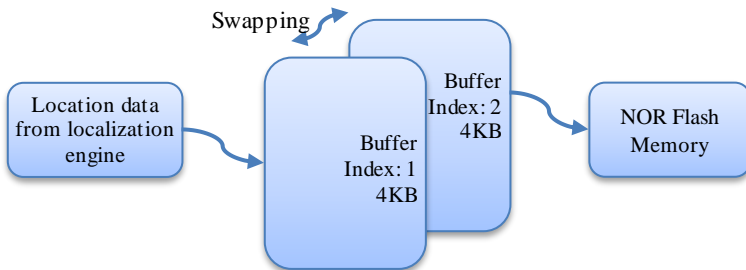


Figure 7.10: Double buffer writing technique with buffer swapping

Another way of increasing the lifetime of the memory is to implement wear leveling techniques. In this technique, different locations of the memory are used to write the data in a way that all the pages of the memory experience almost the same number of write cycles. This approach is implemented by mapping a dynamic address entry table to physical addresses and updating the table based on the number of writes. An example of this technique is provided in [210]. As the memory used in this project is accessed by PC as an external partition, the content of the memory should be formatted according to FAT (File Allocation Table) system. For this purpose, a library is used which provides an abstract version of the FAT format for both accessing the data of the memory as well as writing the data in the memory space. Supported commands of this library are erase, read, write, new file, new folder, and name change. Unfortunately the FAT library does not support wear leveling.

### 7.2.3. Developed module software architecture

The programming language used in this project is C which is developed in Atollic TrueSTUDIO platform provided by STMicroelectronics. Beside the hardware low level drivers provided from ST, other utilized libraries and middleware are CMSIS ARM Core library, DW1000 middleware from Decawave, IMU sensors drivers and FAT library both provided by ST and flash memory driver from Macronix. Different application layers of this project are defined as physical layer, hardware access layer, middleware and libraries, and user applications. Different components of the developed application according to these layers are illustrated in Figure 7.11.

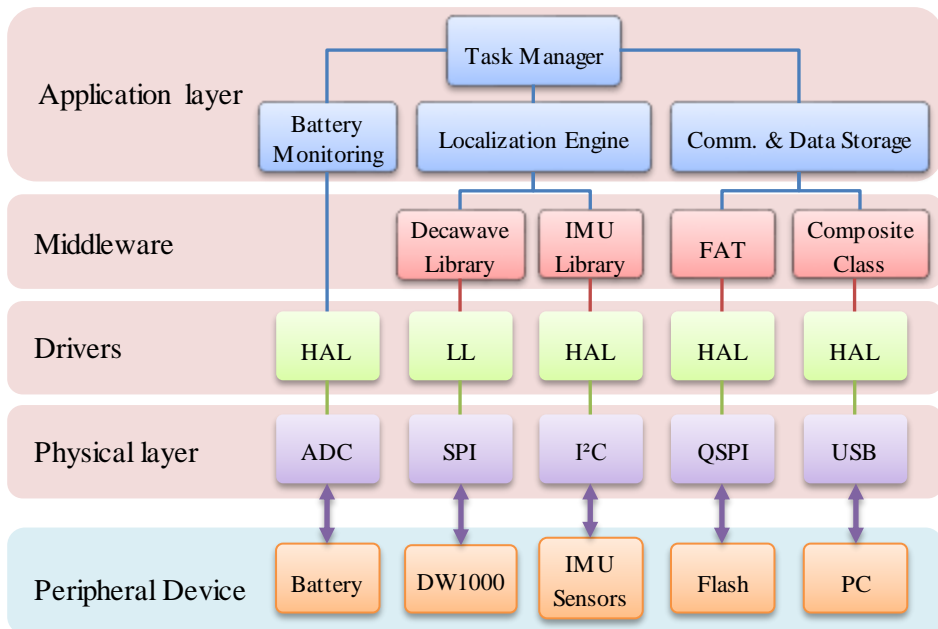


Figure 7.11: The block diagram of software components used in the microcontroller

The ST Company provides two sets of libraries for the low level peripherals. The first one is HAL (Hardware Abstraction Layer) which is designed to be hardware independent and provides the users a set of high level commands to access the peripherals without having the detail knowledge of the hardware. They are easy to understand and to implement as most of the required components are generated by code generating programs automatically. The second type is LL (Low Level) which is designed for advanced users and its structure is closer to hardware language. For this type of driver, deeper knowledge of peripherals as well as their working concept is required but its advantages are higher performance, better resource efficiency and more user control on the process. This is for example used for SPI bus which was connected to Decawave chip. The reason is Decawave

module uses the control lines of the SPI bus for switching to low energy modes and the control over these lines are only supported in LL library.

As another feature, the battery status monitoring can be mentioned. It is important to monitor the battery to avoid completely discharging the battery. Once the voltage of the battery reaches 3 volts, the node stops all the reception and transmission requests and switches to shutdown mode to consume very low amount of power. The latest status of the battery is color-coded and is indicated to user over LEDs of the module.

Due to the different roles of the nodes, three different programs are developed for handling the localization tasks. The first one is the anchor number 1 which is also used as the reference node. This node has the task of periodical transmission with a fixed delay interval. The process starts with a transmission at the first possible moment. The time stamp of the transmitted signal is used to calculate the next time of the transmission and will be programmed into the module as soon as the data packet is formed. This process is repeated as long as the node is in operation. The state diagram of this process is shown in Figure 7.12.

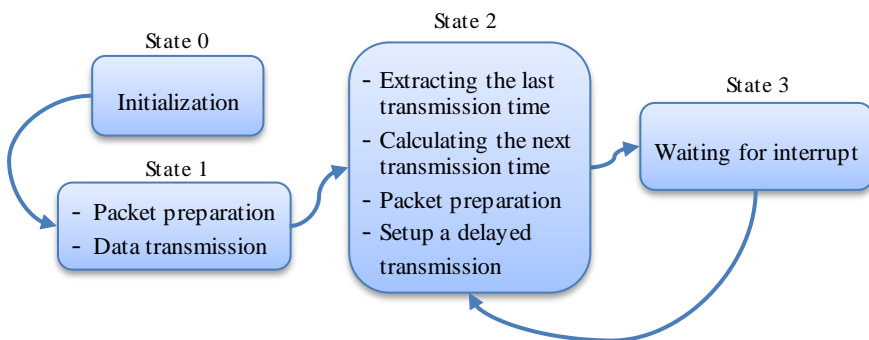


Figure 7.12: State machine of the reference anchor (anchor 1) for setting up a periodical transmission based on the delayed transmission mechanism

The second program is developed for the anchors other than the first one. In case of these nodes, both transmission and reception processes are involved. Same as previous step, a state machine is developed which manages different steps of the program. The process begins with initialization of the UWB module and registers. Then the sniff mode is activated which enables the receive circuitry and waits until a packet from the reference node is detected. In case no packet within the defined time is detected, the program reduces the scan rate to 2 scans per second. Once a packet is detected, the packet is evaluated and the time stamp of the reception is extracted. The next transmission time can be calculated based on the receive time stamp. After this step, a delayed transmission is activated which transmits the packet automatically once the desired time is reached. During this time, the microcontroller is in a delay loop which could be used for handling other tasks of the microcontroller. This process is shown graphically in Figure 7.13.

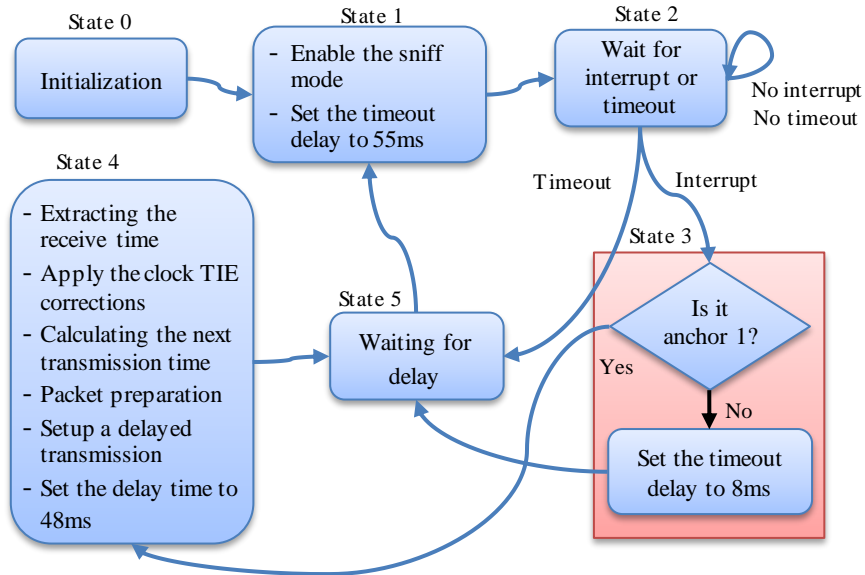


Figure 7.13: State machine of the anchors 2 to 4 describing the process of packet reception and retransmission

In case of the target node, the process includes only receiving the packets from other anchors and performing the localization algorithm. Details of this process are illustrated in Figure 7.14.

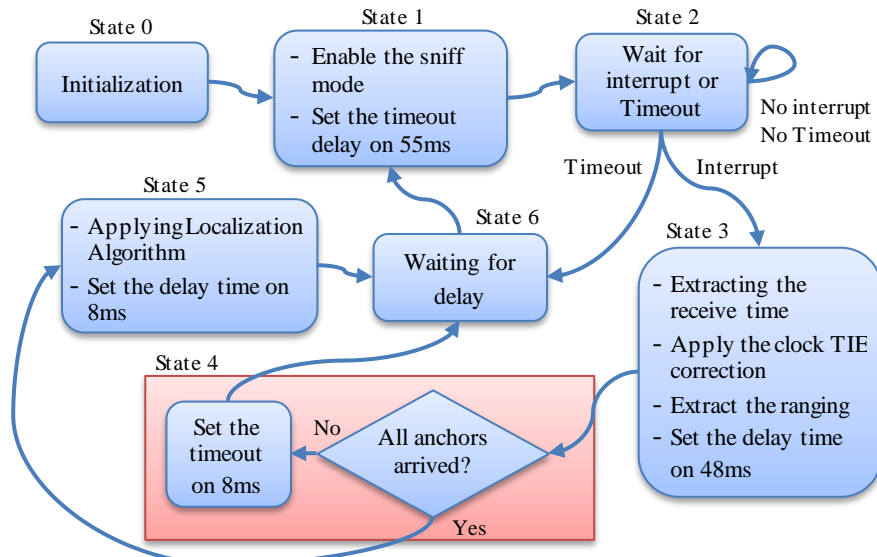


Figure 7.14: State machine of the target node describing the process of packet reception and localization

After implementation of the localization method based on EKF algorithm in a mobile node, the runtime of the program in the hardware platform is measured. One iteration of the algorithm including calculation of the node position for two axes takes roughly 4 ms long. From the total available time of 10 ms between each signal reception, 2 ms is required for data processing in Decawave module (as depicted in Figure 7.6), 1 ms is required to activate the receiver and the rest of time ( $\approx 3$  ms) are defined as constant delay.

### 7.2.4. Frame formatting

In the process of data transmission between the anchors and the target nodes as well as from the target nodes to PC, certain frame formatting is used to control the data flow, detect the erroneous packets and simplify packet detection and decoding. The first frame structure is defined for data exchange between the anchors and the target nodes over UWB radio devices and the second formatting is defined for data exchange between the target nodes and PC over USB port. Details of these protocols are described in this section.

As it was explained in Chapter 2, the IEEE standard supports payload of up to 127 bytes in each packet. In this project, 8 bytes are defined which are transmitted with each packet from anchor nodes to target nodes. Details of the packet's format are presented in Figure 7.15.

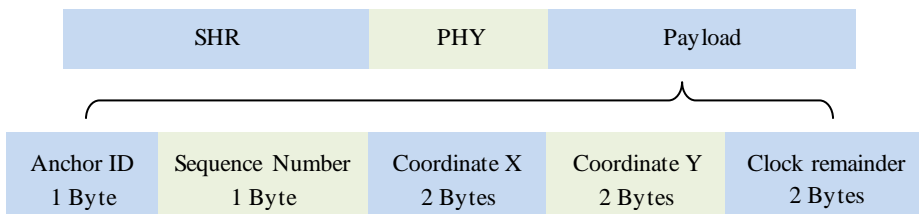


Figure 7.15: Frame format of the packet transmitted from anchors to target nodes

The anchor ID field is used to indicate which anchor has transmitted this packet. The sequence number is a 1 byte field which is increasing by the reference node each time a packet is transmitted. The other anchors only reuse this number for the next transmission so that the target nodes can recognize the missing packets of each anchors. These bytes are followed by two other fields each with two bytes holding the location coordinates of the transmitting anchor in the centimeter unit. The last field is clock remainder which contains the amount of lost time as a result of clock rounding effect as described in Chapter 4.

Another segment of the software which is benefiting from frame formatting is the data transfer protocol between the microcontroller and the PC. This protocol is defined in the form of master-slave communication in that the program in PC is defined as master and the microcontroller as slave. The data of the module need

## 7 System Implementation Aspects

---

to be pulled from the master according to the defined command numbers and the packet structure. In order to simplify the detection of the start and end of each packet, certain command numbers are defined. The start command is followed with the address of register and command type which is indicating whether the packet is writing some configuration parameters or is requesting data from the module. The next fields are number of bytes in each packet, attached with the data as well. For the sake of error detection, a checksum control field is added with one byte which is followed by a stop byte indicating end of the packet. Details of the packet format for master and slave devices are depicted in Figure 7.16 and the fields are described in Table 7.4.

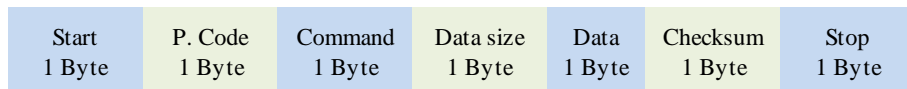


Figure 7.16: Packet structure defined for command transmission and data exchange in USB data transfer protocol

The checksum of the packet is calculated according to the following formula:

$$C = 256 - \left( \sum_{i=1}^{i=N} F_i \right) \% 256 \quad (7.1)$$

Where  $N$  is the number of bytes in the packet not including the start and stop fields,  $F_i$  is the field indicator and  $\%$  operator calculate the remainder of the value which the operator is applied to. This operator guarantees that the final value of summation is not greater than a byte so that the final value of the checksum is one byte as well.

Table 7.4: Description of the fields applied in the USB data transfer protocol

Field name	Description	Value range
Start byte	This byte shows the beginning of the packet	Always 0xaa
Parameter code	The parameter that needs to be read or write	0 to 255
Command	Write or Read command	0 or 1
Data Size	Size of the data that follows the parameter data	0 to 255
Data (optional)	The parameter's data that needs to be transferred	0 to 255 for each byte
Checksum	Safety byte to make sure the data is correct (sum of the data from Command name until the byte before checksum)	$\sim(\text{Parameter Code} + \text{Command} + \text{Data size} + \text{Data})$
Stop byte	This byte determines the end of the packet	Always 0x55

# **8. Experimental Results and Analysis**

The preliminary results and analysis of the localization algorithms as well as NLOS identification and mitigation approaches are presented in Chapter 5 and 6 for the static scenarios. This chapter extends the experiments to real dynamic trials carried out using different robot platforms in indoor as well as outdoor arenas. In total, three different trial setups are utilized. The first one is an indoor robotic mini soccer field developed for learning and education purposes as well as robotic competitions. The second arena is a sports hall with large dimensions which is used to evaluate the communication range of the system and the accuracy in large-scale scenarios. The third setup is performed in an outdoor open area in the university. The purpose of this test is to evaluate the signal characteristics of the UWB systems in open area where signal reflections are less but the energy of the signals are also reduced in comparison to indoor areas. Details of the experiments and their results are provided in the following sections.

## **8.1. Small-scale Indoor Arena**

This experiment is performed in an arena with the dimensions of  $150 \times 100 \text{ cm}^2$  with a cylindrical robot platform with the diameter of 12 cm. The robot carries a UWB node on the top which receives the signals of the four anchors located at each corner of the arena. The location of the mobile node is calculated in the node itself according to the procedure of the unilateral TDoA concept as explained before. The planned paths are marked on the arena which are used as reference lines for evaluating the accuracy of the localization methods. The robot platform is controlled using Wiimote or smartphone over Bluetooth connection. The robot platform is driven by two DC motors which are mounted at the sides and the balance of the robot is managed by two spacers installed at the front and back sides of the robot. The UWB node is mounted in the middle of the robot so that the rotations of the robot has little influence on the location of the robot. The robot in these experiments is driven with the speed of almost 10 cm/s with some stops in between for turning or correction of the direction of the movements. Photos of the arena as well as the utilized platform are shown in Figure 8.1.



Figure 8.1: Photo of the small-scale indoor arena with the blue reference lines (left) and the development platform carrying UWB node (right)

The first round of the experiments in this arena are performed in LOS conditions with the aim of evaluating accuracies of the localization algorithms. For the first path of the robot, a rectangular loop around the arena is selected. In this path, the robot has always started from the bottom-left side of the arena and continued counter-clockwise to arrive back to the start point again. The results of several recorded trajectories calculated using EKF as defined in Section 5.3.1 are shown in Figure 8.2. The first issue observable in these recordings is the strong deviation of the recorded path almost in all the trajectories at certain part of the path. These are mainly visible in the middle point of the path between anchors 1 and 2 and the path between anchor 2 and anchor 3. The reason of these strong deviations is the position of the antenna with respect to other anchors.

Although the ceramic SMD antenna used in the modules is an omnidirectional antenna, it has different gain values in different angles of the arrival as illustrated in Figure 3.8 [211]. This figure shows gain values of antenna in azimuth-phi plane which is a horizontal plate parallel to earth when the module is standing upwards. Referring to this graph, it can be seen that, at the angles of roughly  $345^\circ$  and  $160^\circ$  that represents the sides of the antenna, the gain is drastically reduced with more degradation at one side. When the robot is moving in the area between and close to the anchors 1 and 2, the anchors 3 and 4 are located at the left side of the antenna where a blind spot exists. Since the ranges are calculated differentially, two differential ranges are disadvantaged by low gain problem. This low gain will be translated directly to longer delays as the gain and distance in this module are correlated [159]. This results in the fact that the estimated point is deviated far away from these two anchors. When the robot is moving upwards and close to the anchors 2 and 4, the same issue happens which yields in the nonlinear form of the right path. This problem on the top path between anchor 4 and 3 although exists, it is less noticeable as the opposite anchors (1 and 2) in blind spot are forming only one ranging parameter which has less influence on the location estimation of the mobile node. This problem is affecting only small-scale arenas

below 1 meter square as in these ranges the gain is much higher than larger ranges where the gain correlation to distance gradually disappears.

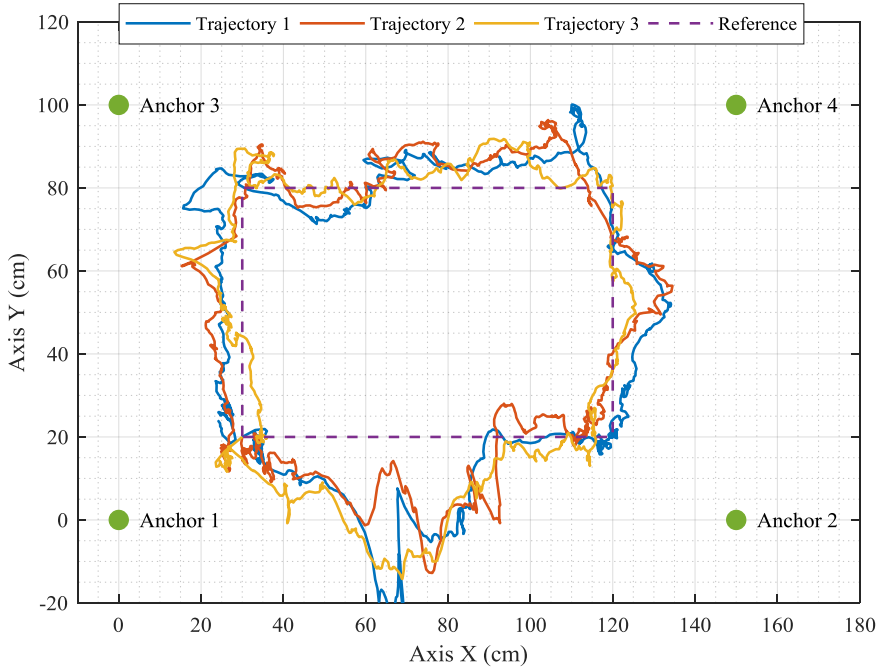


Figure 8.2: Several recorded trajectories of the robot in small-scale arena using EKF localization algorithm

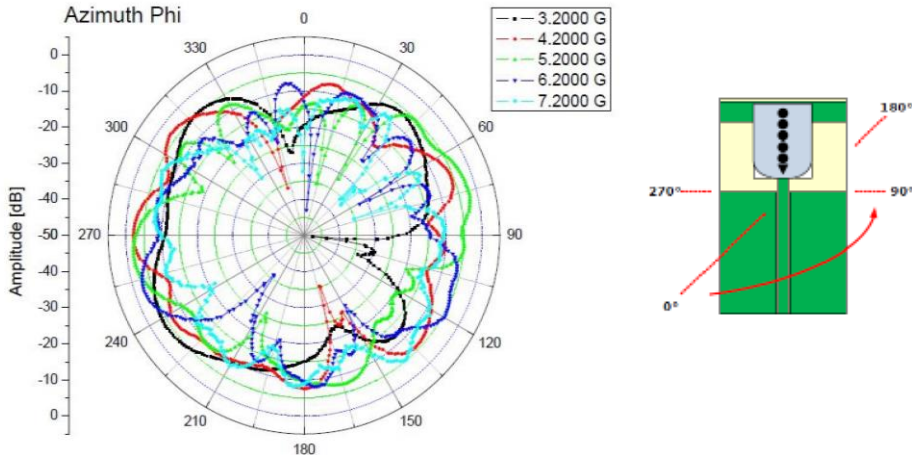


Figure 8.3: Antenna radiation pattern of the DWM1000 module in the azimuth-phi plane. Strong degradation of the gain at  $345^\circ$  and  $160^\circ$  for 4GHz band is visible (borrowed from the datasheet of the DWM1000 module [211])

The problem of antenna direction can be addressed in two ways. The first one is a hardware solution which is using an omnidirectional antenna in conical form with isotropic characteristics as suggested in [52, p. 90] although an ideal isotropic antenna with complete independency to the angle of arrival does not exist. The second approach is to add another state variable as angle of the robot and estimate this parameter through the localization system. Then a model can be developed which compensates the gain of each anchor knowing the current location of the robot and its angle towards the transmitting anchor. One issue in this method is the angle is estimated based on the location data which could be erroneous due to the discussed problem. Therefore, it is recommended to estimate the angle to a reference using other sensors such as a magnetometer.

In this experiment, the PDF of the error is calculated for all the three localization approaches namely EKF,  $H_\infty$  and UKF. These results are presented in Figure 8.4. As the experiments are performed in LOS conditions, the performances of all the approaches are almost identical with slightly better performance of the  $H_\infty$  method. The mean of the root squared error for EKF is measured to be 8.82 vs. 8.66 and 9.04 centimeter for  $H_\infty$  and UKF respectively. As it can be seen from the graph, the majority of the measurement errors are in the range of below 5cm.

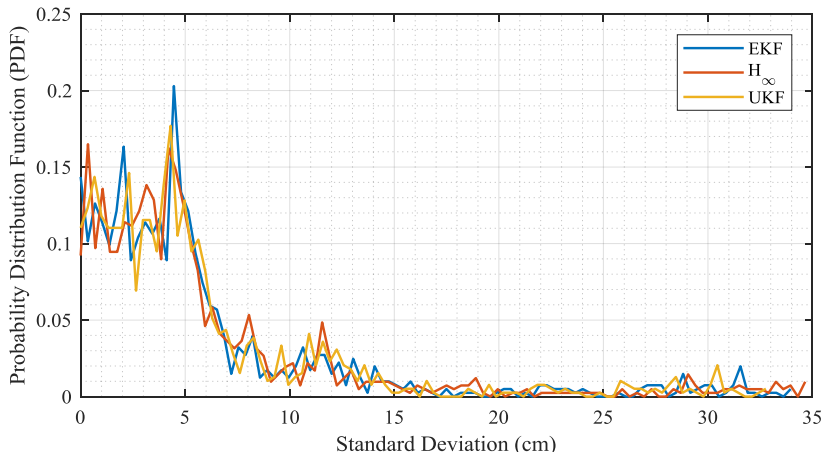


Figure 8.4: PDF of the root square error calculated for different localization approaches

In order to evaluate the accuracies of the localization system in NLOS conditions as well as the NLOS identification and mitigation algorithm, a metal barrier is utilized and positioned at different locations in the arena. As the robot moves along the reference path, the line of sight between the mobile node and the anchors are blocked by this barrier resulting in NLOS case. Then the result of original filters versus the variance and innovation term compensated filters are compared and the error of the localization for each case is evaluated. A photo of the small-scale arena with the barrier used for the NLOS scenario is depicted in Figure 8.5.

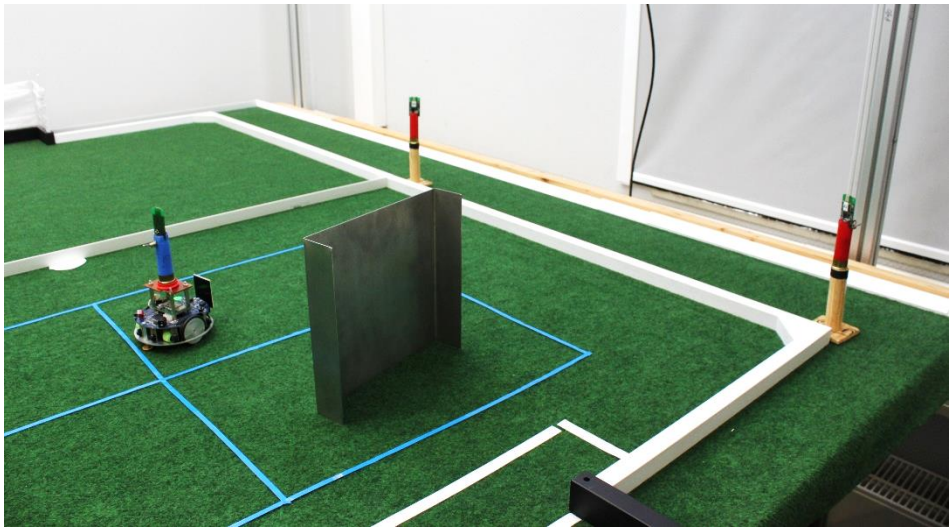


Figure 8.5: Small-scale arena and the robot platform used for evaluation of the localization system including the barrier used for creating NLOS conditions

Among several trajectories, one path is selected and presented in this section. In this case, the robot has moved along an S-shape path starting from the bottom-left side of the arena towards to the top-right. The localization results are provided

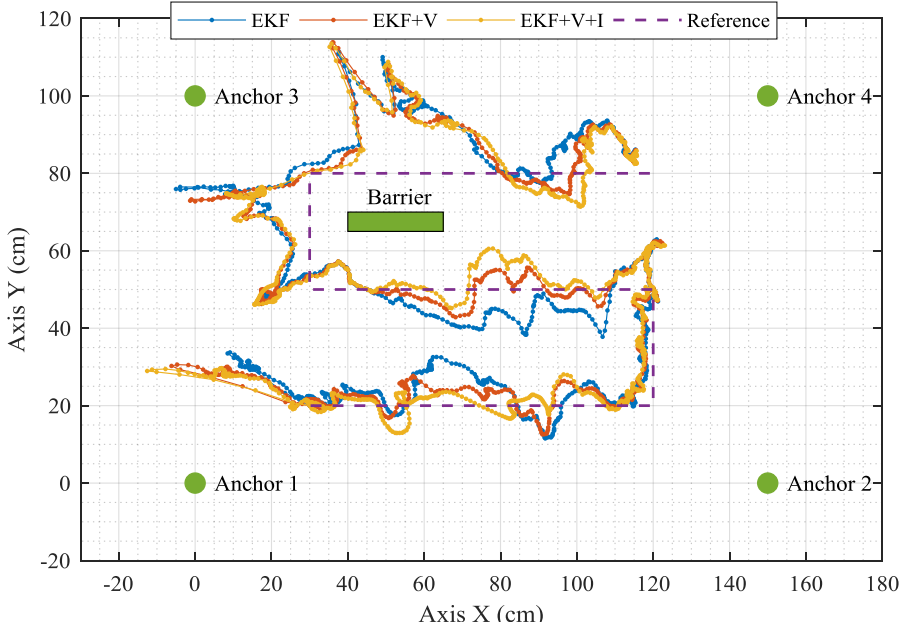


Figure 8.6: Localization results of the small-scale arena using EKF filter and its variants including the barrier used for realizing the NLOS condition

in Figure 8.6 for EKF algorithm. As it can be seen from the graph, at the area between anchor 1 and anchor 2, the barrier is blocking the anchor 3 which results in deviation of the location estimates in blue line (original EKF filter). These areas are clearly visible in the bottom and middle part of the path. Applications of variance and innovation term compensated filters mitigate the effect of the created NLOS bias so that the path seems straight. The large deviation visible on the top path is the result of both NLOS and the antenna direction issue which is appearing this time in this area as the antenna is rotated for this experiment. As it can be seen, this type of error cannot be corrected by the mitigation algorithm. Another deviation can be witnessed on the left side of the barrier. In this case, the mitigation algorithm is suppressing the bias error but with less performance due to lower detected weight of the NLOS severity for anchor 4 which was blocked at this time. The output of the NLOS identification algorithm is presented in Figure 8.7 for different anchor pairs. As it is visible from the graph, at the initial phase, the anchor 4 is in NLOS condition. As the robot moves forward, the NLOS condition appears for anchor 3 (red line). As the robot approaches the bottom and left side of the barrier, the NLOS condition is visible for anchor 2 and 4 (around sample number 700-800). Eventually close to the end of travel path, anchor 1 is blocked, resulting in a negative bias error for all of the anchor pairs.

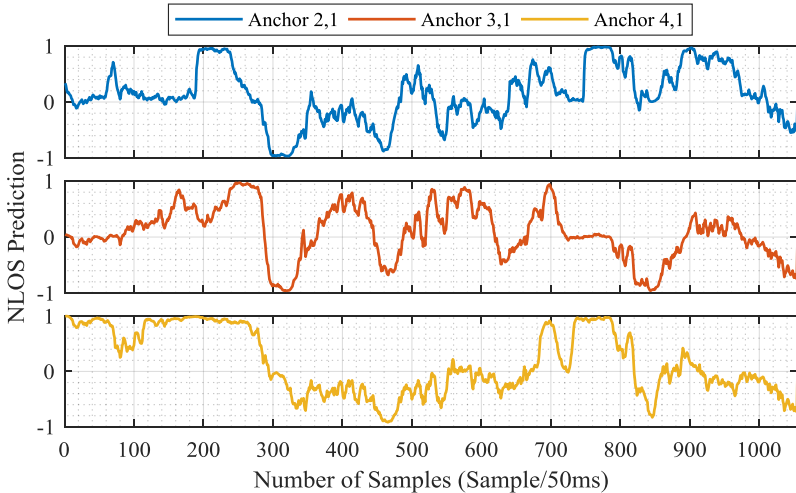


Figure 8.7: NLOS identification result of the logistic regression algorithm (Sec. 6.3.3) for different anchor pairs used for the small-scale experiments

The results of the  $H_\infty$  and UKF filters for the same experiment are provided in Figure 8.8 and 8.9 respectively. Unlike the EKF and UKF approaches, the result of  $H_\infty$  filter is very smooth and with less noise. This is mainly due to the tighter filtering parameters which are selected for this filter. Also in this case, the variance and innovation term compensated filters are performing the mitigation properly so that better accuracy is achieved when the mitigation is applied.

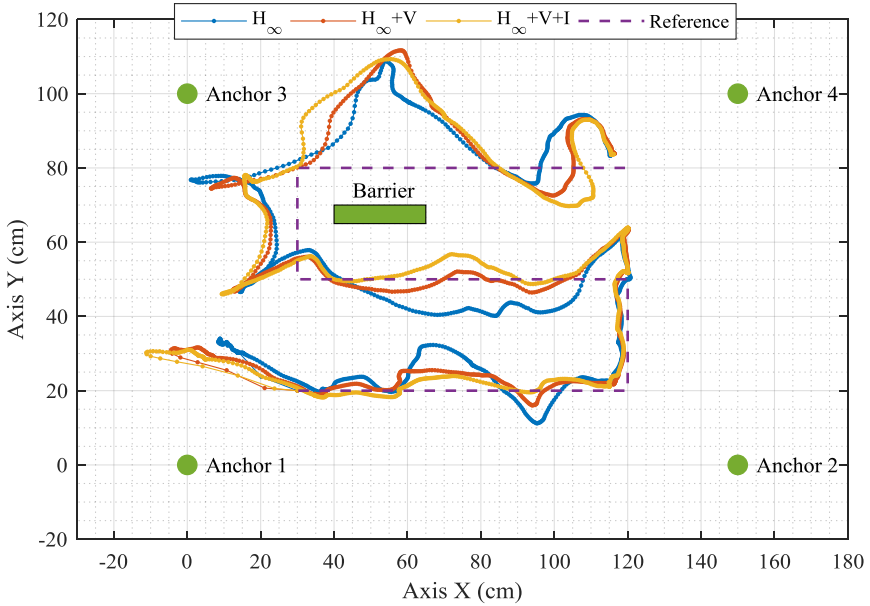


Figure 8.8: Localization results of the small-scale arena using the  $H_{\infty}$  filter and its variants including the barrier used for realizing the NLOS condition

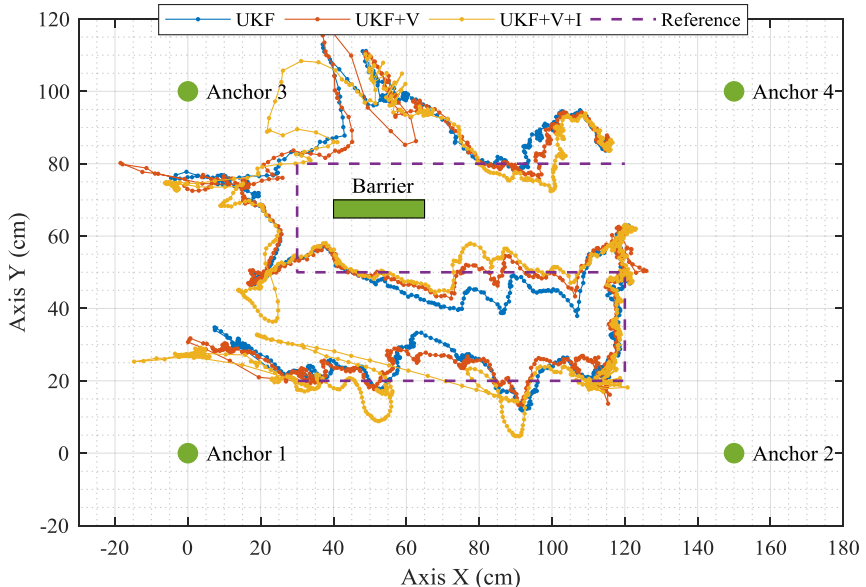


Figure 8.9: Localization results of the small-scale arena using the UKF filter and its variants including the barrier used for realizing the NLOS condition

In case of the UKF filter, it is observable that application of mitigation techniques especially the innovation term, results in more noise and partly instability of the

filter. This shows the sensitivity of this filter against the error of the data. The reason is that the statistics of the filter are estimated statistically from the data itself, so that any manipulation in this part may result in creating badly scaled matrices and eventually filter divergence.

Table 8.1: Mean of the root squared error of localization for different filters applied in the small-scale trials (all the units are cm<sup>2</sup>)

Filter	EKF	$H_\infty$	UKF
Original	6.7694	7.3639	6.9501
Variance compensated	5.7926	6.2131	6.4526
Variance and innovation compensated	5.5775	5.8050	6.7412

For the filters applied on in this trial, the localization error is estimated and the results are demonstrated in Figure 8.10 and the mean of the squared error is provided in Table 8.1. In case of the EKF and  $H_\infty$  filters the mitigation method suppressed the error however for the UKF filter the compensation of innovation term had negative influence on the error accuracy.

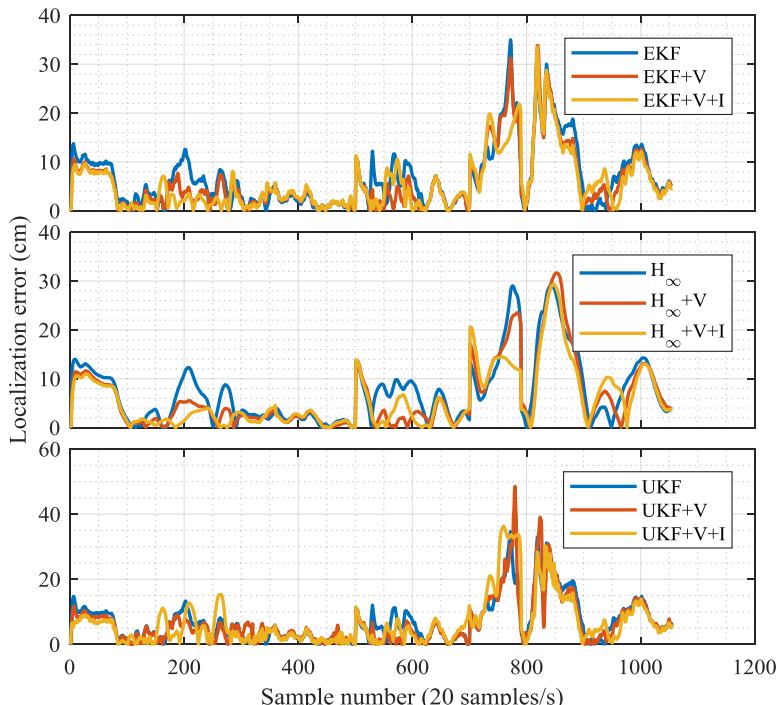


Figure 8.10: Error of the localization in small-scale arena experiment for EKF,  $H_\infty$  and UKF filters including the compensated filters used for NLOS mitigation

## 8.2. Large-scale Indoor Arena

In the second round of the experiments, a larger setup is selected in a sport hall with the dimensions of  $16 \times 10 \text{ m}^2$ . The robot platform used for these experiments is a six-wheels robot with the dimensions of  $40 \times 30 \text{ cm}^2$  capable of carrying a laptop on the top of the platform. This robot can travel with the speed of  $1 \text{ m/s}$ . The robot platform and the measurement arena are shown in Figure 8.11. Same as previous experiments, a smartphone is used to control the robot over Bluetooth connection. The turn points and the traveling paths are marked on the floor so that the robot can be manually driven over the reference lines. In order to create the NLOS conditions, large metal plates and human presence are employed to make noticeable differences in the signal characteristics.



Figure 8.11: The robot platform used for the large-scale indoor experiments (left) as well as the sport hall used in these trials showing NLOS barriers (right)

In the first round of these experiments the robot is moved in LOS conditions. Two of the recorded trajectories are demonstrated in Figure 8.12. In these experiments, the traveled routes seem to be smoother and more accurate compared to small-scale trials. The reason is, the amount of noise and inaccuracies observed in this range is much smaller against the real measured distances. The deviations and the zigzag paths visible in the graph are solely the result of robot failure to follow the defined path as this robot does not have any assistive mechanism for driving straight and therefore the path needed to be corrected often manually. The root squared error for all the localization algorithms are calculated and the PDF of the error is shown in Figure 8.13. The mean of squared root error for EKF method is  $14.14 \text{ cm}$  versus  $14.19 \text{ cm}$  and  $14.35 \text{ cm}$  for  $H_\infty$  and UKF filters respectively that shows superior performance of the EKF in this case. The PDF of the error proves that the majority of the measurements are below  $10 \text{ cm}$  which is an excellent performance in these ranges. The error peak visible in the range of  $20 \text{ cm}$  is the result of robot failure in following the correct path for the reason explained before. The maximum error observed in this experiments is  $35 \text{ cm}$  which represents roughly  $2\%$  of the maximum distance measured. For the sake of comparison, this rate was  $23\%$  for the indoor small-scale experiments.

## 8 Experimental Results and Analysis

---

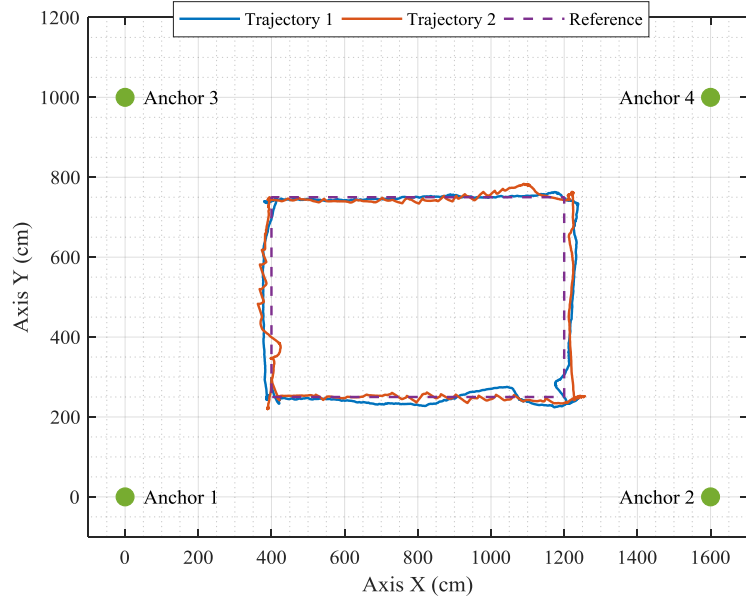


Figure 8.12: Two of the recorded trajectories in indoor large-scale experiments using EKF

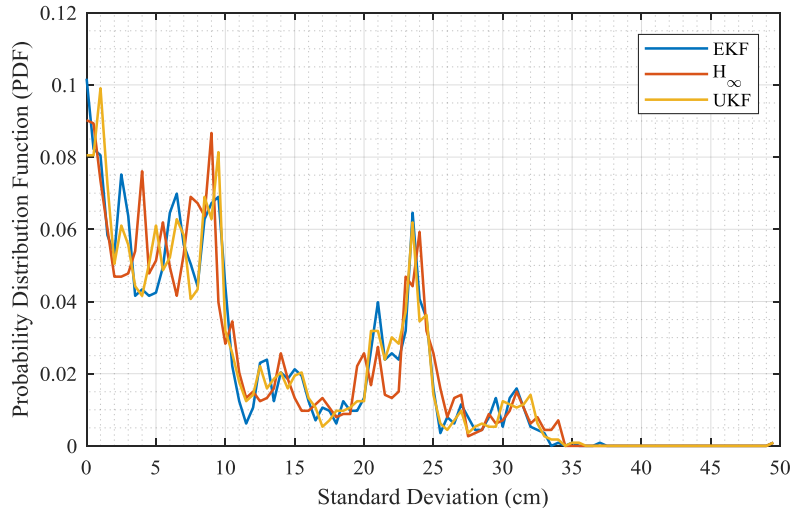


Figure 8.13: PDF of the error of different localization techniques for the indoor large-scale setup showing the majority of the measurements to be less than 10cm

As the next round of trials, the robot is moved around with some barriers in the line of sight to simulate the NLOS conditions. The selected arena used for these experiments is not used for training the NLOS identification algorithm. Indeed the largest arena used for the collection of the training data was only half of the size of this arena. As a result of that, the performance of the NLOS identification method is not satisfactory as almost all of the measurements are recognized as

NLOS case. The reason is, in large distances the signal strength is suppressed reasonably more than the small ranges which can erroneously be recognized as NLOS condition. Furthermore, the signal arrives with a longer delay and also the reflection paths have longer delays than the first path which all together yields in false detection of the NLOS case. In order to avoid this issue, a new database needs to be collected with no inclusion of the measurements from the other arenas for achieving the best performance of the detection system. The results of the NLOS identification method for different anchor pairs are provided in Figure 8.14. The results of the location estimation methods used in this thesis are provided in Figure 8.15 for EKF, Figure 8.16 for  $H_\infty$  and Figure 8.17 for UKF filters. As barrier, a large piece of metal as well as human presence is used but considering the results, no major influence is visible from the NLOS error. The reason is the reflected paths in such large areas have comparably longer delay of arrival which makes detection of the first path easier. Furthermore, the bias errors created due to the slower propagation delays through these barriers are almost ignorable compared to the measured distance. Comparing the performances of the filters, it can be seen that the  $H_\infty$  filter has very smooth response in a way that the zigzag paths that the robot has really passed through is not noticeable. In other words, the small movements of the robot are not detected. Therefore, this type of filter is more useful for self-navigation applications where small errors of the vehicle should be ignored to avoid divergence of the filter. On the other hand, this filter is not performing well in the corners where an immediate detection of direction of the movement is required. This problem is worse in the  $H_\infty$  innovation compensated filter where the NLOS condition is wrongly detected.

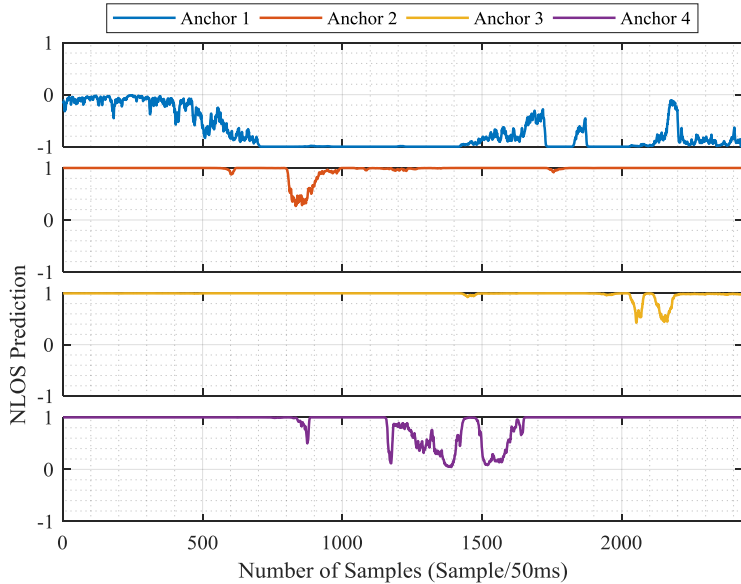


Figure 8.14: The output result of NLOS identification mechanism for different anchors

## 8 Experimental Results and Analysis

---

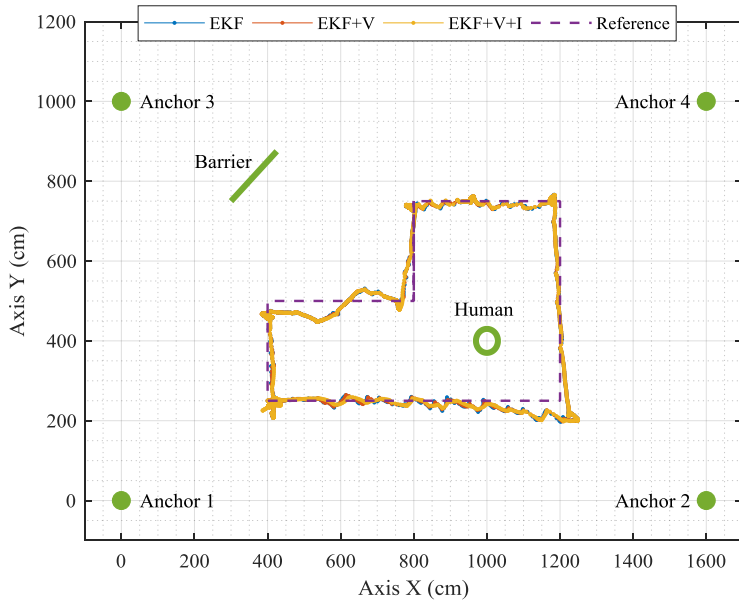


Figure 8.15: Localization results of the large-scale indoor arena using EKF filter and its variants including the barriers used for simulating the NLOS condition

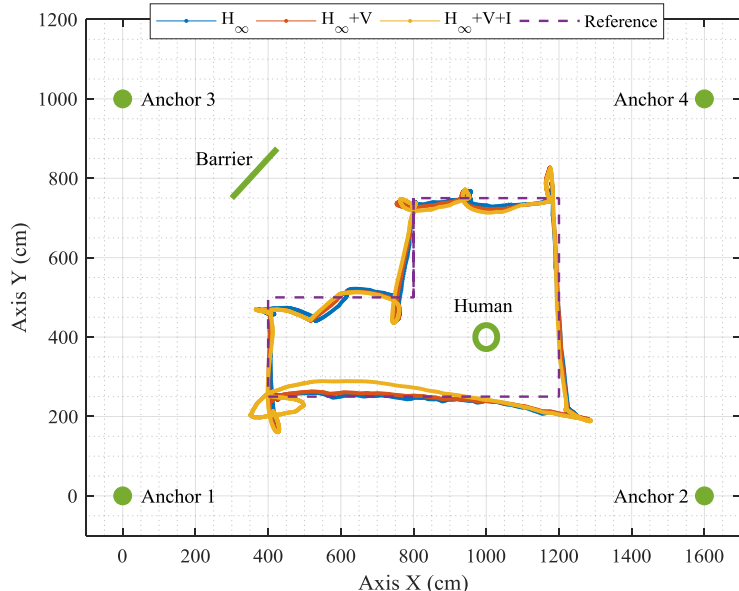


Figure 8.16: Localization results of the large-scale indoor arena using  $H_{\infty}$  filter and its variants including the barriers used for simulating the NLOS condition

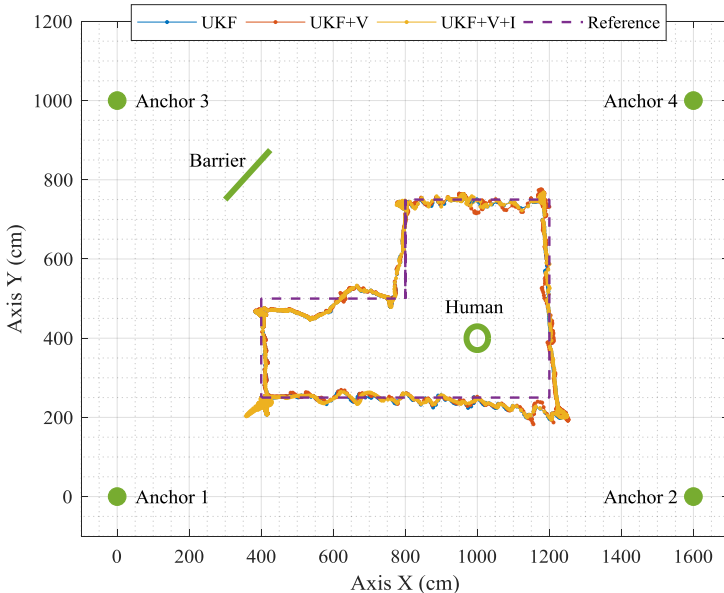


Figure 8.17: Localization results of the large-scale indoor arena using UKF filter and its variants including the barriers used for simulating the NLOS condition

## 8.3. Outdoor Experiments

It is important to evaluate the performance of the localization system in outdoor area as in such scenarios no or very weak reflections are available which may result in misdetection of the first path. It is necessary to mention that, availability of the reflections and in general multipath effect, facilitates the determination of the first path. The reason is these signals have usually higher gain in NLOS cases which is easily detectable by the peak detection algorithms. Once one of these peaks are detected, searching algorithms such as search backward or jump back and search forward can be used to detect the correct first path as described in Chapter 2. The arena used for these experiments is an open field on the campus with the dimensions of  $20 \times 16.5 \text{ m}^2$  with some trees in the field which are used as barriers to simulate the NLOS conditions. The robot platform used here is the same one used for the indoor large-scale setup. This area is still in the maximum range of nodes' coverage which is 35 m where no packet loss is experienced. The nodes are still capable of communicating from 35 m to 120 m but as the distance increases, more packet loss is experienced. Larger areas can be covered using external antennas or using an active low noise amplifier (LNA) as recommended by the manufacturer [212]. The longest communication distance using these modules is reported to be 300 m [213]. A photo of the arena demonstrating the positions of anchors as well as the robot platform is provided in Figure 8.18.

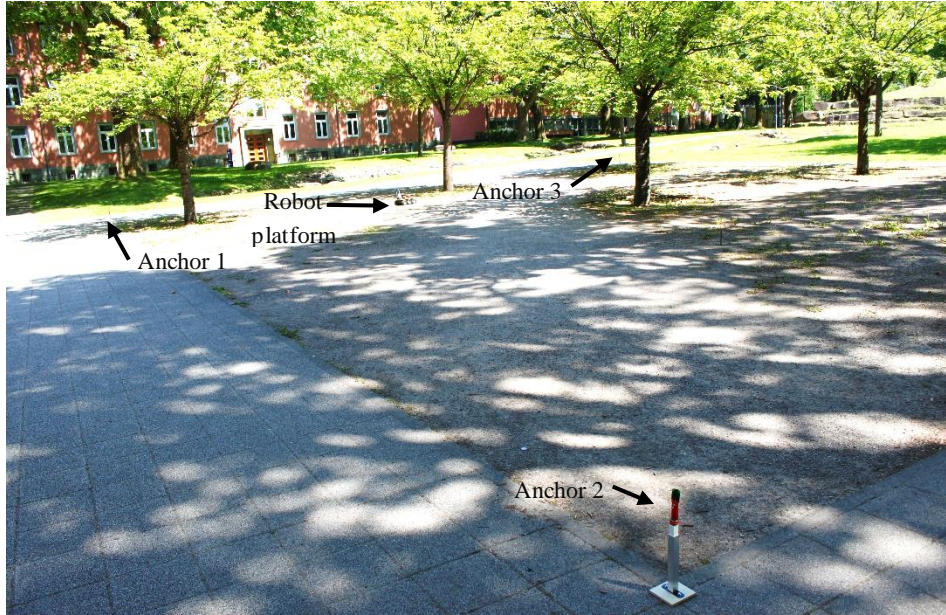


Figure 8.18: The arena used for experimenting the performance of the localization system in large-scale outdoor area

A rectangular path is selected for the robot to move along. Among the recorded trajectories, two of the traveled routes are demonstrated in Figure 8.19. Also the deviations observed here are the result of robot failure in following the planned path. Due to the presence of the trees as barrier, all the measurements are considered as NLOS. However, a similar problem as indoor large-scale case is observed which is failure of the NLOS identification system. The method in this scenario is also permanently detecting NLOS condition which is mainly the result of strong loss of signal strength and long delays in the arrived signal. Application of variance compensation here did not influence the results essentially. However, after applying the innovation term compensation, all the three filters diverge right at the initial phase of iterations. The reason is that the measurement error which is used to improve the initial guess of the filter to its final estimate is rejected by the modification method and therefore the filter cannot converge. This happens as the detection mechanism has erroneously detected severe NLOS condition in all the anchor pairs. As the filters cannot converge to a certain value due to the error removal, a badly scaled matrix appears that results in filter divergence. Therefore, a mechanism is required to activate modification term only after the filter is converged to a minimum gain and after the results are stabilized.

The localization results of the three filters are demonstrated in Figure 8.20. Also here, the performance of all the three filters are almost identical as they are overlapping each other in the graph. In addition to that, no influence due to the presence of the NLOS barriers were observed. It is also experienced that a wrong

initial point for the filters results in divergence of the filters immediately. Therefore, an initial mechanism such as gradient descent algorithm is required to figure out a good initial point before applying it on the iterative approaches.

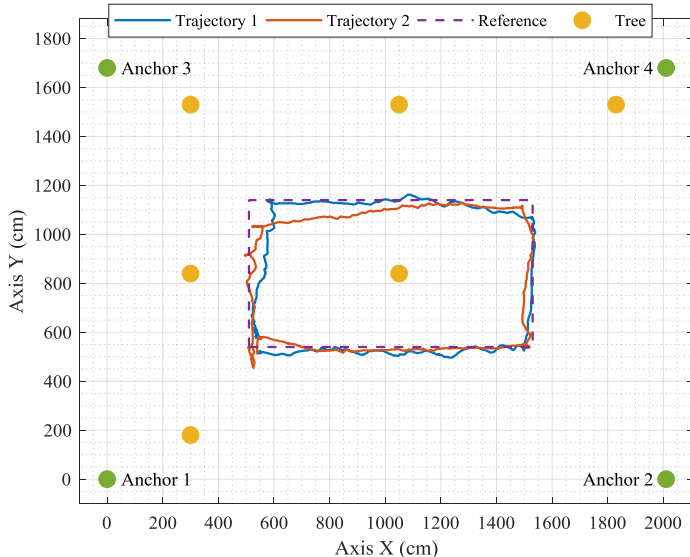


Figure 8.19: Different trajectories of the robot platform used in the large-scale outdoor arena with trees as NLOS barrier

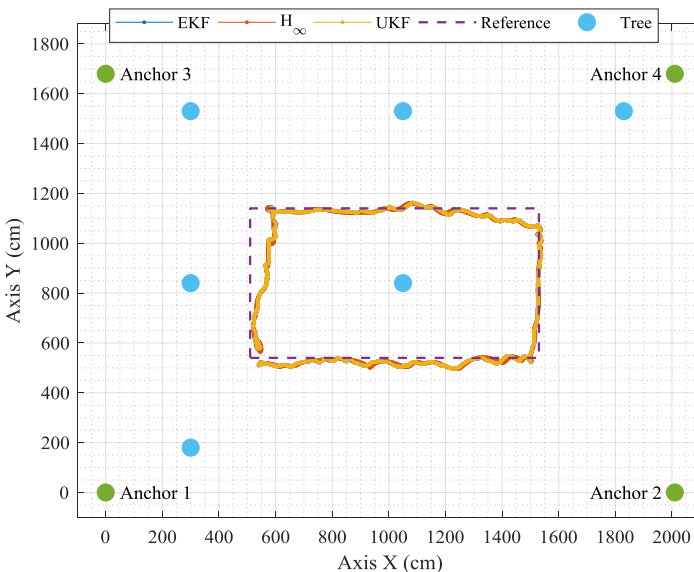


Figure 8.20: Performance comparison of the three localization algorithms in the outdoor arena with trees as NLOS barrier

## 8.4. Results Evaluation and Conclusion

The arenas introduced in this section, which are used for evaluating the proposed localization systems defined in Section 5 and 6, describe the challenging conditions of real environments at their bests. Good accuracy of the localization system (under 10 cm) and long range of coverage (more than 35 m) with capability of mitigating the NLOS error in majority of cases achieved in these arenas justify the effectiveness of the proposed method for indoor localization applications.

Evaluating the results of the NLOS identification system, it can be concluded that the best performance is achieved when the system is explicitly trained for the test environment and the data of the other arenas are excluded. A multi-area model can be used for applications where the robot should dynamically move from one area to another without changing any settings in the software. In such cases, the optimality of the model is reduced with the cost of having a universal model. If the test arena is also used for training of the machine learning algorithm, a better performance is expected for the NLOS identification method as it was the case for the indoor small-scale experiments.

It was also observed that the initial point of the filters is of great importance for the filters, as a point selected far from the real point can immediately lead to filter divergence issue. Therefore, additional startup approaches as discussed in section 5.3.4 are required to support the filters converging to initial point before starting the localization process. This way, the filter can be stabilized against erroneous NLOS identification or selection of a wrong initial point.

In terms of the filter performance, it has been observed that the  $H_\infty$  filter has the smoothest output among the three filters with lazy reactions to abrupt changes of the node. In terms of accuracy, the EKF seems to perform better with less noises as it was visible for the UKF filter. The mitigation methods applied to the filter had almost identical influence when the LOS conditions are applied. However, in the case of the UKF filter, the changes are not always improving the accuracy and in some special conditions, instability of the filter is observed.

In general, it has been witnessed that this localization system performs better in larger arenas where the effect of the antenna and near field problems are almost ignorable. This is not the case in the small-sized arenas as large errors and irregularities are expected in such scenarios. Also it was seen that, the filters have better performance in estimating the location when the nodes are moving with high speed in a certain direction without sudden changes of direction.

## **9. Conclusion**

The origin of the localization and navigation systems dates back to a century ago where terrestrial systems were utilized to locate objects or human mainly for military purposes. Rapid development of technology in aerospace area, especially satellite-based localization and its use for civil purposes, paved the way for the appearance of many new localization related applications such as automobile navigation systems. Development of the Internet and cellular networks further shifted the application areas to the indoor scenarios. In industrial sector, many applications such as logistics, production management, tracking, safety and security are linked to indoor localization systems. Likewise in home sector, applications such as child control, elderly assisted services, robotic house appliances, etc. are directly linked to indoor localization technologies. In addition to the currently available applications, other emerging applications can be mentioned such as LBS, IoT, CoT and in general Industry 4.0 which demand indoor localization systems which are more accurate and robust than before.

Common short range localization technologies are optical methods, sound-based method, radio-based or motion-based technologies. Among these methods, radio-based technology promises better performances in indoor area due to its ability to penetrate through objects without much degradation which is vital in such scenarios. Many radio-based technologies are exploited as localization systems. These are for example Wi-Fi, Bluetooth, RFID, cellular networks, ZigBee and UWB. Comparing the characteristics of these radio technologies as a localization system, it can be observed that the UWB radio systems offer better accuracies amongst the others mainly due to their large bandwidth. This large bandwidth results in generation of short period signals that are easier to detect in indoor area with presence of multipath effect. Therefore, this technology is selected for detailed analysis and to be applied in the experiments of this thesis.

The application of UWB technology for localization has been increasing in the past two decades. Legalization of this technology by FCC organization in 2002 paved the way for further exploitation of this technology in civil applications. In order to restrict the possible distortion of this systems on other radio devices, a certain frequency band in the range of 3.1 to 10.6 GHz are dedicated to UWB technology with extremely limited maximum signal strength of -40dBm/MHz. In

## 9 Conclusion

---

order to benefit from the whole range of the defined bandwidth, but at the same time limit the energy of the signal, certain signal shapes and pulses should be implemented. One way of realizing wide band signals with the desired characteristics is to utilize higher derivatives of the Gaussian signal which can effectively benefit from the large bandwidth without violating the given limits. In order to code the data into these signal shapes, different modulation concepts are applicable. These are for example PAM, OOK, PPM or PSM that encode the data in the amplitude of the signal (PAM or OOK), or phase of the signal (PPM) or in the signal shape (PSM). Further signal modulation techniques such as time hopping or frequency hopping could be applied to make simultaneous band access of several devices possible without signal interference. Details of these modulation techniques are provided in Chapter 2.

In order to standardize the frame formatting of the UWB radio devices, the IEEE 802.15.4a is defined which describes the IR-UWB protocol specifically for localization applications. This protocol, defines three different segments of a frame which are synchronization header (SHR) containing both the preamble and start frame delimiter (SFD), physical header (PHR) and finally the data section holding the user's data. The first part of the frame is modulated using OOK concept whereas the last two sections are modulated using a combination of burst position modulation (BPM) and binary phase shift keying (BPSK) concept. To improve bandwidth utilization by several devices, the IEEE standard defines further coding mechanism known as ternary sequences which are coded in preamble phase. There are many companies offering commercial UWB localization solutions. Chapter 2 introduced a few of commercially available modules and hardware in details. Among the possible solutions, products of the Decawave Company are selected to be used in this project mainly due to their high accuracy, low price, small size and good technical support.

Different topologies of localization systems are introduced in Chapter 3. Possible methods are based on the signal strength (RSSI), angle of arrival (AOA), phase of arrival (PoA) and time-based approaches such as ToA and TDoA with the last one being the main focus of this thesis. The ToA method extracts the estimated range between the two nodes from a set of signal exchanges between the nodes by recording the time of arrival and time of transmission in each case. Each of the estimated ranges is considered as a radius of a circle with its focus on the anchor device. The final location of the node is calculated by finding the point where the circles with their centers on the anchors are intersecting. In this method, at least three anchors are required to locate a node in 2D space or 4 anchors in 3D space. Other variations of this method are developed with the aim of further increasing the accuracies of the localization algorithms by reducing the clock drift of the nodes. A few of these extended variations are single sided two-way ranging (SS-TW), double sided two-way ranging (DS-TW), double response two-way ranging (DR-TW) and double sided cascaded reply (DSCR-TW) which are discussed in detail in Chapter 3.

Another time-based approach introduced in Chapter 3 is time difference of arrival (TDoA) which can be implemented in two constellations. The first topology is multilateral in that the anchors are receiver and the mobile nodes are transmitter sending short messages periodically. The signal arrival time from these mobile nodes are time stamped in anchors and this information is transmitted to a central server for estimating the differential distance between the mobile nodes and the anchors. In this method, synchronization of the nodes with the server is necessary. The other constellation is unilateral which defines the anchors as transmitter and the mobile nodes as receiver. In order to avoid signal interference, the anchors transmit sequentially with a fixed delay interval between each anchor. This technique does not require an exact synchronization of the clock values between the nodes but demands a mechanism to control the clock TIE. The multilateral concept is more suitable for resource tracking and monitoring applications where the location data of the mobile nodes are required in a local server and the mobile node themselves do not need to access these data. Whereas the unilateral concept is used for navigation applications where the mobile nodes need to know their own location. As this type of the localization is especially useful in robot navigations, all the algorithms of this thesis are focused on this approach.

One issue of the time-based methods is the clock TIE compensation. Chapter 4 has covered this issue and a method based on the Kalman filter is proposed to suppress the clock TIE between the nodes. The results proved that this method can effectively remove the clock TIE between the nodes without introducing a large traction delay. This chapter also addresses usual implementation challenges that appear such as time rounding, appearance of outliers, missing packets and filtering. As the concept of the clock TIE compensation is based on equalizing the pace of all the nodes with the reference node, it is important to have a stable and accurate clock source in the reference node. In this chapter different clock devices including a quartz crystal, temperature compensated oscillator and voltage and temperature compensated oscillator are evaluated. According to the results, the quartz crystal has the highest variance among the others with a very high sensitivity to environmental temperature changes, whereas the oscillators are more stable with less frequency variations. They have however other issues such as long time of reaching the steady state point and they may produce more jitter noise. The best localization results is achieved using a 1 ppm voltage and temperature compensated oscillator with 2.5 cm variance of the measurements.

Evaluation of different localization algorithms is the topic of Chapter 5. In this chapter, a localization model is proposed for the TDoA topology. For dynamic systems a dynamic model is proposed which is used to estimate the location of a moving node. In general, two categories of the localization algorithms are introduced. The first group is called static approaches, as they only need the information of the current measurement for estimating the location of a node. Hence in these methods, the previously measured ranging data are not used. Examples of these methods in this group are gradient-descent, Newton method,

## 9 Conclusion

---

Gauss-Newton (G-N) and Levenberg-Marquardt (L-M) methods which are also known as iterative optimization algorithms. The gradient-descent method is the simplest technique among the others which applies the gradient operator to estimate the amount of improvement in each iteration. The Newton approach applies Jacobian and Hessian of the cost function which are the first and second derivatives of the cost function respectively. The Gauss-Newton method utilizes only the Jacobian of the cost function resulting in simpler implementation process compared to the Newton method. The gradient-descent method converges immediately towards the final estimate but it needs many steps at the end phase to converge closer to the final result. The Newton approach although slow at the initial phase, is faster in the final steps of the convergence to optimal estimate. The Levenberg-Marquardt method is a hybrid mechanism which benefits from the advantages of both gradient-descent and Newton methods for achieving a better result in less number of iterations. In terms of the number of iterations, both Gauss-Newton and L-M approach have superior performance compared to other approaches. In terms of stability against far away or badly selected initial points, the L-M technique outperforms the other methods. After measuring the runtime of each algorithm in similar conditions, it turned out that the gradient-descent method is the fastest method although it needs a higher number of iterations.

Another group of algorithms are dynamic methods which consider motion of the nodes in estimating the location as well as the result of the previous estimations. Three of these algorithms are introduced in Chapter 5 which are evaluated for similar conditions. These are extended Kalman filter (EKF),  $H_\infty$  filter and unscented Kalman filter (UKF). The first one is a modified version of the Kalman filter in order to apply it to nonlinear models. This is achieved by performing Jacobian operation on the nonlinear function at the operation point of the model. The  $H_\infty$  filter is designed to be robust against model inaccuracies, excessive noise and non-optimal conditions such as bad initial point, dynamically varying noise, etc. The filter parameters in this technique are estimated deterministically and are not sensitive to changes of the noise characteristics.

The last filter discussed in this chapter, is the UKF which determines the nonlinear characteristics of the model statistically. In this technique, a set of points known as sigma points are defined which are selected accurately to represent the variances of the model in the best way. These points are propagated through the nonlinear model and evaluated to determine the new variance and mean of the operation point. This way, the Jacobian operation is not required and therefore this method is more accurate in highly nonlinear systems than the EKF approach. In a set of practical experiments, all these filters are evaluated in terms of accuracy, robustness, runtime, and implementation complexity. The results show that the simplest algorithm among the three is EKF which is also the fastest. The most complex method in terms of implementation is UKF which is also the slowest. In optimal operating conditions with low noise and LOS case, the performances of all the three filters are almost identical with slightly better

performance of EKF filter. However, in non-ideal conditions especially in NLOS conditions, the  $H_\infty$  filter turned out to be the most accurate and more robust to filter divergence problem.

One major problem of indoor localization systems is non-line of sight (NLOS) condition which results in large bias error and sometimes even divergence of localization engine. In TDoA topology, this problem is even more complex as the resulted bias error may appear as a positive bias if the NLOS condition is created between the second anchor and the target node, or it may be negative if the condition appeared between the reference anchor and the target node. Chapter 6 proposes several methods for detection of the NLOS conditions and mitigation of the resulted bias error. The proposed methods are based on the machine learning algorithms which are categorized into parametric and non-parametric techniques. The parametric approaches, extract the characteristics of the model from training data and fit the parameters into a fixed predefined function. These methods are for example the naive Bayes approach, binary classifier and logistic regression as discussed in detail in Chapter 6. The non-parametric methods determine the model of the system from the training data itself and do not define any function for the final model. These are for example K-th nearest neighbor (KNN), decision trees and Support Vector Machines (SVM).

The parametric methods are best suitable for implementation in small processors as they demand low computation power and they need only a few parameters to be used in estimation process. Therefore, these methods are more focused in the projects of this thesis. The non-parametric approaches, although implemented in PC, are not considered in the final implementation, due to their large memory space requirement and heavy mathematical process. According to the results, the best performance among the parametric methods are achieved using logistic regression with 87.2% overall accuracy vs. 85.9% for naive Bayes and binary classification approach.

For the mitigation stage, two solutions are proposed. The first one is based on modification of the measurement noise covariance matrix in NLOS conditions and the second is based on the reduction of the innovation term in update phase of the filter. A mechanism is defined to apply these changes in differential form so that the sign of the error is considered in mitigation process. The results prove that the proposed methods can successfully reduce the NLOS bias error and stabilize the localization filters in most cases.

Chapter 7 briefly discussed the details of the designed and implemented hardware and software components in the experiments of this thesis. In total, two different prototypes are introduced with different levels of peripherals. Also the flowcharts and machine states of the software parts used in the implementation of unilateral TDoA system is discussed in this chapter. Short run time of the localization algorithm (<4ms) on the developed hardware platform proves the efficiency and

## **9 Conclusion**

---

simplicity of the algorithms even if the applied platform has low processing power and limited memory space.

Three categories of the practical experiments are defined namely indoor small-scale, indoor large-scale as well as outdoor trials. Different robot platforms are utilized to carry the nodes, record the location measurements and simulate the dynamics required to test the algorithms. The performances of the localization system using different filters are evaluated in both LOS and NLOS conditions. It has been observed that the performances of all the three filters are almost identical with slightly better performances of EKF and smoother estimates of  $H_\infty$  filter in LOS conditions. In NLOS conditions, the proposed detection approach has performed successfully in majority of the cases once a similar arena is used for training and extraction of the environment model. The proposed mitigation approaches suppress the bias error effectively given that the NLOS identification approach has detected the right case. In non-ideal scenarios where the arena is not used for training in advance, divergence of the filter is experienced especially when the modification of the innovation term was applied.

In conclusion, the work of this thesis demonstrates the fact that the UWB systems are very suitable for indoor localization systems. Considering the achieved performances, under certain conditions an accuracy of below 10cm even in long range areas up to 35 m is achieved. The applied filtering techniques and NLOS error detection and mitigation mechanism further improve the accuracy in non-ideal conditions, which are probable in indoor environments with barriers and human presence.

In the future works, the proposed system can be further improved by integration of the IMU sensors in the localization engine using data fusion algorithms. Also extension of the localization system to 3D cases as well as with more anchors can be studied in order to use it for localization and navigation of drones or other flying objects in indoor area. Defining different operational zones with the same anchor IDs could be a solution to extend the range of the system in large indoor areas such as a hospital. In this case, care must be taken that the nodes with same IDs are out of the communication range of each other.

As another innovative idea, reinforcement learning algorithms can be applied which can help to improve the estimated model of the system during the operation time of the modules according to the environment in which the system is maneuvering. It can be predicted that the application of UWB systems in indoor localization scenarios will improve rapidly and more advanced methods and solutions will be developed in the future.

# Appendices

## A.1 Characteristics of the Gaussian Signals

One of the main requirements of the Kalman filters or Bayesian theory is to have a signal with Gaussian distribution. The reason of this assumption is the unique characteristic of the Gaussian signal which is not changing when multiplied with another Gaussian signal. This means the Gaussian signals stay Gaussian if they are propagated through a linear function or multiplied by another Gaussian signal. In this section this fact is proved by defining two Gaussian signals as follows:

$$\begin{cases} x_1 = \mathcal{N}(\mu_1, \sigma_1^2) \\ x_2 = \mathcal{N}(\mu_2, \sigma_2^2) \end{cases} \quad (\text{A.1})$$

These two signals have two different mean and variance values as visually shown in Figure A.1.

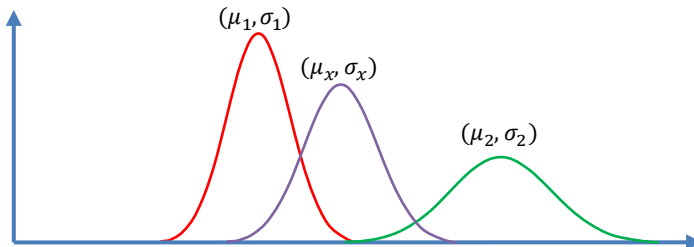


Figure A.1: Two Gaussian signals and the result of their multiplication

The idea is to estimate the result of the multiplication of these two signals and figure out the shape of resulted signal as well as the new mean and variance values. The function of a Gaussian signal is defined as:

$$P(x, \mu, \sigma) = \frac{1}{\sigma\sqrt{2\pi}} e^{-\frac{(x-\mu)^2}{2\sigma^2}} \quad (\text{A.2})$$

Applying this equation for both defined signals, the result of multiplication can be defined as:

$$P(\bar{x}, \mu_x, \sigma_x) = P(x, \mu_1, \sigma_1) \cdot P(x, \mu_2, \sigma_2) \quad (\text{A.3})$$

$$P(\bar{x}, \mu_x, \sigma_x) = \frac{1}{\sigma_1 \sqrt{2\pi}} e^{-\frac{(x-\mu_1)^2}{2\sigma_1^2}} \cdot \frac{1}{\sigma_2 \sqrt{2\pi}} e^{-\frac{(x-\mu_2)^2}{2\sigma_2^2}} \quad (\text{A.4})$$

$$P(\bar{x}, \mu_x, \sigma_x) = \frac{1}{\sigma_1 \sigma_2 2\pi} e^{-\left(\frac{(x-\mu_1)^2}{2\sigma_1^2} + \frac{(x-\mu_2)^2}{2\sigma_2^2}\right)} \quad (\text{A.5})$$

The term in the power of this equation can be extended to:

$$\begin{aligned} -\left(\frac{(x-\mu_1)^2}{2\sigma_1^2} + \frac{(x-\mu_2)^2}{2\sigma_2^2}\right) &= -\frac{1}{2} \left( \frac{x^2 - 2\mu_1 x + \mu_1^2}{\sigma_1^2} + \frac{x^2 - 2\mu_2 x + \mu_2^2}{\sigma_2^2} \right) \\ &= -\frac{1}{2} \left( \frac{x^2 - 2\mu_1 x}{\sigma_1^2} + \frac{x^2 - 2\mu_2 x}{\sigma_2^2} \right) - \frac{1}{2} \left( \frac{\mu_1^2}{\sigma_1^2} + \frac{\mu_2^2}{\sigma_2^2} \right) \end{aligned} \quad (\text{A.6})$$

This means, the equation A.5 can be rewritten as:

$$\begin{aligned} P(\bar{x}, \mu_x, \sigma_x) &= \frac{e^{-\frac{1}{2} \left( \frac{\mu_1^2 + \mu_2^2}{\sigma_1^2 + \sigma_2^2} \right)}}{\sigma_1 \sigma_2 2\pi} e^{-\frac{1}{2} \left( \frac{x^2 - 2\mu_1 x}{\sigma_1^2} + \frac{x^2 - 2\mu_2 x}{\sigma_2^2} \right)} \\ &= Ae^{-\frac{1}{2} \left( \frac{x^2 - 2\mu_1 x}{\sigma_1^2} + \frac{x^2 - 2\mu_2 x}{\sigma_2^2} \right)} \end{aligned} \quad (\text{A.7})$$

In this equation, the term behind the exponential function is a constant which is replaced with a constant parameter  $A$ . Further extension of the exponential term results in:

$$\begin{aligned} e^{-\frac{1}{2} \left( \frac{x^2 - 2\mu_1 x}{\sigma_1^2} + \frac{x^2 - 2\mu_2 x}{\sigma_2^2} \right)} &= e^{-\frac{1}{2} \left( \left( \frac{x^2}{\sigma_1^2} + \frac{x^2}{\sigma_2^2} \right) - 2x \left( \frac{\mu_1}{\sigma_1^2} + \frac{\mu_2}{\sigma_2^2} \right) \right)} \\ &= e^{-\frac{1}{2} \left( x^2 \left( \frac{\sigma_1^2 + \sigma_2^2}{\sigma_1^2 \sigma_2^2} \right) - 2x \left( \frac{\mu_2 \sigma_1^2 + \mu_1 \sigma_2^2}{\sigma_1^2 \sigma_2^2} \right) \right)} \\ &= e^{-\frac{1}{2} \left( \frac{\sigma_1^2 + \sigma_2^2}{\sigma_1^2 \sigma_2^2} \right) \left( x^2 - 2x \left( \frac{\mu_2 \sigma_1^2 + \mu_1 \sigma_2^2}{\sigma_1^2 + \sigma_2^2} \right) \right)} \end{aligned} \quad (\text{A.8})$$

In order to complete the polynomial union term in the power, we add and subtract a constant term in the form of:

$$\begin{aligned} &\left( x^2 - 2x \left( \frac{\mu_2 \sigma_1^2 + \mu_1 \sigma_2^2}{\sigma_1^2 + \sigma_2^2} \right) + \left( \frac{\mu_1 \sigma_2^2 + \mu_2 \sigma_1^2}{\sigma_2^2 + \sigma_1^2} \right)^2 - \left( \frac{\mu_1 \sigma_2^2 + \mu_2 \sigma_1^2}{\sigma_2^2 + \sigma_1^2} \right)^2 \right) \\ &= \left( x - \left( \frac{\mu_1 \sigma_2^2 + \mu_2 \sigma_1^2}{\sigma_2^2 + \sigma_1^2} \right) \right)^2 - \left( \frac{\mu_1 \sigma_2^2 + \mu_2 \sigma_1^2}{\sigma_2^2 + \sigma_1^2} \right)^2 \end{aligned} \quad (\text{A.9})$$

Applying this in Eq. A7 we have:

$$= Ae^{-\left(\frac{\mu_1\sigma_2^2+\mu_2\sigma_1^2}{\sigma_2^2+\sigma_1^2}\right)^2} e^{-\frac{1}{2}\left(\frac{\sigma_1^2+\sigma_2^2}{\sigma_1^2\sigma_2^2}\right)\left(x-\left(\frac{\mu_1\sigma_2^2+\mu_2\sigma_1^2}{\sigma_2^2+\sigma_1^2}\right)\right)^2} \quad (\text{A.10})$$

The new exponential term is also a constant which can be joined to the constant  $A$ . we define the new constant as  $B$ . This results in the final form of:

$$= Be^{-\frac{1}{2}\left(\frac{\sigma_1^2+\sigma_2^2}{\sigma_1^2\sigma_2^2}\right)\left(x-\left(\frac{\mu_1\sigma_2^2+\mu_2\sigma_1^2}{\sigma_2^2+\sigma_1^2}\right)\right)^2} \quad (\text{A.11})$$

Comparing this result with the expected Gaussian model, we have:

$$Be^{-\frac{1}{2}\left(\frac{\sigma_1^2+\sigma_2^2}{\sigma_1^2\sigma_2^2}\right)\left(x-\left(\frac{\mu_1\sigma_2^2+\mu_2\sigma_1^2}{\sigma_2^2+\sigma_1^2}\right)\right)^2} = \frac{1}{\sigma_x \sqrt{2\pi}} e^{-\frac{(x-\mu_x)^2}{2\sigma_x^2}} \quad (\text{A.12})$$

As it can be seen, the final result is also a Gaussian signal with the following mean and variance:

$$\begin{cases} \mu_x = \frac{(\mu_1\sigma_2^2 + \mu_2\sigma_1^2)}{\sigma_2^2 + \sigma_1^2} = \mu_1 + \frac{\sigma_1^2(\mu_2 - \mu_1)}{\sigma_2^2 + \sigma_1^2} \\ \sigma_x^2 = \frac{\sigma_2^2\sigma_1^2}{\sigma_2^2 + \sigma_1^2} = \sigma_1^2 - \frac{\sigma_1^4}{\sigma_2^2 + \sigma_1^2} \end{cases} \quad (\text{A.13})$$

By defining a new term  $K$ , the calculated mean and variance values can be rewritten as:

$$K = \frac{\sigma_1^2}{\sigma_2^2 + \sigma_1^2} \quad (\text{A.14})$$

$$\begin{cases} \mu_x = \mu_1 + K(\mu_2 - \mu_1) \\ \sigma_x^2 = \sigma_1^2 - K\sigma_1^2 = (I - K)\sigma_1^2 \end{cases} \quad (\text{A.15})$$

The final equations achieved in Eq. A.15 are the base of update phase equations in the Kalman filter.

## A.2 Sigma Points Parameter Determination

Recall from Chapter 5, the mean and covariance of the sigma points are defined based on  $\lambda$  which is defined according to the following equation:

$$\lambda = \alpha^2(n + k) - n \quad (\text{A.16})$$

In this equation,  $\lambda$  is defined as scaling parameter,  $\alpha$  is spreading factor of sigma points,  $k$  is scaling factor of the sigma points and  $n$  is the order of the model. In this appendix, the effect of the parameters  $k$  and  $\alpha$  on the positions of the sigma points are graphically demonstrated. In Figure A.2, the sigma points are shown for  $k = 0$  and different values of  $\alpha$ . As it can be seen, increasing the alpha values shift the sigma points farther from the center.

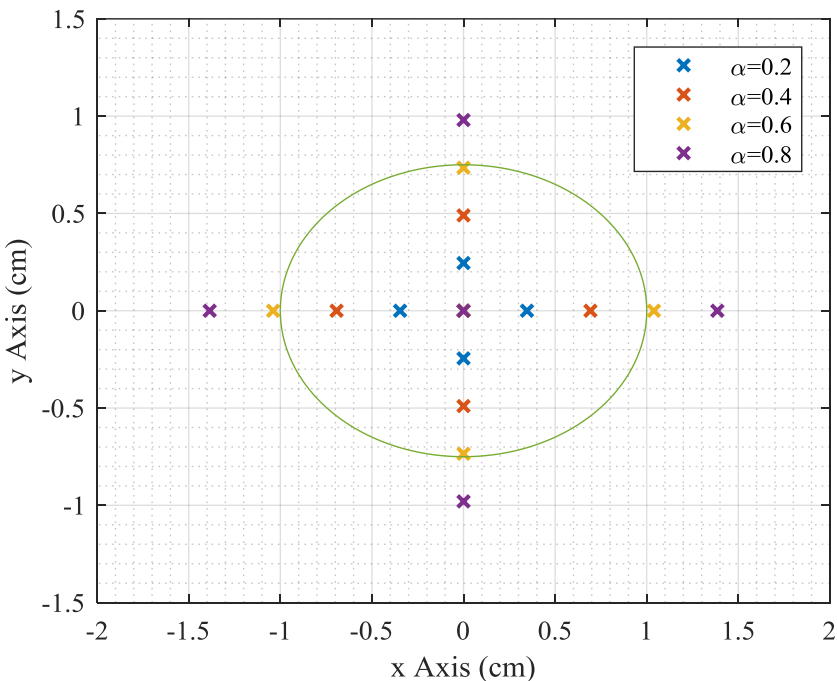


Figure A.2: Sigma points with  $k = 0$  and different values of  $\alpha$

The second involved parameter in determining the  $\lambda$  value and hence the sigma points is  $k$  which is normally considered as zero. The influence of this parameter on the position of sigma points is demonstrated in Figure A.3 for different values of  $k$  in the range of 0 to 50. In case of this experiments, a fixed value of alpha as 0.2 is considered.

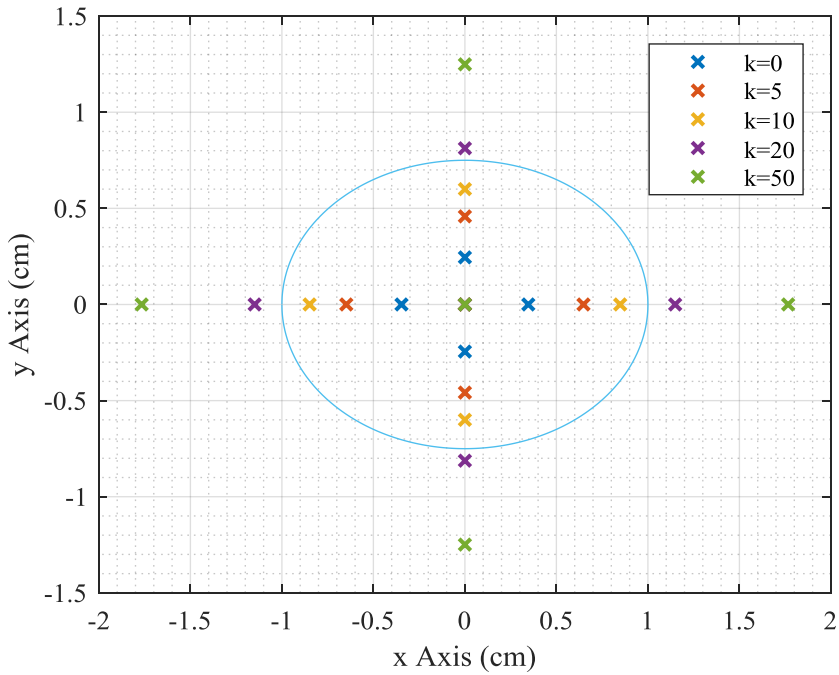


Figure A.3: Sigma points with variable  $k$  and fixed value of  $\alpha = 0.2$

### A.3 Test Arena Information and Details

In this appendix, the details of the arena dimensions and the coordinates of the test points used for the experiments described in Chapter 5 and 6 are provided<sup>1</sup>.

Coordinates	0.5 Table Lab (1)	1 Table Lab (2)	1.5 Table Lab (3)	2 Table Lab (4)	Pass way (5)	Classroom (6)
Anchor 2	60,1	120,1	180,1	240,1	400,1	800,1
Anchor 3	1,42	1,60	1,90	1,120	1,200	1,400
Anchor 4	60,42	120,60	180,90	240,120	400,200	800,400
Point 1	10,10	20,15	45,22	60,30	100,50	200,100
Point 2	30,10	60,15	90,22	120,30	200,50	400,100
Point 3	50,10	100,15	135,22	180,30	300,50	600,100
Point 4	11,22.5	20,30	45,45	60,60	100,100	200,200
Point 5	30,22.5	60,30	90,45	120,60	200,100	400,200
Point 6	50,22.5	100,30	135,45	180,60	300,100	600,200
Point 7	11,35	20,45	45,67	60,90	100,150	200,300
Point 8	30,35	60,45	90,67	120,90	200,150	400,300
Point 9	50,35	100,45	135,67	180,90	300,150	600,300

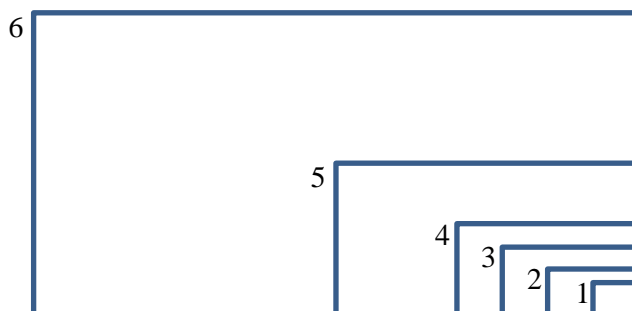


Figure A. 4: Comparison of the dimensions of the test arenas in similar scale

---

<sup>1</sup> All the given dimensions are in cm unit

## A.4 Information Logging Format

The data transmitted over USB port are stored in a text file for logging purposes. In total, there are 25 parameters which are separated in the text file using commas. These parameters are described in the following table in the order of appearance:

Parameter	Description
1	Anchor identification number
2	Received packet sequence number
3	X anchor location
4	Y anchor location
5	Reception time stamp according to the clock of the receiver
6	The planned time stamp according to the clock of the transmitter (lower two bytes)
7	The last time stamp of transmission in anchor (lower two bytes)
8	Time difference to the previous packet
9	Average of the time difference to the previous packet
10	Time difference compared to the reference node
11	Average of time difference compared to the reference node
12	Clock TIE compensated time difference compared to the reference node
13	Measured distance in cm
14	X location calculated by EKF
15	Y location calculated by EKF
16	Standard noise level of the received signal
17	Power measured in channel impulse response
18	Receive preamble count
19	First path amplitude point 1
20	First path amplitude point 2
21	First path amplitude point 3
22	Number of preamble count without saturation
23	Peak path index in CIR array
24	Peak path measured amplitude
25	First path index in CIR array

## **Appendices**

---

# List of Figures

Figure 1.1: Chronological appearance of the radio-based localization technologies which are mainly used for outdoor navigation applications .....	4
Figure 1.2: List of a few branches of science which are heavily dependent on indoor localization techniques that are integrating LBS services [10] .....	6
Figure 1.3: List of different physical characteristics of measurement signal which could be used for range estimation and their related sensory device or technology which integrates these characteristics .....	8
Figure 2.1: The defined bandwidth of the UWB by FCC and EEC and comparison of the effective isotropic radiated power (EIRP) with other wireless technologies .....	16
Figure 2.2: Difference of an ultra-wideband system and a narrow-wideband system in recognition of the original signal in multipath cases .....	17
Figure 2.3: Comparison of three different pulse shapes both in time domain (top) and power spectrum density (PSD) in frequency domain (bottom) to find the best signal with less energy outside of the defined band by regulations .....	18
Figure 2.4: Comparison of the original Gaussian signal with its 3 <sup>rd</sup> to 5 <sup>th</sup> derivatives including the FCC defined limits [46, 48] .....	20
Figure 2.5: Possible single band modulation concepts applied to the Gaussian derivatives representing binary data, a) PAM, b) OOK, c) PPM and d) PSM [49] .....	22
Figure 2.6: Comb line effect as a result of pulse train transmission with fix intervals [51] .....	23
Figure 2.7: Structure of the time hopping (TH) multi-access technique [6] [49] .....	24
Figure 2.8: The structure of the direct sequence (DS) multi-access method utilizing binary pulse amplitude modulation (PAM) [6, p. 60] .....	25
Figure 2.9: Modulation of a Gaussian signal using a cosine signal carrier for the band 2 with center frequency of 3960 MHz in both time and frequency domains ..	26
Figure 2.10: Spectrum division and band grouping of MB-OFDM proposed by WiMedia and standardized by ECMA International [44, p. 32] .....	27

Figure 2.11: Procedure of MF-OFDM modulation implemented on group 1 and according to the sequence code {1,2,3,1,2,3,...} [44, p. 35] .....	27
Figure 2.12: Frame structure of the UWB PHY according to IEEE 802.15.4a [44, p. 159] .....	28
Figure 2.13: Block diagram of an IR-UWB transmitter with BPM modulation [44, p. 40] .....	29
Figure 2.14: The first path detection algorithms based on the jump back forward search (JBSF) or serial backward search SBC for a multi-cluster case .....	34
Figure 2.15: The academic research kit from Ubisense including series of tags, software kit, mechanical holders and antennas (Source: <a href="http://www.rfidstore.it/en/rtls-systems/34-sensore-7000-.html">http://www.rfidstore.it/en/rtls-systems/34-sensore-7000-.html</a> ) .....	35
Figure 2.16: UWB products of Time Domain Company including PulsON440 (left) and PulsON330 (middle) and a development kit (right) [56] .....	36
Figure 2.17: UWB products of Zebra Company including Dart Tag, Dart Hub (top right), Dart Vision Reader (left). Dart Wand (bottom right) and Dart sensor [57] .....	36
Figure 2.18: Nanotron chirp (three modules below left) and UWB (the kit on the right) products used for indoor localization and RTLS [58] .....	37
Figure 2.19: beSpoon series of UWB products including an UWB module, an UWB tag device, a smartphone supporting UWB technology and development kit [59] .....	38
Figure 2.20: Decawave products including the DW1000 development kit (left) and DWM1001 kits (the two on the right) and the modules (in the middle) [60] .....	38
Figure 3.1 Summary of different radio-based localization approaches [73, p. 1329] .....	41
Figure 3.2: Angle of arrival (AoA) localization technique based on trilateration .....	44
Figure 3.3: Geometrical solution of localization in time of arrival (ToA) approach .....	46
Figure 3.4: Time diagram of range estimation process in single sided two-way ranging (SS-TW) method demonstrating the transmission and receive timing .....	46
Figure 3.5: Timing diagram of the range estimation process in double sided two-way ranging (DS-TW) method demonstrating the transmission and receive times .....	48
Figure 3.6: Timing diagram of range estimation process in double response two-way ranging (DR-TW) method demonstrating the transmission and receive times .....	50
Figure 3.7: Time diagram of localization process in DSCR-TW approach for cases where a) the mobile node is initiator and b) the anchor node is initiator .....	51
Figure 3.8: Ranging in TDoA localization topology with a hyperbolic line (half of a hyperbola) between the anchors and the mobile node [6, p. 31] .....	53
Figure 3.9: TDoA localization principle using two hyperbolas derived from three anchors .....	54

Figure 3.10: The multilateral TDoA approach a) network connection structure b) timing diagram of the communication process [84] .....	55
Figure 3.11: The unilateral TDoA approach a) network connection structure b) simplified timing diagram of the communication process [84].....	56
Figure 3.12: Time diagram of unilateral TDoA technique showing $n$ anchors and $m$ mobile nodes with details of the time stamps and delay intervals .....	57
Figure 3.13: Different pair selection approaches for unilateral TDoA topology a) star form, b) chain form, c) hybrid form .....	59
Figure 4.1: Time interval error (TIE) of a crystal oscillator in the same hardware setup recorded in 5 experiments each for the period of 5 minutes .....	66
Figure 4.2: Model of the clock in time-based localization systems with bias and skew rate .....	68
Figure 4.3: Performance comparison of low pass (zero order model) vs. Kalman (second order model) filtering techniques on the measurement noise of the TIE.....	71
Figure 4.4: The rounding effect of the delayed transmission in DW1000 module resulting from lower clock frequency (125MHz) of processing unit .....	73
Figure 4.5: The rounding effect of the signal received from anchor 2 in mobile node showing the 8ns gaps and the signal before and after reconstruction .....	73
Figure 4.6: Effect of the packet loss on the clock TIE which results in large deviation ..	75
Figure 4.7: Output of the modified low pass filter operating with and without outliers. No perceivable changes in the output of the filter is visible in outlier cases. ....	77
Figure 4.8: Clock TIE of different clock source technologies including crystal, TCXO and VCTCXO representing the bias of each device relative to the desired line .....	79
Figure 4.9: Clock stability of different oscillator devices after warm-up phase .....	80
Figure 4.10: Clock TIE noise of difference clock sources. The strange behavior of the noise in TCXO is visible.....	81
Figure 4.11: Probability distribution function (PDF) of the noise monitored on the drift clocks for three different clock devices .....	82
Figure 4.12: Warm-up effect of the TCXO oscillator on distance measurement accuracy .....	83
Figure 4.13: Results of differential ranging for three anchor pairs before (the first three plots) and after (the last plot) compensation.....	85
Figure 4.14: Accuracy analysis of the error of distance measurement for different experiments performed on all the clock sources repeatedly .....	86
Figure 5.1: Block diagram of the processing units in a TDoA localization system .....	87
Figure 5.2: Effect of the measurement noise and model inaccuracies on the localization of TDoA topology where the area of the intersection is formed .....	90
Figure 5.3: Convergence of different optimization algorithms to the position of the mobile node for both $x$ (located at 200) and $y$ (located at -50) axis.....	101

Figure 5.4: Progress of iteration for different optimization approaches in 2D with initial point at the origin of 2D Cartesian coordinates and mobile node at (200, -50) .....	102
Figure 5.5: Progress of iteration for different optimization approaches in 2D with initial point at (200,500) .....	103
Figure 5.6: Behavior of different optimization approaches in 2D with presence of the noise and initial point at (150,-40).....	104
Figure 5.7: Process of Bayesian estimation based on Bayes theorem demonstrating the mean and variance of prior state, observation model and posterior state ..	106
Figure 5.8: The iterative process of EKF algorithm with prediction and update phases .....	109
Figure 5.9: Propagation of sigma points in 2D Gaussian distribution through nonlinear process and determination of the new mean and covariance after transform .....	112
Figure 5.10: Workflow of the $H^\infty$ filter algorithm .....	116
Figure 5.11: Small localization setup with 4 anchors and 5 points measurement technique with results of three different localization algorithm .....	118
Figure 5.12: Measured error of three localization algorithms (EKF, UKF and $H^\infty$ ) at each iteration collected in the small scale experiment .....	119
Figure 5.13: Cumulative distribution function of the error observed in small-scale setup .....	119
Figure 5.14: Large-scale measurement arena with 9 measurement points and 4 anchors presenting the outcomes of EKF, UKF and $H^\infty$ the filters .....	120
Figure 5.15: Differential distance of the anchor pairs recorded in the large-scale arena. The NLOS cases due to presence of hand are visible in the measurements .....	121
Figure 5.16: Measured error of the three localization algorithms (EKF, UKF and $H^\infty$ ) at each iteration collected in large scale experiment .....	122
Figure 5.17: Sample trajectory of the mobile node with dynamic alteration of the speed performed in the large scale arena.....	123
Figure 5.18: The cumulative distribution function of the error results from the experiment performed in the large-scale arena with dynamic speed.....	123
Figure 5.19: Velocity of the mobile node in direction of $x$ axis acquired using different localization techniques .....	124
Figure 5.20: Variance of the localization data(left) and the PDF of the measurement error (right) with its Weibull distribution.....	125
Figure 5.21: Convergence rate of different localization system with different initial point with coordinates from top to bottom diagram as follows: (1,1), (80,50), (-10,80) and (-1,-5) .....	126

Figure 6.1: Different non-line of sight (NLOS) scenarios in indoor localization systems, a) delayed direct path, b) delayed direct path and reflection, c) only reflection	127
Figure 6.2: Differential distance of a target node with anchor pairs in a TDoA structure with positive and negative bias error created as a result of NLOS conditions	130
Figure 6.3: Comparison of the features correlation with a) good correlation (diagonal oval) and b) no correlation (circle)	133
Figure 6.4: Different characteristics of the signal in LOS and NLOS channel conditions. Higher level of noise, wider difference of index and larger power difference in NLOS condition compared to LOS case is visible	137
Figure 6.5: Representation of the symmetry of a signal through skewness parameter	138
Figure 6.6: Skewness of four samples, two of them taken in LOS and two in NLOS cases based on the three measurement points around the first path $F_1, F_2$ and $F_3$	138
Figure 6.7: Outlier detection process performed on the peak path index parameters with determination of data range using histogram plot	140
Figure 6.8: Probability distribution function (PDF) of the collected attributes for both LOS and NLOS channel conditions which the $x$ axis scaled according to the range of each attributes	144
Figure 6.9: Threshold selection of the feature in binary classification approach for the signal to noise ratio (SNR)	145
Figure 6.10: The confidence level of the predictions for each sample (left) and the probability distribution of the predictions (right) based on the outcome of the binary classification approach after applying the collected training data set	146
Figure 6.11: The logistic regression fitted model on the three different attributes namely peak path power (left), power difference (middle) and skewness (right)	148
Figure 6.12: Block diagram of the logistic regression algorithm	148
Figure 6.13: Classification process in decision tree algorithm	149
Figure 6.14: Classification process of the SVM algorithm	149
Figure 6.15: Classification process in k-th nearest neighbor (KNN) algorithm with 10 neighbors and probability estimation feature	150
Figure 6.16: The prediction results of the naive Bayes algorithm using JPD for each sample (left) and the probability distribution of the predicted results (right)	151
Figure 6.17: The prediction results of the naive Bayes algorithm using MFV for each sample (left) and the probability distribution of the predicted results (right)	152
Figure 6.18: Confusion matrix of the naive Bayes approach with JPD (left) and MFV (right) including the TPR, TNR, FPR, FNR and overall accuracy	152

Figure 6.19: Confusion matrix of the binary classification method presenting the final accuracy rate, TNR and FPR (1 <sup>st</sup> row) and TPR and FNR (1 <sup>st</sup> column) ....	153
Figure 6.20: The prediction results of the logistic classification algorithm for each sample (left) and the probability distribution of the predicted results (right).....	153
Figure 6.21: Confusion matrix of the logistic classification method presenting the final accuracy rate, TNR and FPR (1 <sup>st</sup> row) and TPR and FNR (1 <sup>st</sup> colu mn) ....	154
Figure 6.22: The confusion matrix of decision tree approach (left) and the weighted KNN (right) representing the TPR and FNR values for each .....	154
Figure 6.23: The confusion matrix of the supported vector machine (SVM) representing the TPR and FNR values.....	155
Figure 6.24: Differential distance error of the anchor pair 1 and 2 with the output of the three different NLOS identification approaches .....	156
Figure 6.25: Differential distance error of the anchor pair 1 and 3 with the output of the three different NLOS identification approaches .....	157
Figure 6.26: Localization results of the EKF, UKF and H $\infty$ filter before and after the new modified variance term is applied on the stationary node located at (30, 20) .....	159
Figure 6.27: Localization error of different filters for a fixed node evaluated before and after applying the modification in variance term .....	160
Figure 6.28: Differential NLOS identification mechanism based on the comparison of the weights achieved from each anchor .....	161
Figure 6.29: Localization comparison of the EKF, UKF and H $\infty$ filters with variance modification and filters with variance and innovation term modification .	162
Figure 6.30: Localization error of different filters before applying the modification and after applying with variance and finally including both modifications.....	163
Figure 6.31: Localization results of EKF, H $\infty$ and UKF filters in severe NLOS conditions .....	163
Figure 6.32: Localization error of different filters in case of severe NLOS conditions with different modification techniques applied .....	164
Figure 7.1: Block diagram of the hardware components used in the first prototype ....	166
Figure 7.2: Hardware platform used for both anchor module (left) with module holder and additional backup battery and a tag module (right).....	166
Figure 7.3: Photos of the second prototype with and without enclosure designed based on the DWM1000 module from Decawave .....	167
Figure 7.4: Block diagram of the hardware components used in the second prototype .....	168
Figure 7.5: Timing diagram of the unilateral TDoA localization system with 4 anchors demonstrating the applied energy modes and related power consumption .....	170

Figure 7.6: Voltage of the shunt resistor representing the current consumption of a target node in a unilateral TDoA system with different phases of operation modes .....	171
Figure 7.7: Screenshots of the Java program designed for monitoring, configuration and data logging showing the configuration tab (left) and localization tab (right) .....	172
Figure 7.8: Graphical presentation of the anchors' and node's locations in 2D space ..	173
Figure 7.9: Flowchart of the data route selection between online and offline recording .....	174
Figure 7.10: Double buffer writing technique with buffer swapping .....	175
Figure 7.11: The block diagram of software components used in the microcontroller	176
Figure 7.12: State machine of the reference anchor (anchor 1) for setting up a periodical transmission based on the delayed transmission mechanism .....	177
Figure 7.13: State machine of the anchors 2 to 4 describing the process of packet reception and retransmission.....	178
Figure 7.14: State machine of the target node describing the process of packet reception and localization .....	178
Figure 7.15: Frame format of the packet transmitted from anchors to target nodes .....	179
Figure 7.16: Packet structure defined for command transmission and data exchange in USB data transfer protocol .....	180
Figure 8.1: Photo of the small-scale indoor arena with the blue reference lines (left) and the development platform carrying UWB node (right) .....	182
Figure 8.2: Several recorded trajectories of the robot in small-scale arena using EKF localization algorithm .....	183
Figure 8.3: Antenna radiation pattern of the DWM1000 module in the azimuth-phi plane. Strong degradation of the gain at 345° and 160° for 4GHz band is visible (borrowed from the datasheet of the DWM1000 module [211]) .....	183
Figure 8.4: PDF of the root square error calculated for different localization approaches .....	184
Figure 8.5: Small-scale arena and the robot platform used for evaluation of the localization system including the barrier used for creating NLOS conditions .....	185
Figure 8.6: Localization results of the small-scale arena using EKF filter and its variants including the barrier used for realizing the NLOS condition .....	185
Figure 8.7: NLOS identification result of the logistic regression algorithm (Sec. 6.3.3) for different anchor pairs used for the small-scale experiments .....	186
Figure 8.8: Localization results of the small-scale arena using the H <sub>oo</sub> filter and its variants including the barrier used for realizing the NLOS condition .....	187
Figure 8.9: Localization results of the small-scale arena using the UKF filter and its variants including the barrier used for realizing the NLOS condition .....	187

Figure 8.10: Error of the localization in small-scale arena experiment for EKF, $H_\infty$ and UKF filters including the compensated filters used for NLOS mitigation .....	188
Figure 8.11: The robot platform used for the large-scale indoor experiments (left) as well as the sport hall used in these trials showing NLOS barriers (right) .....	189
Figure 8.12: Two of the recorded trajectories in indoor large-scale experiments using EKF .....	190
Figure 8.13: PDF of the error of different localization techniques for the indoor large-scale setup showing the majority of the measurements to be less than 10cm .....	190
Figure 8.14: The output result of NLOS identification mechanism for different anchors .....	191
Figure 8.15: Localization results of the large-scale indoor arena using EKF filter and its variants including the barriers used for simulating the NLOS condition ..	192
Figure 8.16: Localization results of the large-scale indoor arena using $H_\infty$ filter and its variants including the barriers used for simulating the NLOS condition ..	192
Figure 8.17: Localization results of the large-scale indoor arena using UKF filter and its variants including the barriers used for simulating the NLOS condition ..	193
Figure 8.18: The arena used for experimenting the performance of the localization system in large-scale outdoor area .....	194
Figure 8.19: Different trajectories of the robot platform used in the large-scale outdoor arena with trees as NLOS barrier .....	195
Figure 8.20: Performance comparison of the three localization algorithms in the outdoor arena with trees as NLOS barrier .....	195

# List of Tables

Table 1.1: Characteristics of different terrestrial radio-based localization systems [6] .....	3
Table 1.2: Comparison of different radio-based localization technologies and their attributes in terms of positioning .....	12
Table 2.1: Derivatives of Gaussian signal for orders from 1 to 5 .....	19
Table 2.2: Ternary sequences of the SHR section defined by IEEE 802.15.4a [6] .....	30
Table 2.3: PHY header (PHR) bit definition and possible field configurations according to IEEE 802.15.4a standard.....	31
Table 2.4: Comparison of different UW B COTS modules available on the market .....	39
Table 3.1: Comparison of the advantages and disadvantages of different localization approaches [12, p. 251] .....	42
Table 3.2: Pros and cons of the most common ToA ranging approaches [80] .....	52
Table 3.3: Comparison of the characteristics of different TDoA approaches [84][89] ..	64
Table 4.1: List of different clock sources used for the clock evaluation experiments .....	78
Table 4.2: Summary of the clock sources characteristics achieved from the experiments .....	84
Table 4.3: Summary of the clock sources variance analysis achieved from experiments .....	86
Table 5.1: Stochastic models of dynamic systems in the form of state space [110, p. 135] .....	93
Table 5.2: Location estimation with different optimization algorithms for initial point at (0,0) and mobile node position at (200,-50) .....	102
Table 5.3: Location estimation with different optimization algorithms for initial point (200,500) and mobile node position of (200,-50).....	102
Table 5.4: Location estimation with different optimization algorithms for initial point (150,-40) and mobile node position of (200,-50) in presence of the noise	104
Table 5.5: Feature comparison of nonlinear iterative filters from Kalman family .....	117
Table 5.6: Error analysis and performance results of different localization algorithms .....	120

Table 5.7: Error analysis and performance results of different localization algorithms in large scale experiment with 9 measurement points .....	122
Table 6.1: Channel models defined by IEEE 802.15.4a channel modeling subgroup...	131
Table 6.2: Defined thresholds for different attributes based on the binary classification .....	145
Table 6.3: Feature performance evaluation in the binary classification method .....	147
Table 6.4: Summary of the prediction results using different classification algorithms .....	155
Table 7.1: Important characteristics of the selected IMU sensors [205, 206].....	168
Table 7.2: Different operation modes of Decawave chip DW1000 and module DWM1000 .....	169
Table 7.3: Different operation modes of STM32L433 stating current consumption [208] .....	171
Table 7.4: Description of the fields applied in the USB data transfer protocol.....	180
Table 8.1: Mean of the root squared error of localization for different filters applied in the small-scale trials (all the units are cm <sup>2</sup> ) .....	188

# Bibliography

- [1] P. D. Groves, *Principles of GNSS, inertial, and multisensor integrated navigation systems*. Boston, Mass., London: Artech House, 2008.
- [2] S. Frattasi and F. Della Rosa, *Mobile positioning and tracking: From conventional to cooperative techniques*. Hoboken, New Jersey: John Wiley & Sons, 2017.
- [3] S. Sand, A. Dammann, and C. Mensing, *Positioning in wireless communications systems*. Chichester: Wiley, 2014.
- [4] K. Yu, I. Sharp, and Y. J. Guo, *Ground-based wireless positioning*. Chichester: Wiley, 2009.
- [5] C. Specht, A. Weinrit, and M. Specht, “A History of Maritime Radio-Navigation Positioning Systems used in Poland,” *J. Navigation*, vol. 69, no. 03, pp. 468–480, 2016.
- [6] A. Bensky, *Wireless positioning technologies and applications*. Boston: Artech House, 2016.
- [7] M. Wing, A. Eklund, and L. D. Kellogg, “Consumer-Grade Global Positioning System (GPS) Accuracy and Reliability,” *Journal of Forestry*, vol. 103, 2005.
- [8] E. Oleynik and S. Revnivykh, *GLONASS Status and Modernization*. [Online] Available:  
[http://www.navcen.uscg.gov/pdf/cgsicMeetings/51/3\\_GLONASS\\_CGSIC\\_Oleynik.pdf](http://www.navcen.uscg.gov/pdf/cgsicMeetings/51/3_GLONASS_CGSIC_Oleynik.pdf). Accessed on: Feb. 20 2018.
- [9] EUROPEAN GNSS (GALILEO) INITIAL SERVICES, Ed., “Open Service: Quarterly Performance Report,” Jul. 2017. [Online] Available: <https://www.gsc-europa.eu/electronic-library/performance-reports>. Accessed on: Feb. 20 2018.
- [10] M. Werner, *Indoor Location-Based Services: Prerequisites and Foundations*. Springer, 2014.
- [11] P. Davidson and R. Piche, “A Survey of Selected Indoor Positioning Methods for Smartphones,” *IEEE Commun. Surv. Tutorials*, vol. 19, no. 2, pp. 1347–1370, 2017.
- [12] M. A. Al-Ammar *et al.*, “Comparative Survey of Indoor Positioning Technologies, Techniques, and Algorithms,” in *International Conference on Cyberworlds*, pp. 245–252, 2014.

- [13] L. Chen *et al.*, “Robustness, Security and Privacy in Location-Based Services for Future IoT: A Survey,” *IEEE Access*, vol. 5, pp. 8956–8977, 2017.
- [14] X. Lin *et al.*, “Positioning for the Internet of Things: A 3GPP Perspective,” *IEEE Commun. Mag.*, vol. 55, no. 12, pp. 179–185, 2017.
- [15] S. Lee *et al.*, “Construction of an indoor positioning system for home IoT applications,” in *IEEE International Conference on Communications (ICC)*, Paris, France, 2017.
- [16] B. Braem *et al.*, “Designing a smart city playground: Real-time air quality measurements and visualization in the City of Things testbed,” in *Improving the citizens quality of life: IEEE Second International Smart Cities Conference (ISC2 2016)*, Trento, Italy, 2016.
- [17] S. Latre *et al.*, “City of things: An integrated and multi-technology testbed for IoT smart city experiments,” in *Improving the citizens quality of life: IEEE Second International Smart Cities Conference (ISC2 2016)*, Trento, Italy, 2016.
- [18] K. Rajalakshmi and M. Goyal, “Location-Based Services: Current State of The Art and Future Prospects,” in *Optical and Wireless Technologies*, pp. 625–632, 2018.
- [19] S. Wang, J. Wan, Di Li, and C. Zhang, “Implementing Smart Factory of Industrie 4.0: An Outlook,” *International Journal of Distributed Sensor Networks*, vol. 12, no. 1, 2016.
- [20] R. F. Brena *et al.*, “Evolution of Indoor Positioning Technologies: A Survey,” *Journal of Sensors*, vol. 2017, no. 6, article 359, pp. 1–21, 2017.
- [21] J. Gao, F. Yang, and X. Ma, “Indoor positioning system based on visible light communication with gray-coded identification,” in *13th International Wireless Communications and Mobile Computing Conference (IWCMC)*, Valencia, Spain, pp. 899–903, 2017.
- [22] R. Want, A. Hopper, V. Falcão, and J. Gibbons, “The active badge location system,” *ACM Trans. Inf. Syst.*, vol. 10, no. 1, pp. 91–102, 1992.
- [23] S. Tilch and R. Mautz, “CLIPS – a camera and laser-based indoor positioning system,” *Journal of Location Based Services*, vol. 7, no. 1, pp. 3–22, 2013.
- [24] C. Rascon and I. Meza, “Localization of sound sources in robotics: A review,” *Robotics and Autonomous Systems*, vol. 96, pp. 184–210, 2017.
- [25] P. Zhang and M. Martonosi, “LOCALE: Collaborative Localization Estimation for Sparse Mobile Sensor Networks,” in *Information Processing in Sensor Networks; Proceedings*, St. Louis, MO, USA, pp. 195–206, 2008.
- [26] L. Fang *et al.*, “Design of a Wireless Assisted Pedestrian Dead Reckoning System, The NavMote Experience,” *IEEE Trans. Instrum. Meas.*, vol. 54, no. 6, pp. 2342–2358, 2005.
- [27] H. Liu, H. Darabi, P. Banerjee, and J. Liu, “Survey of Wireless Indoor Positioning Techniques and Systems,” *IEEE Trans. Syst., Man, Cybern. C*, vol. 37, no. 6, pp. 1067–1080, 2007.
- [28] W. Kim, S. Yang, M. Gerla, and E.-K. Lee, “Crowdsource Based Indoor Localization by Uncalibrated Heterogeneous Wi-Fi Devices,” *Mobile Information Systems*, vol. 2016, pp. 1–18, 2016.

- [29] O. Hernandez, V. Jain, S. Chakravarty, and P. Bhargava, “Position location monitoring using IEEE® 802.15. 4/zigBee® technology,” *Beyond Bits*, no. 4, pp. 67–69, 2009.
- [30] Xiaojie Zhao, Zhuoling Xiao, Andrew Markham, Niki Trigoni, and Yong Ren, “Does BTLE measure up against WiFi? A comparison of indoor location performance,” in *European Wireless; 20th European Wireless Conference*, Berlin, Offenbach, Germany: VDE Verlag GmbH, pp. 263–268, 2014.
- [31] K. Ahsan, H. Shah, and P. Kingston, “RFID Applications: An Introductory and Exploratory Study,” *ArXiv e-prints*, 2010.
- [32] R. HENRIKSSON, “Indoor positioning in LoRaWAN networks: Evaluation of RSSI positioning in LoRaWAN networks using commercially available hardware,” Master Thesis, Department of Signals and System, Chalmers University of Technology, Göteborg, Sweden, 2016.
- [33] H. Sallouha, A. Chiumento, and S. Pollin, “Localization in long-range ultra-narrow band IoT networks using RSSI,” in *IEEE International Conference SAC Symposium Internet of Things Track*, 2017.
- [34] A. Adhikary, X. Lin, and Y.-P. E. Wang, “Performance Evaluation of NB-IoT Coverage,” in *IEEE 84th Vehicular Technology*, 2016.
- [35] J. A. del Peral-Rosado, J. A. Lopez-Salcedo, and G. Seco-Granados, “Impact of frequency-hopping NB-IoT positioning in 4G and future 5G networks,” in *IEEE International Conference*, pp. 815–820, 2017.
- [36] R. S. Sinha, Y. Wei, and S.-H. Hwang, “A survey on LPWA technology:LoRa and NB-IoT,” *ICT Express*, vol. 3, no. 1, pp. 14–21, 2017.
- [37] R. Faragher and R. Harle, “An Analysis of the Accuracy of Bluetooth Low Energy for Indoor Positioning Applications,” in *27th International Technical Meeting*, pp. 201–210, 2014.
- [38] T. Sanpechuda and L. Kovavisaruch, “A review of RFID localization: Applications and techniques,” in *ECTI-CON: Proceedings of the 5th International Conference on Electrical Engineering Electronics, Computer, Telecommunications and Information Technology*, Krabi, Thailand, pp. 769–772, 2008.
- [39] Z. Xiao, Y. Hei, Q. Yu, and K. Yi, “A survey on impulse-radio UWB localization,” *Sci. China Inf. Sci.*, vol. 53, no. 7, pp. 1322–1335, 2010.
- [40] C. Drane, M. Macnaughtan, and C. Scott, “Positioning GSM telephones,” *IEEE Commun. Mag.*, vol. 36, no. 4, 46-59, 1998.
- [41] J. Kolakowski *et al.*, “UWB localization in EIGER indoor/outdoor positioning system,” in *IEEE 8th International Conference*, pp. 845–849, 2015.
- [42] V. Djaja-Josko and J. Kolakowski, “A new method for wireless synchronization and TDOA error reduction in UWB positioning system,” *International Conference on Microwaves, Radar and Wireless Communications; MIKON; Microwave and Radar Week; MRW*, 2016.
- [43] A. Ledgerber, M. Hamer, and R. D'Andrea, “A robot self-localization system using one-way ultra-wideband communication,” in *IEEE/RSJ International Conference*, pp. 3131–3137, 2015.

- [44] Z. Şahinoğlu, S. Gezici, and I. Güvenç, *Ultra-wideband positioning systems: Theoretical limits, ranging algorithms, and protocols*. Cambridge UK, New York: Cambridge University Press, 2008.
- [45] Ł. Źwirełło, *Realization Limits of Impulse-Radio UWB Indoor Localization Systems*. Karlsruhe: KIT Scientific Publishing, 2013.
- [46] A. Popa, “An Optimization of Gaussian UWB Pulses,” *10th International Conference on DEVELOPMENT AND APPLICATION SYSTEMS*, pp. 156–160, 2010.
- [47] H. Xie *et al.*, “A Varying Pulse Width 5<sup>th</sup>-Derivative Gaussian Pulse Generator for UWB Transceivers in CMOS,” in *Radio and Wireless Symposium*, Orlando, FL, USA, pp. 171–174, 2008.
- [48] T. Wehs, G. von Colln, C. Koch, and T. Leune, “Improved detection of distorted IR-UWB pulses using amplitude spectrum in indoor environments,” in *International Conference on Indoor Positioning and Indoor Navigation*, South Korea, pp. 451–456, 2014.
- [49] S. M.-S. Sadough, “A Tutorial on Ultra Wideband Modulation and Detection Schemes,” 2009.
- [50] Á. Álvarez, D. Rakić, S. Bovelli, and A. Sierra, “Ultra-Wideband: Past, Present and Future: White Paper,” Presented by the EUWB consortium, Oct. 2011.
- [51] M. Abdel-Aleem, S. Shaaban, and M. Aly, “Ultra Wideband Systems and Modulation Techniques Using Different Gaussian Monopulse Waveforms,” *16th International Conference on Computer: Theory & Applications*, vol. ICCTA, 2006.
- [52] R. Aiello and A. Batra, *Ultra wideband systems: Technologies and applications/ edited by Roberto Aiello and Anuj Batra*. Boston, Mass., London: Newnes, 2006.
- [53] M. Yavari and B. G. Nickerson, “Ultra Wideband Wireless Positioning Systems,” Faculty of Computer Science, University of New Brunswick, Canada, Mar. 2014.
- [54] T. K. Moon, *Error correction coding: Mathematical methods and algorithms/Todd K. Moon*. Hoboken, N.J.: Wiley Interscience, 2005.
- [55] Ubisense. [Online] Available: <http://www.ubisense.net>. Accessed on: Apr. 06 2018.
- [56] TDC Acquisition Holdings, Inc. dba Time Domain. [Online] Available: <https://timedomain.com/>. Accessed on: Apr. 06 2018.
- [57] ZIH Corp, Zebra. [Online] Available: <https://www.zebra.com/gb/en/solutions/location-solutions/enabling-technologies/dart-uwb.html>. Accessed on: Apr. 06 2018.
- [58] Nanotron Technologies GmbH. [Online] Available: <https://nanotron.com>. Accessed on: Apr. 06 2018.
- [59] beSpoon. [Online] Available: <http://bespoon.com>. Accessed on: Apr. 06 2018.
- [60] Decawave Ltd. [Online] Available: <https://www.Decawave.com>. Accessed on: Apr. 06 2018.
- [61] OpenRTLS. [Online] Available: <https://openrtls.com/page/homepage>. Accessed on: Apr. 06 2018.

- [62] OÜ Eliko Tehnoloogia Arenduskeskus. [Online] Available: <https://www.eliko.ee>. Accessed on: Apr. 06 2018.
- [63] In-Circuit, “radino32 DW1000: Datasheet,” 2018. [Online] Available: <http://www.radino.cc/>. Accessed on: Apr. 04 2018.
- [64] A. R. Jimenez Ruiz and F. Seco Granja, “Comparing Ubisense, BeSpoon, and Decawave UWB Location Systems: Indoor Performance Analysis,” *IEEE Trans. Instrum. Meas.*, vol. 66, no. 8, pp. 2106–2117, 2017.
- [65] A. R. Jimenez and F. Seco, *Comparing Decawave and Bespoon UWB location systems: Indoor/outdoor performance analysis*. Piscataway, NJ: IEEE, 2016.
- [66] V. Djaja-Josko and J. Kolakowski, “A new transmission scheme for wireless synchronization and clock errors reduction in UWB positioning system,” in *International Conference on Indoor Positioning and Indoor Navigation; Institute of Electrical and Electronics Engineers (IPIN)*: IEEE, 2016.
- [67] W. Chantaweesomboon *et al.*, “On performance study of UWB real time locating system,” in *7th International Conference of Information and Communication Technology for Embedded Systems (IC-ICTES)*, Bangkok, Thailand, 2016.
- [68] S. Leugner, M. Pelka, and H. Hellbruck, “Comparison of wired and wireless synchronization with clock drift compensation suited for U-TDoA localization,” *Proceedings of the 13th Workshop on Positioning, Navigation and Communication (WPNC)*, 2016.
- [69] B. Dewberry and A. Petroff, “SwarmNet: A Distributed Navigation Network using Ultra Wideband Ranging and Communications,” in *European Microwave Conference*, 2013.
- [70] N. Decarli, D. Dardari, S. Gezici, and A. A. D'Amico, “LOS/NLOS detection for UWB signals: A comparative study using experimental data,” in *IEEE 5th International Symposium*, pp. 169–173, 2010.
- [71] A. Prorok, P. Tome, and A. Martinoli, “Accommodation of NLOS for ultra-wideband TDOA localization in single- and multi-robot systems,” in *International Conference on Indoor 2011*.
- [72] M. Tecle Berhe, “Advanced ranging techniques in UWB Based Localization,” Master Thesis, Telecommunication Engineering Group, University of Twente, 2012.
- [73] A. Yassin *et al.*, “Recent Advances in Indoor Localization: A Survey on Theoretical Approaches and Applications,” *IEEE Commun. Surv. Tutorials*, vol. 19, no. 2, pp. 1327–1346, 2017.
- [74] F. Zafari, A. Gkelias, and K. K. Leung, “A Survey of Indoor Localization Systems and Technologies,” *CoRR*, vol. abs/1709.01015, 2017.
- [75] S. Gezici *et al.*, “Localization via ultra-wideband radios: A look at positioning aspects for future sensor networks,” *IEEE Signal Process. Mag.*, vol. 22, no. 4, pp. 70–84, 2005.
- [76] G. Rebel, J. González, P. Glösekötter, F. Estevez, and A. Romero, “A Novel Indoor Localization Scheme for Autonomous Nodes in IEEE 802.15.4a Networks,” *I Jornadas de Computación Empotrada y Reconfigurable (JCER2016)*, Sep. 2016.

- [77] Y. Jiang and V. C.M. Leung, “An Asymmetric Double Sided Two-Way Ranging for Crystal Offset,” in *International Symposium on Signals*, pp. 525–528, 2007.
- [78] D. Neirynck, E. Luk, and M. McLaughlin, “An alternative double-sided two-way ranging method,” in *13th Workshop on Positioning*, 2016.
- [79] Decawave Ltd., “DW1000 UWB Module User Manual,” 2016.
- [80] G. Rebel, J. González, P. Glösekötter, F. Estevez, and A. Romero, “A Novel Indoor Localization Scheme for Autonomous Nodes in IEEE 802.15.4a Networks,” *I Jornadas de Computación Empotrada y Reconfigurable (JCER2016)*, 2016.
- [81] M. Pelka, D. Amann, M. Cimdins, and H. Hellbrück, “Evaluation of time-based ranging methods: Does the choice matter?,” in *14th Workshop on Positioning, Navigation and Communications (WPNC)*, Bremen, Germany, 2017.
- [82] A. Alarifi *et al.*, “Ultra Wideband Indoor Positioning Technologies: Analysis and Recent Advances,” *Sensors (Basel, Switzerland)*, vol. 16, no. 5, 2016.
- [83] S. Kim and J.-W. Chong, “An Efficient TDOA-Based Localization Algorithm without Synchronization between Base Stations,” *International Journal of Distributed Sensor Networks*, vol. 11, no. 9, 2015.
- [84] R. Zandian and U. Witkowski, “Robot self-localization in ultra-wideband large scale multi-node setups,” in *14th Workshop on Positioning, Navigation and Communications (WPNC)*, Bremen, Germany, 2017.
- [85] J. Tiemann, F. Eckermann, and C. Wietfeld, “ATLAS - an open-source TDOA-based Ultra-wideband localization system,” in *International Conference on Indoor Positioning and Indoor Navigation (IPIN)*, Alcala de Henares, Spain, 2016.
- [86] T. Wang, X. Chen, N. Ge, and Y. Pei, “Error analysis and experimental study on indoor UWB TDoA localization with reference tag,” *19th Asia-Pacific Conference on Communications (APCC)*, pp. 505–508, 2013.
- [87] S. He and X. Dong, “High-Accuracy Localization Platform Using Asynchronous Time Difference of Arrival Technology,” *IEEE Trans. Instrum. Meas.*, vol. 66, no. 7, pp. 1728–1742, 2017.
- [88] M. Pelka and H. Hellbrück, “S-TDoA — Sequential time difference of arrival — A scalable and synchronization free approach for Positioning,” in *IEEE Wireless Communications and Networking Conference*, Doha, Qatar, 2016.
- [89] J. Kolakowski, J. Cichocki, P. Makal, and R. Michnowski, “An Ultra-Wideband System for Vehicle Positioning,” *International Journal of Electronics and Telecommunications*, vol. 56, no. 3, p. 748, 2010.
- [90] J. X. Lee, Z. W. Lin, C. L. Law, and P. S. Chin, “Non-synchronised time difference of arrival localisation scheme with time drift compensation capability,” *IET Communications*, vol. 5, no. 5, pp. 693–699, 2011.
- [91] B. Zhen, H.-B. Li, and R. Kohno, “Clock management in Ultra-wideband Ranging,” in *16th IST Mobile and Wireless Communications Summit, 2007*, Budapest, Hungary, pp. 1–5, 2007.
- [92] B. Xu, R. Yu, G. Sun, and Z. Yang, “Whistle: Synchronization-Free TDOA for Localization,” pp. 760–769, 2011.

- [93] B. Xu, G. Sun, R. Yu, and Z. Yang, "High-Accuracy TDOA-Based Localization without Time Synchronization," *IEEE Trans. Parallel Distrib. Syst.*, vol. 24, no. 8, pp. 1567–1576, 2013.
- [94] R. Hach and A. Rommel, "Wireless synchronization in time difference of arrival based real time locating systems," in *9th Workshop on Positioning*, pp. 212–214, 2012.
- [95] Y.-C. Wu, Q. Chaudhari, and E. Serpedin, "Clock Synchronization of Wireless Sensor Networks," *IEEE Signal Process. Mag.*, vol. 28, no. 1, pp. 124–138, 2011.
- [96] W. Ting, G. Di, C. Chun-yang, T. Xiao-ming, and W. Heng, "Clock Synchronization in Wireless Sensor Networks: Analysis and Design of Error Precision Based on Lossy Networked Control Perspective," *Mathematical Problems in Engineering*, vol. 2015, no. 2, pp. 1–17, 2015.
- [97] B. Sundararaman, U. Buy, and A. D. Kshemkalyani, "Clock synchronization for wireless sensor networks: A survey," *Ad Hoc Networks*, vol. 3, no. 3, pp. 281–323, 2005.
- [98] I.-K. Rhee, J. Lee, J. Kim, E. Serpedin, and Y.-C. Wu, "Clock Synchronization in Wireless Sensor Networks: An Overview," *Sensors (Basel, Switzerland)*, vol. 9, no. 1, pp. 56–85, 2009.
- [99] J. Tiemann, F. Eckermann, and C. Wietfeld, "Multi-user interference and wireless clock synchronization in TDOA-based UWB localization," in *International Conference on Indoor Positioning and Indoor Navigation (IPIN)*, Alcala de Henares, Spain, 2016.
- [100] C. McElroy, D. Neirynck, and M. McLaughlin, "Comparison of wireless clock synchronization algorithms for indoor location systems," in *IEEE International Conference on Communications Workshops (ICC)*, Australia, pp. 157–162, 2014.
- [101] E. K. P. Chong and S. H. Źak, *An introduction to optimization*, 2nd ed. New York, N.Y., Chichester: Wiley, 2001.
- [102] J. Smith and J. Abel, "Closed-form least-squares source location estimation from range-difference measurements," *IEEE Trans. Acoust., Speech, Signal Process.*, vol. 35, no. 12, pp. 1661–1669, 1987.
- [103] Y. Weng, W. Xiao, and L. Xie, "Total Least Squares Method for Robust Source Localization in Sensor Networks Using TDOA Measurements," *International Journal of Distributed Sensor Networks*, vol. 7, no. 1, 2011.
- [104] M. D. Gillette and H. F. Silverman, "A Linear Closed-Form Algorithm for Source Localization from Time-Differences of Arrival," *IEEE Signal Process. Lett.*, vol. 15, pp. 1–4, 2008.
- [105] M. Khalaf-Allah, "Differential ultra-wideband (DUWB) for accurate indoor position estimation: Basic concept and simulation results," in *2013 Saudi International Electronics, Communications and Photonics Conference*, pp. 1–4, 2013.
- [106] B. P. Gibbs, *Advanced Kalman filtering, least-squares and modeling: A practical handbook / Bruce. P. Gibbs.* Hoboken, N.J.: Wiley, 2011.
- [107] P. S. R. Diniz, *Adaptive filtering: Algorithms and practical implementation / Paulo S.R. Diniz*, 3rd ed. New York: Springer, 2008.

- [108] R. G. Brown and P. Y. C. Hwang, *Introduction to random signals and applied Kalman filtering: With MATLAB exercises*, 4th ed. Hoboken, N.J.: Wiley; Chichester : John Wiley [distributor], 2011.
- [109] K. Graichen, “Methoden der Optimierung und optimalen Steuerung,” Universität Ulm, Wintersemester 2012/2013.
- [110] P. Zarchan and H. Musoff, *Fundamentals of Kalman Filtering: A Practical Approach, Fourth Edition*. Reston, VA: American Institute of Aeronautics and Astronautics, Inc, 2015.
- [111] E. Brookner, *Tracking and Kalman filtering made easy*. New York: Wiley, 1998.
- [112] P. E. Frandsen, K. Jonasson, H. B. Nielsen, and O. Tingleff, “UNCONSTRAINED OPTIMIZATION,” 3rd Edition, March, 2004.
- [113] C. T. Kelley, *Iterative Methods for Linear and Nonlinear Equations*: Society for Industrial and Applied Mathematics, 1995.
- [114] K. Madsen, H. B. Nielsen, and O. Tingleff, “Methods for Non-Linear Least Squares Problems (2nd ed.),” Richard Petersens Plads, Building 321, DK-2800 Kgs. Lyngby, April, 2004.
- [115] R. Fletcher, “On the Barzilai-Borwein Method,” in *Applied Optimization, Optimization and control with applications: International workshop*, L. Qi, K. Teo, and X. Yang, Eds., New York: Springer-Verlag, pp. 235–256, 2005.
- [116] H. P. Gavin, “The Levenberg-Marquardt method for nonlinear least squares curve-fitting problems,” in 2013.
- [117] C. Kanzow, N. Yamashita, and M. Fukushima, “Levenberg–Marquardt methods with strong local convergence properties for solving nonlinear equations with convex constraints,” *Journal of Computational and Applied Mathematics*, vol. 172, no. 2, pp. 375–397, 2004.
- [118] R. Gonzalez, F. Rodriguez, J. Guzmán, and M. Berenguel, “Comparative Study of Localization Techniques for Mobile Robots based on Indirect Kalman Filter,” *International Symposium on Robotics*, 2009.
- [119] S. Gillijns *et al.*, “What is the ensemble Kalman filter and how well does it work?,” in *American Control Conference*, Minneapolis, MN, USA, 4448–4453, 2006.
- [120] J. González *et al.*, “Mobile robot localization based on Ultra-Wide-Band ranging: A particle filter approach,” *Robotics and Autonomous Systems*, vol. 57, no. 5, pp. 496–507, 2009.
- [121] A. Shareef, Y. Zhu, M. Musavi, and B. Shen, “Comparison of MLP Neural Network and Kalman Filter for Localization in Wireless Sensor Networks,” *19th IASTED International Conference: Parallel and Distributed Computing and Systems*, 2007.
- [122] D. B. Jourdan, J. J. Deyst, M. Z. Win, and N. Roy, “Monte Carlo Localization in Dense Multipath Environments Using UWB Ranging,” in *IEEE International Conference on Ultra-Wideband*, Zurich, Switzerland, pp. 314–319, 2005.
- [123] J. Straub, “Pedestrian Indoor Localization and Tracking using a Particle Filter combined with a learning Accessibility Map,” Bachelor, Technische Universität München, München, 2010.

- [124] S. Thrun, W. Burgard, and D. Fox, *Probabilistic robotics*. Cambridge, Mass., London: MIT, 2005.
- [125] F. L. Lewis, L. Xie, D. Popa, and F. L. O. e. Lewis, *Optimal and robust estimation: With an introduction to stochastic control theory / Frank L. Lewis, Lihua Xie, Dan Popa*, 2nd ed. Place of publication not identified: CRC Press, 2007.
- [126] R. van Handel, “Stochastic Calculus, Filtering, and Stochastic Control,” Spring 2007.
- [127] A. Zaknich, *Principles of adaptive filters and self-learning systems*. Berlin, London, London: Springer, 2005.
- [128] S. A. Zekavat and R. M. Buehrer, *Position location: Theory, practice and advances / edited by Seyed A. (Reza) Zekavat and R. Michael Buehrer*. Hoboken, N.J.: Wiley-IEEE Press, 2012.
- [129] D. Simon, *Optimal state estimation: Kalman, H infinity, and nonlinear approaches / Dan Simon*. Hoboken, N.J.: Wiley; [Chichester] : John Wiley [distributor], 2006.
- [130] M. S. Grewal and A. P. Andrews, *Kalman Filtering: Theory and practice using MATLAB*, 2nd ed. New York: Wiley, 2001.
- [131] F. Hartmann *et al.*, “Design of an embedded UWB hardware platform for navigation in GPS denied environments,” 2015.
- [132] J. Maceraudi, F. Dehmas, B. Denis, and B. Uguen, *Multipath components tracking adapted to integrated IR-UWB receivers for improved indoor navigation*. Piscataway, NJ: IEEE, 2016.
- [133] A. Shareef and Y. Zhu, “Localization Using Extended Kalman Filters in Wireless Sensor Networks,” in *Kalman Filter Recent Advances and Applications*, V. M. and A. Pigazo, Eds.: InTech, 2009.
- [134] Rudy Negenborn, “Robot Localization and Kalman Filters On finding yourposition in a noisy world,” Master of Science, Institute of Information and Computing Sciences, Utrecht University, 2003.
- [135] J. R. Raol, *Multi-sensor data fusion with MATLAB*. Boca Raton: CRC Press, 2010.
- [136] J. V. Candy, *Bayesian signal processing: Classical, modern, and particle filtering methods / James V. Candy*. Hoboken, N.J.: Wiley: IEEE, 2009.
- [137] S. J. Julier, “The scaled unscented transformation,” in *Proceedings of the American Control Conference (IEEE Cat. No.CH37301)*, Anchorage, AK, USA, pp. 4555–4559, 2002.
- [138] M. Pelka, G. Goronzy, and H. Hellbruck, “Impact of altitude difference for Local Positioning Systems and compensation with two-stage estimators,” in *International Conference on Localization and GNSS (ICL-GNSS)*, Barcelona, Spain, 2016.
- [139] S. Konatowski, P. Kaniewski, and J. Matuszewski, “Comparison of Estimation Accuracy of EKF, UKF and PF Filters,” *Annual of Navigation*, vol. 23, no. 1, p. 49, 2016.
- [140] C. Yang, W. Shi, and W. Chen, “Comparison of Unscented and Extended Kalman Filters with Application in Vehicle Navigation,” *J. Navigation*, vol. 70, no. 02, pp. 411–431, 2017.

- [141] A. Umamageswari, J. J. Ignatious, and R. Vinodha, “A Comparative Study Of Kalman Filter, Extended Kalman Filter And Unscented Kalman Filter For Harmonic Analysis Of The Non-Stationary Signals,” in vol. 3, *International Journal of Scientific & Engineering Research*, 7th ed., 2012.
- [142] X.-M. Shen and L. Deng, “Game theory approach to discrete H-infinity filter design,” *IEEE Trans. Signal Process.*, vol. 45, no. 4, pp. 1092–1095, 1997.
- [143] D. Simon, “From Here to Infinity,” *Embedded Systems Programming*, vol. 14, no. 11, 2000.
- [144] K. Madsen, H. B. Nielsen, and O. Tingleff, *Optimization with Constraints*, 2nd ed, 2004.
- [145] G. A. Einicke and L. B. White, “Robust extended Kalman filtering,” *IEEE Trans. Signal Process.*, vol. 47, no. 9, pp. 2596–2599, 1999.
- [146] Héctor Poveda, Guillaume Ferré, Eric J. Grivel, Nicolai Christov, “Kalman Vs  $H^\infty$  Filter in Terms of Convergence and Accuracy: Application to CFO Estimation,” *20th European Signal Processing Conference (EUSIPCO 2012)*, vol. 20, pp. 121–125, 2012.
- [147] Simo Särkkä, “Unscented Kalman filter, Gaussian Filter, GHKF and CKF: Lecture notes,” Finland, Feb. 24 2011.
- [148] P. Batista, C. Silvestre, and P. Oliveira, “Kalman and  $H^\infty$  Optimal Filtering for a Class of Kinematic Systems,” *IFAC Proceedings Volumes*, vol. 41, no. 2, pp. 12528–12533, 2008.
- [149] N. Hu, C. Wu, L. Chen, and H. Wu, “The NLOS Localization Algorithm Based on the Linear Regression Model of Extended Kalman Filter,” *Journal of Image and Graphics*, vol. 4, no. 2, pp. 141–144, Dec. 2016.
- [150] C. Jiang, S.-B. Zhang, and Q.-Z. Zhang, “A New Adaptive H-Infinity Filtering Algorithm for the GPS/INS Integrated Navigation,” *Sensors (Basel, Switzerland)*, vol. 16, no. 12, 2016.
- [151] Kiriakos Kiriakidis and Richard O'Brien, “H-Infinity Parameter Estimation for State-Space Models,” *American control conference*, 2004.
- [152] Rawicz and Lawrence Paul, “H-infinity/H2/Kalman filtering of linear dynamical systems via variational techniques with applications to target tracking,” PhD, Drexel University, Philadelphia, Pennsylvania, USA, 2000.
- [153] Y. Zhuang, Z. Wang, H. Yu, W. Wang, and S. Lauria, “A robust extended filtering approach to multi-robot cooperative localization in dynamic indoor environments,” *Control Engineering Practice*, vol. 21, no. 7, pp. 953–961, 2013.
- [154] F. Yang, Z. Wang, S. Lauria, and X. Liu, “Mobile robot localization using robust extended  $H^\infty$  filtering,” *Proceedings of the Institution of Mechanical Engineers, Part I: Journal of Systems and Control Engineering*, vol. 223, no. 8, pp. 1067–1080, 2009.
- [155] F. C. Cao, G. L. Cheng, and L. R. Wang, “A Tracking Algorithm for Blind Navigation Based on Robust H Infinity Filter,” *AMM*, vol. 448-453, pp. 3580–3585, 2013.

- [156] R. Zhang, F. Hoflinger, and L. Reindl, “TDOA-Based Localization Using Interacting Multiple Model Estimator and Ultrasonic Transmitter/Receiver,” *IEEE Trans. Instrum. Meas.*, vol. 62, no. 8, pp. 2205–2214, 2013.
- [157] W. Zhang, B.-S. Chen, and C.-S. Tseng, “Robust H-infinity filtering for nonlinear stochastic systems,” *IEEE Trans. Signal Process.*, vol. 53, no. 2, pp. 589–598, 2005.
- [158] A. Albaidhani, A. Morell, and J. L. Vicario, “Ranging in UWB using commercial radio modules: Experimental validation and NLOS mitigation,” in *International Conference on Indoor Positioning and Indoor Navigation (IPIN)*, Alcala de Henares, Spain, pp. 1–7, 2016.
- [159] Decawave Ltd., “APS011 Application Note: Sources of Error in DW1000 based Two-way Ranging (TWR) Schemes,” 2014.
- [160] J. Meng, Q.-y. Zhang, and N.-t. Zhang, “Impact of IR-UWB waveform distortion on NLOS localization system,” in *IEEE International Conference on Ultra-Wideband*, Vancouver, BC, Canada, pp. 123–128, 2009.
- [161] J. Li and S. Wu, “Non-parametric Non-line-of-Sight Identification and Estimation for Wireless Location,” in *International Conference on Computer Science and Service System*, Nanjing, China, pp. 81–84, 2012.
- [162] J. Schroeder, S. Galler, K. Kyamakya, and K. Jobmann, “NLOS detection algorithms for Ultra-Wideband localization,” in *4th Workshop on Positioning, Navigation and Communication*, Hannover, Germany, pp. 159–166, 2007.
- [163] B. Le Long, K. Ahmed, and H. Tsuji, “Mobile location estimator with NLOS mitigation using Kalman filtering,” in *IEEE Wireless Communications and Networking (WCNC)*, New Orleans, LA, USA, pp. 1969–1973, 2003.
- [164] C. Rohrig and M. Muller, “Indoor location tracking in non-line-of-sight environments using a IEEE 802.15.4a wireless network,” in *IEEE/RSJ International Conference on Intelligent Robots and Systems*, St. Louis, MO, pp. 552–557, 2009.
- [165] B. Silva, R. dos Santos, and G. P. Hancke, “Towards non-line-of-sight ranging error mitigation in industrial wireless sensor networks,” in *IECON - 42nd Annual Conference of the IEEE Industrial Electronics Society*, Florence, Italy, pp. 5687–5692, 2016.
- [166] N. Alsindi, C. Duan, J. Zhang, and T. Tsuboi, “NLOS channel identification and mitigation in Ultra Wideband ToA-based Wireless Sensor Networks,” in *6th Workshop on Positioning, Navigation and Communication*, Hannover, Germany, pp. 59–66, 2009.
- [167] A. Abbasi and M. H. Kahaei, “Improving source localization in LOS and NLOS multipath environments for UWB signals,” in *14th International CSI Computer*, pp. 310–316, 2009.
- [168] K. Gururaj, A. K. Rajendra, Y. Song, C. L. Law, and G. Cai, “Real-time identification of NLOS range measurements for enhanced UWB localization,” in *International Conference on Indoor Positioning and Indoor Navigation (IPIN)*, Sapporo, 2017.
- [169] I. Guvenc, C.-C. Chong, and F. Watanabe, “NLOS Identification and Mitigation for UWB Localization Systems,” in *IEEE Wireless Communications and Networking Conference*, Kowloon, China, pp. 1571–1576, 2007.

- [170] W. Li, T. Zhang, and Q. Zhang, “Experimental researches on an UWB NLOS identification method based on machine learning,” in *15th IEEE International Conference on Communication Technology*, Guilin, China, pp. 473–477, 2013.
- [171] W. Ke and L. Wu, “Mobile location with NLOS identification and mitigation based on modified Kalman filtering,” *Sensors (Basel, Switzerland)*, vol. 11, no. 2, pp. 1641–1656, 2011.
- [172] L. Yan, Y. Lu, and Y. Zhang, “An Improved NLOS Identification and Mitigation Approach for Target Tracking in Wireless Sensor Networks,” *IEEE Access*, vol. 5, pp. 2798–2807, 2017.
- [173] A. F. Molisch *et al.*, “IEEE 802.15.4a channel model - final report,” in *Converging: Technology, work and learning.*, 2004.
- [174] N. A. Alsindi, B. Alavi, and K. Pahlavan, “Measurement and Modeling of Ultrawideband TOA-Based Ranging in Indoor Multipath Environments,” *IEEE Trans. Veh. Technol.*, vol. 58, no. 3, pp. 1046–1058, 2009.
- [175] M. R. Berthold, C. Borgelt, F. Höppner, and F. Klawonn, *Guide to intelligent data analysis: How to intelligently make sense of real data / Michael R. Berthold ... [et al.]*. London: Springer, 2010.
- [176] E. Garcia, P. Pouderoux, A. Hernandez, J. Urena, and D. Gualda, “A robust UWB indoor positioning system for highly complex environments,” in *IEEE International Conference on Industrial Technology (ICIT)*, Seville, pp. 3386–3391, 2015.
- [177] B. Silva and G. P. Hancke, “IR-UWB-Based Non-Line-of-Sight Identification in Harsh Environments: Principles and Challenges,” *IEEE Trans. Ind. Inf.*, vol. 12, no. 3, pp. 1188–1195, 2016.
- [178] Decawave Ltd., “DW1000 UWB Module User Manual,” 2016.
- [179] A. Maali, H. Mimoun, G. Baudoin, and A. Ouldali, “A new low complexity NLOS identification approach based on UWB energy detection,” in *IEEE Radio and Wireless Symposium*, San Diego, CA, USA, pp. 675–678, 2009.
- [180] J. Han, M. Kamber, and J. Pei, *Data mining: Concepts and techniques / Jiawei Han, Micheline Kamber, Jian Pei*, 3rd ed. Waltham, MA: Morgan Kaufmann, 2012.
- [181] S. J. Russell, P. Norvig, and E. Davis, *Artificial intelligence: A modern approach*, 3rd ed. Upper Saddle River: Prentice Hall, 2010.
- [182] Q. Zhang, D. Zhao, S. Zuo, T. Zhang, and D. Ma, “A low complexity NLOS error mitigation method in UWB localization,” in *IEEE/CIC International Conference on Communications in China (ICCC)*, Shenzhen, China, pp. 1–5, 2015.
- [183] S. Marano, W. Gifford, H. Wymeersch, and M. Win, “NLOS identification and mitigation for localization based on UWB experimental data,” *IEEE J. Select. Areas Commun.*, vol. 28, no. 7, pp. 1026–1035, 2010.
- [184] T. van Nguyen, Y. Jeong, H. Shin, and M. Z. Win, “Machine Learning for Wideband Localization,” *IEEE J. Select. Areas Commun.*, vol. 33, no. 7, pp. 1357–1380, 2015.
- [185] R. Ying, T. Jiang, and Z. Xing, “Classification of transmission environment in UWB communication using a support vector machine,” in *IEEE Globecom Workshops*, Anaheim, CA, USA, pp. 1389–1393, 2012.

- [186] Z. Xiao *et al.*, “Identification and mitigation of non-line-of-sight conditions using received signal strength,” in *IEEE 9th International Conference on Wireless and Mobile Computing, Networking and Communications (WiMob)*, Lyon, France, pp. 667–674, 2013.
- [187] T. van Nguyen, Y. Jeong, and H. Shin, “Relevance vector machine for UWB localization,” in *IEEE Wireless Communications and Networking Conference (WCNC)*, Istanbul, Turkey, pp. 2150–2155, 2014.
- [188] S. ADLIN, “Adaptive Decision Tree Based LOS and NLOS Classification,” *International Journal of Technology and Engineering System (IJTES)*, vol. 7, no. 1, pp. 98–107, 2015.
- [189] W. Cheng and E. Hüllermeier, “Probability Estimation for Multi-class Classification Based on Label Ranking,” in *Lecture Notes in Computer Science*, 7523–7524. Lecture notes in artificial intelligence, *Machine learning and knowledge discovery in databases*, P. A. Flach, T. de Bie, and N. Cristianini, Eds., Heidelberg: Springer, pp. 83–98, 2012.
- [190] P. Flach *et al.*, *On classification, ranking, and probability estimation*: Internationales Begegnungs- und Forschungszentrum fur Informatik (IBFI), Schloss Dagstuhl, Germany, 2008.
- [191] D. D. Margineantu, “Class Probability Estimation and Cost-Sensitive Classification Decisions,” in *Lecture notes in computer science, Lecture notes in artificial intelligence 0302-9743*, vol. 2430, *Machine learning: ECML2002 : 13th European Conference on Machine Learning, Helsinki, Finland, August 19-23, 2002 : proceedings/ Tapio Elomaa, Heikki Mannila, Hannu Toivonen, eds*, T. Elomaa, H. Mannila, and H. Toivonen, Eds., Berlin, London: Springer, pp. 270–281, 2002.
- [192] D. Mease, A. J. Wyner, and A. Buja, “Boosted Classification Trees and Class Probability/Quantile Estimation,” *J. Mach. Learn. Res.*, vol. 8, pp. 409–439, 2007.
- [193] M. Saar-Tsechansky and F. Provost, “Active Sampling for Class Probability Estimation and Ranking,” *Machine Learning*, vol. 54, no. 2, pp. 153–178, 2004.
- [194] D. D. Margineantu and T. G. Dietterich, “Improved Class Probability Estimates from Decision Tree Models,” in *Lecture Notes in Statistics*, vol. 171, *Nonlinear estimation and classification*, D.D. Denison, Ed., New York, London: Springer, pp. 173–188, 2003.
- [195] M. Kuhn and K. Johnson, *Applied Predictive Modeling*. New York, NY: Springer New York, 2013.
- [196] M. C. Belavagi and B. Muniyal, “Performance Evaluation of Supervised Machine Learning Algorithms for Intrusion Detection,” *Procedia Computer Science*, vol. 89, pp. 117–123, 2016.
- [197] I. Alvarez, S. Bernard, and G. Deffuant, “Keep the Decision Tree and Estimate the Class Probabilities using its Decision Boundary,” in *The 20th International Joint Conference on Artificial Intelligence 2007*, pp. 654–659, 2007.
- [198] I. Guvenc and C.-C. Chong, “A Survey on TOA Based Wireless Localization and NLOS Mitigation Techniques,” *IEEE Commun. Surv. Tutorials*, vol. 11, no. 3, pp. 107–124, 2009.

- [199] K. Yu and Y. J. Guo, "NLOS Error Mitigation for Mobile Location Estimation in Wireless Networks," in *IEEE 65th Vehicular Technology Conference - VTC2007-Spring*, Dublin, Ireland, pp. 1071–1075, 2007.
- [200] R. M. Vaghefi, J. Schloemann, and R. M. Buehrer, "NLOS mitigation in TOA-based localization using semidefinite programming," in *10th Workshop on Positioning, Navigation and Communication (WPNC)*, Dresden, 2013.
- [201] X. Jiang and H. Zhang, "Non-line of Sight Error Mitigation in UWB Ranging Systems Using Information Fusion," in *18th International Conference Radioelektronika*, Prague, Czech Republic, pp. 969–976, 2008.
- [202] K. Yu and E. Dutkiewicz, "NLOS Identification and Mitigation for Mobile Tracking," *IEEE Trans. Aerosp. Electron. Syst.*, vol. 49, no. 3, pp. 1438–1452, 2013.
- [203] C.-D. Wann and C.-S. Hsueh, "NLOS mitigation with biased Kalman filters for range estimation in UWB systems," in *TENCON 2007 - IEEE Region 10 Conference*, Taipei, Taiwan, 2007.
- [204] M. Najar and J. Vidal, "Kalman tracking for mobile location in NLOS situations," in *14th IEEE Proceedings on Personal, Indoor and Mobile Radio Communications (PIMRC)*, Beijing, China, pp. 2203–2207, 2003.
- [205] STMicroelectronics, "LSM303C: Ultra-compact high-performance eCompass module: 3D accelerometer and 3D magnetometer," Jun. 2014. [Online] Available: [www.st.com](http://www.st.com).
- [206] STMicroelectronics, "LSM6DSM: iNEMO inertial module: always-on 3D accelerometer and 3D gyroscope," Sep. 2017. [Online] Available: [www.st.com](http://www.st.com).
- [207] Decawave Ltd., "APS002 Application Note: Maximizing Power Consumption in DW1000 Based Systems," Decawave Ltd., 2016. [Online] Available: [www.Decawave.com](http://www.Decawave.com).
- [208] STMicroelectronics, "Datasheet: STM32L433xx: Ultra-low-power ARM® Cortex®, DocID028794, Jun. 2017. [Online] Available: [www.st.com](http://www.st.com).
- [209] Macronix International Co., LTD, "The Ultimate Performance Flash Memory: Macronix Serial Multi I/O(MXSMIOTM) Flash," Apr. 2009. [Online] Available: [www.macronix.com](http://www.macronix.com).
- [210] C.-C. Chung, D. Sheng, and N.-M. Hsueh, "A high-performance wear-leveling algorithm for flash memory system," *IEICE Electron. Express*, vol. 9, no. 24, pp. 1874–1880, 2012.
- [211] Decawave Ltd., "DWM1000 IEEE 802.15.4-2011 UWB Transceiver Module," 2014. [Online] Available: [www.Decawave.com](http://www.Decawave.com).
- [212] Decawave Ltd., "APS004 Application Note: Increasing the Range of DW1000 Based Products using an External LNA," Decawave Ltd., 2016. [Online] Available: [www.Decawave.com](http://www.Decawave.com).
- [213] Decawave Ltd., "APS017 Application Note: Maximising Range in DW1000 Based Systems," Decawave Ltd., 2014. [Online] Available: [www.Decawave.com](http://www.Decawave.com).

# Own Publications

- 1) Zandian, Reza; Witkowski, Ulf; *Differential NLOS Error Detection in UWB-based Localization Systems using Logistic Regression*, Proceedings of 15th Workshop on Positioning, Navigation and Communications (WPNC), IEEE, Bremen, Germany, 2018.
- 2) Zandian, Reza; Witkowski, Ulf; *Non-line of Sight Error Mitigation in Bayesian Differential Localization Systems*, Proceedings of 15th Workshop on Positioning, Navigation and Communications (WPNC), IEEE, Bremen, Germany, 2018.
- 3) Zandian, Reza; Witkowski, Ulf; *NLOS Detection and Mitigation in Differential Localization Topologies based on UWB Devices*, Proceedings of 9th International Conference on Indoor Positioning and Indoor Navigation (IPIN), IEEE, Nantes, France, September 2018.
- 4) Zandian, Reza; Witkowski, Ulf; *Implementation Challenges of Synchronisation of UWB Nodes in TDoA Structures*, Proceedings of 9th International Conference on Indoor Positioning and Indoor Navigation (IPIN), IEEE, Nantes, France, September 2018.
- 5) Zandian, Reza; Witkowski, Ulf; *Evaluation of H-infinity Filter in Time Differential Localization Systems*, Cimdins, M.; Hellbrück, H. (Eds.), Proceedings of the 3rd Expert Talk on Localization, Technical report in TU Braunschweig, DOI: 10.24355/dbbs.084-201807191253-0 , Lübeck, Germany, 2018.
- 6) Zandian, Reza; Witkowski, Ulf; *Anchor Pair Selection in Unilateral TDoA Localization Topologies*, Cimdins, M.; Hellbrück, H. (Eds.), Proceedings of the 3rd Expert Talk on Localization, Technical report in TU Braunschweig, DOI: 10.24355/dbbs.084-201807191327-0 , Lübeck, , Germany, 2018.
- 7) Zandian, Reza; Witkowski, Ulf; *Robot Self-Localization in Ultra-Wideband Large Scale Multi-Node Setups*, Proceedings of 14th Workshop on Positioning, Navigation and Communications (WPNC), IEEE, Bremen, Germany, 2017.
- 8) Zandian, Reza; Witkowski, Ulf: Performance Analysis of Small Size and Power Efficient UWB Communication Nodes for Indoor Localization, Proceedings of 17th Conference Towards Autonomous Robotic Systems (TAROS), Springer, UK, 2016.
- 9) Zandian, Reza; Witkowski, Ulf, B. Kumar Maharjan: *Tree Network Based on Bluetooth 4.0 for Wireless Sensor Network Applications*, In 6th European Embedded Design in Education and Research Conference (EDERC 2014), Milan, Italy, 2014.
- 10) Zandian, Reza; Witkowski, Ulf; Boor, Micheal: *Programming and Debugging using NFC Technology*, First Workshop of Mobile applications, Secure Elements and Near Field Communication MOBISECNFC 2014, Florida, USA, 2014.

- 11) Zandian, Reza; Witkowski, Ulf: *Novel Method of Communication in Swarm Robotics Based on NFC Technology*, 14th Intl. Conf. Towards Autonomous Robotic Systems (TAROS), Oxford, UK, 2013.
- 12) Zandian, Reza; S. Virk, Gurvinder: *A novel method of movement for pipe inspection robot using Uniball*, CLAWAR Conference Maryland, USA, 2012.
- 13) Zandian, Reza; S. Virk, Gurvinder: *Improving Operational Efficiencies of PV systems*, UPEC Conference, Soest, Germany, 2011.

# Co-authored Publications

- 14) Philipp Bolte, Joyce Martin, Ulf Witkowski, Reza Zandian; *Implementation and Validation of Kalman Filter Based Sensor Fusion on the Zorro Mini-Robot Platform*, Proceedings of 19th Conference Towards Autonomous Robotic Systems (TAROS), Springer, UK, 2018.
- 15) Joaquin Sitte, Ulf Witkowski and Reza Zandian; *Learning with small autonomous robots*, Proceedings of 4th International Conference on Robot Intelligence Technology and Applications (RiTA 2015), South Korea, 2015.
- 16) Philipp Kemper, Thomas Tetzlaff, Ulf Witkowski, Reza Zandian, Michel Mamrot, Stefan Marchlewitz, Jan-Peter Nicklas, Petra Winzer, *Small Size Robot Platform as Test and Validation Tool for the Development of Mechatronic Systems*, Proceedings of 4th International Conference on Robot Intelligence Technology and Applications (RiTA 2015), South Korea, 2015.
- 17) Philipp Kemper, Jürgen Grüneberg, Ulf Witkowski, Reza Zandian; *Industry 4.0: Challenges and Potentials through Digitization*, Proceedings of international Conference on Innovation, Entrepreneurship and Technology (ICONIET), BSD City, Indonesia, 2015.
- 18) Reza Zandian, Thomas Tetzlaff, Lukas Drüppel, and Ulf Witkowski; *Smartphone Controlled Robot Platform for Robot Soccer and Edutainment*; Robot Intelligence Technology and Applications 3, Advances in Intelligent Systems and Computing, Volume 345, 2015, pp. 505–518, Proceedings of 3rd International Conference on Robot Intelligence Technology and Applications (RiTA 2014), China, 2014.
- 19) Thomas Tetzlaff, Michael Boor, Ulf Witkowski, and Reza Zandian; *Low Power Network Node for Ambient Monitoring and Heartrate Measurement*, In 6th European Embedded Design in Education and Research Conference (EDERC), Milan, Italy, 2014.
- 20) Michael Boor, Ulf Witkowski, Reza Zandian; *Hybrid Communication System for Long Range Resource Tracking in Search and Rescue Scenarios*, M. Mistry et al. (Eds.): TAROS 2014, LNAI 8717, pp. 120–130. Springer International Publishing Switzerland, 2014.